University of Glasgow

Morton, Graham H. (2013) *Performance Comparison and Simulation of Permanent Magnet AC Drives and Parameter Estimation Techniques.* PhD thesis.

http://theses.gla.ac.uk/3790/

Copyright and moral rights for this thesis are retained by the author

A copy can be downloaded for personal non-commercial research or study, without prior permission or charge

This thesis cannot be reproduced or quoted extensively from without first obtaining permission in writing from the Author

The content must not be changed in any way or sold commercially in any format or medium without the formal permission of the Author

When referring to this work, full bibliographic details including the author, title, awarding institution and date of the thesis must be given

Glasgow Theses Service
http://theses.gla.ac.uk/
theses@gla.ac.uk

Performance Comparison and Simulation of Permanent Magnet AC Drives and Parameter Estimation Techniques

Graham H. Morton
MEng

Submitted to the University of Glasgow, School of Engineering, in fulfilment of the requirements for the Degree of Doctor of Philosophy.

November 2012

©2012 Graham Morton

Abstract

This thesis presents research on common PWM switching strategies implemented with permanent magnet AC machine drives. This study also considers online parameter estimation techniques that can be implemented with such drives. Finally a new simulation model of the drive and tools for modelling the specific machine under test are presented.

Initially the research focuses on comparisons of the performance parameters which are influenced by the differences in current control strategies. Bang-Bang, PI and SVPWM controllers are the three alternative switching strategies which are discussed and then evaluated. The results highlight the impact the strategy selection has on the phase current quality and hence the power output of the motor under test. PI and SVPWM are both strategies that utilise a fixed switching frequency and as a result exhibit larger power losses in the inverter stage of the drive system. Bang-Bang control is seen to exhibit greater power losses in terms of output power in the motor stage as a direct result of the poor quality phase current waveform generated. The experiments conducted allow for a thorough comparison of each strategy outlined.

Techniques used to estimate the average phase voltage commanded under operation are presented in this thesis. Techniques for estimating phase voltage when operating the SVPWM technique on a wye connected machine is described, as are techniques for use with both PI and SVPWM control of a delta connected machine. This is based on published techniques that have been implemented for the PI wye connected case. The voltage estimation techniques are then used to estimate the flux linkage waveforms of the machine under test. Validation for this technique is sought through comparison of measurements with predictions made using commercially available finite element analysis tools; the measurements and predictions are shown to correlate to a significant degree. In search of validating the techniques against measurements made with calibrated measurement equipment – known to be reliable – the validation path results in subsequent techniques to be developed which estimate the average torque output of the machine under test. Torque measurements made using commercially available torque transducer equipment are compared with online estimates allowing for a validation of the voltage estimations.

Using a new simulation environment – Portunus from Adapted Solutions – a modern permanent magnetic synchronous machine drive system has been modelled. Making use of a PMSM component developed by Dr Mircea Popescu of Motor Design Ltd, a model of the drive system is constructed by the addition of customised components of the controller technology and other drive system hardware. This includes a custom developed C++ model of the SPEED laboratory FCIV technology which is used to control the drive system used in this research. Use of standard Portunus logic components is also presented which effectively models the interface of the gate drive signals with the voltage inverter components of the drive system.

Finally the thesis details the results of simulations modelling the comparison of the control strategies of chapter 2 and also the online estimation techniques of chapter 3. The simulation model's inclusion of a dedicated machine component allows for effective tailoring of the system model on a per machine basis; this allows for a comparison of the results presented in the initial testing with the simulated equivalents. Such a comparison is also made between the results of the testing of the online torque estimation techniques and the simulated response of the estimation techniques. Strong correlation is shown between the results of the testing carried out in the early stages of the research using the drive system outlined in chapters 2 and 3 with the simulation results obtained using the model outlined in chapters 4 and 5.

Acknowledgements

I would like to thank my supervisor Calum Cossar for the tremendously positive impact he has made upon my engineering career. Since coming under Calum's stewardship early in my undergraduate career I have had many opportunities to pursue personal and professional interests including working abroad and exploring this PhD research. Calum has been responsible for advising and guiding my research in addition to providing support and solutions for the various hurdles which have had to be overcome throughout my studies. A great deal of thanks is owed to Calum for helping me acquire the knowledge and experience required to write this thesis.

I would also wish to thank Professor Andrew Knox who has in his role as my 2nd supervisor always made available to me his vast knowledge and experience of both academic and industrial engineering. I would also like to acknowledge the technical expertise and support given to me throughout my research by Ian Young and Peter Miller. These gentlemen were strongly influential in providing me with the test facilities and equipment used in this research and for ensuring I used it safely.

I would like to thank the Engineering and Physical Sciences Research Council for providing me with financial support required during my study. I would also like to thank Omar Benzaid of SEM for providing the motors used in this study, Professor T.J.E Miller for allowing me the use of his power analysis equipment for the duration of my research and Lilo Bluhm of Motor Design Ltd for providing me with the required licenses to use the Adapted Solutions/Portunus software tools. I would also like to thank Dr Mircea Popescu of Motor Design Ltd for providing me with his PMSM model component which I have utilised in large portions of this research.

I would like to thank my fellow research colleagues at the University. Dr James Buckle, Dr Joseph Malone, Andrea Montecucco, Matthias Willig, Jeremiah Matthey, Ed Pratt, Jonathan Siviter, Craig Clanachan and Liam MacIsaac. Through both academic and social interaction with this group of academics throughout my research – this thesis has benefited. I would particularly wish to thank Liam MacIsaac whose expertise in software engineering has helped me develop many skills essential to my research.

Finally I would like to acknowledge the enormous debt I owe my family for their support throughout my entire academic career. My Father and Mother - Peter and Margaret Morton, who have given me essential financial support throughout my education and research. My Sister, Louise Morton stands alongside my parents as having offered me a great deal of moral support and motivation throughout my studies. Having guided me through the various highs and lows of my research, my family have been the level foundation upon which I have been able to build my achievements.

Contents

List of Figures

List of Tables

Nomenclature

PMAC – Permanent Magnet Alternating Current

VSI – Voltage Source Inverter

EMF – Electromotive force

Kt – Torque to Current ratio

PMSM – Permanent Magnet Synchronous Machine

PWM – Pulse Width Modulation

EPS – Electrical Power Steering

EV – Electric Vehicles

HEV – Hybrid Electric Vehicles

DSP – Digital Signal Processor

BJT – Bipolar Junction Transistor

MOSFET – Metal Oxide Silicon Field Effect Transistors

IGBT – Insulated Gate Bipolar Transistor

GTO – Gate Turn Off Thyristor

MCT – Metal Oxide Silicon Controlled Thyristors

GIT – Gate Injection Transistors

AC – Alternating Current

PI – Proportional Integral

PID – Proportional Integral Differential

DC – Direct Current

SV – Space Vector

SVPWM – Space Vector Pulse Width Modulation

SVM – Space Vector Modulation

DTC – Direct Torque Control

CAD – Computer Aided Design

FCIV – Flexible Controller version 4

RMS – Root Means Square

ADC – Analogue to Digital Conversion

QEP – Quadrature Encoder Pulse

DAC – Digital to Analogue Conversion

Kp – Proportional Gain Term

Ki – Integral Gain Term

FOC – Field Orientated Control

ANN – Artificial Neural Networks

AI - Artificial Intelligence

FFT – Fast Fourier Transform

FEA – Finite Element Analysis

ψ-i - Flux Linkage versus Current

FEM – Finite Element Method

Ld, Lq – Inductance in the d and q axis

MMF – Magnetomotive Force

IPM – Interior Permanent Magnet

VHDL-AMS – VHDL Analogue and Mixed Signal Extensions

VHDL – VHSIC Hardware Description Language

VHSIC – Very High Speed Integrated Circuits

Chapter 1
Introduction

This chapter begins by first outlining the structure of this thesis, highlighting the research to be presented. This is followed by an outline of the objectives of the research and the original contributions of it. Following this the Permanent Magnet Alternative Current (PMAC) machine is introduced and literature highlighting its role in modern society is summarised. This is followed by a review of literature in relation to the Voltage-Source Inverter (VSI) and modern current control techniques. The previous contributions and works detailing the area of online estimation techniques are also discussed.

1.1. Thesis Structure

The structure of the thesis will be outlined in this section. Further literature related specifically to the topic of a chapter is reviewed in that chapter. The list of the author's publications is given on page 220.

In Chapter 2 a description of the implementation of three common current regulation strategies is described. Comparisons of the performance of each of these regulators are presented for three motors of different power ranges and phase connection.

In Chapter 3 an average phase voltage estimator is described for both the delta and wye connected machine which can be applied under the PI and SVPWM control strategies previously discussed. This is expanded to include an online estimator for both flux linkage and torque output. The chapter also discusses the impact of voltage loss considerations and presents results which validate the techniques outlined.

In Chapter 4 a simulation model of the PMSM test bench used throughout the research is described. This includes a description of the simulation environment used and then discussion of each of the components of the system and how they are constructed for the model. Partial validation of the model is presented in the form of successful phase current regulation results.

In Chapter 5 a more comprehensive validation of the simulation model described in Chapter 4 is presented. This is done through comparing simulated results with the measured results presented in Chapter 2. The chapter also describes a simulation of the online estimation techniques described in Chapter 3 and presents results which further validate both these techniques and also the simulation model itself.

Finally, overall conclusions are summarised and potential expansions of the research are described as future work in Chapter 6.

1.2. Thesis objectives

Modern VSI driven 3 phase PMSM's are capable of utilising a number of different current regulation strategies. From the motor design engineer and application engineer's perspective a comparison of common control strategies is required which defines the impact each strategy has upon key performance characteristics.

DSP controlled drive systems such as that outlined in this thesis are capable of carrying out online estimations of the performance parameters of the machine being driven. In this research "online" is used to describe the real-time estimation of performance parameters. Investigation into such techniques and subsequent validation is required.

The PMSM test bench is a complex electrical and mechanical system which can be optimised when operating conditions can be predicted. A validated simulation model of a typical PMSM drive test system would be beneficial to both a motor design engineer and the applications engineer.

Therefore, the main objectives of the thesis are defined as follows:

- To compare several PMSM performance parameters when tested under different common current control strategies and make evaluations based upon the comparison of these performance criteria.
- To investigate online parameter estimation techniques which can be applied to different machine types and implemented whilst operating the current control strategies investigated.
- To develop and validate a simulation model which can predict the performance of the PMSM test system used throughout this research.

1.3. Original Contributions

The original contributions of the research are listed for each chapter.

Chapter 2 Comparing Common PMSM Switching Strategies

- The chapter describes an “on-the-fly” test process in which the current control strategies are interchangeable and thus steady state conditions and wider experimental conditions are consistent for the results which are compared.
- Measurements of the average switch frequency commanded by the Bang-Bang current regulator are presented.
- The impact of controller selection when testing the torque constant Kt is quantified
- The impact of controller selection on various system power losses and resultant efficiencies is also quantified.

Chapter 3 Online Parameter Estimation

- Wye connected PI regulated voltage estimation (first reported in [1]) has been expanded and SVPWM regulated voltage estimators have been developed.
- Delta connected PI and SVPWM regulated voltage estimators have been developed.
- Wye connected PI (first reported in [1]) and SVPWM regulated flux-linkage estimators have been developed.
- Delta connected PI and SVPWM regulated flux-linkage estimators have been developed.
- Wye connected PI (first reported in [1]) and SVPMM average output torque estimators have been developed.
- Delta connected PI and SVPWM average output torque estimators have been developed.

Chapter 4 Modelling the PMSM Test Bench

- A new mixed signal (incorporating the PM model reported by Mircea Popescu [2]) simulation model of the PMSM test bench.
- A dedicated FCIV DSP controller component has been developed for use in this simulation model.

- The creation of the FCIV DSP controller allows for portability of software functions between actual FCIV and the simulated equivalent.
- Validation of this new model is offered through results which confirm the successful regulation of phase currents under each of the three control strategies investigated.

Chapter 5 Validating the PMSM Test Bench Simulation Model

- Validation of the new simulation through comparison of the aesthetical qualities of the phase current predictions and the measurements presented in chapter 2 in both the time and frequency domains.
- Predictions of the average switch frequency commanded under Bang-Bang regulation which can be directly compared to the results presented in chapter 2.
- Validation of the new simulation model through comparison of torque predictions in response to operating speed and to field weakening conditions with results presented in chapter 2 and chapter 3.
- Validation of the new simulation model through comparison of input/output power and efficiency predictions of drive system with measurements presented in chapter 2.
- Validation of the online torque estimators presented in chapter 3 through simulation of techniques using new FCIV simulation component.
- An online voltage estimation technique when operating a Bang-Bang control is explored following the same principles outlined in Chapter 3.
- An online flux linkage estimation technique when operating a Bang-Bang control is explored following the same principles outlined in Chapter 3.
- An online torque estimation technique when operating a Bang-Bang control is explored following the same principles outlined in Chapter 3.

1.4. PMAC Machines

A typical Permanent Magnet AC (PMAC) motor consists usually of 3 phase windings on the stationary outer frame of the machine (stator) and permanent magnets, typically rare earth magnets such as Neodymium-Iron-Boron (NdFeB), on the rotating shaft (rotor)[3].

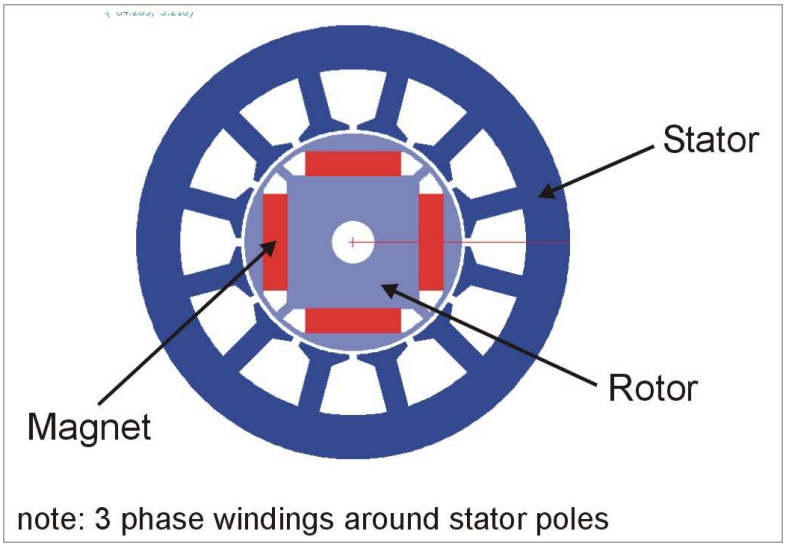

Figure 1-1: Cross section of typical PMAC motor

Figure 1-1 shows a cross section of a typical PMAC machine. It is worth noting the features of the machine [4, 5]:

- The permanent magnets of alternating polarity are fixed to the rotor, the number of these north-south (NS) pairs of magnets attached to the rotor is also known as the number of pole-pairs (p) of the machine.
- There are three phase windings distributed throughout the stator, these are known as the stator windings and are evenly spaced 120° out of phase from each other.
- In PMAC machines the stator windings are distributed sinusoidally around the machine's airgap. This ensures that the Magnetic Flux Density (Ψ) varies sinusoidally along the airgap and also gives rise to a sinusoidal back EMF being generated in the stator windings.

A PMAC machine is generally better known as a Permanent Magnet Synchronous Machine (PMSM) with AC phase excitation; there are also PMSM's with rectangular phase excitation requirements.

1.5. Torque Generation

In order to overcome the sinusoidal back EMF wave produced in the machine, and thus generate torque output from the machine, the excitation currents in the stator winding must also be sinusoidal.

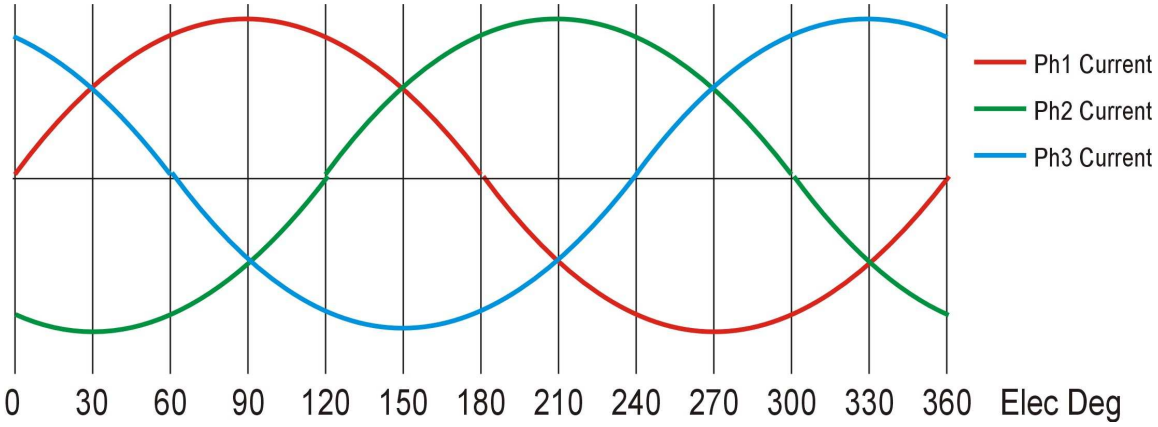

Figure 1-2: Ideal 3 Phase Current Distribution for PMAC motor

Figure 1-2 shows an ideal current distribution for a PMAC machine, this is characterised by sinusoidal current waves of equal magnitude and spatially distributed across the phases by 120°.

In real-world applications the torque generated in a machine will not be without undesired losses and effects. When considering the Torque of the machine there are three main components to consider. The nominal torque (desired) of the entire electromagnetic torque produced is of most interest in the application of the machine. The other relevant forms of torque are the cogging torque and the ripple torque, both of which are undesired. The cogging torque is entirely independent of stator current; it is a result of the interaction between the machines permanent magnets and stator construction. Ripple torque is directly related to stator current, it is caused by the stator currents interaction with the rotor flux [6]. Current content at frequencies other than the fundamental frequency of operation will contribute to the ripple torque. Previous works have shown that in certain machine designs, the ripple torque can be as large as up to 28% of the nominal torque output [7].

Unwanted harmonic content present in the phase current of a PMSM is the result of several system factors. The quality of the phase currents is completely governed by the fundamental limitations on the PWM inverter. This includes characteristics such as switching frequency, dead-time and noise in the current signals [8].

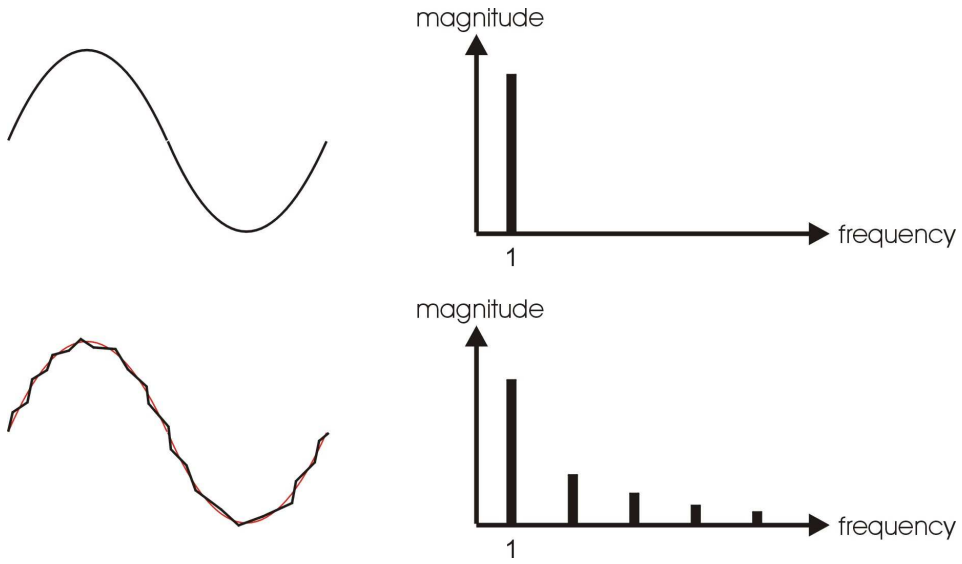

Figure 1-3: Harmonic Components of Phase Currents

In Figure 1-3 an example of well defined harmonic content is given in which the harmonic content is entirely restricted to the fundamental frequency. In this case the torque distribution of the motor will be smooth as the currents active in the phases are relative to the fundamental frequency. In a system with an erratic current signal, also shown in Figure 1-3, harmonics exist at values not relative to the fundamental frequency. This results in the machine producing torque which oscillates at frequencies other than the fundamental. Not only does this cause an inefficient torque distribution but is a problem that can cause the current control strategy to operate incorrectly. This has the potential to cause significant damage to the system. Generally this can be summarised by stating that significant harmonic content is a source of instability in a system [9].

1.6. Applications of PMSM machines

PMSM machines are now used extensively throughout the world in both an industrial and commercial sense. The following list gives some examples of the field of use and particular applications within that field, as described by Geiras and Wing [10]:

- In industry: Industrial drives such as pumps, fans, compressors and robots
- Public Utensils: Systems such as air conditioning units, automatic vending machines and theme park attractions.
- Domestic Equipment: Items such as washing machines, vacuum cleaners and lawn mowers.
- Transportation systems: Devices such as elevators, escalators, trains and boats

- Power Tools: Tools such as grinders, sanders and polishers

Advantages of the PMSM also include a large Torque to Current ratio (Kt), high torque density and wide speed ranges, this gives rise to PMSM's being used frequently in industry for servo systems and machine tool applications. They are also penetrating high volume/low cost applications such as electrical power steering (EPS) [11-14].

EPS is not the only application for PMSM in the automotive industry; electric vehicles (EV) in which an electrical machine is the main component for the generation of torque are also a keen area of research. There are many cases in literature which highlight the known advantages of PMSM's as reasons for selection in these vehicles [15, 16].

Further development in the EV field had given rise to frequent use of these machines in hybrid electric vehicles (HEV) [17-19], in which an electric machine and an internal combustion engine are both components of the powertrain. The Toyota Prius is an example of a HEV in mass production which makes use of PMSM's in its electromechanical transmission system. In fact the Prius makes use of two of these machines, a motor and a generator [4, 20, 21].

1.7. Modern PMAC Control

1.7.1. Hardware

Since the introduction of Digital Signal Processors (DSP) in the late 1970's the control of PMSM machines has moved from the use of linear power amplifiers in favour of using switched-mode power circuits [22]. This has led to the introduction of Voltage Source Inverter's (VSI) which are controlled by a DSP stage. The research of Matsui and Ohashi [23] is among some of the first which detailed the higher level of control a DSP could provide. In addition to this work Pillay et al [24] demonstrated the use of the DSP in current feedback sensing and rotor position sensing in addition to performing control algorithms.

The modern VSI is typically driven using PWM signals generated in the DSP control stage and is typically constructed using power devices capable of being used as switches. Typical device choices have included Bipolar Junction Transistors (BJT's), Metal Oxide Silicon Field Effect Transistors (MOSFET's), Insulated Gate Bipolar Transistors (IGBT's), Gate Turn Off Thyristors (GTO's) and Metal Oxide Silicon Controlled Thyristors (MCT's) [25].

IGBT's are a common choice of switching component in modern applications, offering higher voltage capability, higher input impedance and superior conductivity. However higher switching frequencies can be observed with alternative switch devices such as MOSFET's; thus the drive system requirements need considered analysis before switch device selection can be made [26, 27].

Whilst IBGT's are common place in modern PMSM controllers there are emerging devices which are beginning to challenge the dominance of IGBT's in this field. Gallium Nitride (GaN) based transistors known as Gate Injection Transistors (GIT) are now providing encouraging performance results which promote their use in the future [28, 29].

1.7.2. Motor Control Strategies

Three phase AC machines have long existed in industry and research applications before the PMSM was considered. The machine primarily used in the past, and frequently used today as an established alternative to the PMSM is the Inductance machine. Thus many of the established current control techniques discussed below have been developed using induction machines; however the vast majority of operating principles are the same for PMSM's.

This section will address the historical development of motor control strategies toward the current control strategies which will feature predominantly throughout this thesis. This will begin with a discussion on the earlier VSI based control techniques such as the six-step voltage controller before going on to discuss the development of phase current control strategies such as the Space Vector controller.

1.7.3. Six-Step Voltage Control

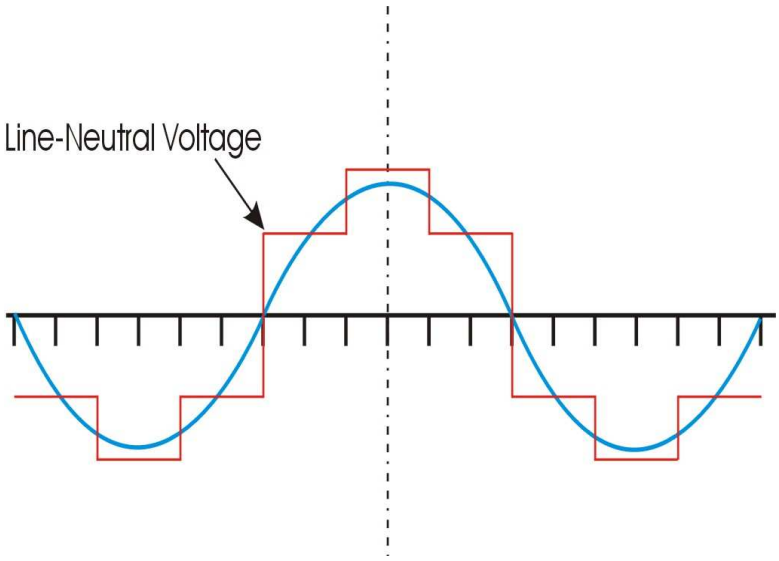

Figure 1-4: Line-neutral voltage wave of a Six Step controller

One of the earliest methods of motor control making use of a VSI or similar device is known as the six-step voltage control. This technique involves sequentially generating each of the 6 non-zero voltage vectors across 60° sections of the current wave (VSI output voltages and operation will be discussed in greater technical detail later) across the phases of the motor [4].

Early examples of research on PWM based drives, which also highlight early switching device limitations, include that of Adams and Fox [30] and also from Grant and Barton [31]. These works investigate how PWM techniques can be applied to a six-step control strategy; thus allowing current, voltage, speed or other output parameter control that a non-modulated six-step controller could not provide.

1.7.4. Hysteresis Current Control

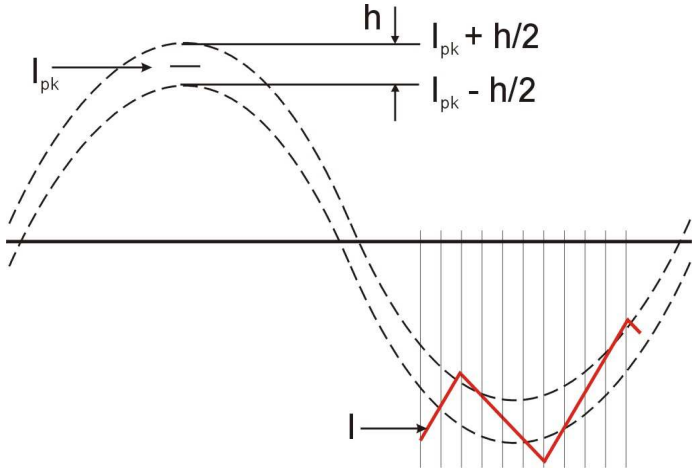

Figure 1-5: Hysteresis Current Controlled Waveform

Hysteresis controllers are another example of an early current control technique. The technique is based upon the switching of the phase voltage connections as a result of feedback from current sensors. The phase current is tested to determine whether or not its value lies within a band of tolerance situated around the desired current value. This band is known as the hysteresis band. Many current control reviews exist which include hysteresis controllers, providing suitable implementation guides and also performance evaluations. They are typically evaluated positively for their simplicity and robustness to load parameter changes; however known disadvantages of hysteresis controllers include widely unpredictable switching frequencies and there are associated difficulties with designing protection circuits for the inverter system [32-35].

Publications continue to be produced in respect to the issue of improving controller performance, at the heart of which is the hysteresis controller. Perhaps the most renowned work on the adaptation of the Hysteresis controller is that of Bose [36], who presented an adapted version, aimed at addressing the main disadvantage of unpredictable switching frequency. Research from Malesani et al [37] sought to make use of improved hysteresis controllers in the more complex modern motor control systems. This is also demonstrated in the more recent publications of Kovari, Tiwari et al, Bolognani and Chen [38-41].

1.7.5. Triangle Comparison Regulation

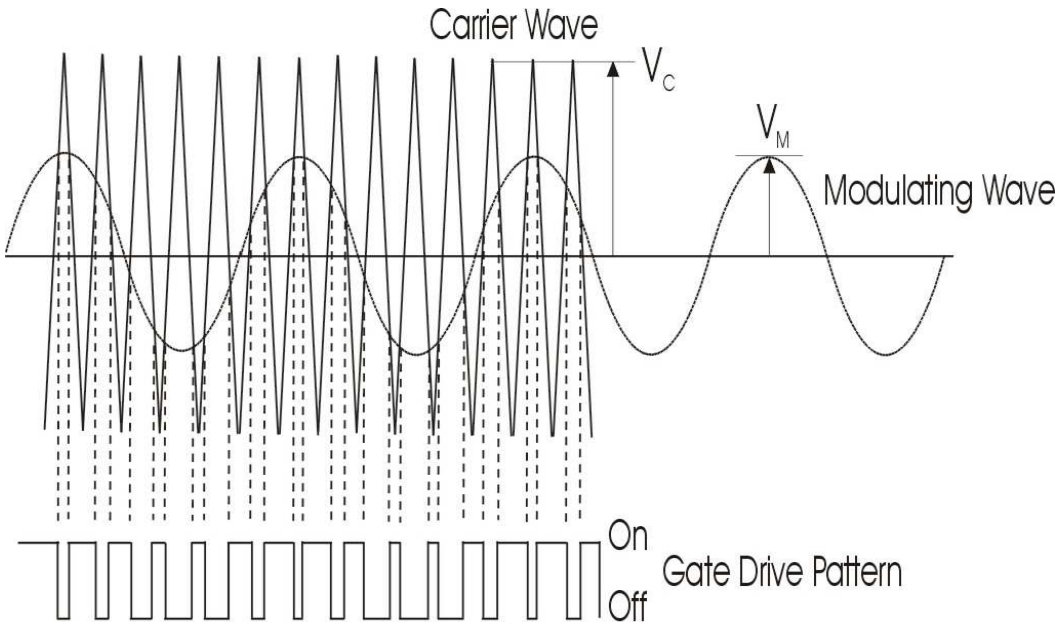

Figure 1-6: Triangle Comparison Regulation example

Sine/Triangle ramp comparison controllers are referred to in the publications of Hendershot and Miller [4] and of Yu [42]. These controllers are among the first to be considered as a PWM control method. The method is based upon generating PWM gate drive signals for the complimentary phase switches of the inverter. A sinusoidal modulating wave is compared to a triangular carrier wave which oscillates at the sampling frequency. The intersections of the two waves determine the switching of the phase switches with a modulating index that is related to the respective wave amplitudes. This method is now outdated and very rarely arises in industry or research areas; thus explaining a lack in significant research publications on the method. Despite this the controller is commonly recognised as being important in the history of PWM based control techniques.

1.7.6. PI Current Control

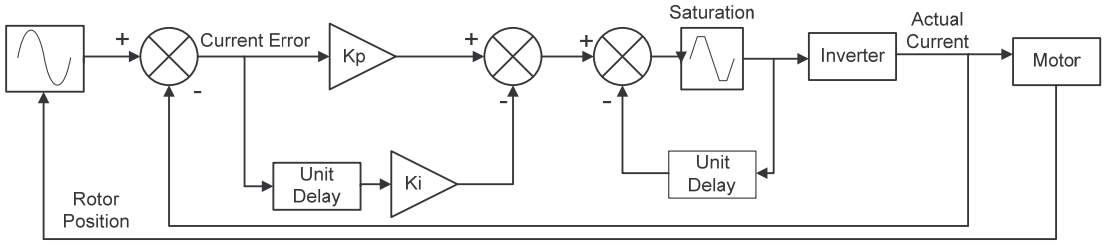

Figure 1-7: Block Diagram of a Typical PI Controller

An established PWM current control technique which sees continued use in both industrial and research environments is that of Proportional-Integral (PI) control; different combinations of the Proportional-Integral-Differential (PID) control options exist, however PI control is the most popular in motor control applications. The PI controller was developed at a time when fixed switching frequency of VSI's was sought in order to better understand the effects that switching has upon the current content of the motor system.

Early research such as that of Maswood [43] detailed the implementation of a PI controller with DSP technology, citing the fixed switching frequency as a main advantage of the approach. The technique involves making use of gain terms defined by a user with phase current feedback. Control logic then determines a PWM gate drive signal which when fed to the VSI commands the desired current during the next sample cycle. In a direct phase implementation of a PI control, there will be three separate PI control algorithms each of which are responsible for controlling a single phase; PI control logic is however used in far more complex approaches than this, as will be detailed later.

One of the largest areas of research in PI control techniques is that of determining the gain terms to be used. The use of fuzzy logic in adaptive PI control approaches are outlined in the works of Suyitno et al [44] in an original research which explored the automation of PI gain tuning. This has been furthered explored by Miki et al [45] and more recently reviewed by Tan Chee et al [46].

1.7.7. Synchronous Current Control

Synchronous control, often referred to as field oriented control, is a mathematically intensive control strategy that became popular in motor control during the late 1970's thanks to the strong research works of Leonhard et al [47] who first explained the use of the technique with DSP technology.

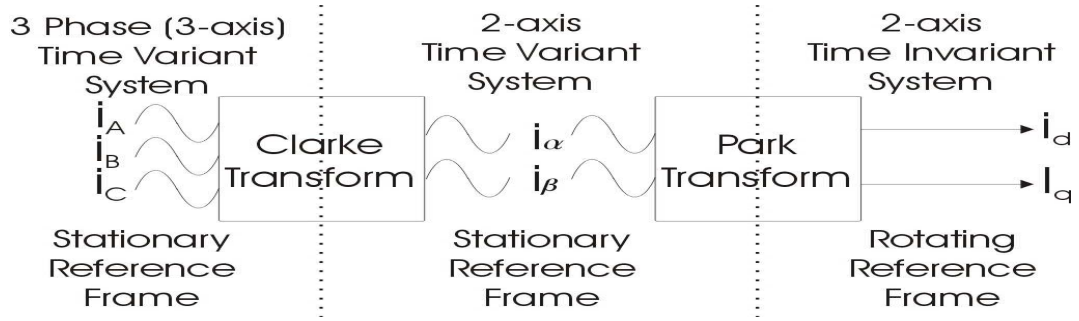

Figure 1-8: Transformation of 3 phase AC system to 2 phase DC System

The principle objective of synchronous control is to consider the 3 phase AC electrical machine as an equivalent DC machine. This is achieved through the use of mathematically intense transformations. The first transformation converts the stationary 3 axis reference frame (3 phase AC machine) to a 2 axis rotating reference frame; this transformation was first outlined by Edith Clarke [48] in 1938. The second transform converts the 2 axis rotating reference frame to a 2 axis stationary frame; this transformation was first detailed in 1929 and developed in 1933 by R.H Park [49, 50]. The resultant reference frame axes are referred to as the direct (d) axis and quaderature (q) axis, collectively referred to as the dq axes. The use of these transforms in representing a 3 phase AC machine as a 2 phase DC machine has been reviewed effectively many times in literature [51-53].

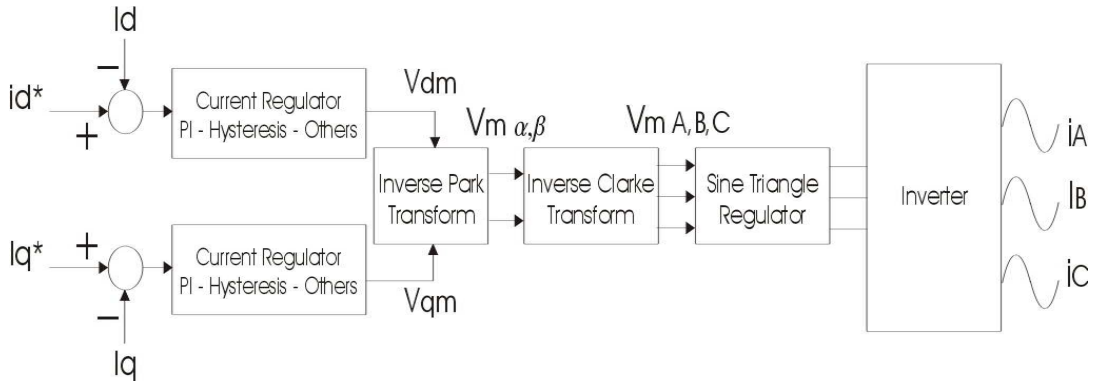

Figure 1-9: Synchronous Regulator

With the phase currents represented as dq axes currents, the current regulation can now occur on the two DC current signals. The control logic used at this step can be any of the previously outlined techniques, operating upon current feedback and reference current waves which are represented in the dq axes. Hendershot and Miller [4], outline a synchronous controller which makes use of a sine-triangle strategy in generating the phase voltage waveforms.

1.7.8. Space Vector Control

Space Vector (SV – sometimes SVPWM) control can be thought of a form of synchronous control. SV makes use of the same Park and Clarke transforms; the current regulation is where the controller differs. The publication of Stulrajter et al [54] reviews the differences in synchronous regulation and SV regulation. The SV regulator generates reference voltage vectors, from the current control loop, which are used to create PWM drive signals; these are fed to the inverter [25, 55]; greater detail of this process will be described later.

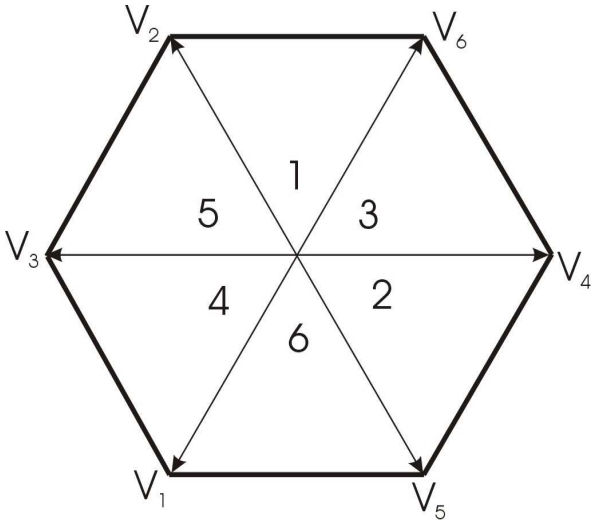

Figure 1-10: Space-vector hexagon

Early research into the combination of DSP and VSI technology for machine drive systems, such as that of Pfaff and Wick [56], widely recognises the contribution of Kovacs and Racz [57] in developing the space vector representation of the terminal voltages and currents of a synchronous machine. The space vector makes consideration of the possible configurations of stator voltages that can be applied to a machine at any time. The earliest available publications of its use include those of Pfaff et al [56] and A. J. Pollmann [58] . Joachim Holtz first published work which features the space vector modulator (SVM) in 1988 [59]. Since this first publication there are many further examples of Holtz's work with SVM which have led to a high regard toward his work in this field [60-64].

There are several other areas of exploration in relation to the control of PMAC and other synchronous machines; these include and are not limited to multi-level converters and artificial neural networks. These topics are relevant in modern PMAC control; however they are not of interest in this thesis.

1.8. Field Weakening

Field Weakening is a concept that arises frequently in motor control; it is of particular importance when the application involves the use of a machine towards the higher end of its rated speed range. The initial works regarding the use of field weakening were introduced by Bader and Stephan [65] who had sought to extend the range of applications for early electric vehicles. Their research explored how a constant power output could be maintained in the high speed region of a machine, thus extending the useful speed range of existing machines. This concept was more thoroughly developed in the work of Nabae et al [66] who further explained that field weakening was achieved through the weakening of the d-axis flux in the machine. This is achieved through the injection of current into the d-axis. A more comprehensive evaluation of the application of field weakening was presented by Soong and Miller [67] which also introduced the concept of designing the machine to allow for optimal use of field weakening. This is a subject which is still frequently revisited in research. Publications such as that of Chaithongsuk et al [68], which seeks to optimize machine design for field weakening performance in drives intended for transportation applications, continue to be produced. In addition to this there are also a number of publications which seek to incorporate field weakening into more modern regulation techniques, such as Direct Torque Control (DTC), the research presented by Rahman [69] and Lixin [70] are typical examples of this.

1.9. Online Parameter Estimation

Parameter estimation plays an important role in modern machine design. With initial introduction of synchronous machinery in heavy plant, there has been a requirement to better understand the output of a machine under specific operating conditions. An early example of such considerations is that of Penney [71] who sought to predict the short circuit torque produced in synchronous machines, a research prompted by damages caused to early Niagara Falls generators. In the more recent past, torque calculation has had to become more precise as the applications of synchronous machines have become more precise, machine tool spindles being a key example of an application where reliable torque performance is sought. The application of these estimations has also changed, the research of Howe and Low [72] being amongst the first publications to suggest performance predictions be used to optimize machine design. The publication of Clenet et al [73] is also among the earliest examples of Computer Aided Design (CAD) simulations being used to test design performance. More recently there have been many more high quality publications based upon the use of performance predictions in the optimisation of machine design [74-77].

The development of the current – flux-linkage diagram for online estimation of machine torque output was first introduced by Miller et all in 2003 [78]. This was motivated by the limitations of using the classical phasor diagram, which is heavily dependent upon the assumption of parameters such as open circuit back EMF remaining constant at constant speed. This work looked into the development of the torque based upon knowledge of the machine flux linkage and the instantaneous current. The results were heavily reliant upon making use of flux linkage values pre-determined from initial back EMF testing, limiting the “online” claim of the technique. This however was addressed in the follow up research of Cossar [1] published in 2006 which detailed methods for an online reconstruction of the terminal voltages. This then enables the online estimation of the flux linkage wave, removing the need for initial back-EMF sampling of the machine. The latest publication [79] on the technique details even further analysis of the diagram (commonly referred to as the i-ψ loop) has been furthered developed to cover the online estimation of the synchronous inductances present in the machine.

Chapter 2
Comparing Common PMSM Switching Strategies

This chapter investigates three common current control strategies. These strategies are the Bang-Bang Controller (similar in operation to the previously outlined Hysteresis controllers), the PI controller and the Space Vector PWM Regulator. The chapter gives greater insight into the author's previous publication [80] which compares three common switching strategies implemented as a current controller. The implementation of each of the controllers is described, highlighting the advantages and disadvantages of each approach. A detailed look at the output performance parameters is also discussed, highlighting the performance of each technique with respect to parameters such as inverter efficiency and also torque to current ratio (constant Kt). Such considerations are rare in the popular and well cited publications in literature which addresses the comparisons between control strategies. The evaluation attempts to address the goals that a typical design engineer would target when designing for new applications.

The chapter initially discusses the history of the VSI and DSP technology with respect to the control of electrical machines. This is followed by a description of the common synchronous motor drive system which is implemented in the study presented in this chapter. Following this the control techniques under scrutiny are described in detail with particular focus on their implementation using a common motor drive DSP platform. Following this there is a description of the "on-the-fly" test process used to gather the results presented, giving the comparison an experimentally valid foundation. The performance data acquired and supplementary calculations are then explained to allow for an understanding of the performance parameters upon which the drive systems are compared. Following this is a comprehensive presentation of the results gathered using each control technique on a range of electrical motors of varying current, speed, torque and power ratings. This is followed by a summary of concluding statements drawn from

the results presented, highlighting in particular the key contributions this study has made in this particular research area.

The conclusions highlight the merits of selecting each of the techniques based upon entirely separate performance criteria. The Bang-Bang controller is shown to offer greater returns in terms of efficiency in the Inverter and as a result of this performs well in considering the overall system efficiency; the PI controller offers greater returns when a trade-off between cost and performance is required and the SVPWM controller offers the most optimal performance in high precision applications in terms of both highest and most stable torque output across the range of operating speed. These conclusions are all drawn based upon the data gathered using the test process outlined.

2.1. Introduction

Direct comparisons of VSI based current control techniques have been researched in the past. As DSP technology has advanced over the years, the capability of digital current controllers has grown to accommodate ever more advanced regulation techniques. Periodically this has led to the publication of reviews of regulation techniques. One such review is that of Freere and Pillay [35] in 1990. This paper focussed heavily upon the comparison of synchronous regulation. Four techniques were compared, these were:

- Delta Modulator
- Hysteresis Modulator
- Ramp Comparison Modulator
- Space Vector Modulator

The publication contributed an insight to the design of each of these synchronous regulators and offered a useful performance comparison based upon test results, ultimately concluding that the highest performing controllers were the Hysteresis and Space Vector Modulator controllers; by contrast the poorest controller was the Delta Modulator. Whilst this publication provides a useful contribution to the field, there are some notable limitations to its usefulness. The results comparison itself could have been strengthened by comparing more of the output parameters of the systems under test. The evaluation is limited to switching frequency and RMS current error values, when in fact a number of additional performance parameters (such as efficiency) would be of

interest. Despite these limitations, this publication was among the first to review DSP based VSI techniques and as such made a valuable contribution to the field.

As the advancement of DSP and VSI technology accelerated heavily during the 1990's, the need soon arose for a more comprehensive evaluation of the modern current control techniques available. In 1998 Marian Kazmierkowski sought to address this with a more detailed review [32] of control strategies available. Unlike the publication of Freere, the work of Kazmierkowski looked to encompass a wider range of techniques, not restricted to the domain of synchronous regulations. By identifying first that the established techniques could be described in two main categories, linear and non-linear, the publication also identifies that the majority of techniques are available in either a stationary (per phase) operation or a synchronous operation. This research is a valuable contribution to the field in that it offers greater exposure to the wider variety of control techniques available, and also through a great level of detail towards the operation of each of these methods. By grouping these techniques as is outlined the author has been able to offer observations on the particular advantages and disadvantages associated with each approach thus offering a suitable platform from which to trade-off techniques under consideration for any given application. Unlike Freere's publication, Kazmierkowski's offers no direct comparison of the output performance of the techniques it describes. It does however provide an account of the techniques which are implemented commonly throughout PMSM drives in research and industry, thus its publication has provided a valued contribution to the field.

A comparison value of three strategies will be presented with an evaluation of performance across three different machines; these are outlined in the table below.

TABLE 2-1: Test Machine Profiles

Machine	Pole Pairs	Peak Torque Output (Nm)	Peak Power Output (W)	V_{DC} Link Voltage (V)
Interroll SD4BCu8S – 008	4	0.7	80	90
SEM HRS92C4-44S	2	1.2	250	100
Heidenhain QSY-1E	3	5.8	420	150

2.2. DSP based control - a Historical Review

The Voltage Source Inverter (VSI) has been a key component of machine drive technology since the early 1960's. During the early 1980's the machine drives field also expanded rapidly with the integration of ever-improving Digital Signal Processing (DSP) technology. In 1988, the highly respected B.K Bose produced a number of publications which provided a valuable review of machine drive advancement. One of these publications covered the emergence of new power electronic switch devices and how they were improving VSI technology [81]. A second publication [82] showed a clear path of progression of the VSI switch device from the thyristor through to Gate Turn Off (GTO) thyristors followed by MOSFET devices. There was even the foresight in this publication to highlight the emergence of the Insulated Gate Bi-Polar Transistor (IGBT) as an emerging technology that would improve VSI's.

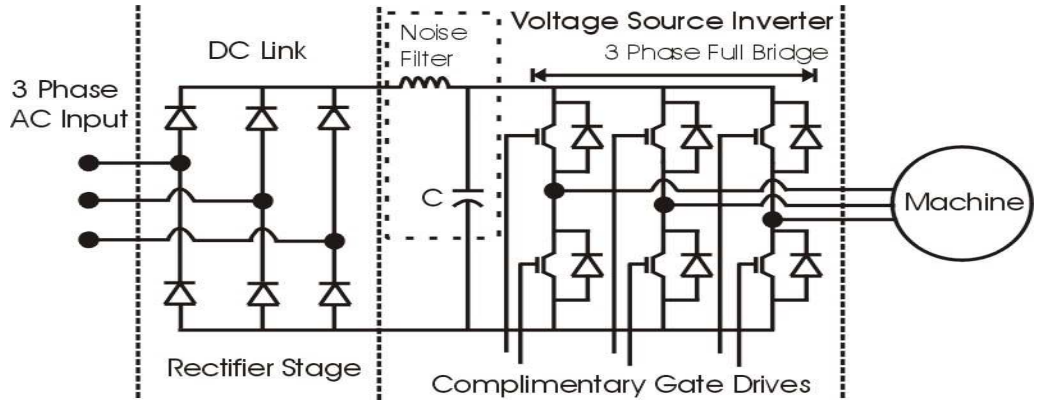

Figure 2-1: Typical Voltage Source Inverter with DC Link

Figure 2-1 shows a simplified diagram of a typical VSI and DC link configuration which is common in machine drive systems. The main operating component of the VSI is the inverter bridge which is comprised of 2 switch devices per phase leg. IGBT's are a common switch device selection in modern VSI's. An important feature of the bridge hardware is the free-wheel diodes shown in Figure 2-1. The diodes act to protect the switching devices from high negative current flow which occurs with inductive loads. The two switch devices of each phase leg are driven by complimentary gate signals from a logic controller (commonly a DSP).

In addition to the development of inverter technology, Bose also reviewed the emergence of DSP technology in motion control systems [83]. This particular publication highlights many of the advantages of DSP technology which make it common place in modern machine drive systems. Design concepts based on universal hardware, flexible control

software and the reduced volume of control electronics are correctly highlighted as strong advantages of the technology whilst the issue of quantization is correctly cited as an associated disadvantage. Bose also remarks upon the advancement of DSP technology itself allowing for the development of peripheral capabilities such as analogue to digital conversion (ADC) and configurable PWM outputs which are required in machine drive systems.

Whilst VSI and DSP technology has advanced over the years since the publications of Bose, allowing for far more advanced inverter technology and control techniques, the earlier publications in the field were responsible for contributing a generalised drive system model which has shown little change over time.

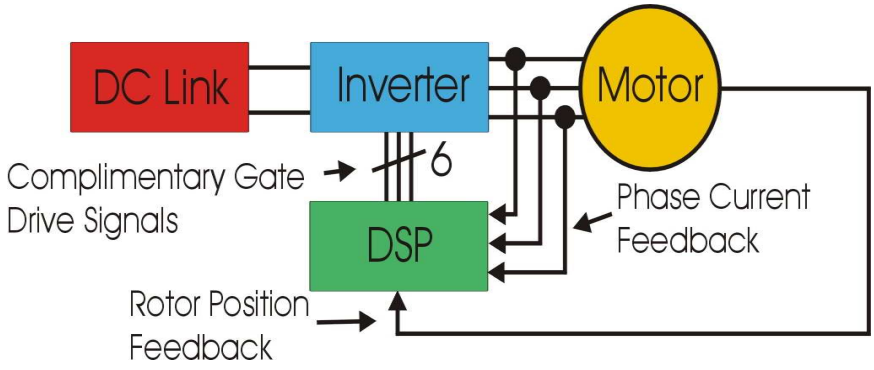

Figure 2-2: Block Diagram of Typical Motor Drive System

Figure 2-2 is a block representation of a typical PMSM drive system. The DC link supplies the inverter which receives drive signals from the DSP stage. The Inverter drives current through the phase connections of the motor thus producing a torque output on the rotor shaft. The DSP is usually dependant on feedback from rotor position sensors such as encoders or resolvers and also phase current feedback information from current sensors (however there is a wealth of literature available which considers sensorless systems in which these devices are not required). The DSP stage is the primary variable in a machine drive system; the hardware remains constant however the DSP can be programmed to utilize a variety of control strategies.

2.3. The modern PMSM Test Bench

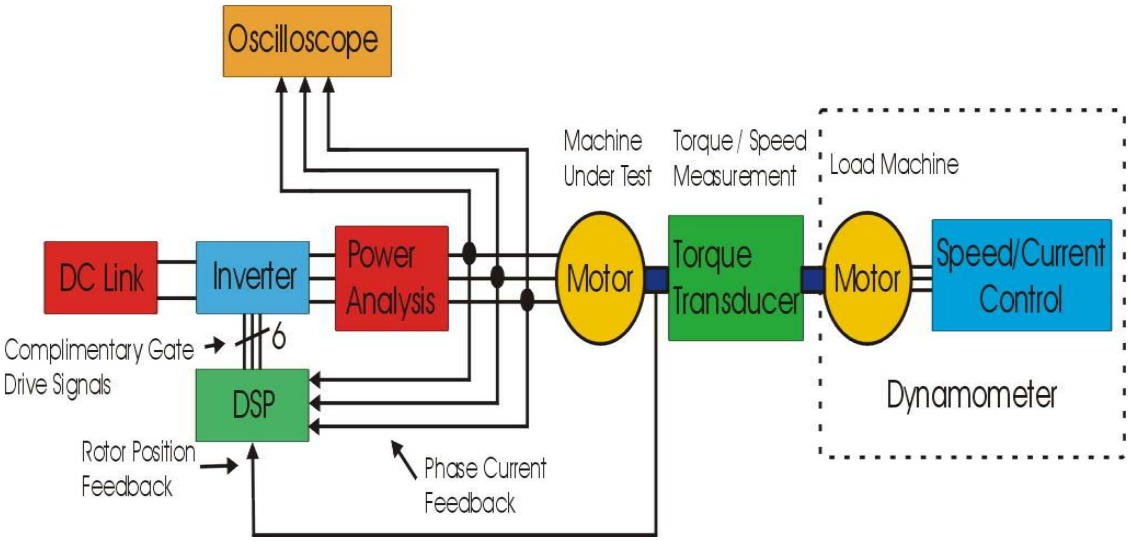

Figure 2-3: Block Diagram of Typical PMSM Test Bench

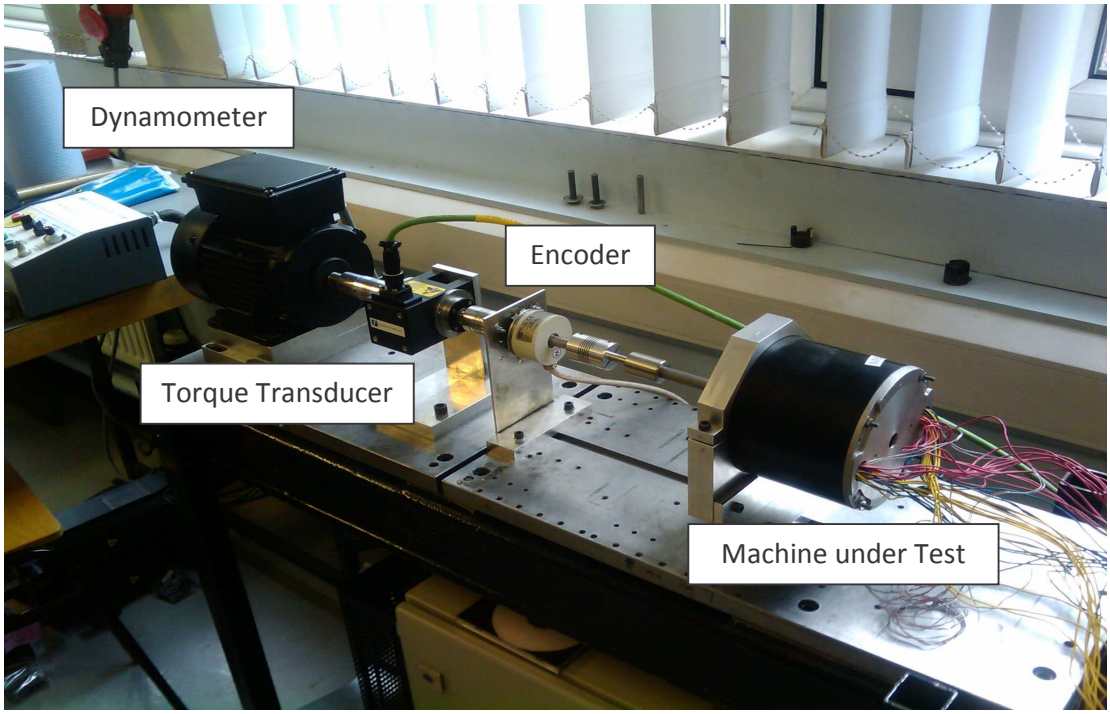

Figure 2-4: Photograph showing Test Bench used in this research

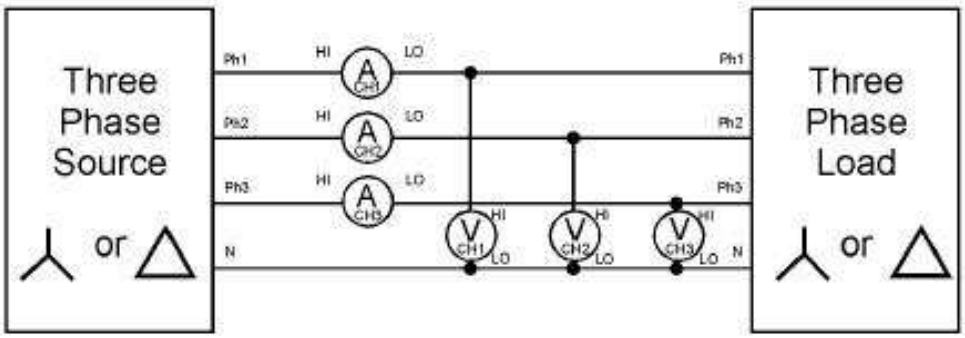

Figure 2-5: Wiring configuration for Power Analyser Equipment

Figure 2-3 is a block diagram representing a typical PMSM test bench; it represents that used in acquiring the results which are presented in this research. In addition to the components listed in Figure 2-2, there is also an Oscilloscope which provides a visual representation of the phase currents in addition to essential data acquisition capabilities. The power analysis equipment provides test data such as fundamental phase voltage and current measurements. The torque transducer provides torque and speed measurement from the motor shaft. The other key component in the test bench is the Dynamometer which is comprised of an additional machine and its associated control components. The dynamometer is capable of operating either a speed or torque control and through its use of dynamic braking is ideal for testing torque output at fixed speeds. The results presented in this research are gathered using the test bench outlined in Figure 2-3. Figure 2-4 shows a photograph take of the drive equipment used in this research, the machine shown is the SEM motor. Figure 2-5 shows a connection diagram for connecting three phase machines when a neutral line is not available from the equipment, it is commonly referred to as the three wattemeter method.

The specific equipment used in the test bench is typical of systems used in motor drive test rigs; however particular mention should be made of the DSP module. The DSP hardware is consistent for the three machines under test. It is used to implement each of the control strategies under test. The DSP stage is the SPEED laboratory Flexible Controller IV (FCIV) [84]. This system contains the Texas Instruments (TI) TMS320F2812 eZdsp^{TM} [85] board which utilises the TI TMS320F2812[86] DSP which is marketed primarily for use in motor control development. This DSP in combination with other hardware included in the FCIV contains a number of essential features which are used in motor control applications, including the work presented in this research. These include but are not limited to:

- PWM Waveform generation
- Programmable Deadband Generator
- Quadrature-Encoder Pulse (QEP) Circuit
- Analogue to Digital Conversion (ADC)
- Digital to Analogue Conversion (DAC)

The FCIV system has 4 phase complimentary gate drive outputs which are transmitted to the inverter via fibre optic transmitters which provide isolation between power and control supplies. In addition to this the FCIV also has inputs for QEP encoders or resolvers for rotor position information and 4 dedicated ADC channels for phase current feedback. The FCIV operates at a fixed sampling frequency of 20kHz for all machine tests presented in this research.

2.3.1. FCIV Main Control Loop

The FCIV (DSP stage) is identified as the main significant variable in the test bench outlined in Figure 2-3. There are however a number of consistencies within the operation of the FCIV which are important to describe.

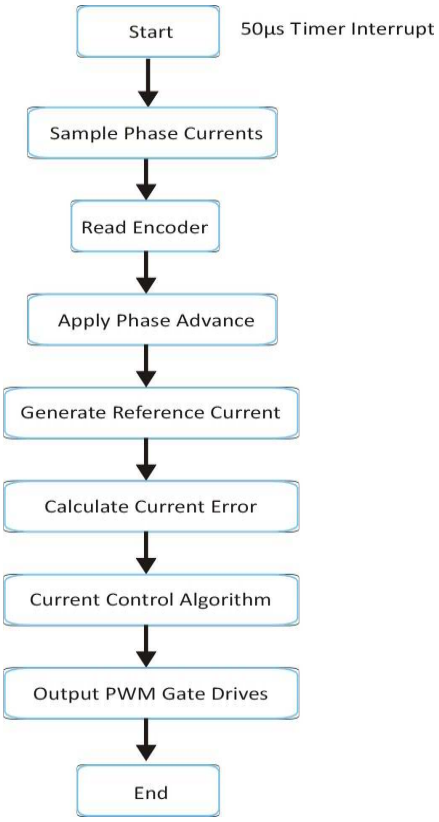

Figure 2-6: FCIV Main Control Loop Flow Diagram

Figure 2-6 gives a simplified flow diagram of the FCIV main control loop which is carried out every 50µs. This control loop is consistent for all machine tests presented in this research with one exception. The Current Control Algorithm block is changed to implement each of the three strategies studied.

2.4. Bang-Bang Control

The Bang-Bang controller has a relatively short history in the field of current regulation. The strategy has only seen use since the introduction of digital technology replacing hardware control stages in machine drive systems. The Bang-Bang controller can best be described as a modern digital adaptation of the classic Hysteresis regulator.

The Hysteresis controller is commonly attributed to an A.B Plunkett publication from 1979 on the introduction of transistorised machine drives; it is featured heavily in publications on PMSM drive systems [4, 32, 87-89]. The 1985 review of VSI drive techniques by Brod and Novotny [33] provides useful insight into the operation of the strategy. Figure 1-5 shows a typical Hysteresis waveform. The reference current wave resides at the midpoint of the hysteresis-band at any time during operation. The controller simply inverts the direction of current flow such that the actual current tracks the reference current with a defined level of current ripple (the hysteresis-band h). This has the distinct advantage of being simple in operation (thus easier to implement) and has a well defined current ripple (allowing losses to be better estimated). However an inherent disadvantage is that of the uncontrolled switching frequency. In hysteresis control the switching event is triggered when the actual phase current exceeds the hysteresis band. The rate at which the current changes in the phase winding is heavily dependant upon the operating voltage and machine parameters such as back EMF and phase inductances. An additional flaw of the Hysteresis-band method is that for ideal operation it is reliant upon an infinite sample rate; ideally the direction of current flow would be switched the instant the hysteresis-band is exceeded. Before the introduction of DSP technology in PMSM drive systems, this requirement was generally well handled through the use of amplifier based electronic control designs. However with the dominance of DSP based machine drives, further limitations to the technique have arisen. DSP technology is limited to a finite sampling frequency (albeit this can be very large) thus ideal operation of the Hysteresis-band controller is not possible and the technique is subject to current “leakage” issues in which a small current may be present which exceeds the hysteresis band. This diminishes the advantage of having well defined current ripple. The controller is not commonly used in this original per-phase state; however hysteresis-band regulation is a subject which continues to arise in modern research topics.

The publication of Dawande [90] in 1995 is among the first to describe the Bang-Bang controller as a simple DSP based adaptation of the Hysteresis controller. Further publications such as that of Kjaer et al [91] describe in detail the distinct characteristics of the Bang-Bang control technique and how it can be applied in the regulation of 3 phase AC currents in a PMSM.

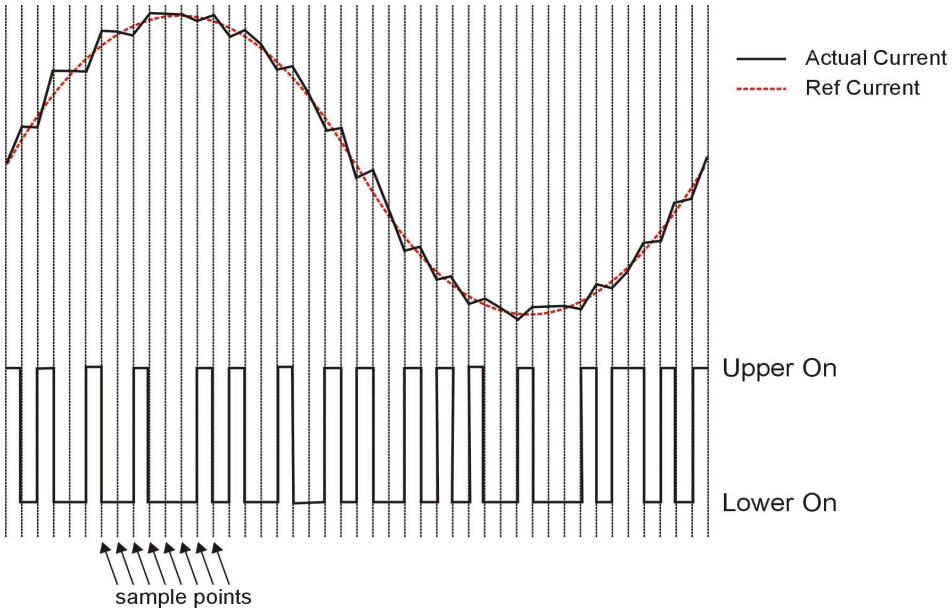

Figure 2-7: Bang-Bang control Waveform

Figure 2-7 demonstrates the Bang-Bang control waveform. At each sample point (50µs in the case of the FCIV) the actual phase current is subtracted from the reference phase current.

$$i_{err} = i_{ref} - i_{act} \tag{1}$$

The result of (1) determines the next step taken by the controller. If (1) is negative this indicates that the actual current needs to be reduced. The controller will achieve this by turning off the upper phase switch and turning on the lower phase switch. This action connects the negative rail of the DC link (for the full control cycle duration of 50µs) in order to reduce the current in the phase. The opposite (upper switch turned on and lower turned off) occurs if the actual current is less than the reference current value. The FCIV implementation of this strategy is quite simplistic.

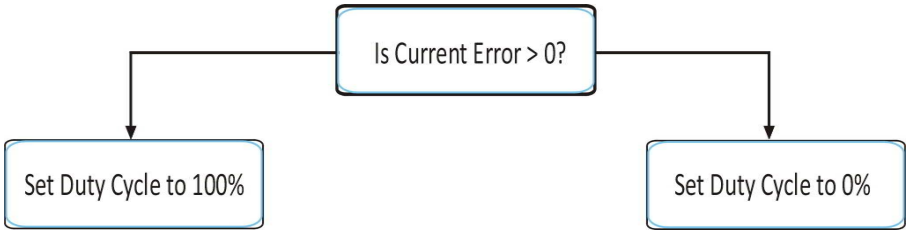

Figure 2-8: Bang-Bang Control Algorithm (single phase)

Figure 2-8 shows a flow diagram of the Bang-Bang control algorithm for a single phase; this is repeated for the three phases individually. As is clear from the simplicity of the diagram shown in Figure 2-8, the Bang-Bang technique is very straightforward in its implementation. The technique requires no additional mathematical steps in calculating its outputs. The name of Bang-Bang arises as the controller commands only the two extremes of the voltage range from the inverter. This is also leads to the control technique being described as non-linear as it has only these two extreme output states.

The Bang-Bang waveform shown in Figure 2-7 clearly demonstrates that there is the possibility of no requirement to switch the gate drive signal at any given sample point. Thus the Bang-Bang controller shares the same disadvantage as Hysteresis-Band control in that it has no fixed switching frequency. The sample frequency is however fixed and this means that whilst the switching frequency is not fixed it is restricted to integer fractions of the sample frequency. This is a distinct disadvantage in attempting to determine switching current components in the frequency analysis of the phase current waveforms. An additional disadvantage to the Bang-Bang controller is that the current ripple shown is not limited. This means that the current ripple can not be designed into the controller and as a result is entirely influenced by the load parameters of the machine under test. This lack of control over the switching frequency and the current ripple mean that the Bang-Bang controller is not often encountered in industry or research. This research aims to investigate the impact the disadvantages discussed have upon the output performance of the system based upon evaluation of a number of output parameters; the objective is to evaluate whether or not the Bang-Bang control technique is justifiably overlooked in favor of more complex techniques.

2.5. PI Control

PI control is generally considered to have existed throughout the entire 20th century, initially seeing use in Naval applications – automatic ship steering specifically [92]. The extensive history of PI control makes it difficult to pin down the precise origins of the

stationary (per-phase) PI controller. The work of Ziegler and Nichols in 1942 is, however, widely recognised as crucial in the propagation of PI controllers in industrial electronic control systems [93]. The paper of Wang et al [94] demonstrates an effective example of tuning (PID in the synchronous frame) using the Ziegler-Nichols approach. Considering the stationary frame PI controller, yet another review of Kazmierkowski [95] describes the technique quite effectively.

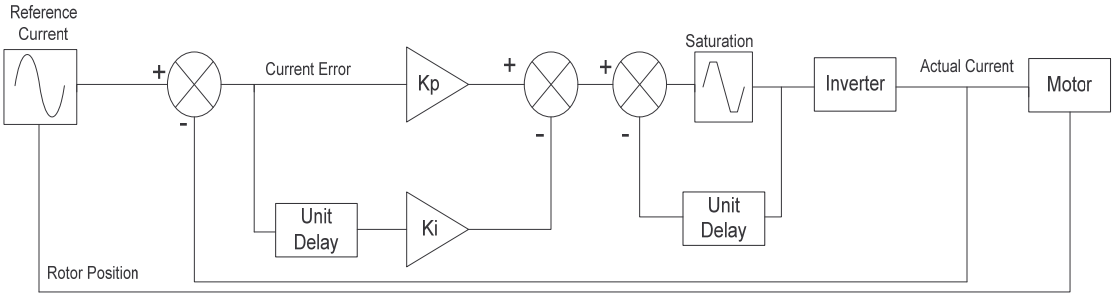

Figure 2-9: PI control loop (single-phase)

Figure 2-9 is a block representation of the stationary phase PI current controller frequently implemented in PWM-VSI drive systems [32, 43, 91, 95, 96]. The stationary reference frame is often listed as an advantage of this controller as it avoids the complex mathematical transformations involved in converting to the synchronous frame, as is frequently stated in the given literature. PI control is generally favoured over hysteresis or Bang-Bang techniques as it enjoys a fixed switching frequency (thus clearly defined frequency distribution of current content) and reduced current ripple (minimizing torque pulsations and increasing overall system efficiency). The FCIV implementation of this PI controller is far more complex than the Bang-Bang implementation – this is highlighted in the flow diagram of the PI control algorithm shown in Figure 2-10.

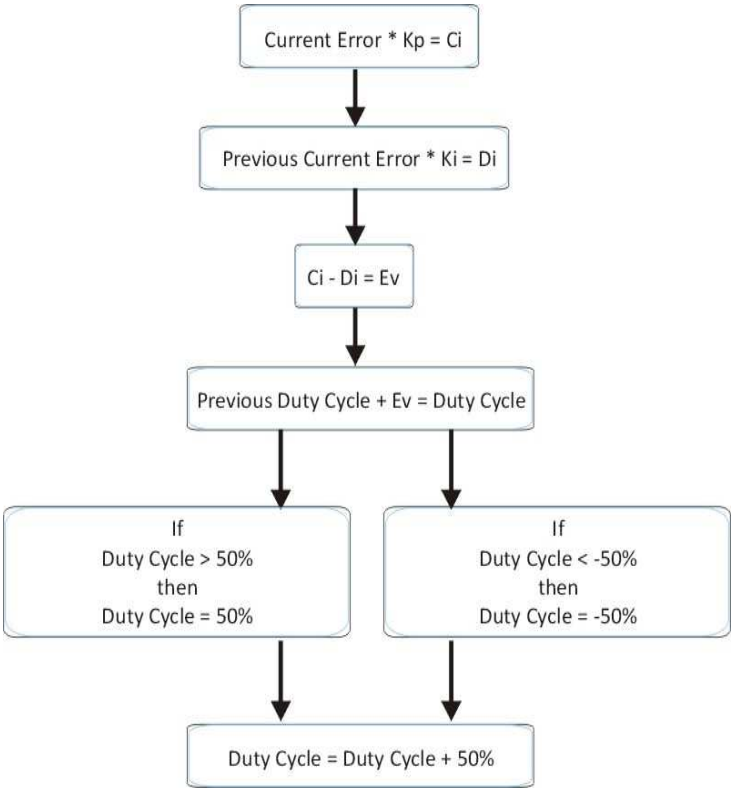

Figure 2-10: FCIV PI controller algorithm (single phase)

The strategy is also frequently described as a linear control technique. This is due to the techniques output voltage commands being capable of linearly adjusting from the extreme negative voltage reference to the extreme positive reference. In terms of PWM commanded reference voltages, this is simply described as having a linear duty cycle output range of 0% to 100%. The DSP based implementation, however, is not an ideal linear controller. Quantization affects the resolution with which the controller can adjust commanded reference voltages (PWM quantization). The research of Grolling [97] provides a research of generalized quantization effects which can degrade the performance of a typical servo system. The research concludes that whilst PWM quantization is in general a parasitic loss in the system, it should not be neglected in servo drive design.

One of the main disadvantages of the stationary PI control is that the regulator is vulnerable to load conditions, specifically Back-EMF induced in phase windings. It is not uncommon at higher operating speeds to witness the PI regulated current wave lagging the reference current wave significantly, as is demonstrated in the research of Zmood and Holmes[98]. Another associated disadvantage of the PI regulator is the tuning of the gains used (Kp and Ki) in Figure 2-9. As is already stated, Ziegler and Nichols created the original methods of PI loop tuning, however it is widely recognised that whilst this

particular method is simplistic in theory, in practise it is not particularly straightforward and does not have satisfactory transient performance. Whilst tuning methods are generally beyond the scope of this research, it would be unwise not to highlight the wealth of research in relation to the tuning of PI loops. The review of PID controllers presented by Ang, Chong and Li [99] is perhaps best cited in respect to the tuning of controllers. This publication highlights the inherent difficulties in tuning the gain terms of a controller; it even discusses the common practice of dropping the Derivative gain term (as is the case in this research). A practise often adopted in recognition of the tendency of the derivative gain term to lead to instability in drive systems. Furthermore the publication offers an analysis of the evolution of PID research into the expanding field of intelligent tuning techniques.

The inclusion of the PI current controller in the comparison presented in this research is based on a number of reasons. The strategy implemented represents an increase in complexity of stationary frame controller when compared to the Bang-Bang controller. The intention is to highlight the perceived improvements in phase current control offered by the PI controller in comparison to the Bang-Bang control. The controller (in its stationary frame implementation) is generally considered a simplistic and reliable control application for industrial applications; it can be implemented using Proportional and Integral gains tuned through a trial and error approach. That is the case presented in this research; this is explained by the desire to present the controller comparison in terms that can easily be replicated; the emphasis being placed on the use of a reliable and simple current controller. The additional performance concerns of the PI controller (sensitivity to load conditions) is of interest to the investigation presented in this research; do the output parameters of the machine (such as output power and efficiency) degrade as a result of the limitations of the PI controller and if so how does this compare with the Bang-Bang controller?

2.6. Space Vector Control

The Space Vector PWM (SVPWM) Controller is a synchronous (rotating frame) control technique, unlike the Bang-Bang and PI control techniques which operate in the stationary reference frame. The works of Clarke [48] and Park[49, 50] have already been acknowledged in terms of their contribution to synchronous theory – Park in particular through his research of the synchronous machine. Further publications such as that from

Vas [55], Leonhard [47] and Holtz [59, 60] on the commonly recognised space vector controller often make reference to the earlier works which pioneer the concept of Field Oriented Control (FOC). FOC is essentially the origin of Space Vector control.

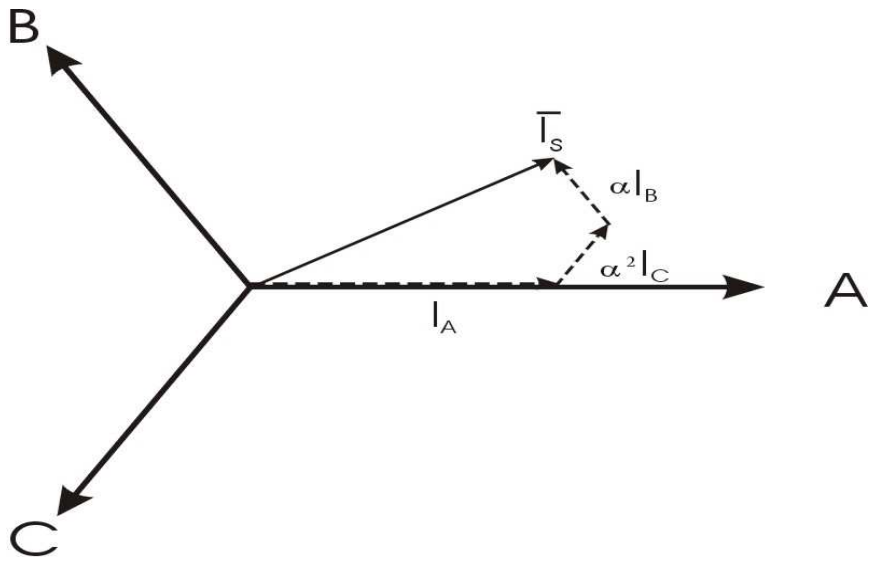

Figure 2-11: The stator current vector represented in the Stationary Reference Frame

$$\bar{I}_s = I_A + \alpha I_B + \alpha^2 I_C \quad \text{Where} \quad \alpha = e^{j\frac{2}{3}\pi} \tag{2}$$

Figure 2-11 shows the stator current vector (2) in its typical 3 phase (stationary frame) representation. The first step in the synchronous control process is to consider the stator current vector in the rotating reference frame - $I_s(d,q)$. This is achieved by first applying the Clarke transform:

$$I_{s\alpha} = \frac{2}{3}(I_A - \frac{1}{2}I_B - \frac{1}{2}I_C) \tag{3}$$

$$I_{s\beta} = \frac{2}{3}(\frac{\sqrt{3}}{2}I_B - \frac{\sqrt{3}}{2}I_C) \tag{4}$$

$$I_A + I_B + I_C = 0 \tag{5}$$

(3) + (4) give the standard Clarke Transform; it is common practice in machine control applications to align the α-axis with the A-axis. This allows for a simplification of the terms, assuming a balanced three phase load (5):

$$I_{s\alpha} = I_A \tag{6}$$

$$I_{s\beta} = \frac{1}{\sqrt{3}}I_A + \frac{2}{\sqrt{3}}I_B \tag{7}$$

$$\bar{I}_s = I_\alpha + I_\beta \tag{8}$$

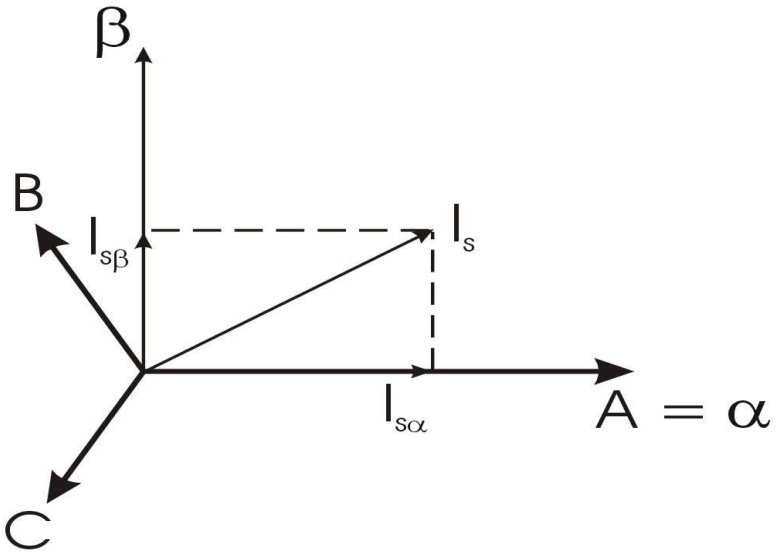

Figure 2-12: Stator Current Vector represented in the 2-axis stationary reference frame

(6) + (7) represent the current 3 phase current vector in a 2-axis stationary reference frame. This is best represented in graphical form (Figure 2-12).

The Park transform immediately follows the Clarke transform. This step transforms the stator current vector from the stationary 2-axis frame to a rotating frame (d,q axes).

$$I_{sd} = I_{s\alpha} Cos\theta + I_{s\beta} Sin\theta \tag{9}$$

$$I_{sq} = -I_{s\alpha} Sin\theta + I_{s\beta} Cos\theta \tag{10}$$

Where θ is the rotor position.

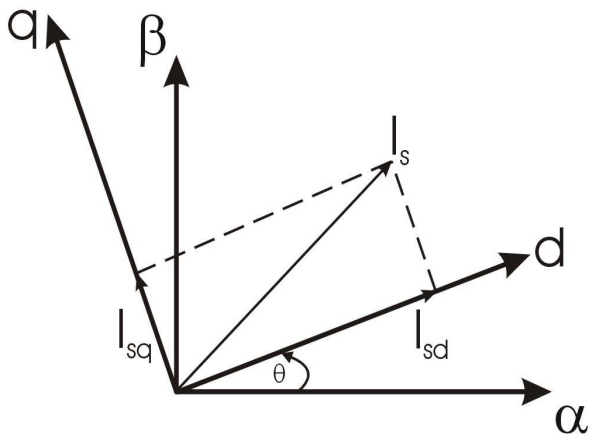

Figure 2-13: Stator Current Vector in the Rotating Reference Frame

Figure 2-13 demonstrates the final representation of the stator current vector I_s as a 2-axis current vector in the rotating reference frame. The two separate currents (Isd and

Isq) are DC in nature and can be regulated independently, allowing for separate torque control and field orientation control, where current I_q is proportional to the torque output and current I_d regulates the field orientation [4, 25, 100]. Typically $I_d = 0$, setting a no field weakening or normal field orientation state.

Having transformed the actual phase currents and the reference currents to the rotating frame, the control process can begin. At this point, any regulation technique can be implemented in order to command the reference stator voltages (in the d,q axis). The common approach is to adopt a PI control loop of the same nature as that outlined in the stationary frame PI controller [98, 101]. In this instance the current error signals acted upon by the controller are given as (11)+(12).

$$I_{derr} = I_{dref} - I_{sd} \tag{11}$$

$$I_{qerr} = I_{qref} - I_{sq} \tag{12}$$

The obvious advantage the synchronous controller has over the stationary controller is that the regulated signals are now in DC form instead of AC. This reduces the magnitude in current error from one sample point to the next, thus improving the control response.

The outputs of the d and q axes PI controllers are d and q axes voltage references (rotating reference frame). These voltage references are required in stationary frame representations for the SVPWM algorithms to use. The first step in this process makes use of the Inverse Park Transform [102].

$$V_\alpha = V_d.Cos\theta - V_q.Sin\theta \tag{13}$$

$$V_\beta = V_d.Sin\theta + V_q.Cos\theta \tag{14}$$

(13)+(14) give the equations used in the Inverse Park Transform. The 2 axis stationary frame reference Voltages ($V\alpha$, $V\beta$) are used in the calculation of timing values critical to the SVPWM process, this will be explained in greater detail. In many implementations highlighted in research, the SVPWM controller makes use of only the Inverse Park Transform, using the reference voltage vector in the 2-axis representation given in (13)+(14). The implementation utilized in this research, however, also makes use of the Inverse Park Transformation.

$$V_A = V_\alpha \tag{15}$$

$$V_B = -\frac{1}{2} V_\alpha + \frac{\sqrt{3}}{2} V_\beta \tag{16}$$

$$V_C = -\frac{\sqrt{3}}{2} V_\alpha - \frac{1}{2} V_\beta \tag{17}$$

The 3-axis stationary representation given in (15), (16) and (17) is important in the FCIV implementation of SVPWM. With the mathematical transformations of the feedback and reference signals used in the SVPWM having been described in detail, it is important to consider the drive system more widely in order to fully understand the SVPWM control theory.

The PMSM drive system described in this research is a typical example of a 3 phase equilibrate system. With this being the case, there are a number of wider considerations of the system which must be made in order to fully understand the SVPWM operation. The first thing to consider is the output states of the 3 phase inverter based on the input gate drive signals.

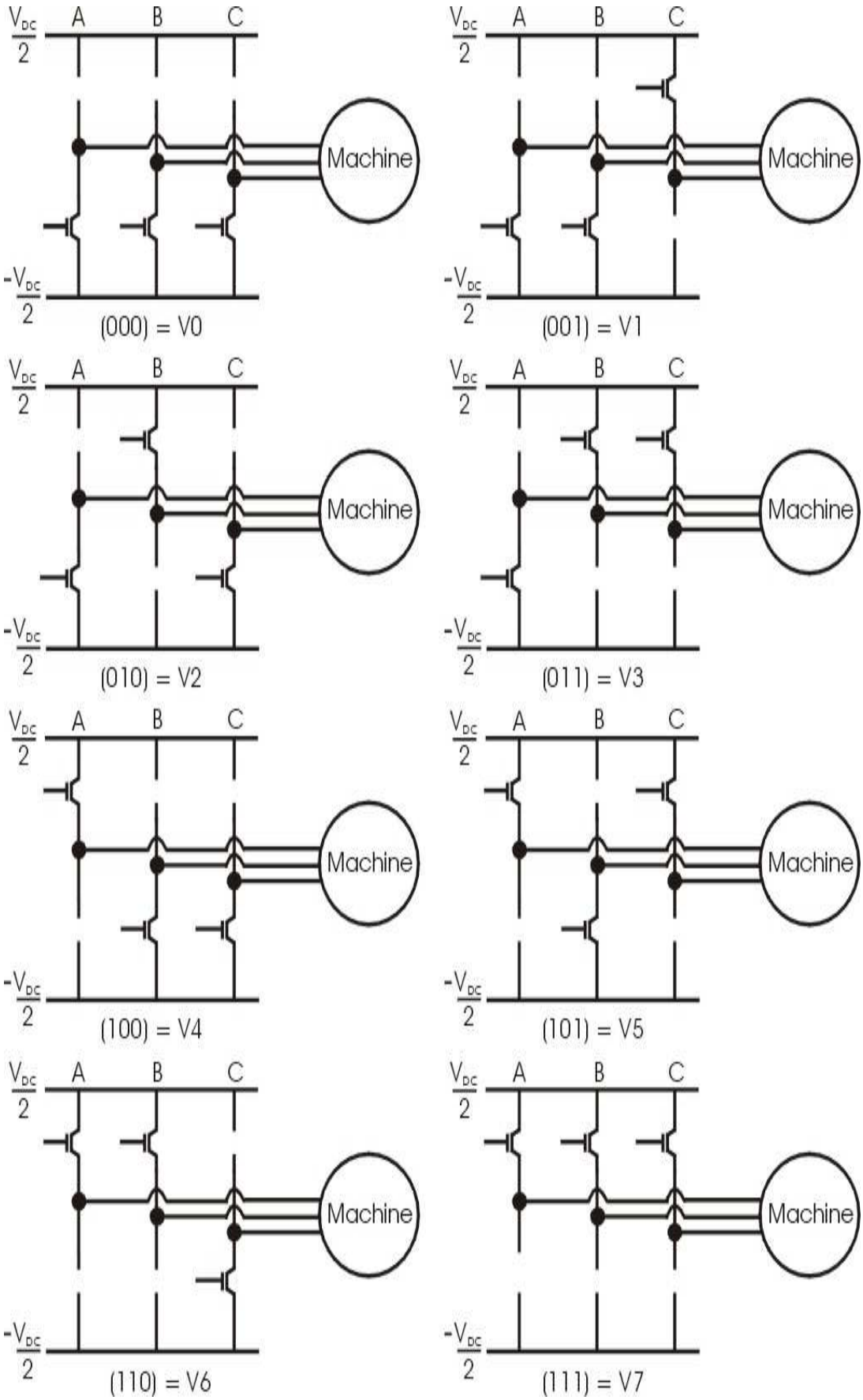

Figure 2-14: Inverter Switch Configurations

Fig 12 shows the 8 different switch configurations (8 different stator voltage vectors) possible from a 3 phase VSI, the voltage vectors V_0 and V_7 are commonly referred to as zero voltage vectors; in theory they command no voltage since there is zero potential difference across any phase connection. The work of Stanke et al [103] shows the application of Figure 2-14 to generate the Space-Vector hexagon which is commonly referred to in SVPWM publications. The switch considerations and SV hexagon (shown in Figure 2-15) are commonly attributed to the earlier works of Kovacs and Racz [57].

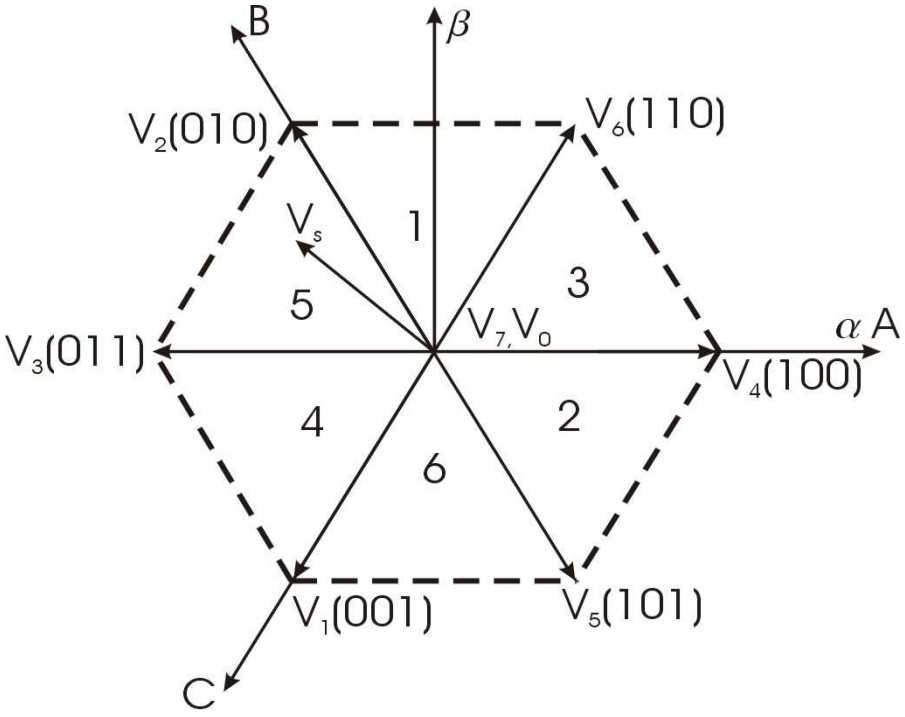

Figure 2-15: Space Vector Hexagon showing both stationary reference frames

Using the Space-Vector Modulation (SVM) method, it is assumed that the load is a balanced 3 phase system. A simplified model of this drive system would be to consider three common sinusoidal sources with equal amplitude and 120° phase separation driving 3 common resistive and inductive loads.

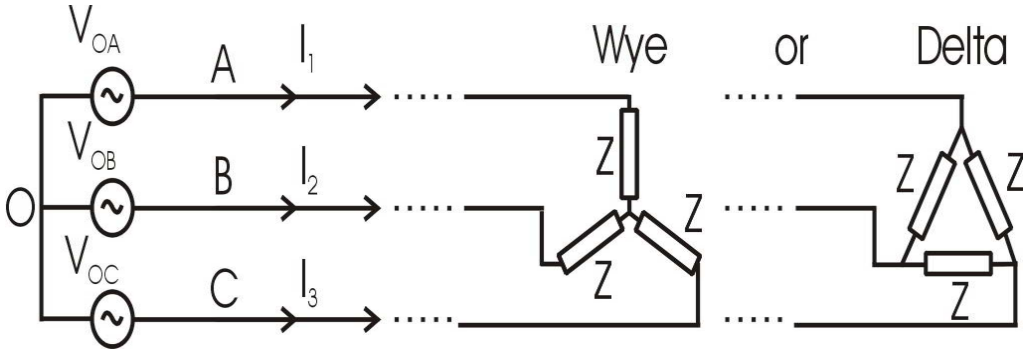

Figure 2-16: 3 Phase Equilibrate System

$$V_{Oa} = V_{OA} + (I_1.Z) or (\frac{Z}{\sqrt{3}} I_1) \quad (18)$$

$$V_{Ob} = V_{OB} + (I_2.Z) or (\frac{Z}{\sqrt{3}} I_2) \quad (19)$$

$$V_{Oc} = V_{OC} + (I_3.Z) or (\frac{Z}{\sqrt{3}} I_3) \quad (20)$$

Figure 2-16 shows a balanced 3 phase drive system. The source voltages for each phase are given as (18)-(20); these can be combined as a single source voltage.

$$3 \times V_O = V_{OA} + V_{OB} + V_{OC} + Z(I_1 + I_2 + I_3) or \frac{Z}{\sqrt{3}} (I_1 + I_2 + I_3) \quad (21)$$

Once again the assumption of (5) can be applied and thus (21) can be simplified.

$$V_O = \frac{1}{3} (V_{OA} + V_{OB} + V_{OC}) \quad (22)$$

The simplification to (22) allows a simple manipulation to give the phase voltages

$$V_A = V_{OA} - V_O = V_{OA} - (\frac{1}{3})(V_{OA} + V_{OB} + V_{OC}) = (\frac{1}{3})(2V_{OA} - V_{OB} - V_{OC}) \quad (23)$$

$$V_B = V_{OB} - V_O = V_{OB} - (\frac{1}{3})(V_{OA} + V_{OB} + V_{OC}) = (\frac{1}{3})(2V_{OB} - V_{OA} - V_{OC}) \quad (24)$$

$$V_C = V_{OC} - V_O = V_{OC} - (\frac{1}{3})(V_{OA} + V_{OB} + V_{OC}) = (\frac{1}{3})(2V_{OC} - V_{OA} - V_{OB}) \quad (25)$$

Using Figure 2-14 and (23)-(25), a table relating the relationships between the voltage vectors in the 3-axis stationary frame can be generated.

TABLE 2-2: 3 Phase Voltages in a 3 phase equilibrate system with respect to Inverter Switch Connections

Voltage Vector	Gate A	Gate B	Gate C	V_{OA}	V_{OB}	V_{OC}	V_A	V_B	V_C
V_0	0	0	0	$\frac{-V_{DC}}{2}$	$\frac{-V_{DC}}{2}$	$\frac{-V_{DC}}{2}$	0	0	0
V_1	0	0	1	$\frac{-V_{DC}}{2}$	$\frac{-V_{DC}}{2}$	$\frac{+V_{DC}}{2}$	$\frac{-V_{DC}}{3}$	$\frac{-V_{DC}}{3}$	$+2\frac{V_{DC}}{3}$
V_2	0	1	0	$\frac{-V_{DC}}{2}$	$\frac{+V_{DC}}{2}$	$\frac{-V_{DC}}{2}$	$\frac{-V_{DC}}{3}$	$+2\frac{V_{DC}}{3}$	$\frac{-V_{DC}}{3}$
V_3	0	1	1	$\frac{-V_{DC}}{2}$	$\frac{+V_{DC}}{2}$	$\frac{+V_{DC}}{2}$	$-2\frac{V_{DC}}{3}$	$\frac{+V_{DC}}{3}$	$\frac{+V_{DC}}{3}$
V_4	1	0	0	$\frac{+V_{DC}}{2}$	$\frac{-V_{DC}}{2}$	$\frac{-V_{DC}}{2}$	$+2\frac{V_{DC}}{3}$	$\frac{-V_{DC}}{3}$	$\frac{-V_{DC}}{3}$
V_5	1	0	1	$\frac{+V_{DC}}{2}$	$\frac{-V_{DC}}{2}$	$\frac{+V_{DC}}{2}$	$\frac{+V_{DC}}{3}$	$-2\frac{V_{DC}}{3}$	$\frac{+V_{DC}}{3}$
V_6	1	1	0	$\frac{+V_{DC}}{2}$	$\frac{+V_{DC}}{2}$	$\frac{-V_{DC}}{2}$	$\frac{+V_{DC}}{3}$	$\frac{+V_{DC}}{3}$	$-2\frac{V_{DC}}{3}$
V_7	1	1	1	$\frac{+V_{DC}}{2}$	$\frac{+V_{DC}}{2}$	$\frac{+V_{DC}}{2}$	0	0	0

TABLE 2-2 can be applied with equations (3)+(4) to give rise to the relationships between the voltage vector and the 2-axis stationary frame.

TABLE 2-3: 2-axis stationary frame voltage vectors

Voltage Vector	V_α	V_β
V_0	0	0
V_1	$-\frac{V_{DC}}{3}$	$-\frac{V_{DC}}{\sqrt{3}}$
V_2	$-\frac{V_{DC}}{3}$	$\frac{V_{DC}}{\sqrt{3}}$
V_3	$-2\frac{V_{DC}}{3}$	0
V_4	$+2\frac{V_{DC}}{3}$	0
V_5	$+\frac{V_{DC}}{3}$	$-\frac{V_{DC}}{\sqrt{3}}$
V_6	$+\frac{V_{DC}}{3}$	$\frac{V_{DC}}{\sqrt{3}}$
V_7	0	0

The commanded reference stator voltage vector (13) + (14) generated by the control algorithms (the PI regulators in the case of the FCIV implementation) will reside anywhere within the hexagon shown in Fig 13. The concept of Space Voltage Modulation (SVM) is to realise the reference voltage vector V_s using a combination of the surrounding voltage vectors and if necessary a zero voltage vector. In the example shown in Figure 2-15, the voltage vector V_s would be achieved through a combination of V_2, V_3 and either V_0 or V_7 (the selection of which will be explained in greater detail at a later stage).

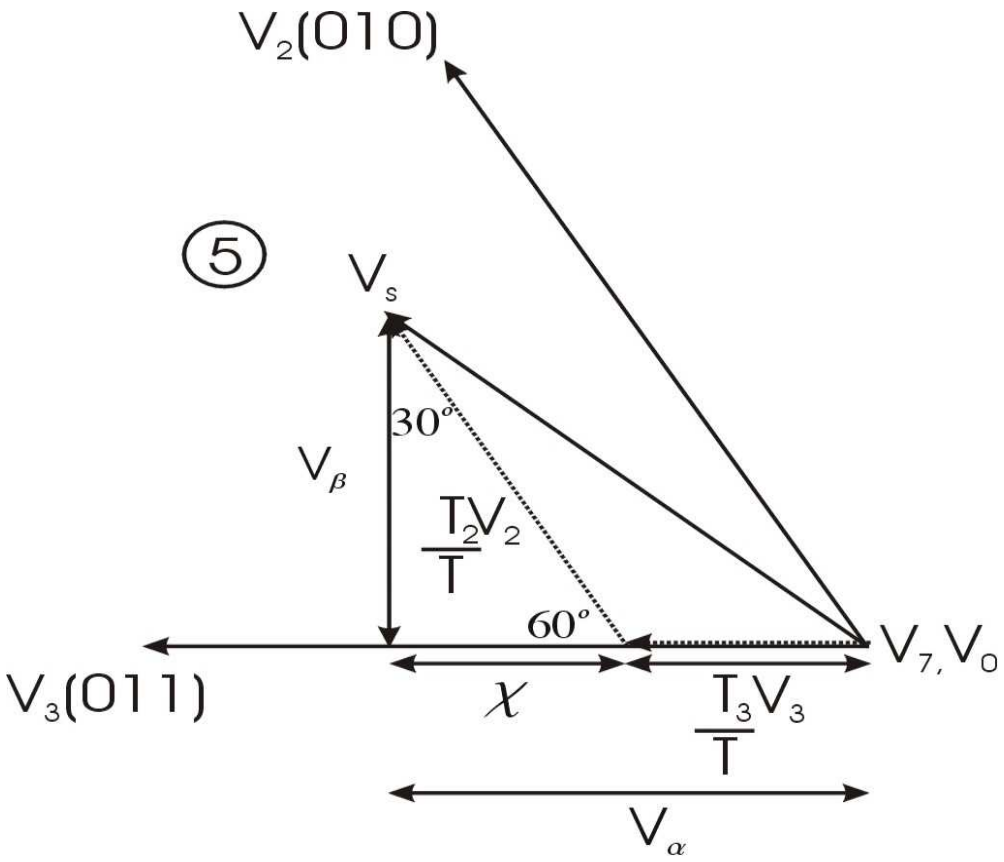

Figure 2-17: Example of Voltage Vector residing in Sector 5

Figure 2-17 shows an example where the commanded reference voltage vector V_s resides in Sector 5. As was stated previously, in any SVM controller, V_s will be realised through a combination of V_2, V_3 and most likely V_7 or V_0 (some occurrences exist where no zero voltage vector is required). This is true for the SVPWM controller where the reference voltage vector will be realised through generating gate signals which produce a combination of the required voltage vectors for a specific time interval within each switch period (50µs for the FCIV as was explained earlier).

$$T = T_3 + T_2 + T_{0or7} \tag{26}$$

$$V_s = \frac{T_3}{T} V_3 + \frac{T_2}{T} V_2 + \frac{T_{0or7}}{T} V_{0or7} \tag{27}$$

Eq (26) gives the relation between the switch period and time interval of each applied voltage vector; (27) represents the commanded voltage vector in terms of the applied voltage vectors and associated timing intervals. In any implementation the zero voltage vector is generally not calculated as it is simply the result of the switch period minus the combined time interval that the two non-zero voltage vectors are applied for. Thus only T3 and T2 require calculating. Having predetermined the values of V_α and V_β, the controller is able to use these values in order to determine the timing intervals.

$$V_\beta = \frac{T_2}{T}\left|V_2\right| Cos30° \tag{28}$$

$$V_\alpha = \frac{T_3}{T}\left|V_3\right| + \chi \tag{29}$$

$$\chi = \frac{V_\beta}{\tan 60°} \tag{30}$$

Eq (28)-(30) are taken from Figure 2-17. The voltage vectors can be simplified as follows:

$$\left|V_2\right| = \left|V_\alpha + V_\beta\right| = \left|\frac{-V_{DC}}{3} + \frac{V_{DC}}{\sqrt{3}}\right| = \sqrt{(\frac{-V_{DC}}{3})^2 + (\frac{V_{DC}}{\sqrt{3}})^2} = \frac{2}{3} V_{DC} \tag{31}$$

$$\left|V_3\right| = \left|V_\alpha + V_\beta\right| = \left|\frac{-2V_{DC}}{3} + 0\right| = \sqrt{(\frac{-2V_{DC}}{3})^2} = \frac{2}{3} V_{DC} \tag{32}$$

If the methods of (31)+(32) are applied to all non-zero voltage vectors in TABLE 2-3, then it can be shown that all have a magnitude equal to (2/3)V_{DC}.

$$V_\beta = (\frac{T_2}{T})(\frac{2V_{DC}}{3})(\frac{\sqrt{3}}{2}) \therefore T_2 = (\frac{T}{V_{DC}}) V_\beta \sqrt{3} \tag{33}$$

$$V_\alpha = (\frac{T_3}{T})(\frac{2V_{DC}}{3}) + \frac{V_\beta}{\sqrt{3}} \therefore T_3 = (\frac{T}{V_{DC}})(\frac{3}{2} V_\alpha - \frac{\sqrt{3}}{2} V_\beta) \tag{34}$$

(33)+(34) are the required time intervals for which V_2 and V_3 must be applied in order to realise the voltage vector V_s in Sector 5. If the considerations shown in (28)-(34) are applied to all the sectors of the hexagon then it becomes apparent that three generalised timing equations are required:

$$T_X = (\frac{T}{V_{DC}}) V_\beta \sqrt{3} \quad (35)$$

$$T_Y = (\frac{T}{V_{DC}})(\frac{3}{2} V_\alpha + \frac{\sqrt{3}}{2} V_\beta) \quad (36)$$

$$T_Z = (\frac{T}{V_{DC}})(\frac{3}{2} V_\alpha - \frac{\sqrt{3}}{2} V_\beta) \quad (37)$$

The selection and application of (35)-(37) is dependant upon the sector of the space-vector hexagon that the reference voltage vector V_s resided in.

TABLE 2-4: Timing Vector Selection with respect to Space Vector Sector

Sector	T_1	V_x	T_2	V_y
1	T_Z	V_6	T_Y	V_2
2	T_Y	V_4	$-T_X$	V_5
3	$-T_Z$	V_4	T_X	V_6
4	$-T_X$	V_3	T_Z	V_1
5	T_X	V_2	$-T_Y$	V_3
6	$-T_Y$	V_5	$-T_Z$	V_1

TABLE 2-4 shows the selection of timing vectors based on the SV sector, where V_x, T_1 are the first voltage vector and associated time vector commanded and V_y, T_2 are the second vector commanded. There is also a simplified approach to determining the sector that makes use of the results from the inverse Clarke transform - Eq (15)-(17).

Sector 1: $V_B > V_A > V_C$

Sector 2: $V_A > V_C > V_B$

Sector 3: $V_A > V_B > V_C$

Sector 4: $V_C > V_B > V_A$

Sector 5: $V_B > V_C > V_A$

Sector 6: $V_C > V_A > V_B$

The FCIV makes use of DSP hardware including a SVPWM peripheral module; this makes the commanding of reference voltages somewhat straightforward for the control developer. The peripheral requires each of the parameters shown in a single row of

TABLE 2-4 in order to generate the PWM drive signals to be fed to the inverter. As was mentioned earlier, the selection of the zero-volt vector used in the realization of V_s is not arbitrary. It is selected as a result of the technique used to generate the SVPWM drive signals. The method of SVPWM wave generation is based on a triangle comparison method which is described in the research publications of Blasko [104] and of Zhenyu et al [42]. The example of V_s residing in sector 5 can demonstrate this in greater effect.

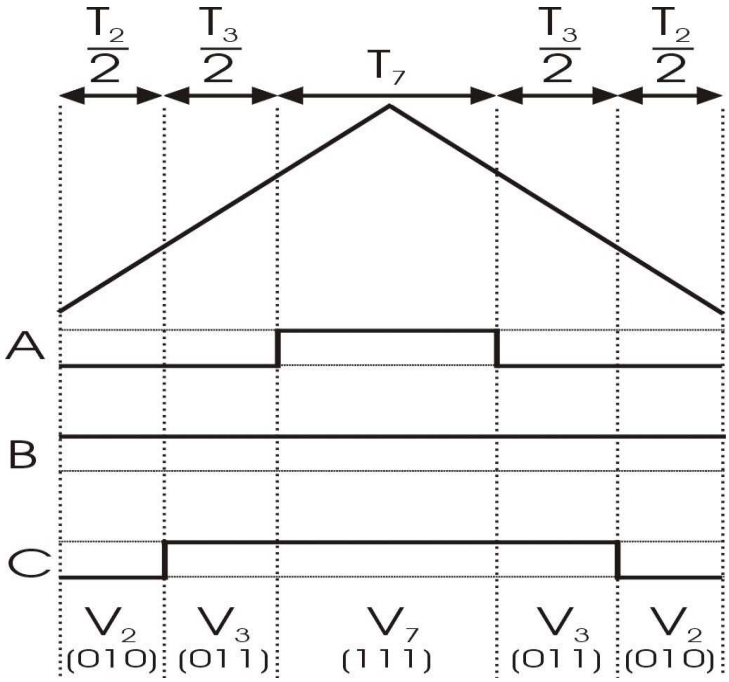

Figure 2-18: Sector 5 Switch Pattern

Figure 2-18 demonstrates the way the FCIV generates SVPWM signals using the voltage vectors and associated time vectors. The waveform is symmetrical in nature with the zero-voltage vector central to the wave. In this instance it can be seen that the phase B control signal is at all times high (turned on). This is because the two voltage vector used command phase B as high. The SVPWM peripheral within the FCIV selects the zero-voltage vector such as to minimize switch losses; therefore in the transition shown in Figure 2-18, to obtain the zero voltage vector from the V_3 vector, phase A is set high for the duration of T_7 – two switch transitions. A transition to V_0 would have resulted in both phase B and phase C requiring lowering for the duration of T_7, this would have resulted in 4 switch transitions occurring; thus the selection of V_7 is more efficient. Such consideration of the all the sector switch patterns allows an extension of Table 3 to include the zero-volt vector implemented.

TABLE 2-5: Vectors Selection Based on Sector including zero-volt vectors

Sector	T_1	V_x	T_2	V_y	T_{ZERO}	V_{ZERO}
1	T_Z	V_6	T_Y	V_2	$T-(T_1+T_2)$	V_0
2	T_Y	V_5	$-T_X$	V_4	$T-(T_1+T_2)$	V_0
3	$-T_Z$	V_4	T_X	V_6	$T-(T_1+T_2)$	V_7
4	$-T_X$	V_3	T_Z	V_1	$T-(T_1+T_2)$	V_0
5	T_X	V_2	$-T_Y$	V_3	$T-(T_1+T_2)$	V_7
6	$-T_Y$	V_1	$-T_Z$	V_5	$T-(T_1+T_2)$	V_7

The overall SVPWM control operation has been described; the technique itself can be illustrated in a block diagram similar to those outlined in previous publications [101, 102, 105].

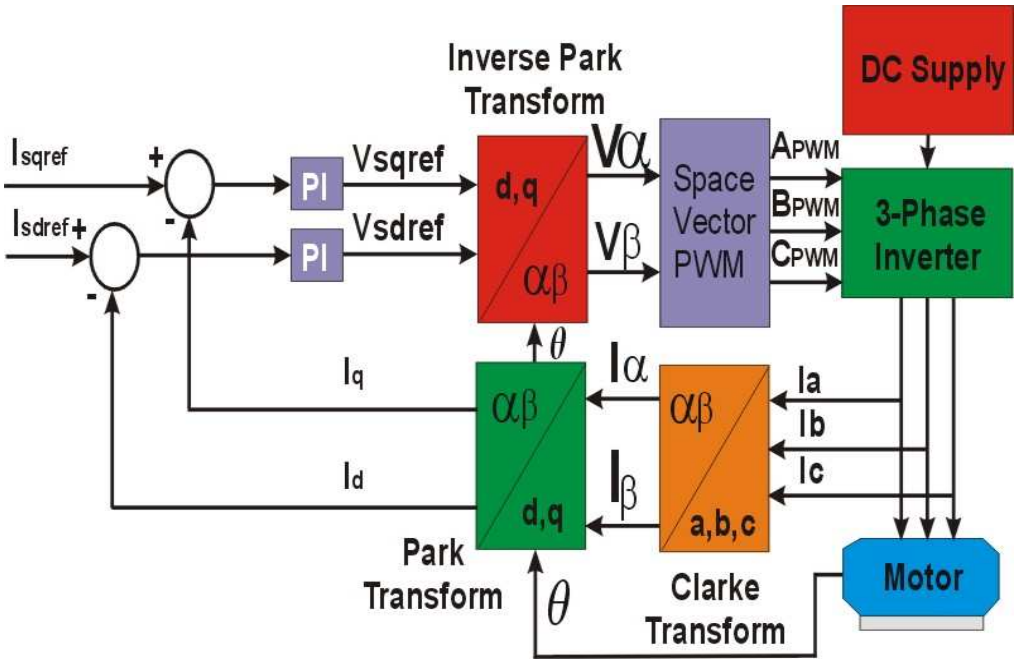

Figure 2-19: Vector Control Block Diagram

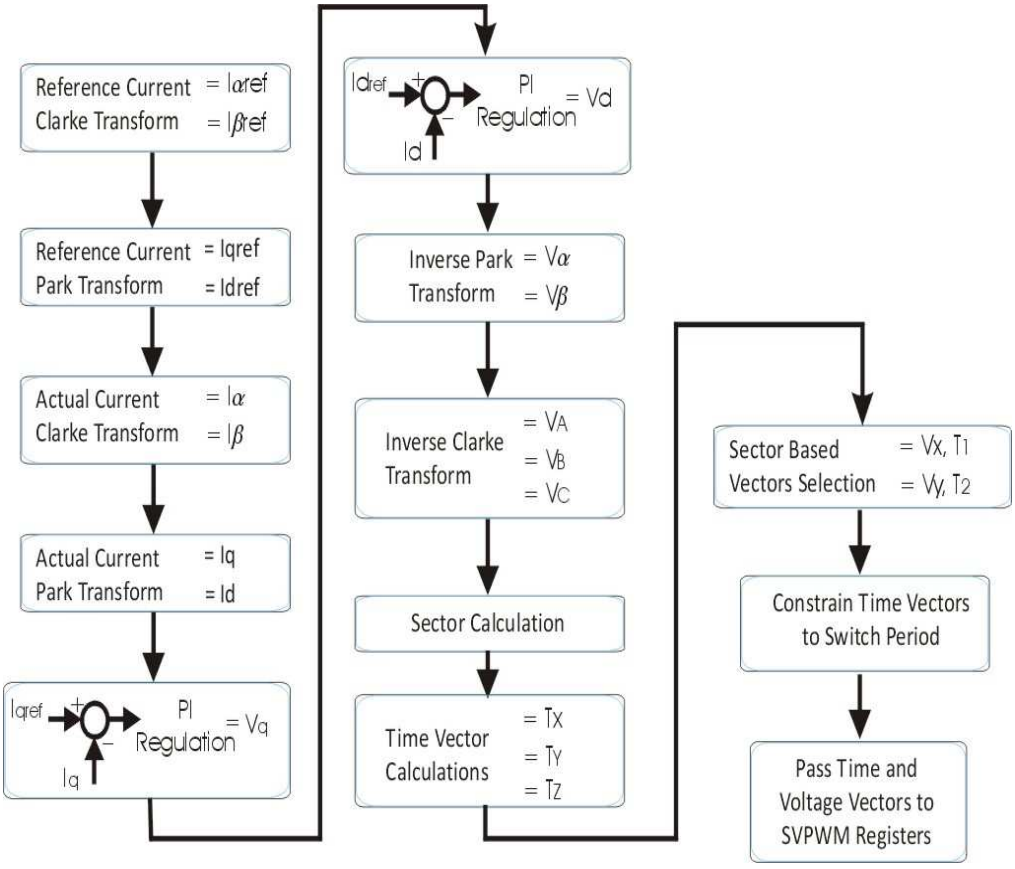

Figure 2-20: FCIV SVPWM Controller Algorithm

Figure 2-19 displays the classical block diagram of the Vector controller; the block labelled Space Vector PWM in this particular implementation encompasses the inverse Clarke calculations outlined, the selection of the two voltage vectors and the calculation of the associated time vectors.

The SVPWM control algorithm implemented also falls into place with the overall FCIV flow diagram given in Figure 2-6. The calculation of the current error shown in Figure 2-6 is however disregarded in the SVPWM control algorithm; this is due to the SVPWM controller acting upon the rotational frame current errors instead of the stationary frame current errors.

The SVPWM controller described in this research represents a significant increase in software due to the limitations of the hardware when compared to the Bang-Bang or PI controllers previously described. The fixed point architecture of the DSP used in the FCIV enforces a far more considered approach to the application of the trigonometric transformations used in SVPWM. This is perhaps most apparent when comparing the flow diagrams of Figure 2-10 and Figure 2-20. There are again a number of arguments for inclusion in the comparison presented in this research. The SVPWM controller has a

distinct advantage over the other two controllers in the respect that it actively addresses phase imbalance in its nature; this is due to the transformation of the 3-axis currents to the d,q axis currents – the other two controllers operate on a per phase basis. A key advantage the SVPWM controller has over the PI controller is that the (rotating) PI regulators operate on DC current signals instead of AC signals (as is the case in the stationary frame PI controller). This leads to a general reduction in the magnitude of the current error signals generated – thus allowing for a stronger gain response. This is particularly true at higher speeds where the stationary frame PI controller is known to exhibit phase lag issues whereas the SVPWM controller does not. SVPWM clearly has a significant disadvantage in terms of additional computing cost in comparison to the other techniques; there are multiple areas of consideration and complexity in the construction of the SVPWM controller outlined in this research – this would almost certainly restrict a motor design engineer in any attempts to achieve a fast verification of a new design and it would clearly impact upon the cost of a drive design for a new application. The SVPWM controller also shares the stationary PI regulators disadvantage of complex gain tuning.

With respect to the additional mathematical complexity of the SVPWM controller, it is in fact not among the more complex control strategies which are prominent in modern research. More modern control comparisons are heavily focussed towards use of adaptive gain tuning, fuzzy control strategy, multilevel inverter strategies and also the use of Artificial Neural Networks (ANN) or Artificial Intelligence (AI) based control strategies. These are not serious options for the general motor engineer in industry, for whom the primary concerns would be a fast method of verifying torque to current performance ratio (kt) and perhaps producing a generalised motor drive for fast to market applications. The three control strategies outlined in the comparison are however all strategies that could be considered in these circumstances. The aim of this comparison is to address whether the present consensus that the stationary PI controller is the most suitable control strategy in this context.

2.7. The Steady State Test Process

An important aspect to the comparison presented in this research is the nature of the steady state testing in which the results are obtained. The hardware of the test bench is not consistent across each machine; however, for each machine test bench the hardware does not vary with respect to the control strategy selected. This allows for a comparison

of the controllers using an unchanged experimental setup for each machine tested. This gives rise to the on-the-fly test process which is unique to the controller comparison presented in this research.

The on-the-fly test process is based upon the ability of each machine test bench (through the use of the FCIV) to test each control strategy at any given test point in a single process – the strategy implemented is entirely software defined; thus the user may switch between current control strategy from one switch period to the next. This has the advantage of allowing each strategy to be compared under identical operating conditions – mainly through unaltered hardware (for example the back EMF alignment of the machine is not compromised possibly offsetting power factor) but also such variables as ambient temperature and instantaneous phase resistance (a parameter which can vary with respect to temperature). This allows for a scientifically stronger comparison of strategy than has previously been available.

As has been discussed previously, the comparison presented in this research will seek to expand the analysis of the controllers to include a wider range of vital operating characteristics. As is shown in Figure 2-3 and highlighted in section 2.3, the test bench makes use of a series of devices which provide power measurements and wave capture abilities which are used to capture the results presented in this research. The measurements taken and how they are applied to create the results presented are outlined in Appendix B.

2.8. Aesthetical Analysis

The figures presented in this section demonstrate typical phase current waveforms that are produced when operating each of the control techniques that have been described. Capture of waveforms allow for an aesthetical analysis which primarily confirms correct regulator operation but also allows for the differences in waveforms to be quantified.

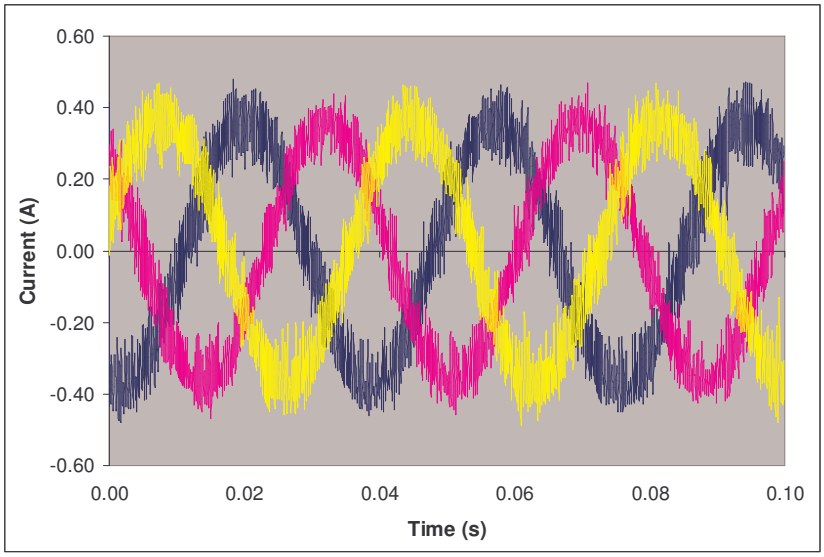

Figure 2-21: 3 phase current waveform capture of Interroll machine using Bang-Bang regulation operating at 400rpm, 0.4A reference current operating point.

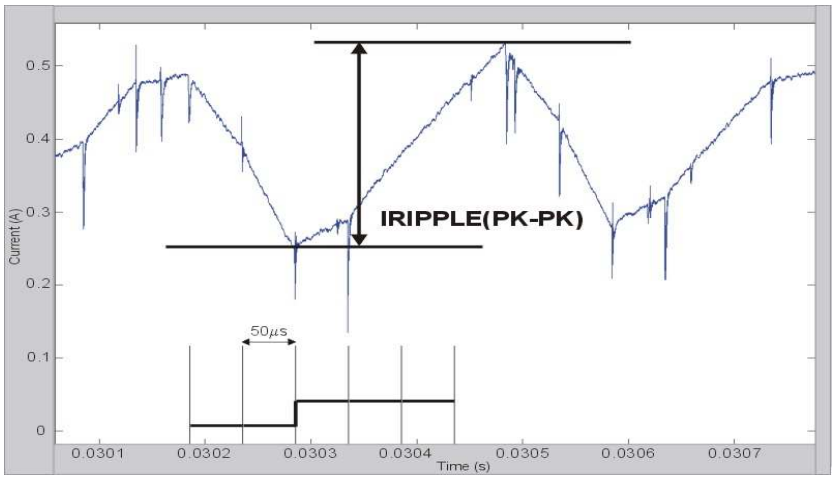

Figure 2-22: Phase A Current wave of Interroll machine using Bang-Bang regulation at 400rpm, 0.4A reference current

The waveform shown in Figure 2-21 is typical for the Bang-Bang controller operating with 0.4A reference current on the Interroll machine – the smallest in the test range. Cleary shown in the waveform is the expected large current ripple and unpredictable switching frequency of the current waveforms. Figure 2-22 shows a high resolution (unfiltered) view of the phase A current waveform shown in Figure 2-21. Switch events have been highlighted at their 50µs intervals highlighting the non predictable switching frequency – the only certainty is that the instantaneous switch frequency can not exceed 20kHz (meaning sub-harmonic switch related content). Also shown is a measure of $I_{RIPPLE(PK-PK)}$, the peak to peak current ripple which is greater than 0.2A in this particular case – 50% of the commanded current, although performance at higher currents has shown the current

ripple is often around 15% of the commanded current. These are key disadvantages of the Bang-Bang controller and are the main source of expected performance deficiencies in the technique.

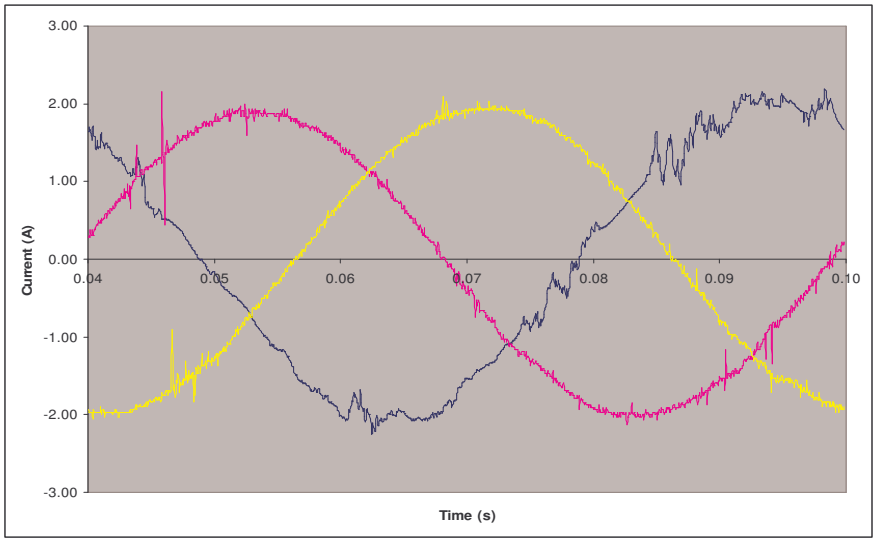

Figure 2-23: 3 phase current waveform capture of SEM machine using PI regulation operating at 500rpm, 2A reference current operating point.

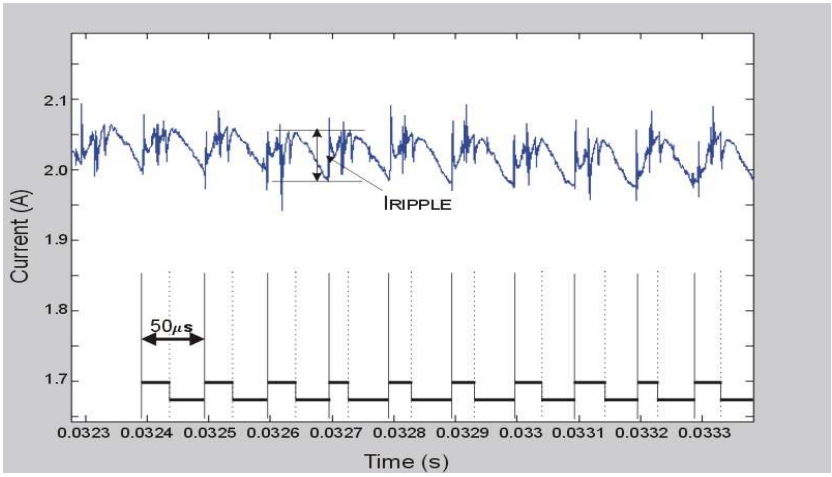

Figure 2-24: Phase A Current wave of SEM machine using PI regulation at 500rpm, 2A reference current

Figure 2-24 shows an unfiltered high resolution view of the phase A current waveform shown in Figure 2-23, these are waveforms captured when operating the PI control strategy on the medium sized SEM machine. Switch cycles are highlighted at their 50µs intervals highlighting the PWM nature of the drive signal – these switch patterns produce current content at the switch frequency and its superharmonics (this is a fundamental difference between Bang-Bang and the other controllers). Also shown is a measure of $I_{RIPPLE(PK-PK)}$ which is around 0.07A in this particular case (3.5% of the commanded current) – much less than Bang-Bang despite operating at a significantly higher reference current.

It is clear already that the PI controller addresses the particular disadvantages of the Bang-Bang controller – namely the unpredictable switch frequency and large current ripple.

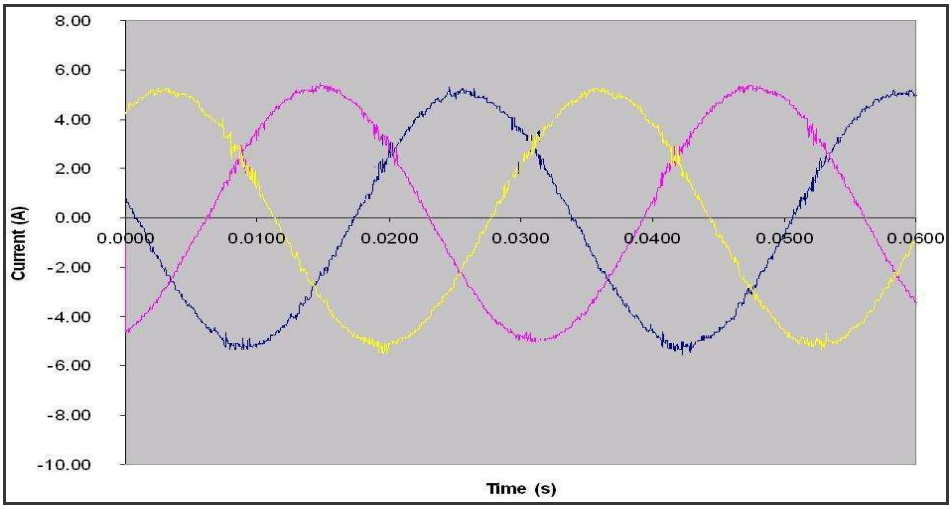

Figure 2-25: 3 phase current waveform capture of Heidenhain machine using SVPWM regulation operating at 600rpm, 5A reference current operating point.

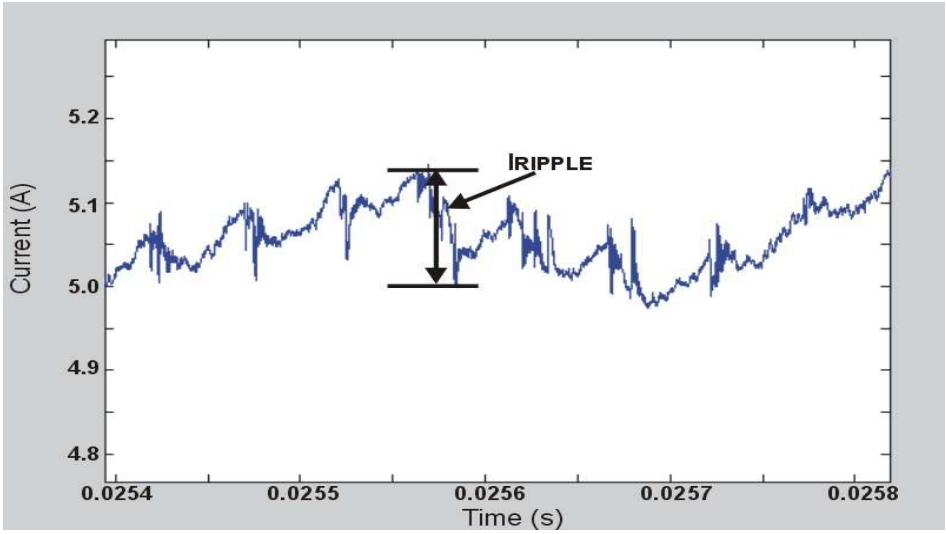

Figure 2-26: Phase A Current wave of Heidenhain machine using SVPWM regulation at 600rpm, 5A reference current

Figure 2-26 shows an unfiltered high resolution view of the phase A current waveform shown in Figure 2-25, waveforms captured under SVPWM control when operating the largest machine – the Heidenhain motor. The nature of these signals is common with the PI controller; there is current content at the switch frequency and its superharmonics. The ripple at this higher reference current level is around 0.15A or 3% of the commanded current. The SVPWM control is shown to also address the disadvantages associated with the Bang-Bang control.

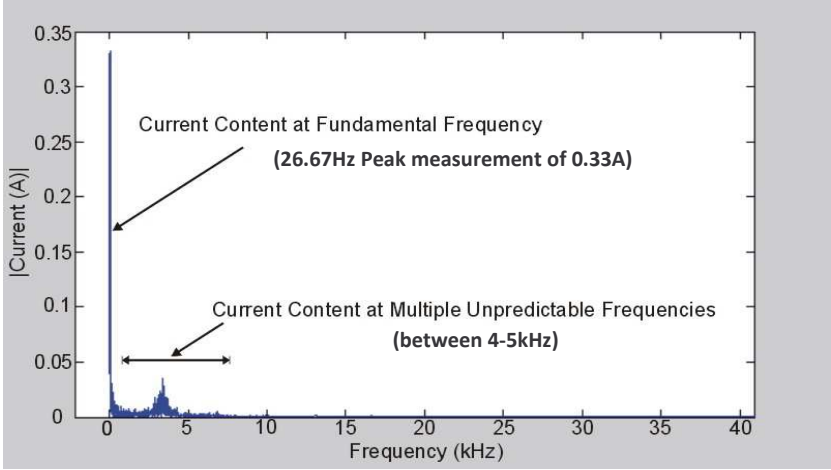

Figure 2-27: Harmonic Spectra of Interroll Machine Phase Current under Bang-Bang Control at 400rpm 0.4A Reference Current

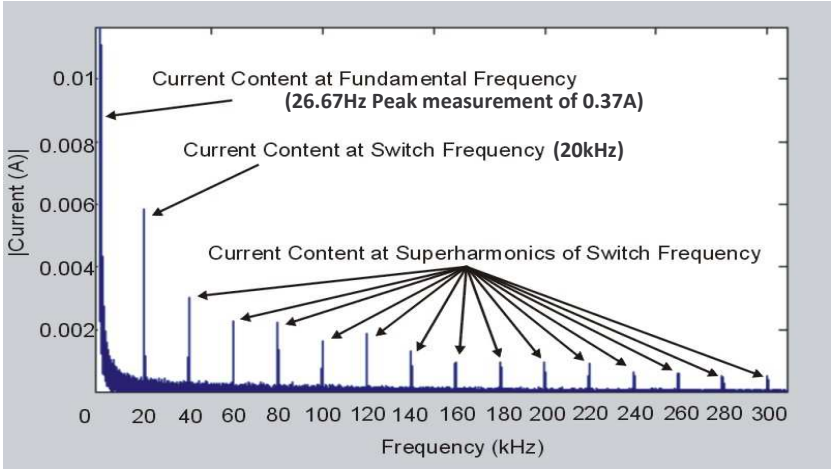

Figure 2-28: Harmonic Spectra of Interroll Machine Phase Current under PI Control at 400rpm 0.4A Reference Current

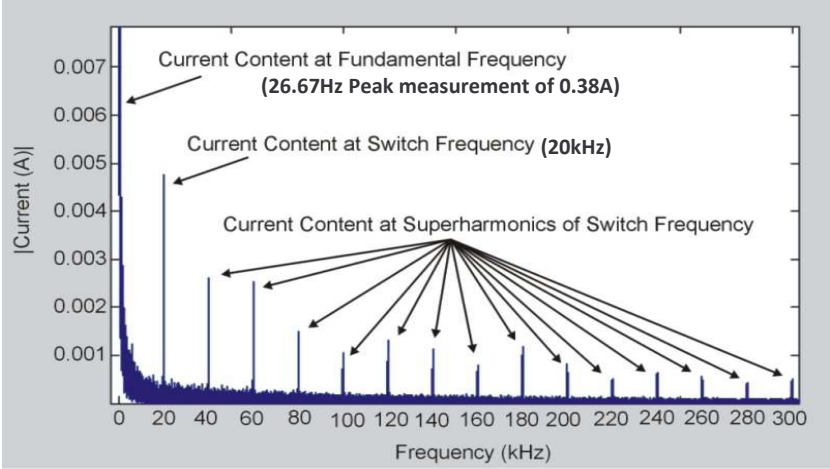

Figure 2-29: Harmonic Spectra of Interroll Machine Phase Current under SVPWM Control at 400rpm 0.4A Reference Current

Figure 2-27 shows the Fast Fourier Transform (FFT) of a single phase current wave under Bang-Bang control at 400rpm 0.4A reference current using the Interroll motor. The figure demonstrates the magnitude of current content at each frequency in the sample window.

Quite clearly demonstrated is the large majority of current content at the fundamental frequency (26.67Hz in this case) of the system at this test point. This is the desired frequency for all current content and represents the frequency at which torque output is desired. There is however also a clearly identifiable section of the frequency spectrum (approximately 2.5kHz – 4.5kHz) which makes a visible contribution to the current content. This is quite obviously representative of the unknown switch frequency. The frequency range at which this content resides confirms the expectation that the Bang-Bang controller will produce switch related content at frequencies lower than the sample rate (20kHz). At the fundamental frequency the magnitude of the current (in the example given in Figure 2-27) is 0.3318A (82% of the desired magnitude). The peak content in the switch related region is measured as 0.0354A (8.85% of the desired current). This indicates that in terms of torque performance, under Bang-Bang control this machine could produce torque ripple at unknown frequencies which could be as high as 8.85% of the desired torque – this could make the controller unsuitable for precision tool applications, however due to the nature of this distribution it is difficult to specifically quantify these effects (an often cited disadvantage of Bang-Bang control).

Figure 2-28 shows the FFT of the phase current in the Interroll motor under PI control at 400rpm 0.4A reference current (the sample window is restricted to an amplitude of only 0.012A in order to better highlight the switch harmonics.) Immediately noticeable is the easily identified harmonic content of the controller when compared to the Bang-Bang controller. The content can clearly be labelled at the fundamental frequency (26.67Hz), the switch frequency (20kHz) and its associated superharmonics, the last of which is visible up to 2.6MHz (not shown in Figure 2-28). The magnitude of the current at the fundamental frequency is measured as 0.3657A (91.4% of the desired current). The largest additional current content is present at the switching frequency (the magnitude at each of the following superharmonics is seen to gradually decrease). The magnitude of the current content at the switch frequency is measured as 0.00583A (1.46% of the desired current). This indicates that the PI controller has far more preferable performance in terms of current content at frequencies other than the desired – this minimises the impact upon torque ripple.

Figure 2-29 shows the FFT of the phase current in the Interroll motor under SVPWM control operating at 0.4A; the sample window is restricted to an amplitude of only 0.04A in order to better highlight the switch harmonics. The switch frequency is again clearly

visible at 20kHz and at the following superharmonics. In the case of the SVPWM controller the superharmonics are observed up until 2.86MHz which is similar to the PI controller which continues up to 2.6MHz. The amplitude of the current at the fundamental frequency (26.67Hz) is measured as 0.3813A (95.3% of the desired current) and the amplitude at the switching frequency is measured as 0.00475A (1.1875% of the desired current at the fundamental frequency). It is obvious from this analysis that the SVPWM also has major advantages against the Bang-Bang controller with respect harmonic current content and performance predictability. The analysis also shows that the SVPWM marginally outperforms the PI controller; however this improvement could justifiably be described as negligible with consideration to most applications.

It should be noted that Figures 2-27 to 2-29 for only the Interroll machine at one speed and at one reference current. However the differences exhibited between the spectra given are consistent across the range machines, the range of speeds and the range of reference current level.

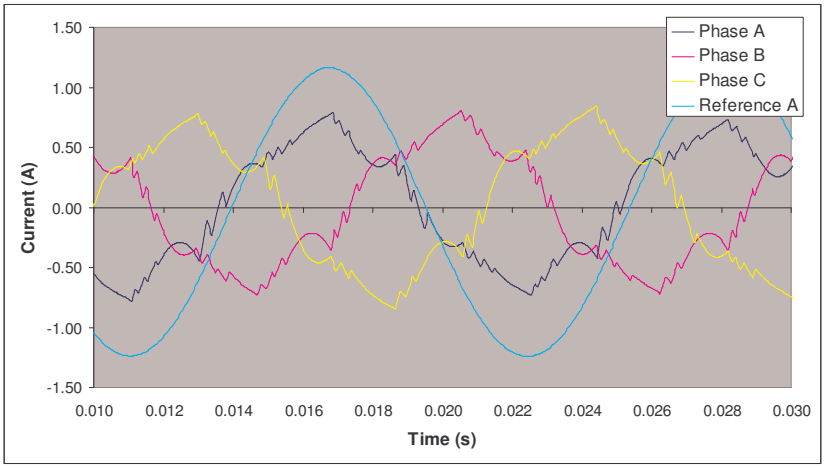

Figure 2-30: 8 pole Interroll Machine operating under Bang Bang control at 1300rpm 1.2A test point.

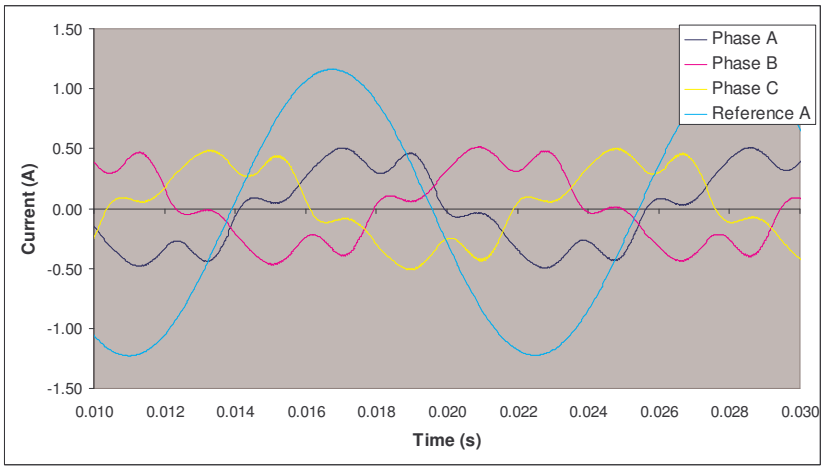

Figure 2-31: 8 pole Interroll Machine operating under PI control at 1300rpm 1.2A test point.

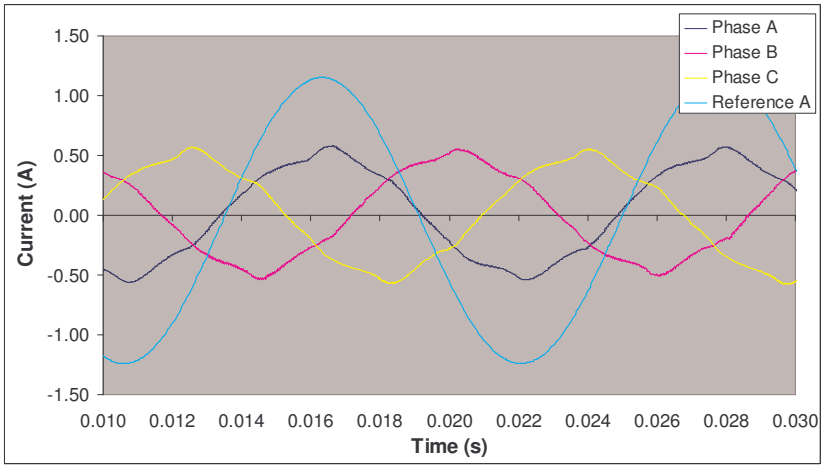

Figure 2-32: 8 pole Interroll Machine operating under SVPWM control at 1300rpm 1.2A test point.

So far only examples of typical phase current waves for each controller operating at relatively low demand (low speeds) have been presented. Generally the controllers are expected to produce waveforms of this nature throughout the constant torque region of

the torque/speed profile of the machine. Aesthetically speaking the SVPWM control appears most optimal in consideration of the sinusoidal current requirements of an AC machine (this can be concluded based upon the superior current ripple performance).

Figure 2-30 shows the Bang-Bang controller operating beyond the constant torque region of the machine. It can clearly be seen that the controller maintains strong phase alignment with the commanded current wave (Phase A and Reference A are in phase). However it can also be seen that the controller is incapable of achieving the desired current magnitude in the phases around the peak regions. This is due to the limitation of the DC voltage – the controller is incapable of generating a high enough voltage in the phases to overcome the back EMF generated and produce the desired current waveform.

Figure 2-31 shows the PI controller operating beyond the constant torque region of the machine. It can clearly be seen that in the case of the PI controller, there is a poor phase alignment with the commanded current wave (Phase A and Reference A are not in phase). The resultant phase current lags the commanded phase current by a considerable margin. This is commonly observed in the PI controller; the controller (in the stationary frame) struggles to change its commanded gate drives by the degree required to maintain alignment. This issue is often cited as a particular disadvantage of the PI controller. The limitation of the DC voltage again results in failure to achieve the desired current magnitude in the phases around the peak regions.

Figure 2-32 shows the SVPWM controller operating beyond the constant torque region of the machine. In the case of the SVPWM it can be clearly seen that the phase alignment is as good as the Bang-Bang example in this region. This is due to the controller working in the rotating reference frame; the internal control loops remain capable of commanding sufficient change in the drive signals to maintain phase alignment. Once again the limitation of the DC voltage can be seen to affect the current magnitude of the resultant current wave.

The results presented at this stage have backed up many of the classical expectations from the control techniques outlined. Bang-Bang control has been shown to exhibit higher ripple levels than the other techniques and in the frequency domain the current content is extremely difficult to quantify. It remains to be seen how each of the strategies will impact upon more meaningful performance characteristics.

2.9. Torque Output Analysis

The figures presented in this section highlight the quality of current regulation offered by each of the control strategies across the speed range. The quality of regulated current in the phase windings of the machine has a direct impact upon the torque output of the machine and this will be highlighted clearly in the figures presented.

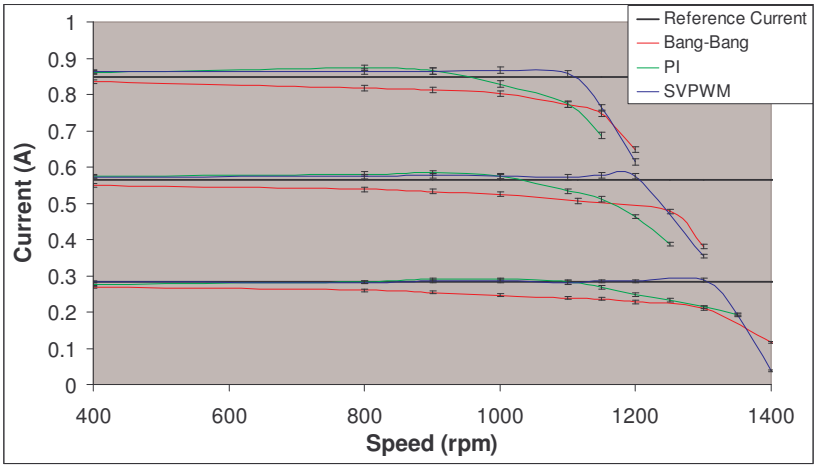

Figure 2-33: Regulation of Current (RMS) in Interroll machine at 0.4A, 0.8A and 1.2A reference current intervals

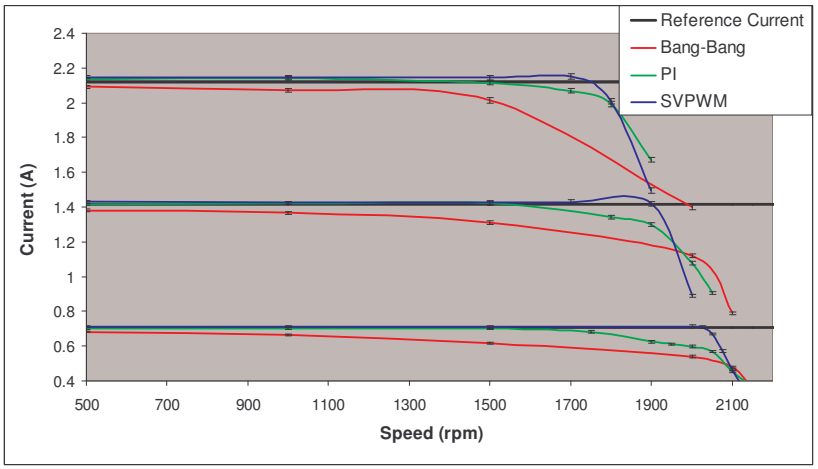

Figure 2-34: Regulation of Current in SEM machine at 1A, 2A and 3A reference current intervals

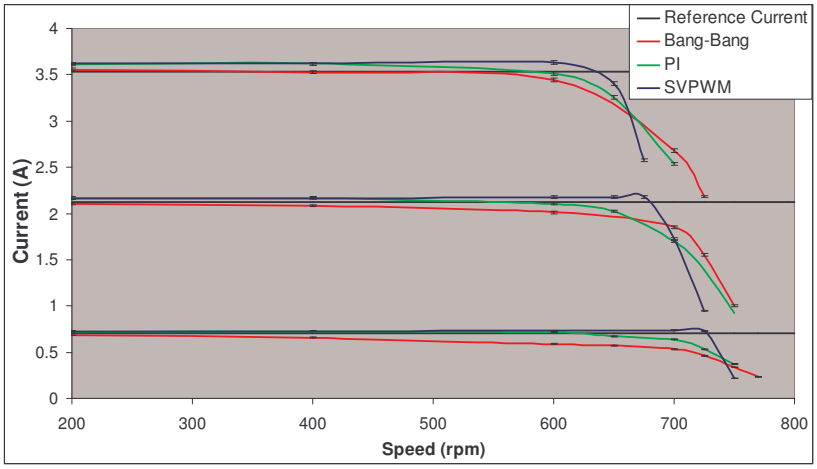

Figure 2-35: Regulation of Current in Heidenhain machine at 1A, 3A and 5A reference current intervals

Figure 2-33 - Figure 2-35 illustrate the differences in performance of each strategy with respect to the regulation of the commanded reference current. It can be seen that in general the Bang-Bang controller will never regulate current at the desired reference magnitude – typically only achieving a maximum of 95% - 98% the desired reference current; this is mainly due to the large current ripple present in the Bang-Bang controller. In general both PI and SVPWM perform very similarly in the constant torque region with respect to regulating the phase current. This is due to the predictive nature of the controls (each cycle the controllers generate a drive signal intended to effectively regulate the current whereas the Bang-Bang controller has a purely reactionary response). The two controllers generally regulate the phase current around the ideal reference value. Also illustrated in these figures is that the SVPWM regulator regulates the desired current for a larger period of the speed range than the other two controllers. The other two controllers both show a decline in the phase current regulation at lower speeds compared to the SVPWM controllers; however the Bang-Bang controller shows an extended range of regulation than compared to the other two. This is due to the Bang-Bang controller's poorer quality of regulation; the controller performance inadvertently injects current into the synchronous direct axis (essentially introducing field weakening operation) thus extending the operating speed range.

The Torque/Speed profiles for each controller are inevitably going to share the profile of the current regulation given in Figure 2-33 - Figure 2-35.

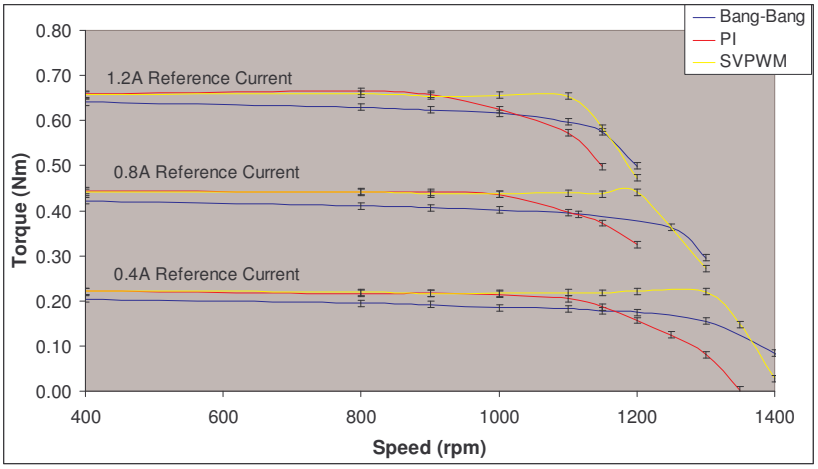

Figure 2-36: Torque/Speed Profile Comparisons for Interroll motor

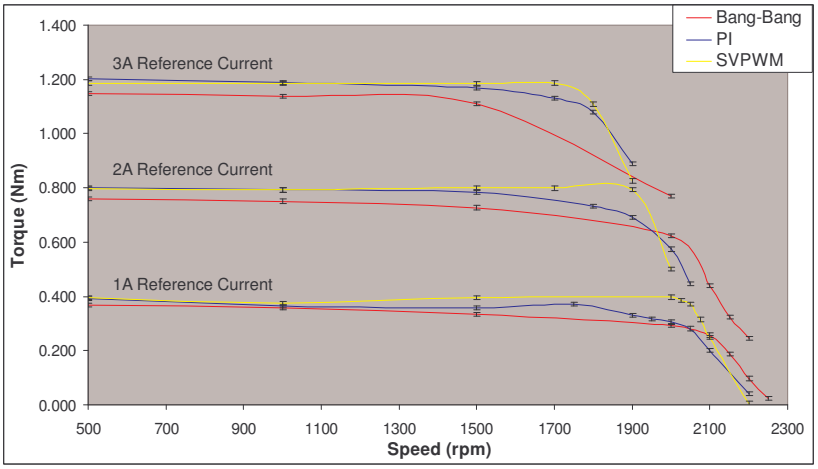

Figure 2-37: Torque/Speed Profile Comparisons for SEM motor

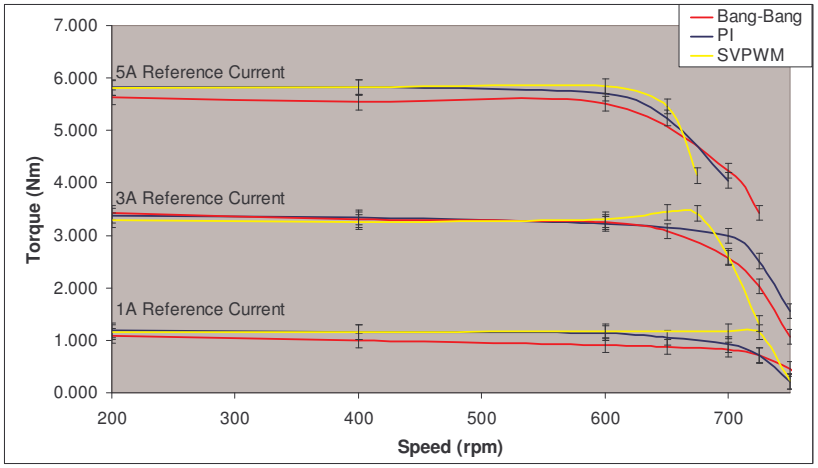

Figure 2-38: Torque/Speed Profile Comparisons for Heidenhain motor

Figure 2-36 - Figure 2-38 compares the torque outputs of the three control strategies. It is clear that the most optimal constant torque region performance comes from the SVPWM controller and that the Bang-Bang controller appears to achieve the widest speed range in terms of maintaining a torque output. The Bang-Bang controller however can be

seen to produce a significantly smaller torque output than the other two controllers at all times – this is due to the poor current regulation that is demonstrated in Figure 2-33 - Figure 2-35. The figures show that the other two control techniques regulate current far closer to the desired reference current with the SVPWM overshooting the value less than the PI regulator does. In terms of torque/speed profile performance, the most obvious preference would be for the use of the SVPWM controller. This is down to the larger higher quality constant torque region it generates. However depending on application, the argument could be made that were the application expected to exploit the region beyond the constant torque then the greater output range is offered by the Bang-Bang controller – however this is traded against the poorer torque output. The PI controller offers no particular advantage over either technique with respect to these arguments.

2.10. Voltage Source Inverter Efficiency

Clearly the quality of current regulation has an impact upon the torque output of the machine and the range of speed over which this torque can be maintained (the constant torque region). The impact this has upon the efficiencies of the drive is also of interest.

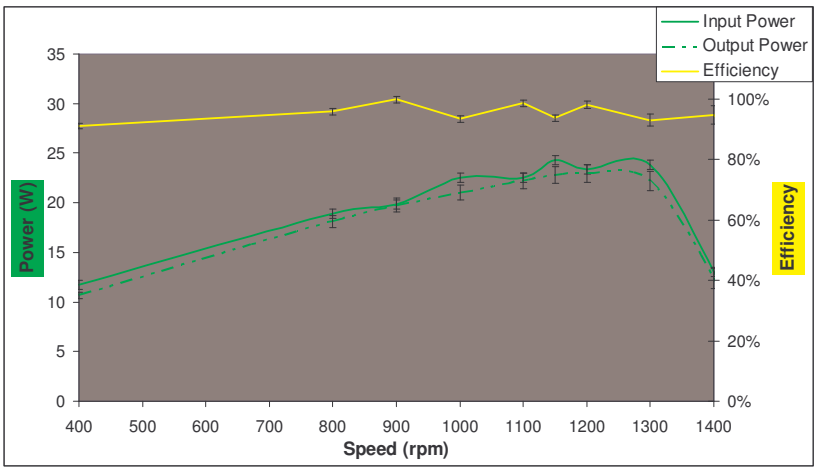

Figure 2-39: VSI Efficiency and Power Calculations of Interroll machine under Bang-Bang controller 0.4A Reference Current

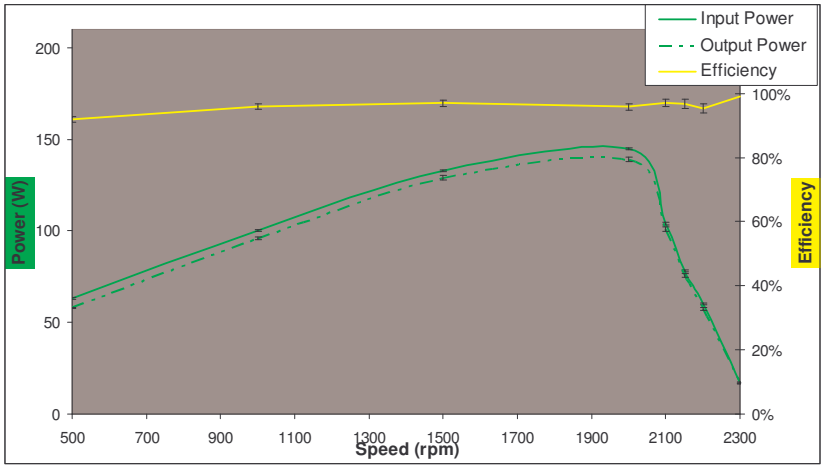

Figure 2-40: VSI Efficiency and Power Calculations of SEM machine under Bang-Bang controller 2A Reference Current

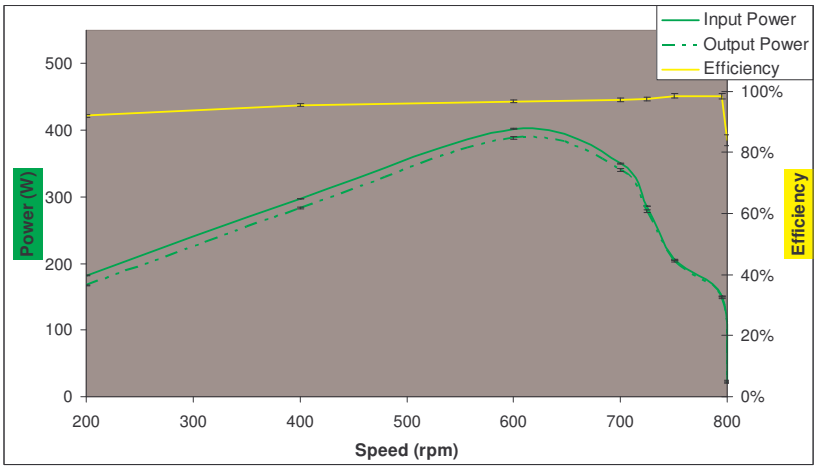

Figure 2-41: VSI Efficiency and Power Calculations of Heidenhain under Bang-Bang controller 5A Reference Current

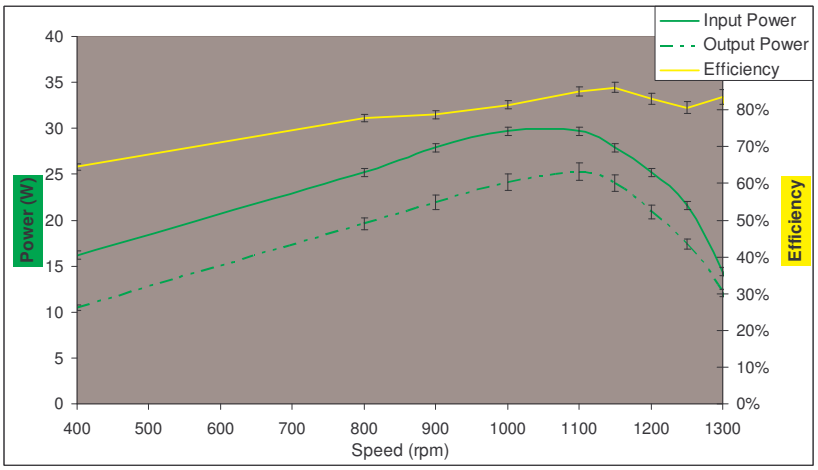

Figure 2-42: VSI Efficiency and Power Calculations of Interroll machine under PI controller 0.4A Reference Current

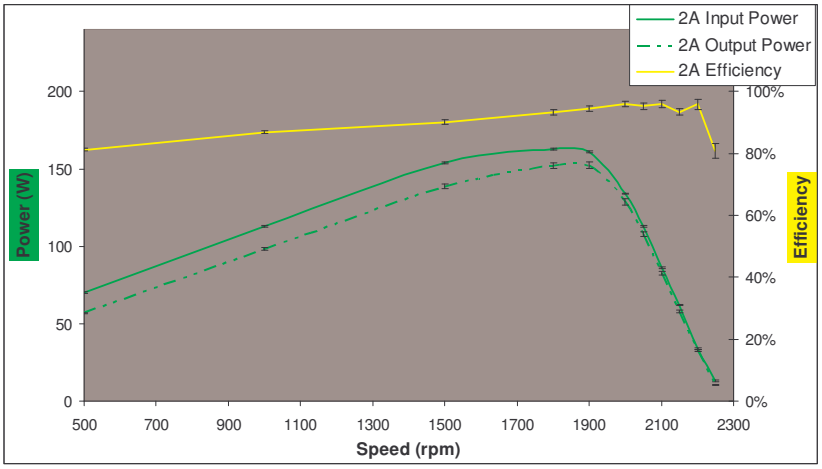

Figure 2-43: VSI Efficiency and Power Calculations of SEM machine under PI Control 2A Reference Current

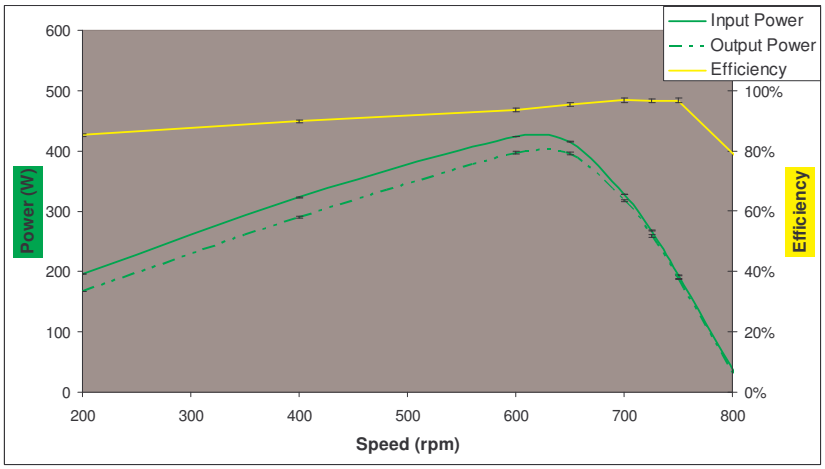

Figure 2-44: VSI Efficiency and Power Calculations of Heidenhain machine under PI controller 5A Reference Current

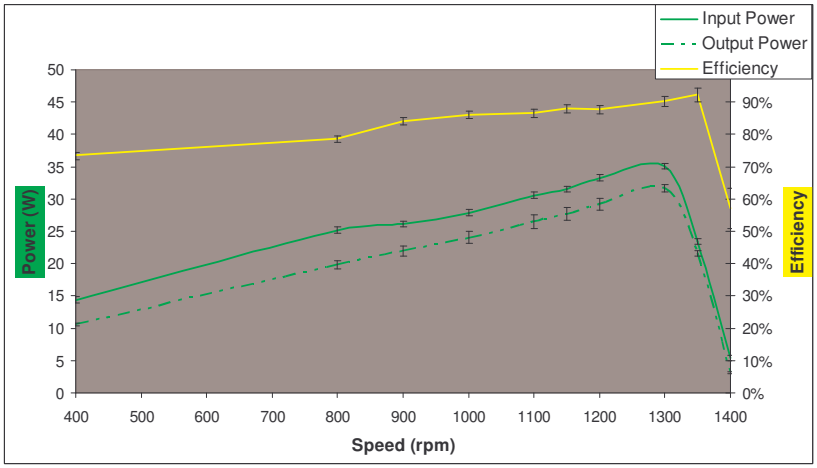

Figure 2-45: VSI Efficiency and Power Calculations under SVPWM controller 0.4A Reference Current

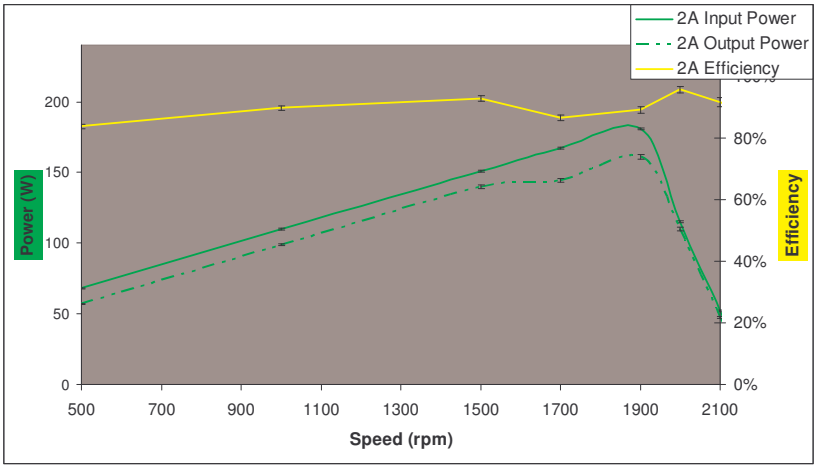

Figure 2-46: VSI Efficiency and Power Calculations under SVPWM Control 2A Reference Current

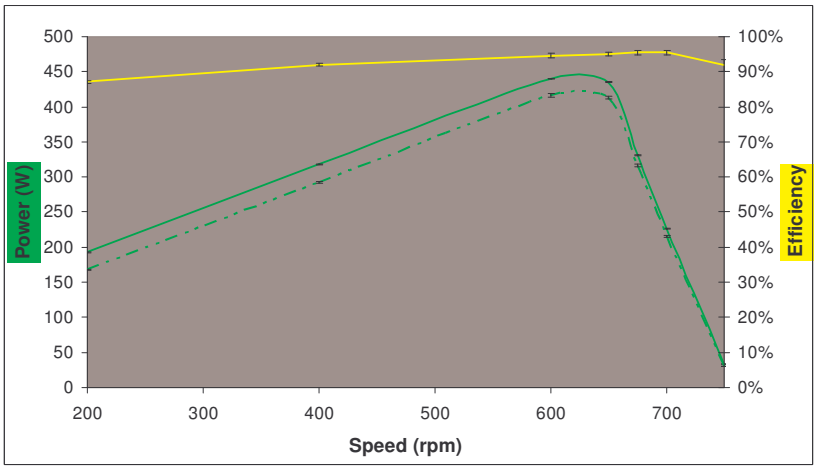

Figure 2-47: VSI Efficiency and Power Calculations under SVPWM controller 5A Reference Current

Figure 2-39 - Figure 2-41 show the inverter efficiencies calculated under Bang-Bang control during steady state testing. The power losses vary widely across the reference current range. In Figure 2-39, the lowest reference current operated under Bang-Bang control, the losses in the inverter stage are generally shown to be very low, less than 2W. At the maximum reference current, 5A, the maximum power loss in the inverter is just under 15W. The increase in reference current can be seen to result in a small increase in the inverter efficiency at higher speeds. This is generally to be expected with Bang-Bang control, the technique ensures the maximum power capability of the DC Link is made available to the phase windings of the machine. This is achieved through the direct switching response of the technique, thus minimizing the inverter losses commonly attributed to switching.

Figure 2-42 - Figure 2-44 show the Inverter efficiencies calculated under PI control during steady state testing. Again the power losses vary widely across the reference current

range for the PI controller. At the lowest reference current tested, the losses in the inverter stage are generally shown to be higher than the Bang-Bang losses, generally just under 6W. At the maximum reference current, 5A, the maximum power loss in the inverter is just under 35W which represents a serious increase from the Bang-Bang results. The efficiency is again observed to improve as the reference current increases, in much the same manner as the Bang-Bang efficiency does (albeit with larger power losses). The poorer power loss performance in comparison to the Bang-Bang controller is generally to be expected. This is because the Bang-Bang technique ensures the maximum power capability of the DC Link is made available to the phase windings of the machine. This is achieved through the direct switching response of the technique, thus minimizing the inverter losses commonly attributed to switching. A noticeable feature of the efficiency curves under PI control is the dramatic drop at the highest speeds, this could be associated with the difficulties the PI control has maintaining phase alignment with the reference and actual currents.

Figure 2-45 - Figure 2-47 show the inverter efficiencies calculated under SVPWM control during steady state testing. The power losses in the inverter stage are larger than Bang-Bang but lower than PI at lower speeds and higher reference current values. It is the lowest reference current tested, 0.8A the inverter power losses reach a maximum of just under 5.5W (comparable to the PI control). At the highest reference current tested the maximum power loss observed was just under 26W which is both considerably better than the PI controller but also considerably worse than the Bang-Bang control. This provides further evidence that the flexible switch frequency utilised by the Bang-Bang controller helps to reduce power losses in the inverter stage.

In consideration of inverter performance it seems as though the most favourable control technique is the Bang-Bang controller, the power losses being the most minimal and there is also no apparent decrease in efficiency in the higher speed regions. The PI controller appears to be the least efficient with respect to the inverter. Whilst the trend is generally similar to that of SVPWM, the power losses are greater for the PI controller. These results suggest that the Bang-Bang controller is the most optimal selection in terms of inverter losses, however it must be stressed that the switch devices are not of optimal selection for this power range. In inverters with switch devices of a lower power specification, these results are unlikely to be repeated.

2.11. Average Switch Frequency Analysis

The VSI efficiency calculations, in particular the analysis of the power losses, have shown that the Bang-Bang controller benefits from not having a fixed switching frequency in terms of minimising these losses. A closer analysis of the average switch frequency observed in the Bang-Bang controller is of interest in attempting to verify this theory.

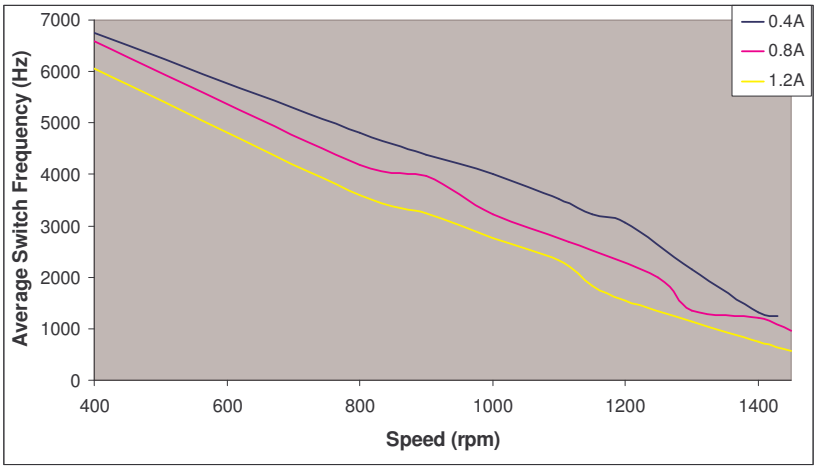

Figure 2-48: Average Switch Frequency of Bang-Bang controller during steady state testing with the Interroll machine

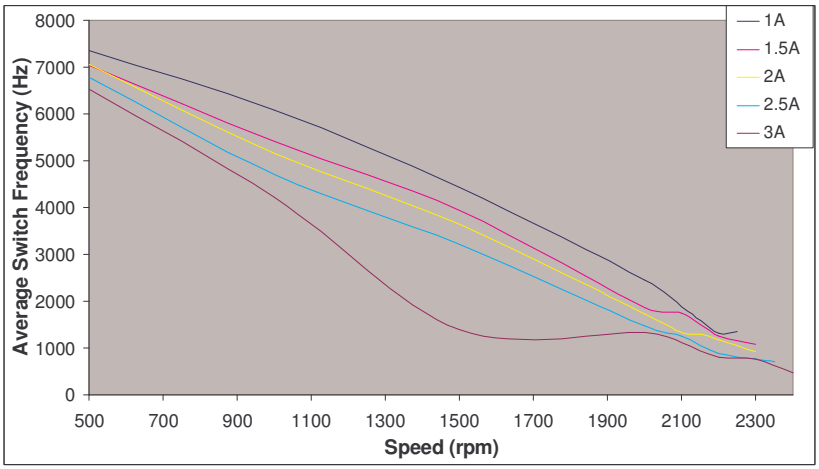

Figure 2-49: Average Switch Frequency of Bang-Bang controller during steady state testing with the SEM machine

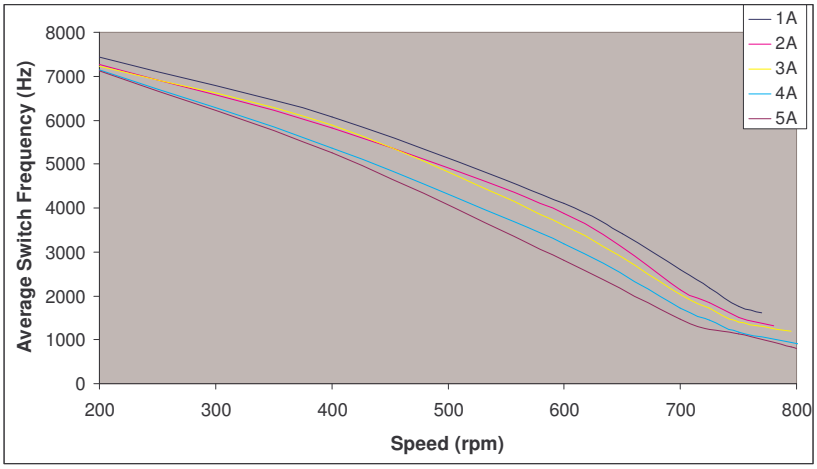

Figure 2-50: Average Switch Frequency of Bang-Bang controller during steady state testing with the Heidenhain machine

Figure 2-48 highlights the particular advantage the Bang-Bang controller gains with respect to speed from the flexible switching strategy it implements. Normally cited as a disadvantage, the non-fixed switching frequency is seen to decrease with respect to both speed and reference current. This allows for minimal switch event related power losses with respect to the other two control techniques. This feature of the Bang-Bang controller extends the operating speed of the machine when compared to other controllers. Figure 2-49 is very similar to Figure 2-48 in highlighting the advantage the Bang-Bang controller has in terms of its dynamic switching behaviour. The range of frequencies measured in the mid-range torque tests under Bang-Bang control are only slightly extended at both ends of the speed range than is the case in the low torque tests. The ability of the controller to switch at frequencies far lower than the other two controllers, especially at the higher speeds, suggests that the Bang-Bang controller is capable of limiting the switching losses at the high speed region of operation. This perhaps explains why the Bang-Bang controller achieves greater efficiency and is generally seen to maintain this across the speed range. Figure 2-50 shares the characteristics of Figure 2-48 and Figure 2-49 which highlight changes in switching frequency of the Bang-Bang controller with respect to speed and current demands. Comparing the results of the 3 separate torque tests ranges, the switch frequencies generally progress through the same range of switch frequencies in response to their respective speed and current demands.

2.12. Motor Efficiency

Whilst the Inverter has been shown to be a source of considerable power losses in the overall drive system, the motor is responsible for the conversion of power from an electrical input to a mechanical output. Thus the efficiency of the power conversion observed in the motor is of particular interest under each of the control strategies under investigation.

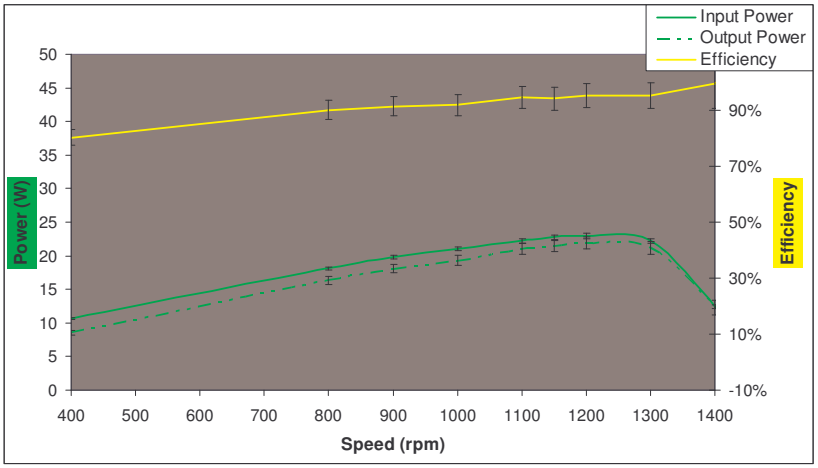

Figure 2-51: Efficiency of Interroll Motor under Bang-Bang control 0.4A Reference Current Range

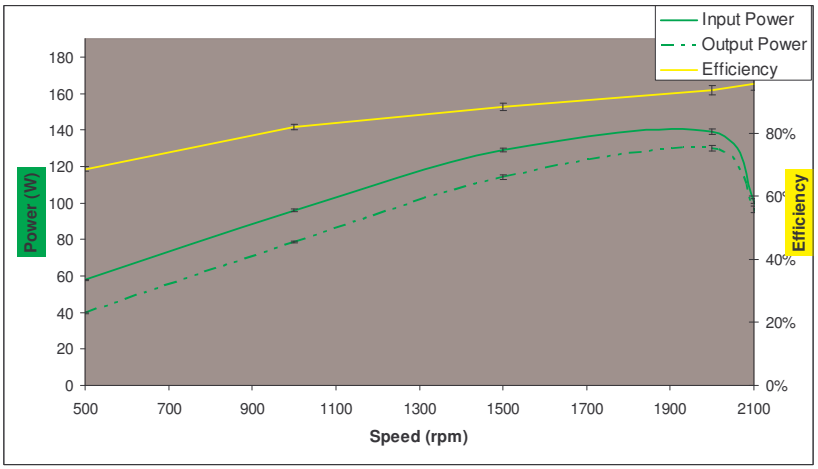

Figure 2-52: Efficiency of SEM Motor under Bang-Bang control 2A Reference Current Range

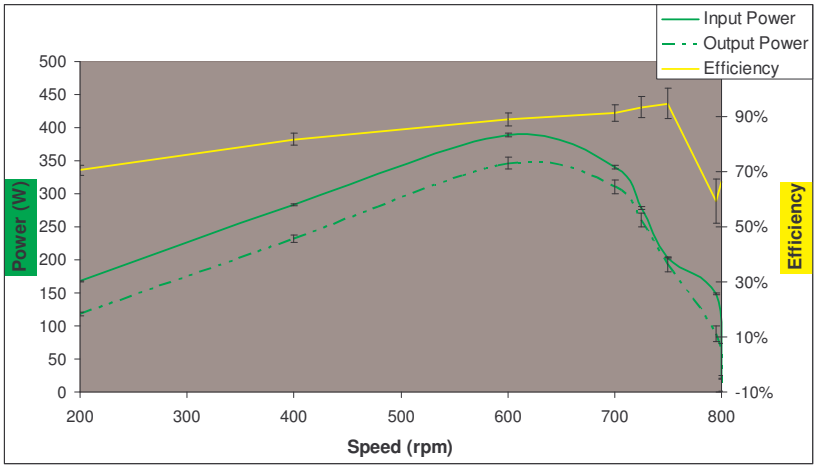

Figure 2-53: Efficiency of Heidenhain Motor under Bang-Bang control 5A Reference Current Range

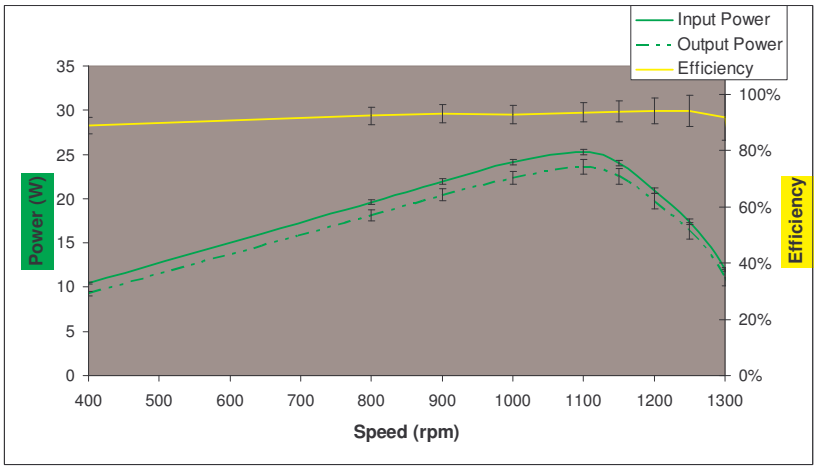

Figure 2-54: Efficiency of Interroll Motor under PI control 0.4A Reference Current Range

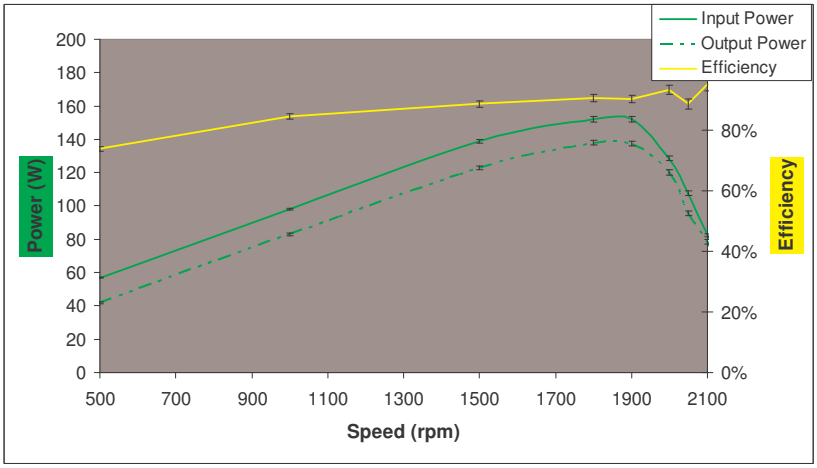

Figure 2-55: Efficiency of SEM Motor under PI control 2A Reference Current Range

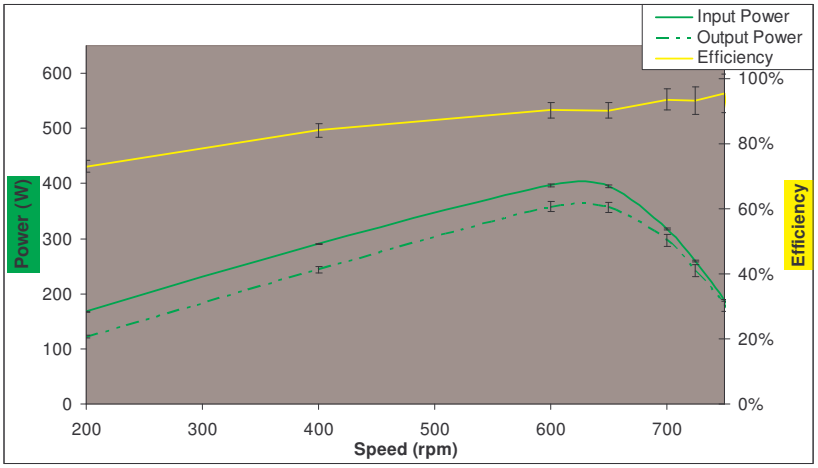

Figure 2-56: Efficiency of Heidenhain Motor under PI control 5A Reference Current Range

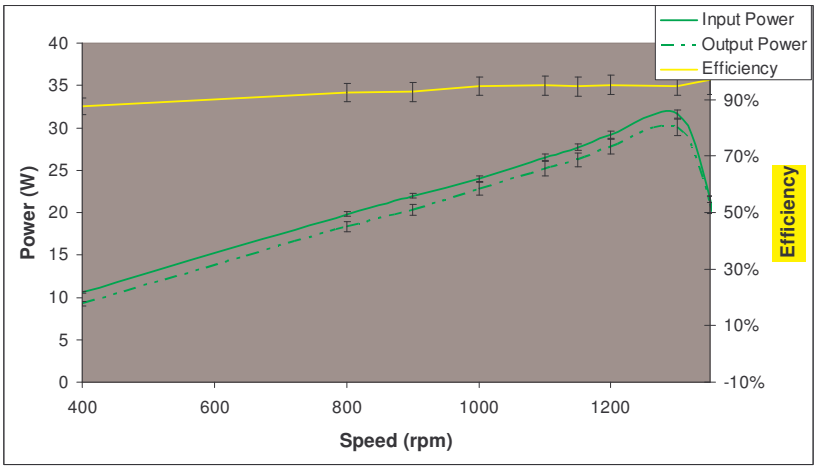

Figure 2-57: Efficiency of Interroll Motor under SVPWM control 0.4A Reference Current Range

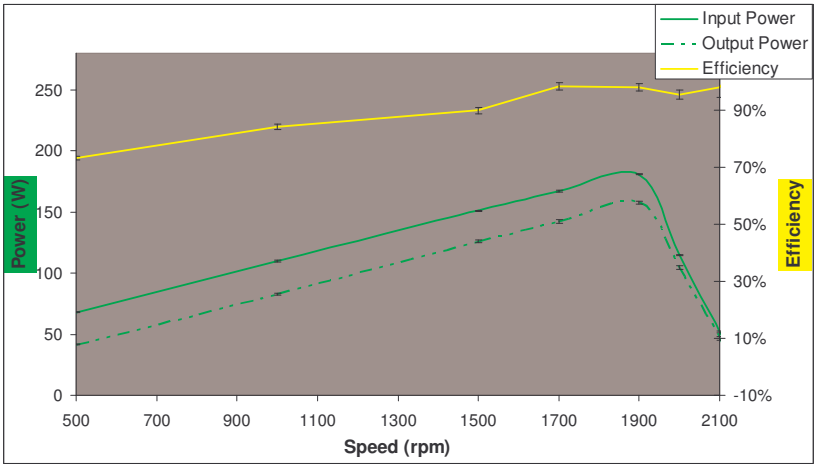

Figure 2-58: Efficiency of SEM Motor under SVPWM control 2A Reference Current Range

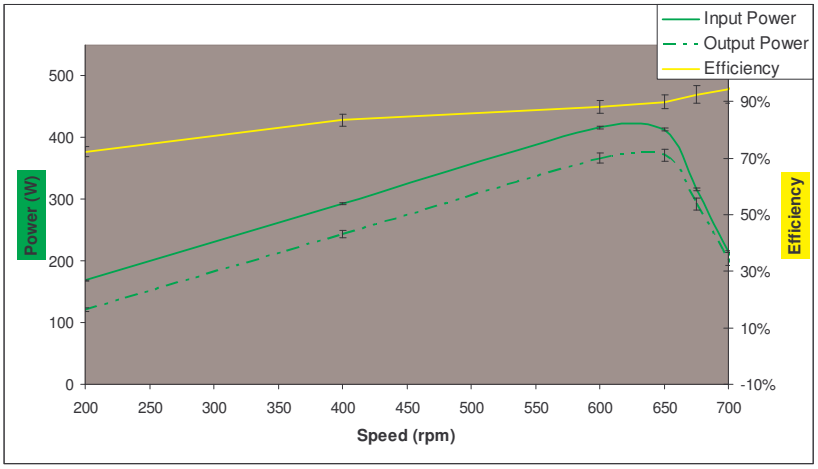

Figure 2-59: Efficiency of Heidenhain Motor under SVPWM control 5A Reference Current Range

Figure 2-51 - Figure 2-53 show the efficiencies and power calculations of the motor parameters under Bang-Bang control. At the lowest reference current operated, 0.4A, the power losses are observed to be very low, around 2W. At the highest reference current, 5A, the power losses are as high as 60W. This represents a large variation in power losses in the motor which reflects the differences in the power ratings of the respective motors. The power losses in the motor are a direct result of the quality of the current which flows in the phase windings, the expectation is that with a poorer quality of current the Bang-Bang controller will exhibit the highest power losses in the motor stage.

Figure 2-54 - Figure 2-56 show the efficiencies and power calculations of the motor parameters under PI control. Again there is a wide range of power loss observed in the motor stage. At the lowest reference current operated, 0.4A, the power losses are around 1.5W – slightly lower than the Bang-Bang technique. At the highest reference current, 5A, the power losses are as high as 45W noticeably lower than the Bang-Bang result. This falls in to place with expectations, the PI controller regulates a higher quality of phase current in the machine and these results in lower power losses in the motor.

Figure 2-57 - Figure 2-59 show the efficiencies and power calculations of the motor parameters under SVPWM control. The expectation in these results is that the power losses will be most closely matched with the PI controller as the quality of phase current is far higher than in the Bang-Bang regulator. At the lowest reference current operated, 0.4A, the power losses are also around 1.5W – matched very closely to the PI results. At the highest reference current, 5A, the power losses are as high as 50W which is a slight increase in power loss compared to the PI controller.

The results obtained considering the motor losses fall in line with expectations, the Bang-Bang controller regulates the poorest quality of current through the machine phase windings and thusly is subjected to the highest measured losses at this stage. SVPWM exhibits slightly higher power losses than the PI controller which wouldn't necessarily fall in line with expectations, however with such a small difference in performance this could perhaps be eliminated with a more considered approach to the tuning of the PI control stages at the heart of the technique. The PI regulated results once again exhibit a drop in efficiency in the highest speed regions of two of the tests presented; this perhaps directs attention once again at the poor phase alignment of the technique in this region.

2.13. Overall Drive Efficiency

The overall drive efficiency represents a more broad analysis of the power losses in the system by comparing the measured electrical power input to the system with the output rotational power measured by the torque transducer. The vast majority of these losses are expected to be contributed by both the inverter and the motor stages, however there is an expectation that some parasitic losses may be present elsewhere in the system. These tests will highlight any significance that may exist in these losses between the control strategies under test.

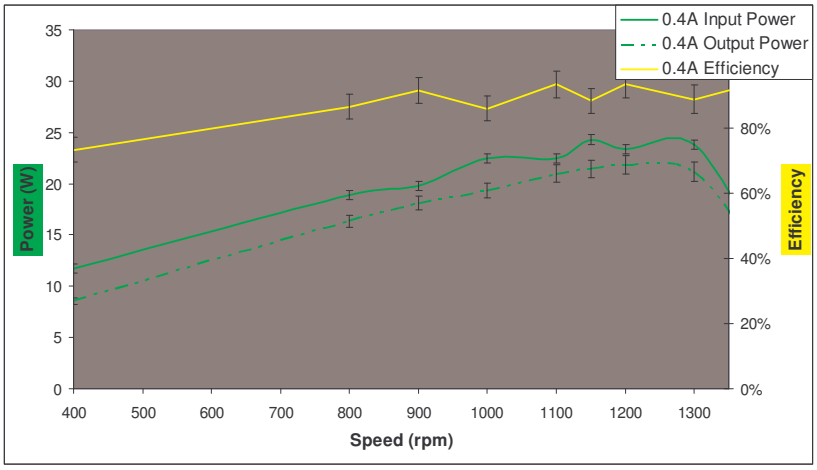

Figure 2-60: Bang-Bang Drive Efficiency and Power Calculations for the Interroll machine - 0.4A Reference Current

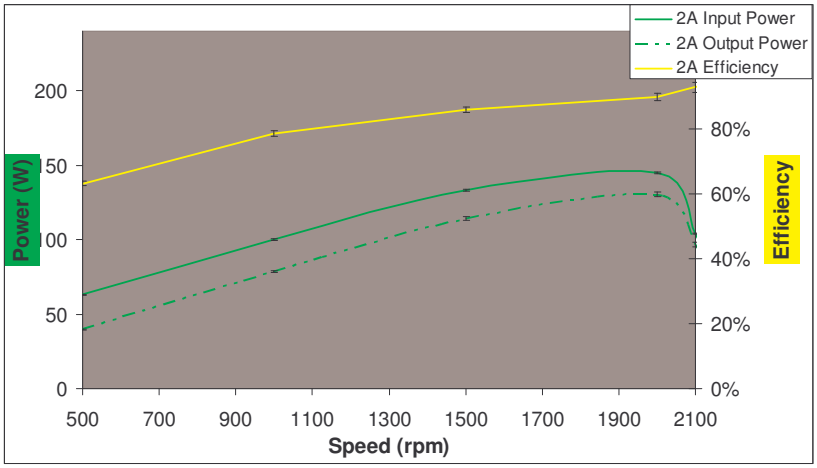

Figure 2-61: Bang-Bang Drive Efficiency and Power Calculations for the SEM machine - 2A Reference Current

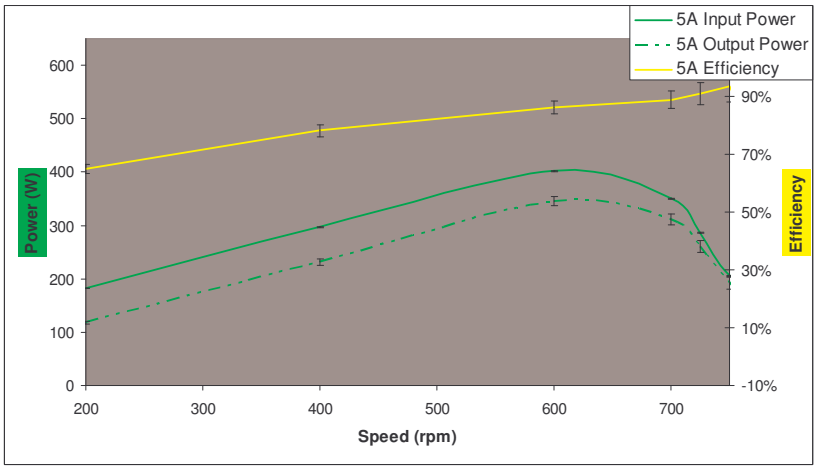

Figure 2-62: Bang-Bang Drive Efficiency and Power Calculations for the Heidenhain - 5A Reference Current

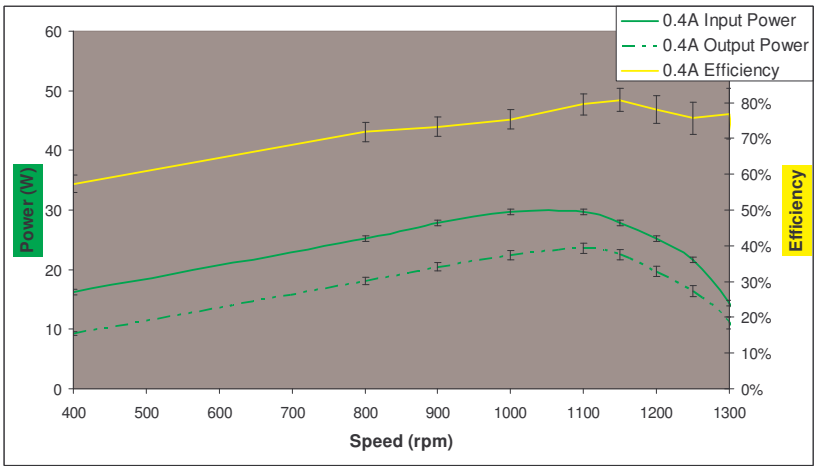

Figure 2-63: PI Drive Efficiency and Power Calculations for 0.4A Reference Current

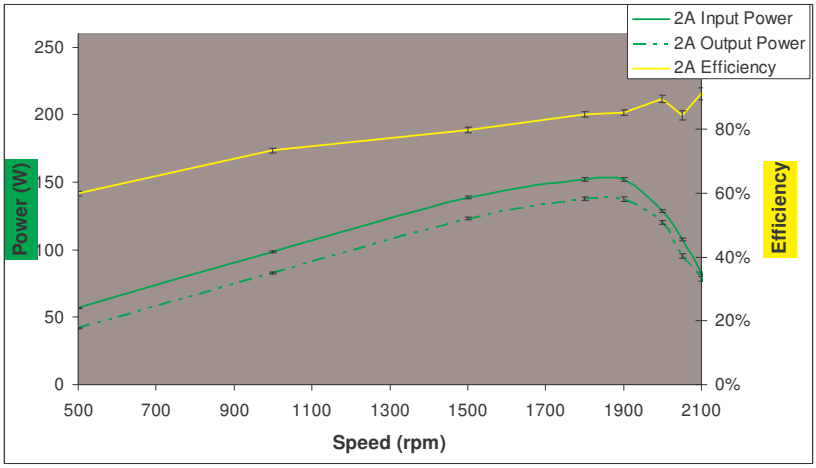

Figure 2-64: PI Drive Efficiency and Power Calculations for 2A Reference Current

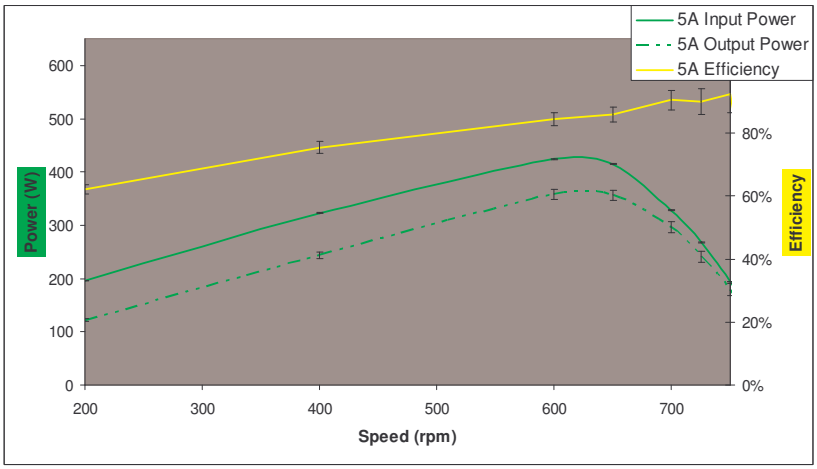

Figure 2-65: PI Drive Efficiency and Power Calculations for 5A Reference Current

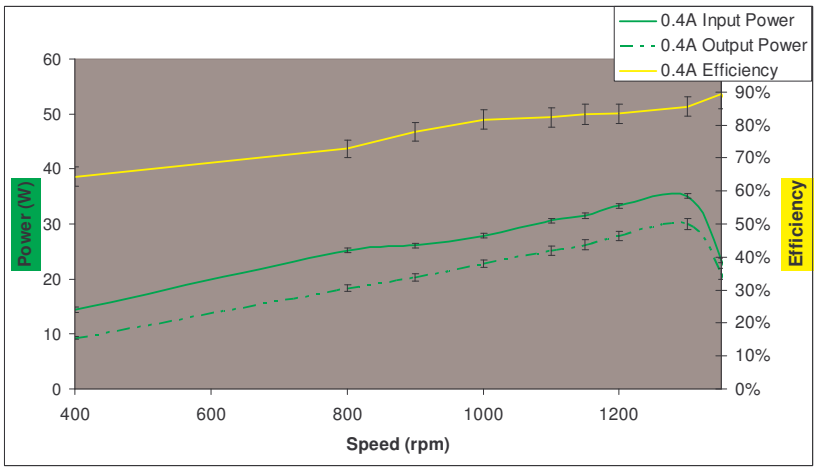

Figure 2-66: SVPWM Drive Efficiency and Power Calculations for 0.4A Reference Current

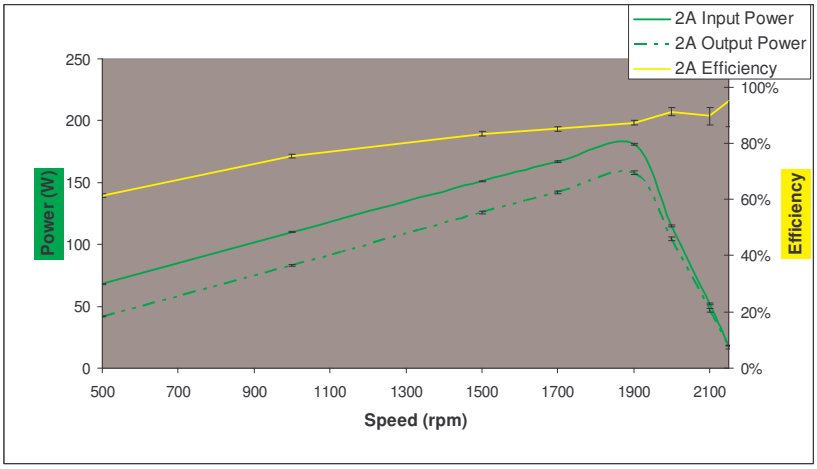

Figure 2-67: SVPWM Drive Efficiency and Power Calculations for 2A Reference Current

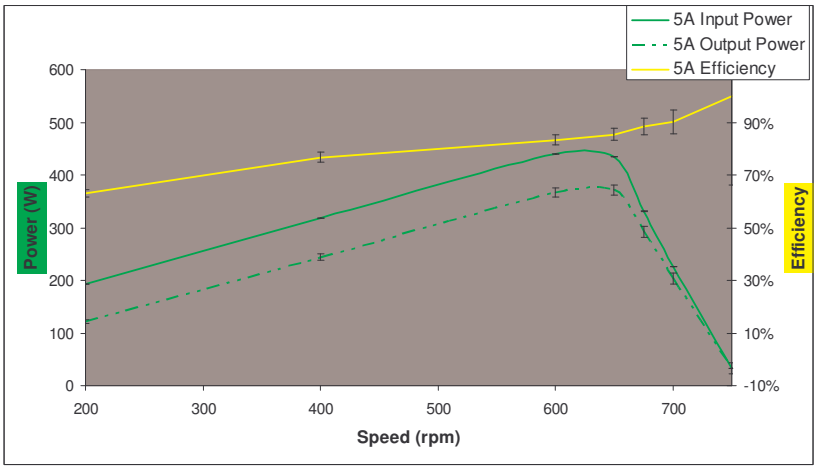

Figure 2-68: SVPWM Drive Efficiency and Power Calculations for 5A Reference Current

Figure 2-60 - Figure 2-62 show the efficiencies and power calculations of the overall drive system under Bang-Bang control. The lowest overall power losses observed, at the 0.4A reference current, are under 4W. The maximum losses observed, at the 5A reference current, are seen to reach just under 75W. This clearly demonstrates that the majority of the losses in this particular drive system are contributed in the motor stage. This would lead to the expectation that the Bang-Bang controller would perform most poorly in these comparisons; however, the impact of the motor losses is offset in this system by the considerably lower inverter losses the Bang-Bang benefits from. This is not something that can be relied upon as consistent for all drive system setups, but in this particular case the benefit is noticeable.

Figure 2-63 - Figure 2-65 show the efficiencies and power calculations of the overall drive system under PI control. The lowest overall power losses observed, at the 0.4A reference current, are under 8W. The maximum losses observed, at the 5A reference current, are

seen to reach just under 80W. In this case at the lower range of the losses the majority are clearly contributed in the inverter however in the higher end of the power loss scale for the PI controller the losses are split more evenly between the inverter and the motor stage. The overall losses for the PI controller are largely comparable to the Bang-Bang controller, only slightly worse. Whilst the PI controller has shown a higher level of performance in the motor in terms of losses, the switch component selection for the system has proven to be significantly beneficial to the Bang-Bang controller to the extent that its efficiency performance is stronger. This clearly demonstrates that despite the PI controller being proven to generate higher quality phase currents (the benefit of this having been highlighted in the motor loss comparison) – the Bang-Bang controller can still outperform PI regulation in terms of efficiency if an appropriate inverter circuit is utilised.

Figure 2-66 - Figure 2-68 show the efficiencies and power calculations of the overall drive system under SVPWM control. The power losses at the lowest reference current, 0.4A, are under 7W. The maximum losses observed, at the 5A reference current, are just under 75W. The results echo those observed in the PI results, in which over the range of losses considered the contributions between the inverter losses and the motor are relatively even. In terms of overall efficiency performance, the SVPWM controller closely matches the results of the Bang-Bang controller, which as has been highlighted benefits from the switch device selection in this particular drive system. The expectation would be that the device selection would generally be less favourable in most other drive systems and that both the PI and SVPWM controllers would outperform the Bang-Bang controller in terms of efficiency.

2.14. Torque/Current (Kt) Performance

The final aspect for consideration in the regulator comparisons is that of the torque constant. It is a measure of the torque output with respect to the current input - this is often cited as a performance characteristic by machine manufacturers and thus is either a design goal of the machine design or is a parameter which is tested before the product is marketed. Given it is a parameter referenced by both manufacturer and customer in system design considerations, it is crucial that the figure quoted is reliable and consistent irrespective of implementation. Thus the current regulator implemented in the drive system has no effect on the Kt of the machine (as expected) but does on the drive on system Kt.

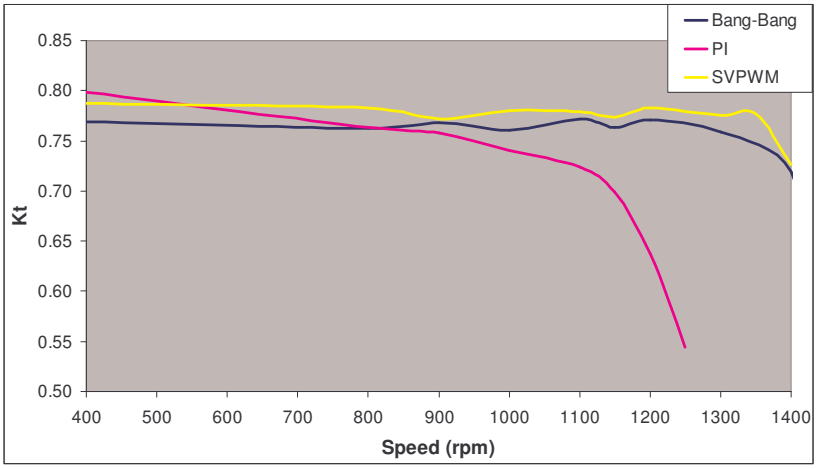

Figure 2-69: Interroll drive system Kt measurement for all regulators 0.4A Reference Current

Figure 2-69 gives the Kt measurements for the different controllers at the 0.4A reference current, the Kt calculations are generally of this magnitude for all reference currents. The Kt factor is relatively equal for all test points at the higher reference currents but does show some slight variation at the lower reference currents. In general the value of Kt typically resides around 0.77. It is clear from the graph, however, that there are optimal controllers and test points at which to reference the constant Kt. The PI controller appears to be the poorest controller with which to define Kt as it maintains a constant over the smallest speed range and particularly at lower reference currents it shows the greater variance of Kt. The SVPWM and the Bang-Bang controller appear to be far more capable of maintaining a fixed value of Kt over a wider speed range than PI – SVPWM having slightly more continuity of this value at the higher speeds.

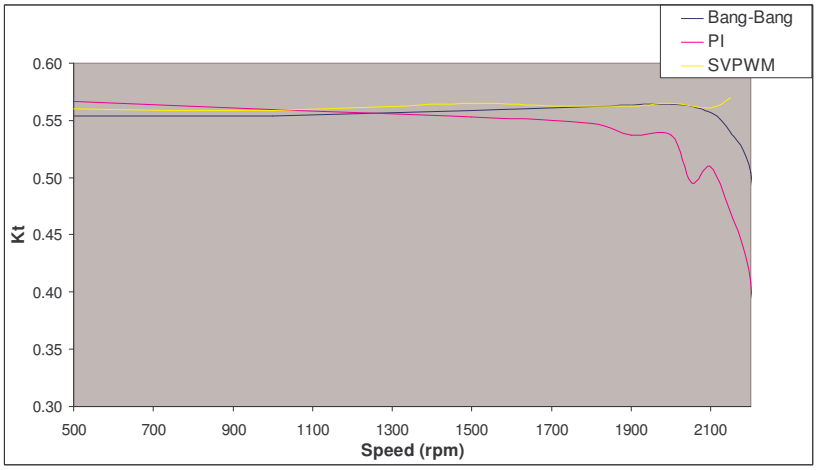

Figure 2-70:SEM drive system Kt measurement for all regulators 2A Reference Current

Figure 2-70 gives the Kt measurements for the different controllers at each of the reference currents. The constant Kt is generally well matched for all three controllers

around a value of 0.55, with the measurement only becoming poor in the high speed regions as was the case in the Interroll tests. Once again the results tend to indicate that across the speed range the poorest measure of Kt is given by the PI controller. Despite the Kt measurement in the PI control being the highest at low speed, the value is seen to generally decrease steadily through the speed range before rolling off completely at a lower speed than the other two controllers. The SVPWM controller shows reasonably consistent measurement of the Kt value at the higher reference current, usually a value slightly higher than that measured by the other controllers over the majority of the speed range.

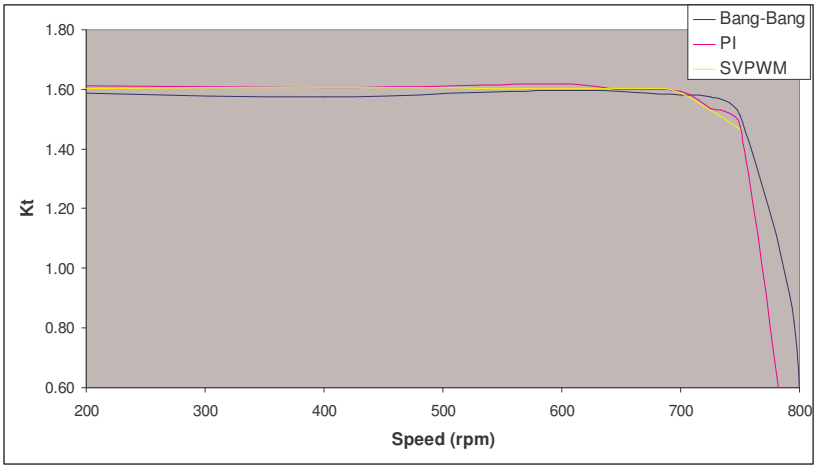

Figure 2-71: Heidenhain drive system Kt measurement for all regulators 5A Reference Current

Figure 2-71 gives the Kt measurement of the Heidenhain drive system under each control strategy in the 5A reference current range. A Kt value of around 1.6 is generally observed using all techniques. The Bang-Bang controller is generally the technique which sustains the measured value of Kt over the longest speed range however the tail of the high speed region is reasonably matched across the control strategies. In this example the Bang-Bang technique is quite clearly the most optimal with which to make Kt measurements. The superior Kt measurements offered by the SVPWM controller, as observed in the other test ranges, is no longer distinctly visible.

In analysis of the Kt measurements made, the SVPWM controller stands out at the lower reference current as a considerably more favourable method for making the measurements. This however is not the case when the reference current is increased and this confirms the expectation that the Kt factor is predominantly influenced by the characteristics of the motor rather than the quality of current in its phase windings.

2.15. Conclusions

This chapter has investigated a thorough comparison of three common current controllers utilised in 3 phase AC permanent magnet motors. The three controllers selected represent three unique levels of complexity. The Bang-Bang controller offers the simplest controller implementation available; however it is infrequently used due to the negative impacts of its unpredictable current ripple and switch frequency characteristics. The stationary frame PI controller is generally regarded as the most commonly implemented controller in 3 phase AC motor applications despite its higher level of complexity (particularly associated with gain design). This is due to a more consistent torque output coupled with low current ripple and fixed switch frequency operation which give the design engineer a reliable estimation of harmonic current content, thus allowing for confidence in system stability. The chapter has sought to detail the implementations of each control technique on a commonly used motor drive. From this analysis it is clear to see why the PI controller is the preferential selection of the two more complex techniques.

This chapter sought to compare these techniques, not only upon there complexity and cost of implementation but also their performance characteristics when implemented in a common motor drive system. The drive systems used to test each technique were designed specifically to allow the “on-the-fly” test process described in the chapter. This test practise ensures validity in the comparisons of the performance parameters. Prior to direct comparison of measured parameters, the analysis in this chapter sought to verify the perceived performance characteristics of the regulators. Through analysis of waveform captures, the superior current ripple performance of the PI and SVPWM techniques was confirmed – as was the commonly discussed phase misalignment of the PI controller in the higher speed regions. FFT analyses of the phase current waveforms were also used to identify the larger, unpredictable current content that exists at non-ideal frequencies in the Bang-Bang controller. The PI and SVPWM were shown to have easily identified non-ideal current content related to the fixed switching frequency. Such analysis yet again isolated the Bang-Bang controller as the poorest in operation and also highlights the seemingly similar performance of the PI and SVPWM controller.

In analysis of measured performance parameters, the chapter sought to form a comparison of performance based upon the quality of torque output, the efficiencies within the system with respect to power losses and also the effectiveness of each

controller at maintaining the often cited current constant Kt (a ratio of output torque to phase current). In the case of comparing the torque outputs, the SVPWM controller was shown across all torque ranges to command the most optimal torque output, characterised as the most consistent torque output across the widest speed range available (more easily described as the nearest to ideal constant torque region). In contrast to this the Bang-Bang controller is shown to have the poorest torque output available (which could justifiably be described as having no constant torque output region) however the technique does achieve positive output torque (in all torque ranges) at the highest speeds of any of the techniques. In consideration of the power losses and efficiencies experienced in the inverter, the results are repeated across all three motors – the Bang-Bang controller is the most optimal selection of the controllers. The explanation for this is explored through consideration of the dynamic switching strategy implemented in Bang-Bang control. The SVPWM controller is shown to outperform the PI controller in this respect but the differences are almost negligible compared to the performance of the Bang-Bang controller. In consideration of efficiencies and losses experienced in the motor, the results are somewhat less conclusive. The general observation is that there is little difference between the strategies in terms of losses experienced in the motor. Only at the highest of torque demands and reference currents is the Bang-Bang controller shown to experience poorer efficiencies and higher losses than the other techniques – possibly associated with the poorer quality of current available using this technique. In consideration of the overall drive system power losses and efficiencies, the results appear to be closely matched showing that the slightly more efficient motor performance in PI and SVPWM control is matched by the superior inverter performance of the Bang-Bang controller. In the final consideration of the comparison, the Kt measurements, the results are also inconclusive. In the low torque range the SVPWM controller is shown to yield a Kt ratio more consistently with respect to the reference current and across the speed range more effectively than the other techniques. However as the reference current is increased the benefit of using the SVPWM regulator to make these measurements becomes less noticeable.

The conclusions of the chapter generally spread opinion as to the most optimal controller selection. Design goals such as ease of implementation, cost of implementation, precision of control required and system efficiency all lead to different technique selection. The study presents a detailed description of the implementation issues of each

technique. The classical behavioural characteristics of each strategy are identified in the results of tests carried out on the machines described. The study also contributes a comparison of the techniques based on assessment of system performance parameters. These are the parameters upon which design goals are based and thusly the chapter contributes a better review of the controllers based upon results obtained following an experimentally valid test process.

Chapter 3
Online Parameter Estimation

This chapter describes the development of online parameter estimation techniques applicable to the motor control system outlined in Chapter 2. This chapter describes in far greater detail the voltage estimation technique and loss considerations which are outlined in the author's previous publication [106] which investigated the validity of the classical phasor diagram in machine parameter estimation. Average phase voltage estimation techniques are outlined for the PI and SVPWM control strategies outlined in Chapter 2 and specific methods for considering the machine's phase connection (wye or delta) are also detailed. Validation of the techniques is explored firstly through the development of online flux-linkage estimates and then through the development of an online torque estimator. Several of the average voltage estimators outlined are original contributions of this research and the subsequent delta connection considerations in the flux-linkage and torque estimators are also new contributions.

The chapter begins with a brief description of the motivation for the development of online parameter estimation techniques and gives examples of alternative research which implements parameter estimation techniques. The average phase voltage estimators for the wye connected machine are then described. During this description the fundamental difference between the gate drive waveforms and control variables of each of the PI and SVPWM strategies is highlighted giving rise to the necessity for a unique estimator in each case. This is then followed by consideration of the delta connected machine in each of the existing estimation techniques giving rise to the description of the three further unique techniques required due to the connection type. Following the description of the voltage estimators, extension of this theory into flux-linkage estimation is described. Through comparison with FEA predicted flux-linkage versus current loops (ψ-i loops) a validation of the voltage estimators is sought. This is followed via validation through online torque estimations which are compared to measurements taken under steady state test conditions with the commercially available torque transducer equipment (the results presented in Chapter 2). As a result of describing the flux-linkage and torque

estimators, further considerations of the delta connected machine gives rise to the development of unique estimation techniques based upon the machine connection type.

The voltage estimation techniques are validated in varying degrees through the comparison of ψ-i loops and torque measurements with the online estimates of flux-linkage and average torque. The results show the PI and SVPWM methods are highly reliable but in the wye connected machine, only once voltage losses in the system are taken into consideration. The chapter also highlights areas of the research which have validated the techniques to some extent but would benefit from further research.

3.1. Introduction

The operating parameters of the PMSM are of keen interest to motor design engineers throughout testing and validation of new designs. An understanding for the interactions between the various characteristics of the machine and its operating parameters has long been a goal of research on electric motors. The phasor diagram [106] is a commonly referenced representation of the relationships between electrical characteristics such as the back EMF, resistance losses, synchronous reactances and terminal voltage. A standardized version of it was first proposed in 1969 in an IEEE rotating machinery committee publication [107].

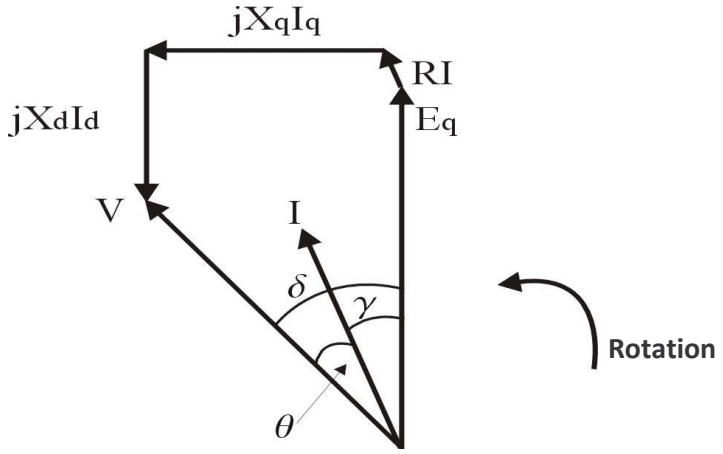

Figure 3-1: Classic Phasor Diagram (Motor Convention)

The phasor diagram, as already mentioned, is used in a wealth of literature and study relating to the analysis of PMSM's. The work of Petkovska [108], in which modern FEM analytical techniques are compared against classical theories, demonstrates the use of the classical phasor diagram in determining the load angle for a machine operating under rated conditions. The estimation of parameters such as the synchronous inductances Ld and Lq (not shown in Figure 3-1) is also highly desirable for use in sensorless drive

systems and Direct Torque Control (DTC) strategies. The recent publication of Nexteer Automotive Corporation [109] makes consistent use of the classical phasor diagram in the calculation of the synchronous inductances whilst assessing a variety of analytical and simulation methods of assessing motor parameters. These publications which make use of the phasor diagram demonstrate the ongoing interest in the operating parameters of the PMSM. The parameters targeted by various techniques (analytical or simulations) are done so with a variety of goals in mind (hardware minimisation through sensorless control is one example).

3.2. Voltage Estimation Techniques

The terminal voltage shown in Figure 3-1 is a parameter which has been pursued from an online estimation perspective in previous study. The authors previous publication [106] demonstrates the use of voltage estimation in assessment of the classical phasor diagram. The technique referenced was first described in the publication by Cossar [1] which described a new on-line torque estimator. The technique described is done so using a stationary frame PI controller, such as that outlined and tested in Chapter 2, operating on a wye connected motor. In this new study an expansion of this voltage estimation technique is offered. Through consideration of the specifics of the three control strategies implemented in Chapter 2, the requirement for a dedicated estimator is demonstrated. In addition to this a separate set of estimators is required in instances where the windings of the machine are in a delta configuration.

3.2.1. Wye Connection Voltage Estimation – Independent Phase Controllers

The stationary frame PI controller described in [1] is an example of an independent phase controller. Its operation is based upon 3 identical PI control algorithms sharing a common set of control gains to regulate each phase current independently. Operating under the principles described in sections 2.3.1 and 2.5 the controller generates independent duty cycle commands for each phase being controlled – these are to be applied for the duration of the following 50μs control cycle. The DSP hardware used in the FCIV (upon which the techniques described are implemented) is common in motor control applications. The FCIV generates symmetrical PWM waveforms for the gate drive signals using a triangle comparison method.

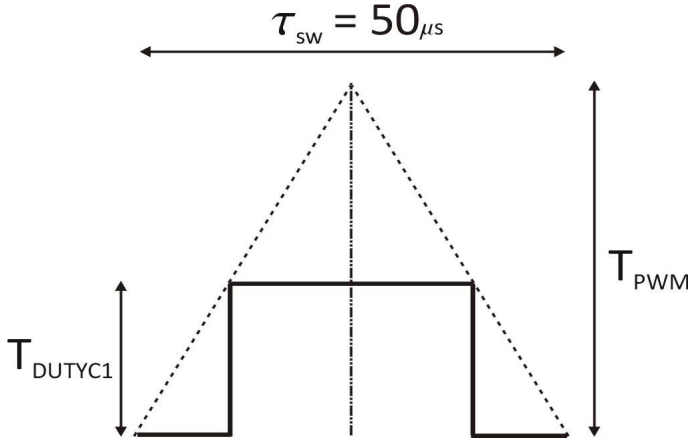

Figure 3-2: Triangle Comparison PWM wave generation

Figure 3-2 demonstrates the method by which the FCIV DSP technology generates its PWM gate drive signal (there is a separate peripheral for SVPWM control which will be discussed later). A timer register (up/down counter) of the DSP is set to a value T_{PWM} which represents the 50μs control period and is the value which the timer register will count up to and down from in a single control period. The phase A PWM register can then be set with the value T_{DUTYA} from the output of the controller algorithm; T_{DUTYA} is a duty cycle fraction of T_{PWM} which is then subtracted from T_{PWM}, e.g. for 50% $T_{DUTYA} = T_{PWM} – (T_{PWM} / 2)$. The PWM output signal is raised high when the up/down counter value is above the T_{DUTYC1} and low when it is not. Each phase operates in this manner and an understanding of this process is critical to the voltage estimation technique.

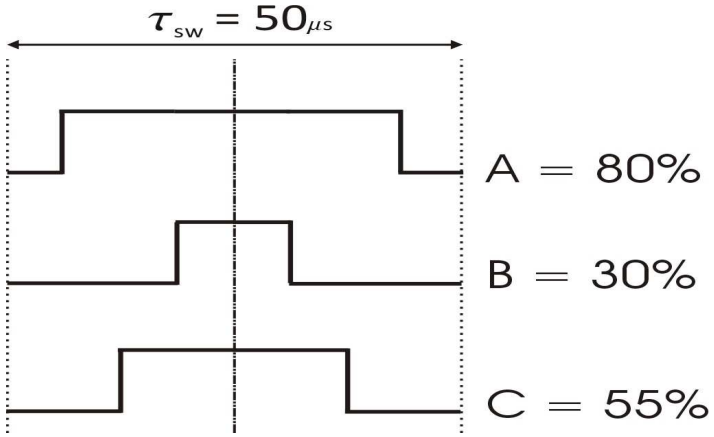

Figure 3-3: Symmetrical 3 phase PWM waveform

Consider the example in which the control algorithm commands a phase 1 duty cycle of 80%, a phase 2 duty cycle of 30% and a phase 3 duty cycle of 55% as demonstrated in Figure 3-3. The symmetrical nature of the waveform allows for a simplified approach using only half of the switch period to estimate the average phase voltage for the

duration of the 50µs control cycle. This simplified approach allows for consideration of the voltage vectors commanded during the control cycle.

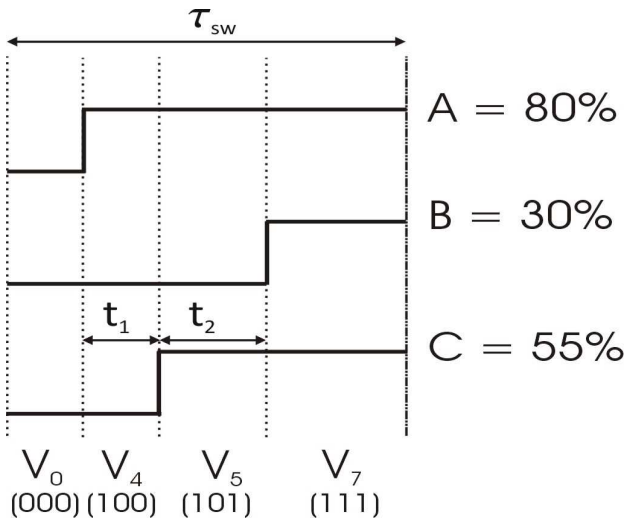

Figure 3-4: Switch Period example showing switch vectors commanded

Figure 3-4 demonstrates a simplified view of Figure 3-3 highlighting the 4 separate voltage vectors which occur in one half of the symmetrical PWM waveforms previously described. There are two zero state vectors (V_0 and V_7) and two other voltage vectors (V_4 and V_5) commanded, which are repeated in the second half of the waveform; however as stated the theory is developed for a half wave in order to simplify the method. Next a consideration of the phase circuit as a result of the commanded voltage vector is required.

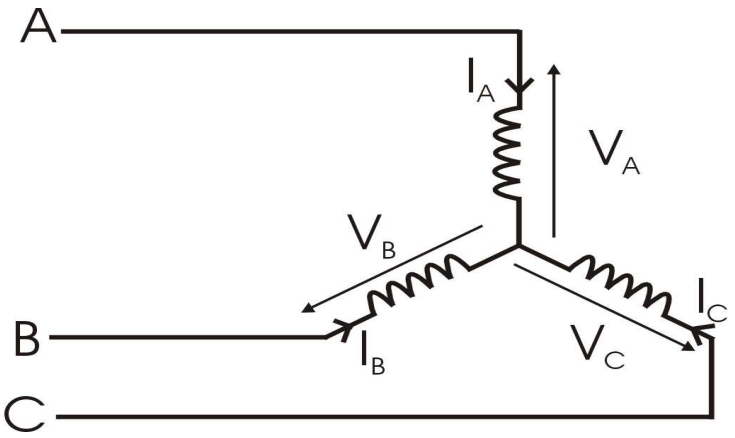

Figure 3-5: Wye Connected 3 phase motor equivalent circuit

Figure 3-5 shows an equivalent circuit for a 3 phase wye connected motor. The phase voltages V_A, V_B and V_C are indicated as are the phase currents I_A, I_B and I_C. Through consideration of this circuit and the operation of the VSI (connections A, B and C will be connected to either V_{DC} or 0V in any particular instance) then an equivalent circuit can be drawn for each voltage vector which can be commanded by the VSI.

TABLE 3-1: Equivalent phase circuits as a result of commanded voltage vector

Voltage Vector	Equivalent Phase Circuit
V_0	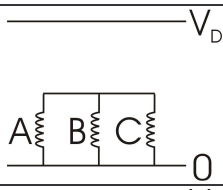
V_1	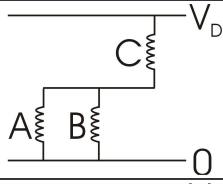
V_2	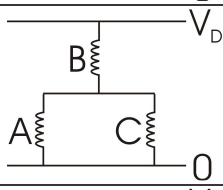
V_3	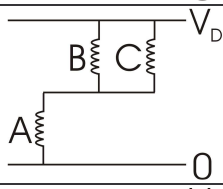
V_4	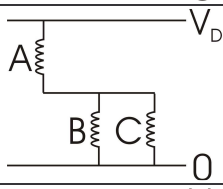
V_5	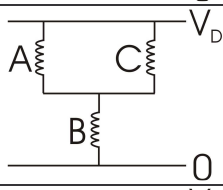
V_6	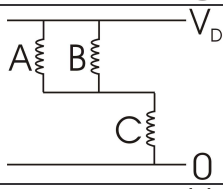
V_7	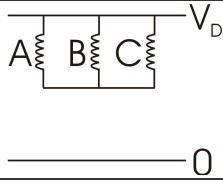

TABLE 3-1 gives the equivalent circuit connections under each voltage vector commanded. The voltage estimations are constructed on a per phase basis. Using TABLE 3-1 the equivalent phase voltage for phase A based on the voltage vectors being commanded can be calculated.

TABLE 3-2: Phase A voltage with respect to commanded voltage vector

Voltage Vector	Phase A Voltage
V_0	$V_{ph} = 0$
V_1	$V_{ph} = -\frac{1}{3} V_{DC}$
V_2	$V_{ph} = -\frac{1}{3} V_{DC}$
V_3	$V_{ph} = -\frac{2}{3} V_{DC}$
V_4	$V_{ph} = \frac{2}{3} V_{DC}$
V_5	$V_{ph} = \frac{1}{3} V_{DC}$
V_6	$V_{ph} = \frac{1}{3} V_{DC}$
V_7	$V_{ph} = 0$

TABLE 3-2 gives the resultant phase A voltages due to the commanded voltage vectors. Looking again at the example given in Figure 3-4; it is shown that the voltage vector V_4 is applied for time t_1 and V_5 is applied for time t_2, during the switch period τ_{sw}. The rest of τ_{sw} is spent commanding the zero state vectors. This leads to the final steps in the construction phase voltage estimate; calculation of the timing variables.

Owing to the nature of independent phase control, the resultant voltage vectors are not known at any stage before the commanded duty cycles are generated. Thus the timing variables t_1 and t_2 must be extracted from the duty cycle values. Consider again the example given in Figure 3-4. Given the triangle comparison method implemented in the DSP, the values t_1 and t_2 are fractional parts of T_{PWM} which is known to be 50µs; they are calculated (in this example) as:

$$t_1 = T_{DUTYC} - T_{DUTYA} \tag{1}$$

$$t_2 = T_{DUTYB} - T_{DUTYC} \tag{2}$$

Having calculated the timing variables, the average phase voltage for the 50µs control period can be estimated as:

$$V_{ph} = \left(V_4 \times \frac{t_1}{\tau_{sw}} \right) + \left(V_5 \times \frac{t_2}{\tau_{sw}} \right) \tag{3}$$

$$V_{ph} = \left(\frac{2}{3} V_{DC} \times \frac{t_1}{\tau_{sw}}\right) + \left(\frac{1}{3} V_{DC} \times \frac{t_2}{\tau_{sw}}\right) \quad (4)$$

$$V_{ph} = \frac{V_{DC}}{3\tau_{sw}}(2t_1 + t_2) \quad (5)$$

Equation (5) gives the simplified calculation for the average phase voltage (phase A) during the 50µs command cycle given in Figure 3-4. This however can be developed for each possible PWM duty cycle configuration that can be commanded by the three independent controllers.

TABLE 3-3: Average Phase A Voltage Estimate for each possible gate PWM configuration

Configuration #	Commanded Duty Cycle Configuration	Timing Variable Calculations	Resultant Phase A Voltage
1	$T_{DUTYA} \geq T_{DUTYB}$ $T_{DUTYA} \geq T_{DUTYC}$ $T_{DUTYB} \geq T_{DUTYC}$	$t_1 = T_{DUTYB} - T_{DUTYC}$ $t_2 = T_{DUTYA} - T_{DUTYB}$	$V_{ph} = \frac{V_{DC}}{3\tau_{sw}}(-2t_2 - t_1)$
2	$T_{DUTYA} \geq T_{DUTYC}$ $T_{DUTYA} \geq T_{DUTYB}$ $T_{DUTYC} \geq T_{DUTYB}$	$t_1 = T_{DUTYC} - T_{DUTYB}$ $t_2 = T_{DUTYA} - T_{DUTYC}$	$V_{ph} = \frac{V_{DC}}{3\tau_{sw}}(-2t_2 - t_1)$
3	$T_{DUTYB} \geq T_{DUTYA}$ $T_{DUTYB} \geq T_{DUTYC}$ $T_{DUTYA} \geq T_{DUTYC}$	$t_1 = T_{DUTYA} - T_{DUTYC}$ $t_2 = T_{DUTYB} - T_{DUTYA}$	$V_{ph} = \frac{V_{DC}}{3\tau_{sw}}(t_2 - t_1)$
4	$T_{DUTYB} \geq T_{DUTYC}$ $T_{DUTYB} \geq T_{DUTYA}$ $T_{DUTYC} \geq T_{DUTYA}$	$t_1 = T_{DUTYC} - T_{DUTYA}$ $t_2 = T_{DUTYB} - T_{DUTYC}$	$V_{ph} = \frac{V_{DC}}{3\tau_{sw}}(2t_1 + t_2)$
5	$T_{DUTYC} \geq T_{DUTYA}$ $T_{DUTYC} \geq T_{DUTYB}$ $T_{DUTYA} \geq T_{DUTYB}$	$t_1 = T_{DUTYA} - T_{DUTYB}$ $t_2 = T_{DUTYC} - T_{DUTYA}$	$V_{ph} = \frac{V_{DC}}{3\tau_{sw}}(t_2 - t_1)$
6	$T_{DUTYC} \geq T_{DUTYB}$ $T_{DUTYC} \geq T_{DUTYA}$ $T_{DUTYB} \geq T_{DUTYA}$	$t_1 = T_{DUTYB} - T_{DUTYA}$ $t_2 = T_{DUTYC} - T_{DUTYB}$	$V_{ph} = \frac{V_{DC}}{3\tau_{sw}}(2t_1 + t_2)$

TABLE 3-3 gives the resultant phase A voltage estimation for each potential PWM output configuration of the independent phase linear controller. In order to make the average phase voltage estimation the controller requires the user to input the DC Link voltage (V_{DC}), the switch cycle period (τ_{sw} = 50µs) and equations (1) and (2) require solving before finally applying TABLE 3-3. This calculation must be carried out each switch interval after the control algorithm has completed its calculations.

The average phase voltage estimator, first described in [1] is presented in this study and its operation thoroughly defined based upon the implementation of the control

techniques outlined in Chapter 2. This study has contributed a greater understanding of the technique and its applicability to all varieties of independent phase control regulator.

3.2.2. Wye Connection Voltage Estimation – Synchronous Controllers

The SVPWM controller described in Chapter 2 is often implemented in modern research concerned with the modelling and simulation of a variety of PMSM applications [110, 111]. Further to this the prevalence of the tms320f2812 DSP in the use of motor control applications [112-114] gives rise to the potential application of an average phase voltage estimator which can be applied to the SVPWM technique. The publications highlighted also effectively demonstrate the alternative approaches to generating the PWM gate drive signals once the voltage vector timing variables are obtained. Unlike the implementation described in Chapter 2, a commonly adopted approach is to use the triangle comparison method such as that described in section 3.2.1 to generate the SVPWM drive signals. This requires calculation of the equivalent phase duty cycles (T_{DUTYA}, T_{DUTYB}, and T_{DUTYC}). Following the calculation of T_1 and T_2 and once they have been scaled against T_{PWM} (τ_{sw}) a new set of duty cycle variables can be calculated which satisfy the triangle comparison PWM generation method:

$$T_{AON} = \frac{T_{PWM} - T_1 - T_2}{2} \tag{6}$$

$$T_{BON} = T_{AON} + T_1 \tag{7}$$

$$T_{CON} = T_{BON} + T_2 \tag{8}$$

Once equations (6)-(8) have been calculated a lookup table can be accessed to make the correct phase to duty cycle variable assignments based upon which sector the reference voltage vector Vs is situated in.

TABLE 3-4: SVPWM Gate Drive PWM Duty Cycle Assignments

	Sector 1	Sector 2	Sector 3	Sector 4	Sector 5	Sector 6
T_{DUTYA}	T_{BON}	T_{AON}	T_{AON}	T_{CON}	T_{CON}	T_{BON}
T_{DUTYB}	T_{AON}	T_{CON}	T_{BON}	T_{BON}	T_{AON}	T_{CON}
T_{DUTYC}	T_{CON}	T_{BON}	T_{CON}	T_{AON}	T_{BON}	T_{AON}

TABLE 3-4 gives the sector based duty cycle assignments for each phase when the triangle comparison PWM method is being used to generate the gate drive signals. When this method is implemented the gate drive signals have waveforms over the 50µs control cycle which are similar to those shown in Figure 3-3. With this being the case the estimator outlined in 3.2.1 is used in order to construct the phase voltage.

The SVPWM method described in Chapter 2 focuses upon making use of the built-in SVPWM hardware peripheral of the tms320f2812 DSP which is commonly implemented in the literature referenced. The peripheral requires knowledge only of the first voltage vector Vx, the second voltage vector Vy and the two timing variables T_1 and T_2. Once this information is passed to the SVPWM peripheral the SVPWM gate drives are commanded for the following 50µs control cycle.

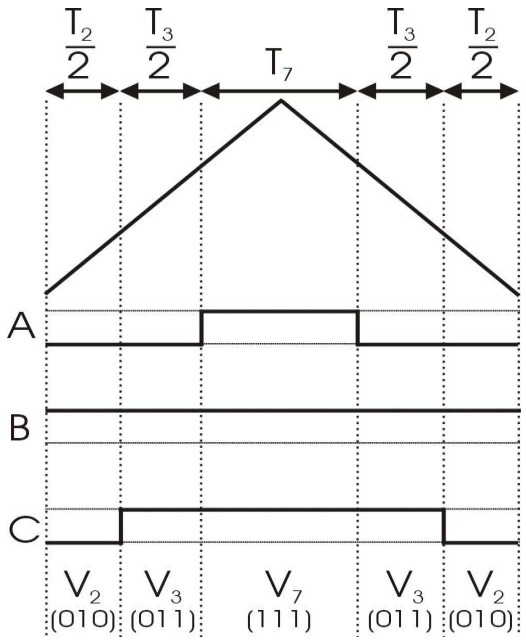

Figure 3-6: SVPWM gate drive waveform using built-in SVPWM peripheral

Figure 3-6 is a copy of Figure 2-18 demonstrating the waveform typical of the SVPWM peripheral available in the tms320f2812 DSP. This waveform is largely similar to that shown in Figure 3-3 in as much as it is also symmetrical and also shows the control cycle makes use of two of the available non-zero voltage vectors (V_1-V_6). The only difference, which is critical to the principle of the phase voltage estimator, is that there is now only one zero state voltage vector instance whereas in the previous case (Figure 3-3) there were 3 in total (2 in the half wave which shall be used once again). This owes to the fact that the built-in peripheral makes use of a method which minimises unnecessary switch events. In realisation of the reference voltage vector Vs the controller is required to command vectors V_2 and V_3 and will usually be required to command the zero voltage vector V_7 for some period. As a result of these being the only critical voltage vectors in realising Vs, the controller does not need to switch phase B at any stage (in the example given in Figure 3-6). This has the benefit of removing 2 unnecessary switch occurrences in phase B which would be present in other PWM generation techniques; the peripheral is

consistent in this behaviour, arguably making it a more efficient implementation of the SVPWM technique.

Essential to the technique outlined in section 3.2.1 is the knowledge of T_{DUTYA}, T_{DUTYB} and T_{DUTYC}. Whilst it would be an option to determine these values using the process already outlined, this would not be a true consideration of the actions being taken by the regulator. Additionally, due to the minimised switching nature of the SVPWM peripheral it could be validly argued that the quality of control between the two SVPWM implementations is not parallel; thus it is highly unlikely the phase current or phase voltage will be identical for either method. This gives rise to the necessity of a new voltage estimator which makes use of only the parameters determined in the SVPWM control process, identified and described in greater detail in Chapter 2.

The SVPWM control technique described in Chapter 2 is not restricted to either clockwise or anti-clockwise travel. Both directions are available to the controller and these have different effects upon the control cycle waveform. Consider the inverse scenario to that outlined in Figure 3-6. Reference voltage vector Vs will be achieved through application of V_3 followed by V_2.

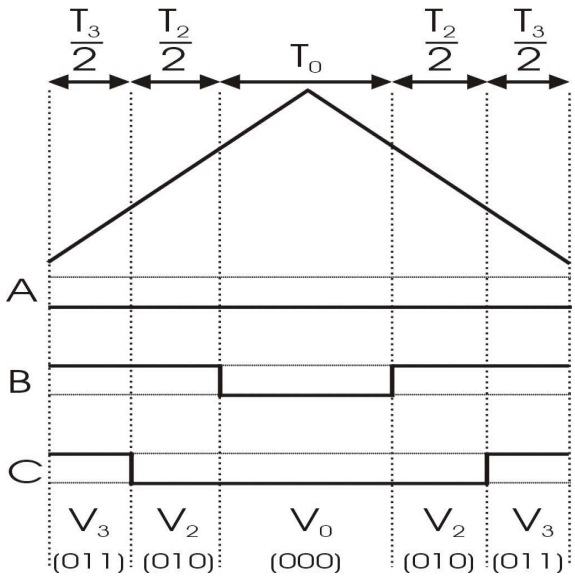

Figure 3-7: Sector 5 control waveform moving in clockwise direction

Figure 3-7 shows the new scenario described where the reference voltage vector Vs residing in sector 5 is realised in a clockwise transition from the first voltage vector (V_3) to the second (V_2). This is in contrast to the example shown in Figure 3-6 in which Vs in sector 5 is realised in an anti-clockwise transition from the first voltage vector to the second. In this new scenario the zero voltage vector required is now V_0 instead of V_7

however, the built-in SVPWM peripheral accommodates this change thus preserving the minimal switching advantage it has over the triangle comparison implementation. Considering this scenario a new representation of the space vector hexagon can be constructed to demonstrate the switch pattern of each control cycle for each direction of travel through the hexagon for each sector.

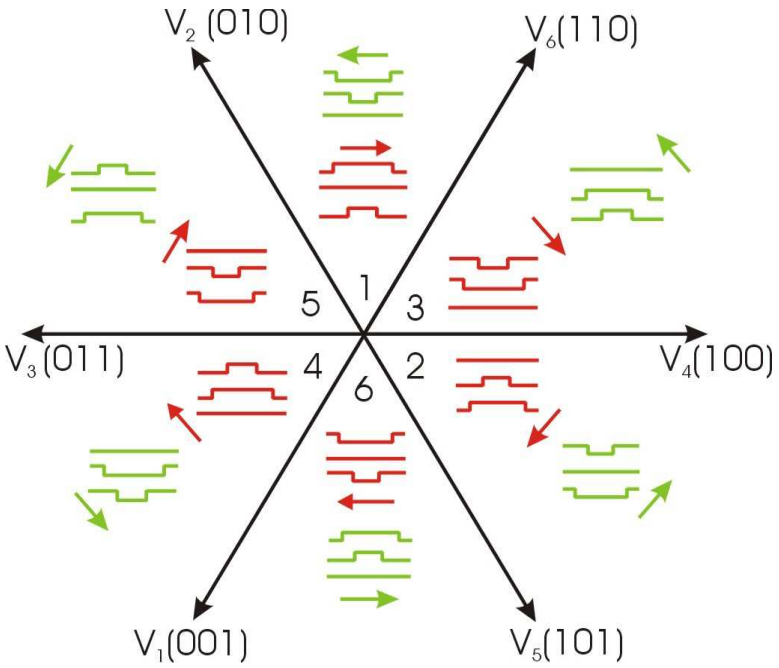

Figure 3-8: Control Cycle SVPWM waveforms for both directions of travel

Figure 3-8 shows the space vector hexagon and within it the control cycle waveforms for each sector in both directions of travel. These are the waves which must be considered in the voltage estimator for this particular SVPWM implementation. Consider again the scenario outlined in Figure 3-6; given the symmetrical nature of the waveform the consideration is again more easily developed through consideration of the half wave.

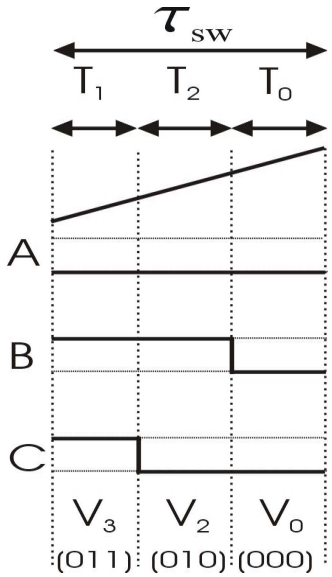

Figure 3-9: Sector 5 clockwise control waveform - half-wave

Figure 3-9 shows the half wave for the SVPWM control waveform generated by the built-in SVPWM peripheral. As was explained earlier there is now only one zero volt vector applied during the half wave. Without knowledge of T_{DUTYA}, T_{DUTYB} or T_{DUTYC} for this waveform the known variables T_1 and T_2 must be used instead. As is highlighted in Figure 3-9, the waveform is characterised by T_1 and T_2 so the construction of the average phase voltage is similar to the previous method outlined in 3.2.1; however the resultant estimations are subtly different. In the example outlined it can be seen that V_3 is applied for time T_1 and V_2 is applied for period T_2. The resultant phase voltage can then be determined:

$$V_{ph} = \left(V_3 \times \frac{T_1}{\tau_{sw}} \right) + \left(V_2 \times \frac{T_2}{\tau_{sw}} \right) \tag{9}$$

$$V_{ph} = \left(-\frac{2}{3} V_{DC} \times \frac{T_1}{\tau_{sw}} \right) + \left(-\frac{1}{3} V_{DC} \times \frac{T_2}{\tau_{sw}} \right) \tag{10}$$

$$V_{ph} = \frac{V_{DC}}{3\tau_{sw}} \left(-2T_1 - T_2 \right) \tag{11}$$

Equation (11) gives the estimation used in the clockwise realisation of the voltage vector located in sector 5. This method can be applied to each of the estimations used in the SVPWM controller making use of the built-in SVPWM peripheral.

TABLE 3-5: SVPWM Voltage Estimator Calculations

Sector	Clockwise Estimation	Anti-Clockwise Estimation
1	$V_{ph}=\frac{V_{DC}}{3\tau_{sw}}(T_2-T_1)$	$V_{ph}=\frac{V_{DC}}{3\tau_{sw}}(T_1-T_2)$
2	$V_{ph}=\frac{V_{DC}}{3\tau_{sw}}(2T_1+T_2)$	$V_{ph}=\frac{V_{DC}}{3\tau_{sw}}(2T_2+T_1)$
3	$V_{ph}=\frac{V_{DC}}{3\tau_{sw}}(2T_2+T_1)$	$V_{ph}=\frac{V_{DC}}{3\tau_{sw}}(2T_1+T_2)$
4	$V_{ph}=\frac{V_{DC}}{3\tau_{sw}}(-2T_2-T_1)$	$V_{ph}=\frac{V_{DC}}{3\tau_{sw}}(-2T_1-T_2)$
5	$V_{ph}=\frac{V_{DC}}{3\tau_{sw}}(-2T_1-T_2)$	$V_{ph}=\frac{V_{DC}}{3\tau_{sw}}(-2T_2-T_1)$
6	$V_{ph}=\frac{V_{DC}}{3\tau_{sw}}(T_1-T_2)$	$V_{ph}=\frac{V_{DC}}{3\tau_{sw}}(T_2-T_1)$

TABLE 3-5 gives the resultant phase voltage estimations for the SVPWM controller based upon the direction of travel through the space vector hexagon (which is a known variable in the controller) and the timing variables T_1 and T_2.

The requirement for an SVPWM phase voltage estimator has been outlined due to the lack of knowledge of the duty cycle variable used in the independent phase controllers. In addition to this there is a subtle difference in the control cycle waveforms between the stationary frame controllers outlined in 3.2.1 and the control waveforms of the built-in SVPWM peripheral. This gives rise to the requirement for an estimator which makes direct considerations for the waveform produced. This study has contributed a detailed description of the method for estimating the phase A voltage whilst operating the SVPWM controller.

3.2.3. Delta Connection Voltage Estimator – Independent phase controllers

The voltage estimators outlined in sections 3.2.1 and 3.2.2 are valid for the control techniques being discussed when the machine under test is a wye connected configuration. However these methods are not valid for the delta connected machine, which is often encountered in research and industry particularly in higher power output applications. This gives rise to the requirement of a voltage estimator for all control techniques in the case of delta connected motors.

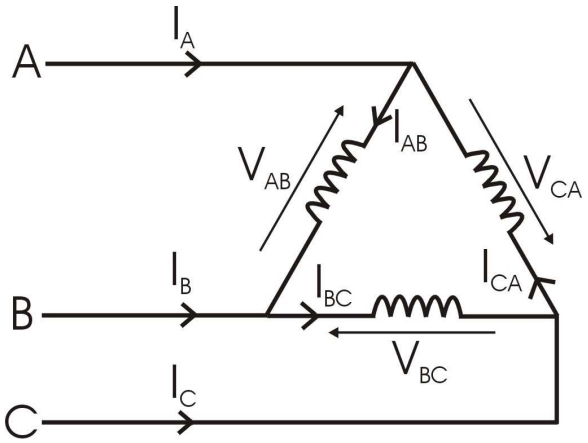

Figure 3-10: Delta Connected 3 phase motor equivalent circuit

Figure 3-10 shows the equivalent circuit for a delta connected 3 phase motor. In the interest of focussing upon the voltage estimator, the delta connection theory will be generally overlooked other than to specify in the case of the phase voltage estimator the voltage being estimated is V_{AB} shown in Figure 3-10. All of the following estimation methods are outlined with the specific focus being upon that particular phase voltage (similar to the method outlined in sections 3.2.1 and 3.2.2 which specifically estimate V_A shown in Figure 3-5).

The control of the delta connected motor makes use of the control techniques outlined in Chapter 2; they remain unchanged irrespective of the phase winding connection. Phase lines A,B and C are ultimately still only ever connected to V_{DC} or 0V; however in the delta connected machine the line currents I_A, I_B and I_C are those under regulation and not the phase currents I_{AB}, I_{BC} or I_{CA}. With this being said in the case of the stationary frame PI controller, the waveforms shown in Figure 3-3 and Figure 3-4 are still representative of the waveforms that will be applied to the delta machine. However the equivalent phase circuits as a result of the commanded voltage vector (TABLE 3-1) will be significantly different owing the physical differences of the delta connection.

TABLE 3-6: Equivalent Phase Circuits as a result of voltage vector (Delta Connection)

Voltage Vector	Resultant Equivalent Phase Circuit
V_0	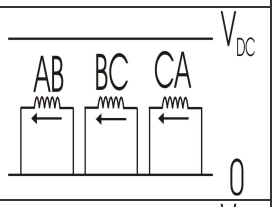
V_1	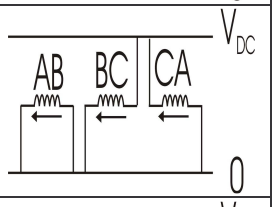
V_2	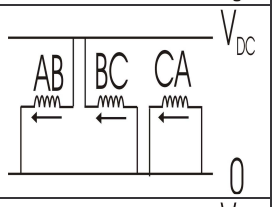
V_3	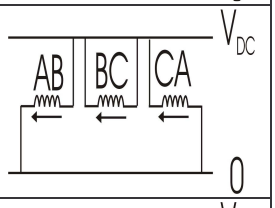
V_4	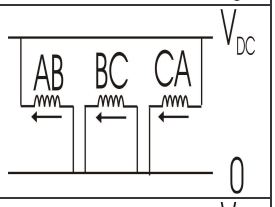
V_5	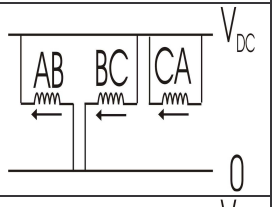
V_6	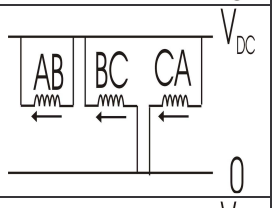
V_7	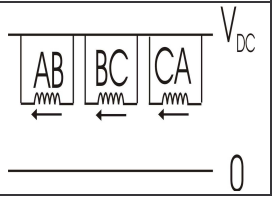

TABLE 3-6 gives the equivalent circuits for a delta a connection as a result of the commanded voltage vector. This allows for the equivalent phase voltage calculation for V_{AB} to be tabulated.

TABLE 3-7: Phase Voltage Calculations as a result of the commanded Voltage Vector

Voltage Vector	Phase AB Voltage
V_0	$V_{ph} = 0$
V_1	$V_{ph} = 0$
V_2	$V_{ph} = -V_{DC}$
V_3	$V_{ph} = -V_{DC}$
V_4	$V_{ph} = V_{DC}$
V_5	$V_{ph} = V_{DC}$
V_6	$V_{ph} = 0$
V_7	$V_{ph} = 0$

TABLE 3-7 shows the phase voltage calculations for each voltage vector for a delta connected motor. It is plain to see upon review of TABLE 3-6 and TABLE 3-7 that there are no phase interactions with respect to the phase voltage estimation in the delta connected machine and thus each phase experiences the full V_{DC} potential when connected across the terminals of the DC link (this is not the case in the wye connected machine). This characteristic simplifies the voltage estimation process, however the timing intervals of the control wave must still be considered. Consider again Figure 3-10, the phase voltage V_{AB} is seen clearly to be connected across phases A and B. The state of phase C makes no contribution to the voltage connected across V_{AB}. The waveform shown in Figure 3-4 demonstrates a period in the waveform (t_1+t_2) during which there is a voltage potential (V_{DC} in the case of the delta connected machine), the switching even on phase C makes no contribution to this connection; thus the phase C duty cycle can be neglected from the calculations. The equations outlined in TABLE 3-3 may all be simplified such that during each configuration of duty cycle command the resultant phase voltage is given by:

$$V_{ph} = \frac{V_{DC}}{\tau_{sw}}\left(T_{DUTYA} - T_{DUTYB}\right) \tag{12}$$

Equation (12) gives the delta connected estimator when operating the stationary frame PI controller. This equation is applied in the exact same manner as those described in TABLE 3-3.

A consideration of the phase interactions of the delta connected machine has been presented. This included a description of the resultant phase voltage commanded with respect to the commanded voltage vector. The operation of the control strategies does not change with respect to the machine connection type; thus the average phase voltage estimator described in section 3.2.1 has simply been expanded. The study has contributed a method for online voltage estimation the delta connected machine.

3.2.4. Delta Connection Voltage Estimation – Synchronous Controllers

The SVPWM controller, like the independent phase controllers, has no requirement to be altered when controlling a delta connected machine. This being the case it is therefore possible, to work out once again the three equivalent duty cycles (T_{DUTYA}, T_{DUTYB} and T_{DUTYC}) that are being commanded by the SVPWM controllers (given knowledge of T_1 and T_2). Equations (9)-(11) are still applicable as is TABLE 3-4. This allows the controller to estimate the average phase voltage using Eq (12).

As has already been described in section 3.2.2 the method for estimating the phase voltage under SVPWM control can be tailored to more accurately reflect the control waveform being applied; this method makes use of the timing variables T_1 and T_2 which form part of the control process and reflects the more optimal switch behaviour of the technique. The considerations made in the delta connection case are largely similar to those made previously; this is due to the estimation method being heavily dependent on the control technique itself which has not changed. This being the case Figure 3-8 is still valid; however equations (9)-(11) require slight adjustment (to reflect the delta connections) to be valid for the example given in Figure 3-9.

$$V_{ph} = \left(V_3 \times \frac{T_1}{\tau_{sw}} \right) + \left(V_2 \times \frac{T_2}{\tau_{sw}} \right) \tag{13}$$

$$V_{ph} = \left(-V_{DC} \times \frac{T_1}{\tau_{sw}} \right) + \left(-V_{DC} \times \frac{T_2}{\tau_{sw}} \right) \tag{14}$$

$$V_{ph} = \frac{V_{DC}}{\tau_{sw}} \left(-T_1 - T_2 \right) \tag{15}$$

The differences between equations (9)-(11) and (13)-(15) are representative of the new considerations that are made when operating the delta connected motor. This results in a completely new set of estimations being required for a reference voltage vector travelling in either direction.

TABLE 3-8: SVPWM Voltage Estimator Calculations (delta connection)

Sector	Clockwise Estimation	Anti-Clockwise Estimation
1	$V_{ph} = \frac{V_{DC}}{\tau_{sw}} \left(-T_2 \right)$	$V_{ph} = \frac{V_{DC}}{\tau_{sw}} \left(-T_1 \right)$
2	$V_{ph} = \frac{V_{DC}}{\tau_{sw}} \left(T_1 + T_2 \right)$	$V_{ph} = \frac{V_{DC}}{\tau_{sw}} \left(T_1 + T_2 \right)$
3	$V_{ph} = \frac{V_{DC}}{\tau_{sw}} \left(T_1 \right)$	$V_{ph} = \frac{V_{DC}}{\tau_{sw}} \left(T_2 \right)$
4	$V_{ph} = \frac{V_{DC}}{\tau_{sw}} \left(-T_1 \right)$	$V_{ph} = \frac{V_{DC}}{\tau_{sw}} \left(-T_2 \right)$
5	$V_{ph} = \frac{V_{DC}}{\tau_{sw}} \left(-T_1 - T_2 \right)$	$V_{ph} = \frac{V_{DC}}{\tau_{sw}} \left(-T_1 - T_2 \right)$
6	$V_{ph} = \frac{V_{DC}}{\tau_{sw}} \left(T_2 \right)$	$V_{ph} = \frac{V_{DC}}{\tau_{sw}} \left(T_1 \right)$

The requirement for a separate SVPWM voltage estimator has been outlined previously as being due to the difference in control variables available and also to a subtle difference in the gate drive waveforms. This study has extended the stand-alone SVPWM voltage estimator such that it can also be applied to the delta connected machine.

3.3. Validation of the phase voltage estimator

Validation of the online phase phase voltage estimator is not a straight forward subject; the lack of a neutral line in most commercial motors is one particular problem. This is the case in the wye connected test machine used in this study (the 4 pole SEM machine). More fundamental to the issue is that a direct comparison with measured results is not possible. This is due to the actual phase voltage waveforms being PWM in nature and the voltage estimates being a voltage representation of the command waveform. The waveforms are naturally going to be different. In an effort to validate the techniques outlined, a more convoluted approach is adopted.

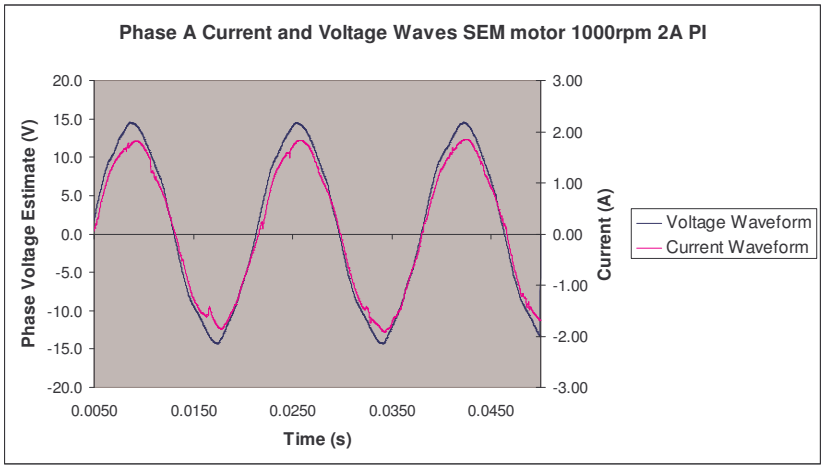

Figure 3-11: Phase A Current and Command Voltage Estimate of SEM (wye) motor operating under PI control

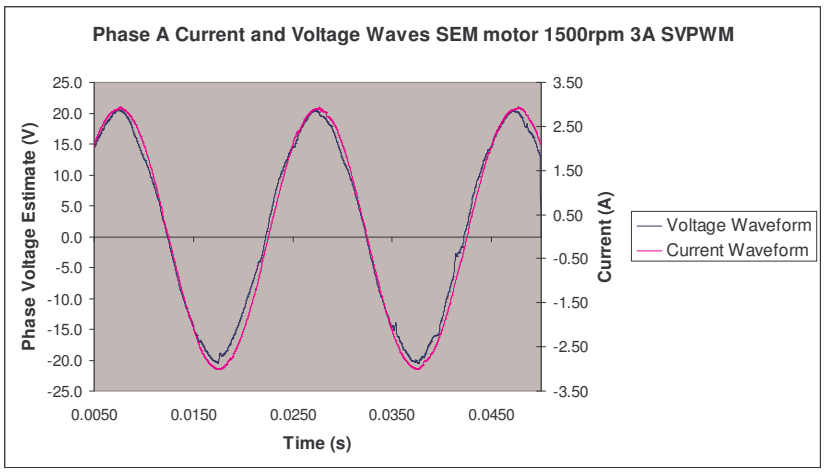

Figure 3-12: Phase A Current and Command Voltage Estimate of SEM (wye) motor operating under SVPWM control

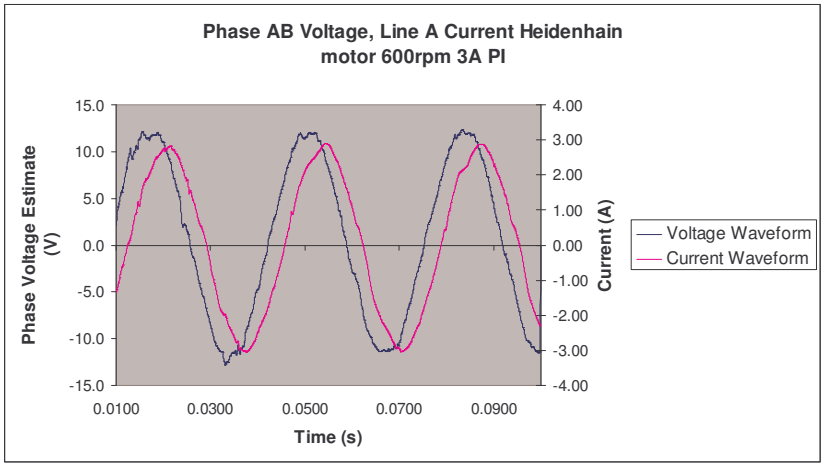

Figure 3-13: Phase AB Command Voltage Estimate of Heidenhain (delta) motor operating under PI control

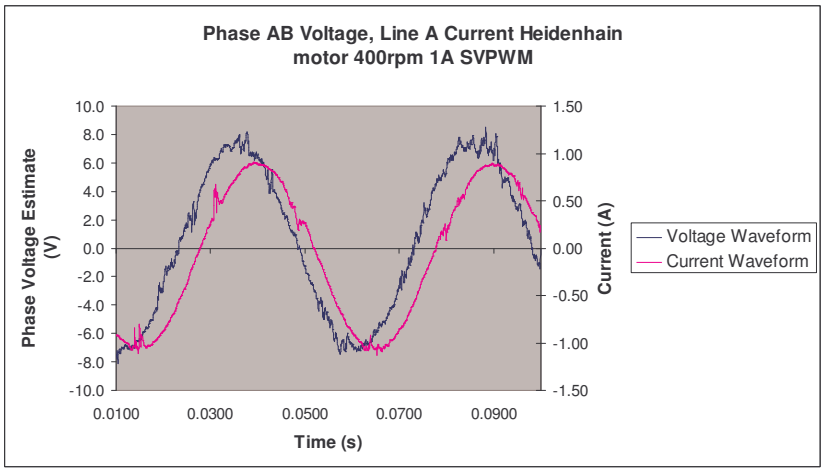

Figure 3-14: Phase AB Command Voltage Estimate of Heidenhain (delta) motor operating under SVPWM control

Figure 3-11 and Figure 3-12 give resultant command voltage estimates for both the PI and SVPWM control strategies when tested on the wye connected SEM machine. Whilst a direct comparison with measured results is not possible, some degree of confidence in the phase alignment of the reconstructed voltage waves with their respective current waves can be ascertained. Given that no gamma advance or field weakening is being applied, results given in Figure 3-11 and Figure 3-12 show that the current and voltage waveforms are very nearly in phase, suggesting an estimated power factor of near to 1. From this purely aesthetical analysis, the voltage estimator appears to be operating as expected for the wye connected machine. What is still to be validated, however, is the magnitude of the estimated average phase voltages.

Figure 3-13 and Figure 3-14 give the resultant phase voltage estimates for the delta connected Heidenhain machine. Again reliable measurements of the actual phase voltages are unavailable however another aesthetical analysis is possible. The current

waves now appear to lag the voltage waves by around 30°. However it should be remembered that the current waveforms shown in Figure 3-13 and Figure 3-14 are representative of the line currents I_A and not the phase currents I_{AB}. Common delta connection theory suggests that the reconstructed phase currents, observed 30° from the line currents is to be expected.

3.3.1. The flux-linkage versus current (ψ-i) loop

The use of the flux-linkage versus current (ψ-i) loop in the analysis of PMSM's was first introduced by Staton et al in the 1994 publication which investigated the theory of torque production in a number of electric motor types [115]. The study establishes the flux-MMF diagram (derived from the ψ-i loop) for each machine type allowing a common analysis to be carried out. Following this study, many further publications on the use of the (ψ-i) loop and flux-MMF diagram followed including the 2003 publication of Miller et al which focussed specifically on the interior permanent magnet (IPM) motor [78]. This study details the method for constructing the flux-linkage waveform from measurements carried out during steady state testing and gives the equation with which the flux linkage is determined:

$$\psi = \int (v - Ri)\,dt \tag{16}$$

Where v is the terminal voltage, i is the phase current and R is the phase resistance. The study then goes on to compare the measured ψ-i loop with one produced using finite element analysis (FEA) methods.

Addressing the initial problem of validating the phase voltage estimator, the study which first described the technique [1] makes use of the ψ-i loop. In this study the flux-linkage versus current loops generated using the online voltage estimator with equation (16) are compared against the flux-linkage loops obtained using commercially available FEA software (PC-BDC, part of Motor-CAD SPEED software [116]). Using this approach the voltage estimators implemented in the wye connected example can be validated.

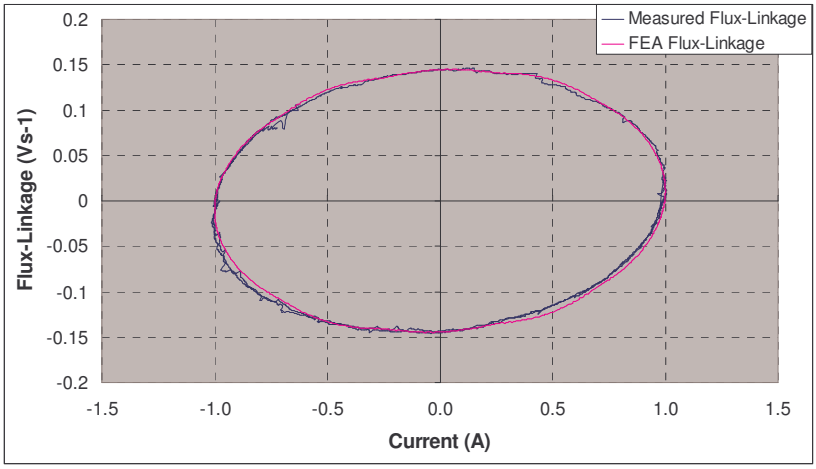

Figure 3-15: ψ-i loop for SEM machine under PI control zero gamma 1A Reference Current 500rpm

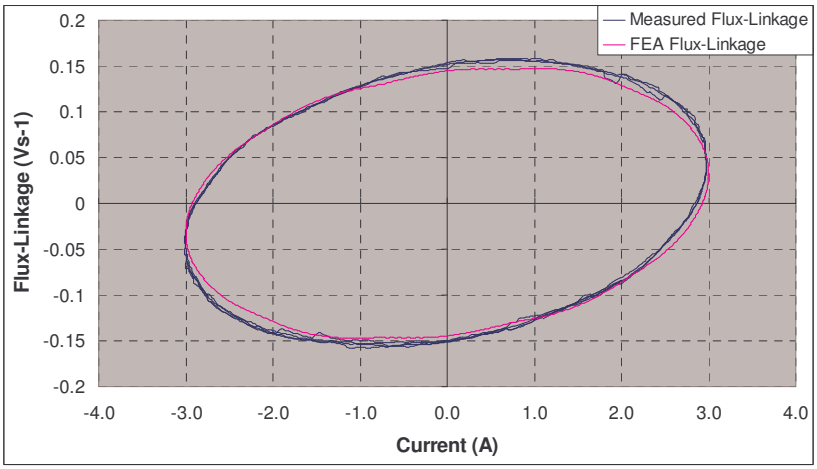

Figure 3-16: ψ-i loop for SEM machine under PI control zero gamma 3A Reference Current 500rpm

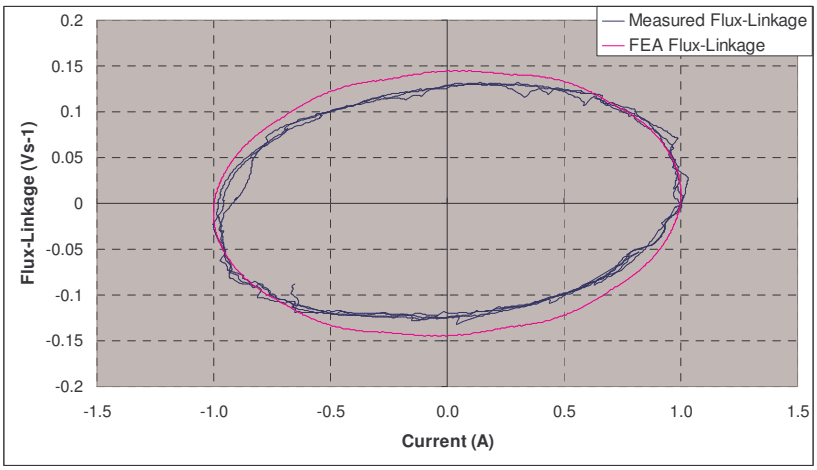

Figure 3-17: ψ-i loop for SEM machine under PI control zero gamma 1A Reference Current 1000rpm

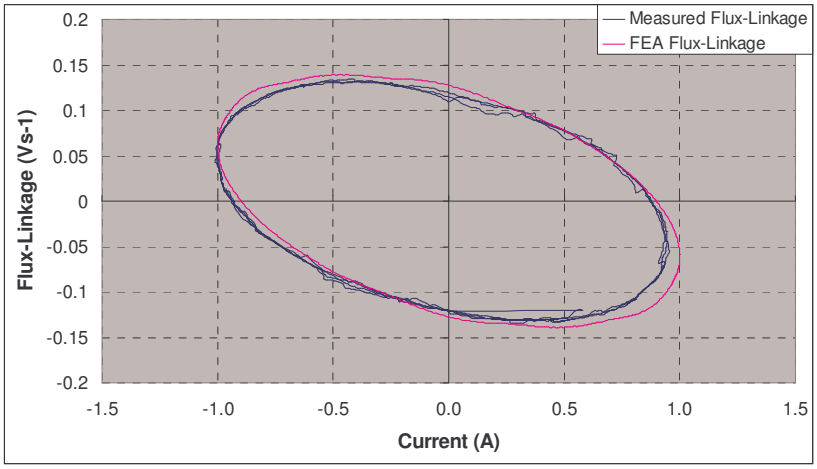

Figure 3-18: ψ-i loop for SEM machine under PI control 30° gamma advance 1A Reference Current 500rpm

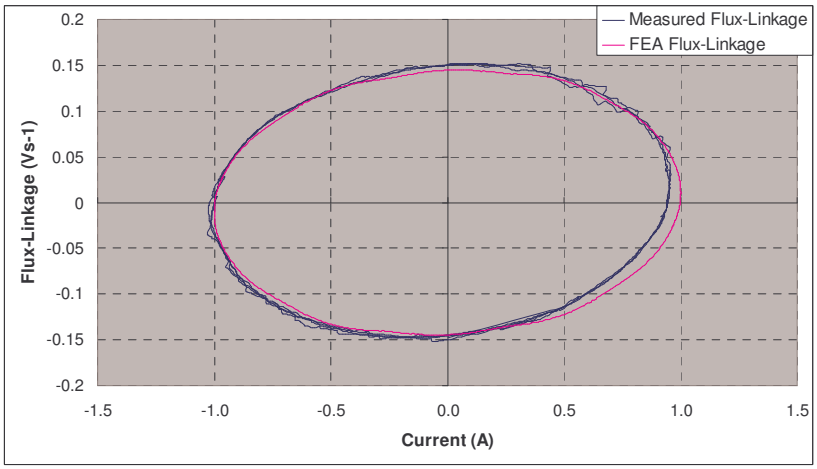

Figure 3-19: ψ-i loop for SEM machine under SVPWM control zero gamma 1A Reference Current 500rpm

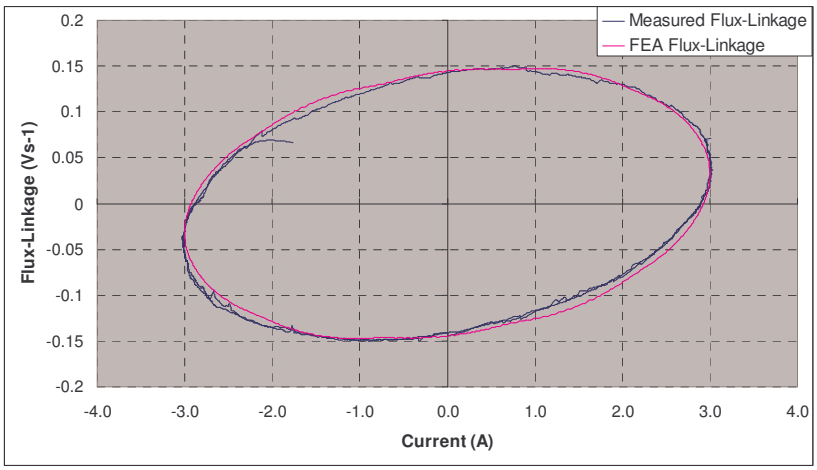

Figure 3-20: ψ-i loop for SEM machine under SVPWM control zero gamma 3A Reference Current 500rpm

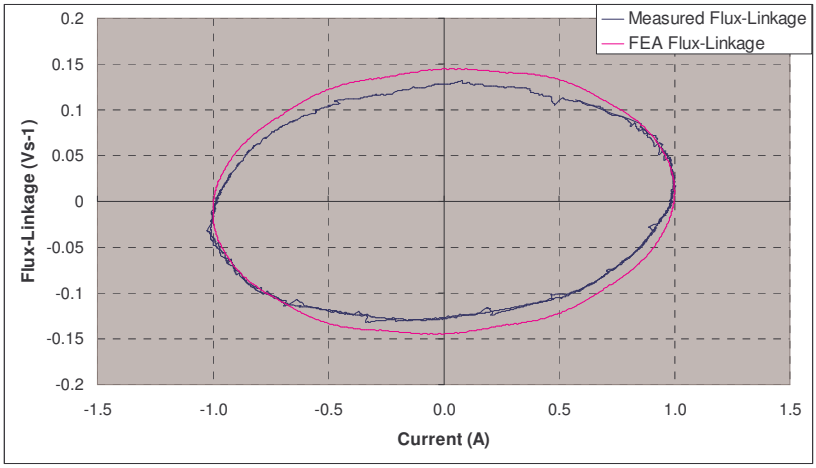

Figure 3-21: ψ-i loop for SEM machine under SVPWM control zero gamma 1A Reference Current 1000rpm

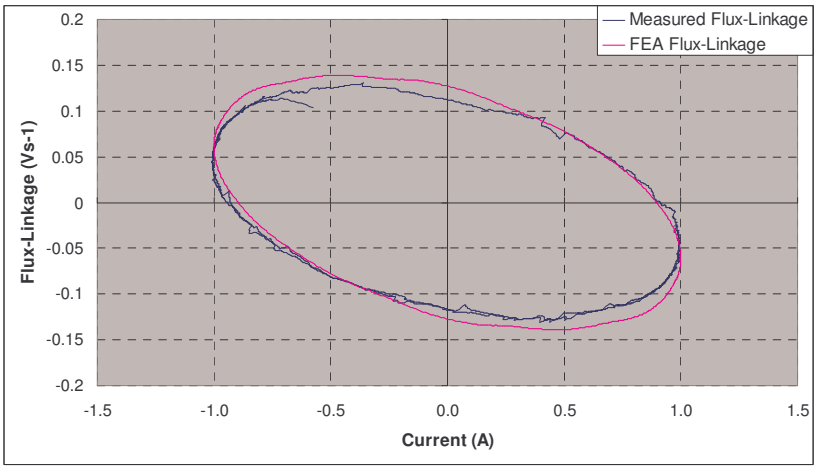

Figure 3-22: ψ-i loop for SEM machine under SVPWM control 30° gamma advance 1A Reference Current 500rpm

Figure 3-15 - Figure 3-18 give the ψ-i loop comparisons for the PI controller over a variety of test points. The figures contain a single electrical cycle as predicted by the PC-BDC software and a number of loops as measured online by the DSP controller. Figure 3-15 shows that the measured loops are a close match for the loop predicted using PC-BDC. This reflects the accuracy of the estimate of the average phase voltage using the PI related prediction method outlined in section 3.2.1. Figure 3-16 shows the loop comparison at a higher reference current however the measured loop is still closely matched with the FEA predicted loop, critically the shape and approximate areas of the loop are very similar. At higher speeds, however, as indicated in Figure 3-17 there appears to be a reduction in the measured magnitudes of ψ and the loops are less well matched; PC-BDC predicts a larger loop area than is observed in measurements. Susequant conversations have taken place with Dr Mircea Popescu with regards to this observed reduction in magnetic flux; this conversation is available in the DVD appendix. In

summary however the phenomenon observed is explained as being due to localised temperature variation in the stator winding, not manifesting in a measureable change in resistance but that does cause reduction in the magnetic flux. Figure 3-18 gives the results obtained when field weakening is applied and there is once again relatively good matching of the predicted loop with the measured loops. The measured loops having a slightly smaller area than the FEA predicted loop.

The results in the PI series of tests are closely matched with the predicted loops obtained from PC-BDC. Given the loops observed in Figure 3-15 to Figure 3-18 it is reasonable to conclude that the phase voltage estimation method outlined for use when operating the PI controller is valid and reasonably accurate, suffering from reduced accuracy at higher speeds and when field weakening is implemented.

Figure 3-19 - Figure 3-22 give the loop comparisons for the SVPWM controller over the same series of tests. Figure 3-19 shows a good match between the measured results and the predicted loop. In Figure 3-20 the loops are also very accurately matched between measurements and FEA predictions – despite the increased reference current. This was also observed in the PI controller based estimator. Figure 3-21 shows the higher speed test results and once again a drop in the measured magnitude of ψ is observed meaning that the loops are not as closely matched. This is also observed in Figure 3-22 where field weakening has been applied. These results act to validate the voltage estimation technique outlined when operating the SVPWM controller in a similar manner to which the PI based technique was.

Considering the results presented in Figure 3-15 to Figure 3-22, similarities between the behaviour of each estimation technique becomes apparent. The ψ-i loops measured at lower speeds across the full current range are generally well matched with the FEA predicted loops. However when the speed is increased or field weakening is applied the magnitude of ψ measured decreases. In the case of the PI and SVPWM based estimators the reduction in the magnitude of ψ results in a measured loop area which is smaller than the predicted loop. However the difference is fairly minimal and the loops can still be said to match fairly well.

Unfortunately in the case of the delta connected Heidenhain machine, no PC-BDC model is available meaning that the FEA predicted ψ-i loop is unavailable for this machine. However the ψ-i loops observed are still worth consideration; if the behaviours discussed

in Figure 3-15 to Figure 3-22 are also observed in the delta connection tests then this would offer some confidence in the voltage estimations outlined for the delta connected machine.

Before the ψ-i loops obtained from the delta connected machine can be discussed; there is a subtle difference between the two motor types which must be considered in order to construct the loop. Equation (16) describes how the flux-linkage is calculated and features the current i – this current also forms the x-axis of the loop diagram. In the case of the wye connected machine this current is simply the regulated phase current. However, in the delta connected machine, the regulated current is the line current. The estimate voltage is the average phase voltage – thus in order to accurately calculate the flux-linkage and to depict the loop accurately the phase current must be constructed.

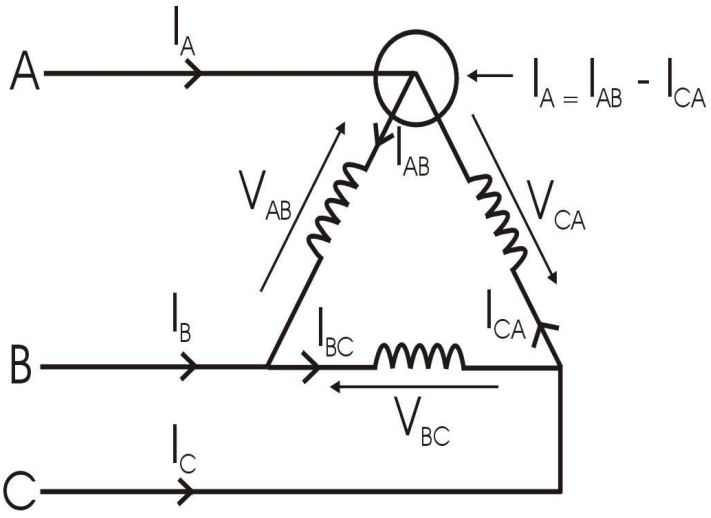

Figure 3-23: Delta Connected Machine with Current Flow Considerations

Consider again the delta connected machine, shown in Figure 3-23. Consider the junction circled at which line current I_A connects to the machine. According to Kirchhoff's circuit laws, the total current entering a junction is equal to the current leaving that junction. Therefore each line current can be expressed in terms of the phase currents:

$$I_A = I_{AB} - I_{CA} \tag{17}$$

$$I_B = I_{BC} - I_{AB} \tag{18}$$

$$I_C = I_{CA} - I_{BC} \tag{19}$$

Equations (17)-(19) give the regulated line currents in terms of the phase currents present in the delta connected machine. It should also be remembered that in a balanced three phase system there is no net current flow.

$$I_{AB} + I_{BC} + I_{CA} = 0 \tag{20}$$

This allows for manipulation of the phase current so that it may be expressed in terms of the line currents:

$$I_{AB} = \frac{2I_{AB} - I_{CA} - I_{BC}}{3} \tag{21}$$

$$I_{AB} = \frac{(I_{AB} - I_{CA}) - (I_{BC} - I_{AB})}{3} \tag{22}$$

$$I_{AB} = \frac{I_A - I_B}{3} \tag{23}$$

Equation (23) gives the representation of the phase current in terms of the line currents which are being regulated. This allows for an online reconstruction of the phase current in the delta machine. Flux-linkage can therefore be calculated using the phase current and thus the ψ-i loops can be depicted accurately.

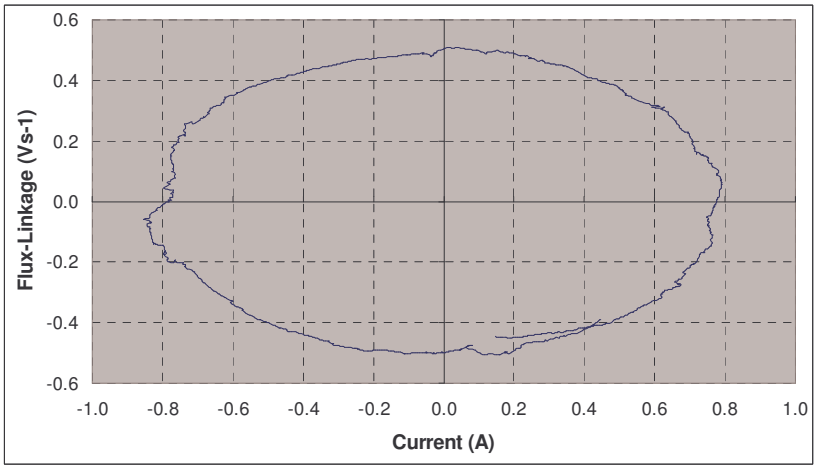

Figure 3-24: ψ-i loop for Heidenhain machine under PI control zero gamma 1A Reference Current 200rpm

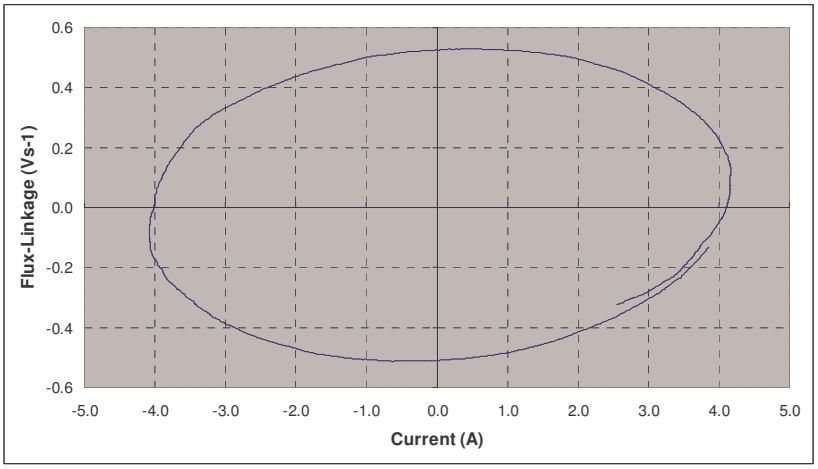

Figure 3-25: ψ-i loop for Heidenhain machine under PI control zero gamma 5A Reference Current 200rpm

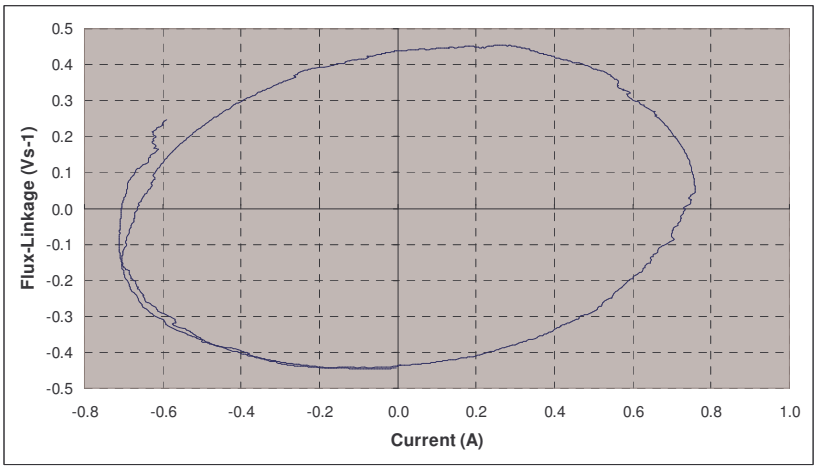

Figure 3-26: ψ-i loop for Heidenhain machine under PI control zero gamma 1A Reference Current 600rpm

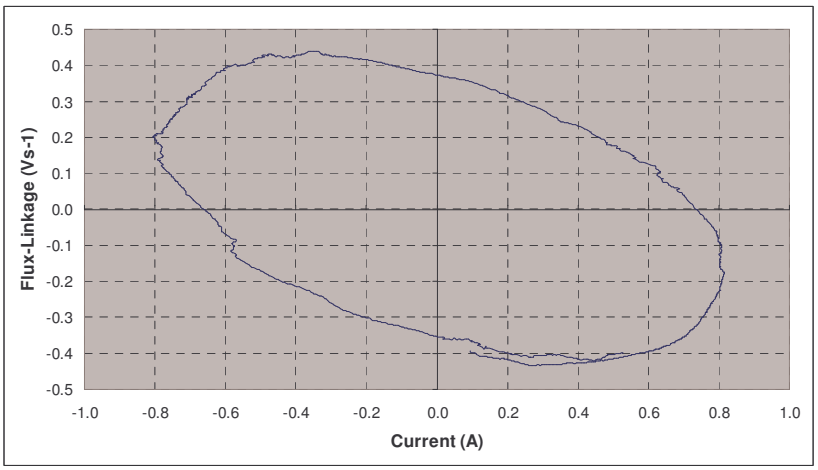

Figure 3-27: ψ-i loop for Heidenhain machine under PI control 30° gamma advance 1A Reference Current 200rpm

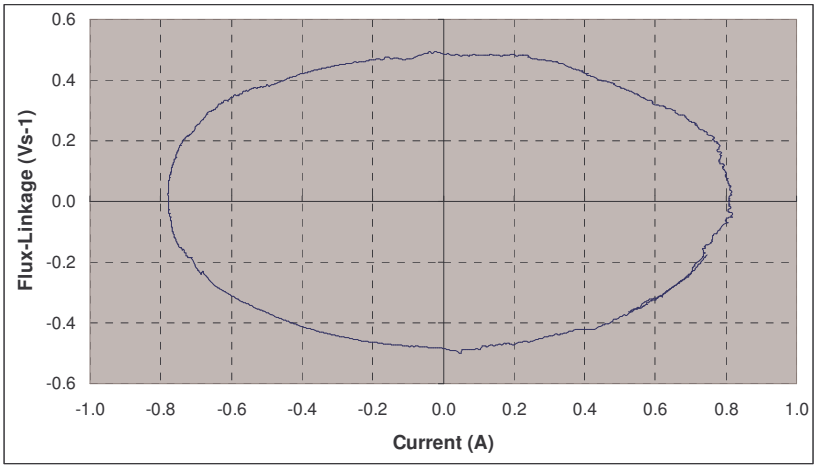

Figure 3-28: ψ-i loop for Heidenhain machine under SVPWM control zero gamma 1A Reference Current 200rpm

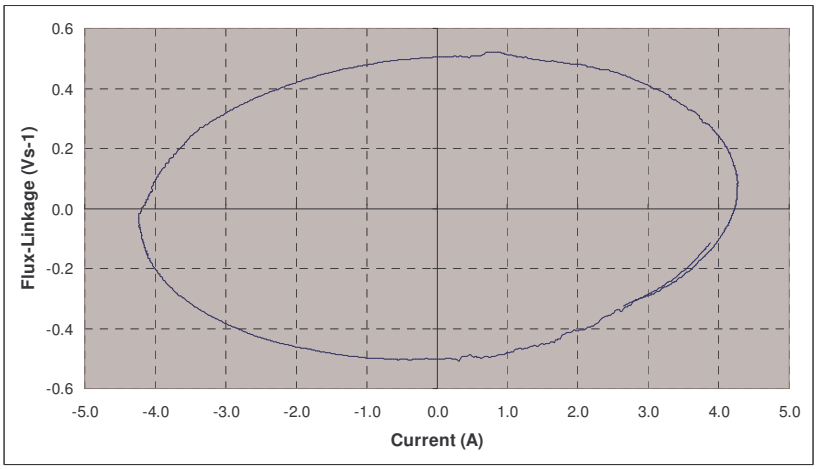

Figure 3-29: ψ-i loop for Heidenhain machine under SVPWM control zero gamma 5A Reference Current 200rpm

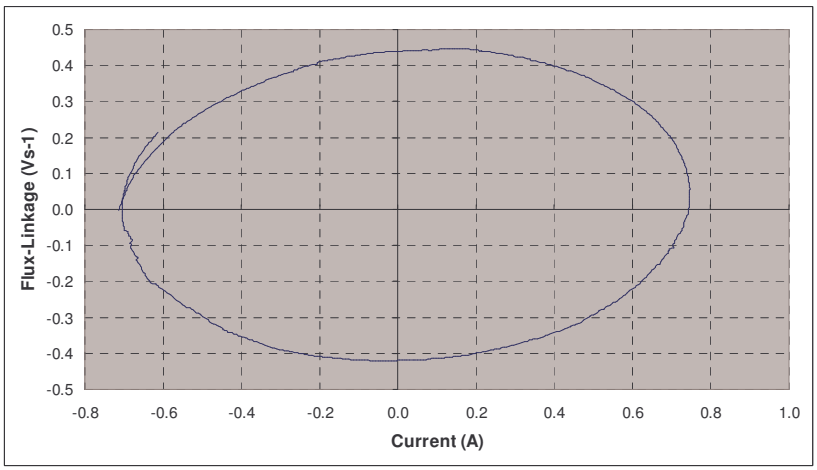

Figure 3-30: ψ-i loop for Heidenhain machine under SVPWM control zero gamma 1A Reference Current 600rpm

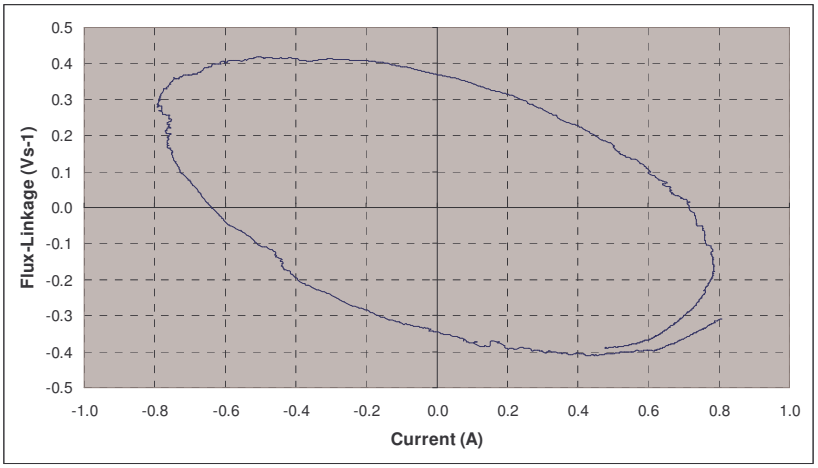

Figure 3-31: ψ-i loop for Heidenhain machine under SVPWM control 30° gamma advance 1A Reference Current 200rpm

Figure 3-24 - Figure 3-27 give the ψ-i loop measurements for the PI controller. The figures do not contain a PC-BDC predicted loop for comparison, however the measured loops can be compared with each other in order to establish if the ψ-i loops follow the same characteristics across the test range as in the wye connected example. The loop in Figure 3-24 is largely similar in shape to that observed in Figure 3-15 (the wye connected equivalent) – this establishes a basis for comparison between the two machine connections. Consider the loop shown in Figure 3-25, measured at higher current, a similar flux-linkage magnitude is repeated – behaviour previously observed in the wye connected example (the shape of the loops being consistent across both connection types). Figure 3-26 gives the loop observed at higher speed. A lower flux linkage magnitude is observed but the decrease is not of significant magnitude – once again a trait observed in the wye connected equivalent. Finally Figure 3-27 shows the loop observed in the case of field weakening, once again a marginal drop in the magnitude of ψ is observed and again this has previously been observed in the wye connected results.

These observations are encouraging, in terms of validating the PI based estimator for the delta connected machine. Should the SVPWM results follow a similar pattern to the PI results and also to their equivalent wye connected results then this will serve to validate the SVPWM estimator in the delta connection.

Figure 3-28 - Figure 3-31 give the ψ-i loop measurements for the SVPWM controller. Immediately obvious is the similarity between the loops in Figure 3-24 to Figure 3-27 and in Figure 3-28 to Figure 3-31. The loops obtained at low speeds without field weakening are very closely matched between the SVPWM and PI results (Figure 3-28 and Figure 3-29). The slight drop in the magnitude of flux-linkage is once again witnessed at higher

speeds and when field weakening is applied (Figure 3-30 and Figure 3-31) – the magnitude is also similar to the drop observed in the PI results.

The validity of the delta connected PI and SVPWM estimation techniques is weakly based upon the similarities with the corresponding wye connected results – there is no FEA based machine model with which to compare. There is however some additional validity of the results offered via an analysis of the open circuit back EMF of each machine. An estimate of the machines magnetic flux-linkage value can be obtained through the integration of a back-emf wave captured under open circuit steady state conditions.

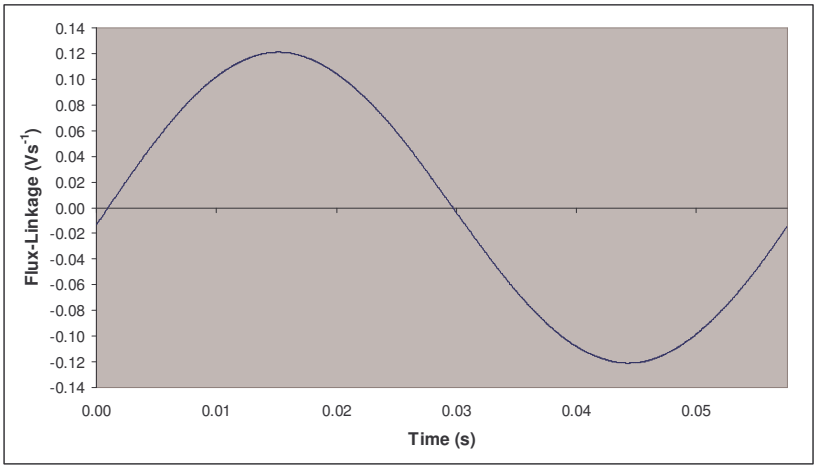

Figure 3-32: Flux-Linkage wave of SEM machine constructed from open circuit back-EMF

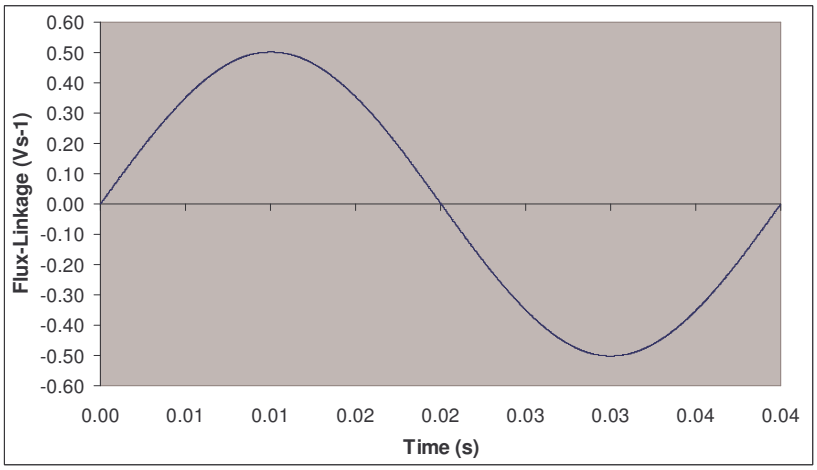

Figure 3-33: Flux-Linkage Wave of Heidenhain machine constructed from open circuit back-EMF

Figure 3-32 and Figure 3-33 show flux-linkage waves for each machine reconstructed from back-EMF waveforms. In the case of the SEM machine the peak magnitude of the reconstructed flux-linkage is around 0.121 Vs^{-1} which compares favourably to both the FEA predictions and measured ψ-i loops under both PI and SVPWM control which suggest a value near 0.15Vs^{-1}. The discrepancy in the measurement can be applied to unreliability

in the test method which captures the waveform given in Figure 3-32. The Back-EMF waveform has been captured at a single operating speed, hence a single test point has been produced to capture the waveform and to generate the 0.121Vs^{-1} value. A greater range of testing with this methodology may have helped to correlate the result with the prediction of 0.15Vs^{-1}. Similarly the reconstructed flux-linkage magnitude for the Heidenhain machine is around 0.502Vs^{-1}. This also compares favourably with the results obtained using both the SVPWM and PI controllers which suggest a value around 0.45 – 0.5Vs^{-1} shown in Figures 3-29 to 3-31.

Whilst the presentation of the ψ-i loops does offer some notion of validity of the voltage estimation techniques (at least in the case of PI and SVPWM), the lack of FEA results available in the delta connected example is an issue. The ψ-i loops do not offer a comprehensive validation of the voltage estimators. Therefore an alternative avenue for validation is required.

3.3.2. Online Torque Estimation

Considering again the literature which first described the online voltage estimator, this study develops the technique in order to estimate the output torque online [1]. This is work which has been further studied, the emphasis of the study being the use of the flux-linkage versus current diagrams in order to carry out a number of online parameter estimations, including output torque [79, 117].

The torque estimation techniques outlined in these studies deduce an average torque estimate through consideration of the sum of instantaneous electromagnetic torque across the fundamental cycle period. The average torque over one fundamental cycle is given as [79, 117]:

$$T_{avg} = \frac{mp}{2\pi}\Delta W \tag{24}$$

where m is the number of phases, p the number of pole pairs and ΔW' is the energy converted per phase during a fundamental period. It is clear from equation (24) that ΔW' is proportional to the area of the ψ-I loop. Given the need to validate the voltage estimators which have been described, the generation of ψ-i loops has been detailed and the resultant loops have been shown (compared with FEA equivalents where possible). Therefore in order to fully validate the voltage estimates for each machine and validate the ψ-i loops generated, the average torque calculations can be compared with output

torque measurements taken from torque transducer equipment. This will allow for a comprehensive evaluation of the techniques.

In order to evaluate equation (24) the energy converted (ΔW') can be calculated by measuring the energy of the phase per cycle and subtracting the energy lost in that cycle.

$$W_{cycle} = \left(\sum_{0}^{N} i_{ph} v_{ph} \right) \tau_{cycle} \tag{25}$$

Equation (25) is used to calculate the energy per phase during a single fundamental cycle; where N is the number of samples taken within a single cycle and τ_{cycle} is the period of that single fundamental cycle.

$$W_{Cu} = (I_{rms})^2 R_{ph} \tau_{cycle} = \frac{1}{N} \left(\sum_{0}^{N} (I_{ph})^2 \right) R_{ph} \tau_{cycle} \tag{26}$$

$$\Delta W = W_{cycle} = \left(\sum_{0}^{N} i_{ph} v_{ph} \right) \tau_{cycle} - \frac{1}{N} \left(\sum_{0}^{N} (I_{ph})^2 \right) R_{ph} \tau_{cycle} \tag{27}$$

Where R_{ph} is the phase resistance. The DSP controller estimates the average torque output by assessing equations (25)-(27) before using the result of (27) with (24). In order to make these calculations the controller needs to count the number of samples (which occur at a frequency of 20kHz) per fundamental cycle period. The current signal i_{ph} is the regulated parameter in wye connected machines; in delta connected machines it is reconstructed from the line currents which are regulated. This allows sufficient confidence that the current values are accurate when used. The R_{ph} parameter is input directly to the controller from the user and is therefore as accurate as the measurement process with which it was obtained – usually with commercially available multi-meter apparatus which provides a value of more than sufficient accuracy for these calculations, measurements taken throughout testing have shown that there is negligible temperature and thus resistance variation throughout testing. The number of phases (m) and pole-pair (p) are also provided by the user and are checked during commissioning. The other parameter used, Vph, is the only potentially unreliable parameter used in these calculations. However, as this is the estimate which requires validation it is obvious that comparing the resultant torque calculations with the torque values measured using torque transducers will allow for an assessment of the reliability of V_{ph} – thus providing an avenue for a comprehensive validation of the techniques outlined.

The torque estimations will be captured on both machines previously outlined. The torque estimates presented have been recorded during the same series of tests which provided the results outlined in Chapter 2 – during these tests the controller's online estimates were also recorded. In addition to this series of testing – further testing was carried out to assess the torque estimations across a range gamma advances (varying strength of field weakening).

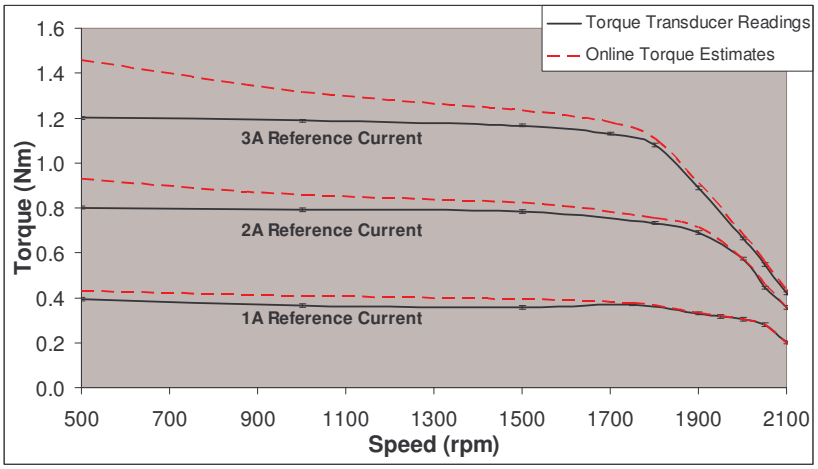

Figure 3-34: Torque estimates versus Torque measurements under PI control on SEM machine – no field weakening.

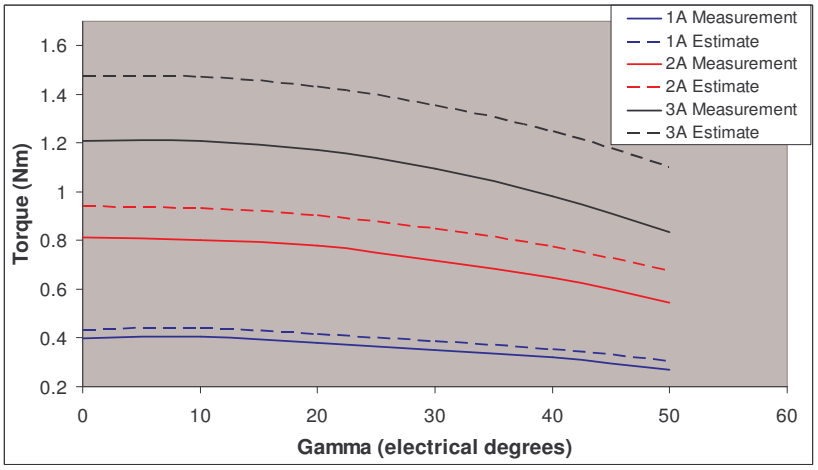

Figure 3-35: Torque Estimates versus Measurements under PI Control on SEM machine with respect to Gamma Advance at 500rpm

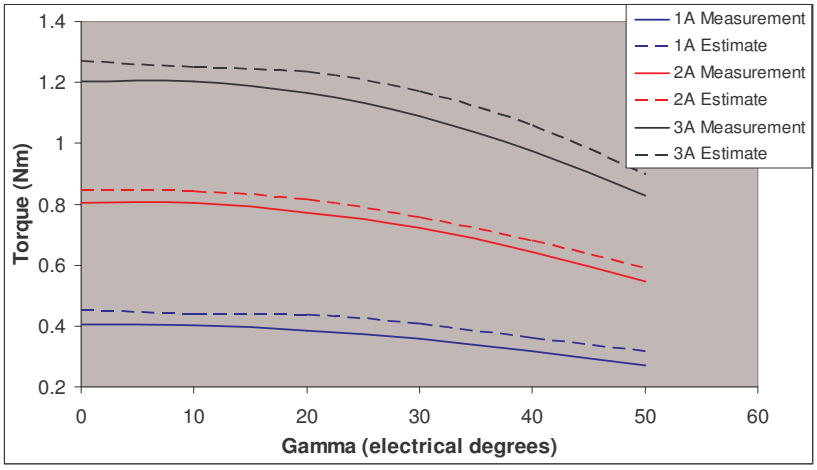

Figure 3-36: Torque Estimates versus Measurements under PI Control on SEM machine with respect to Gamma Advance at 1000rpm

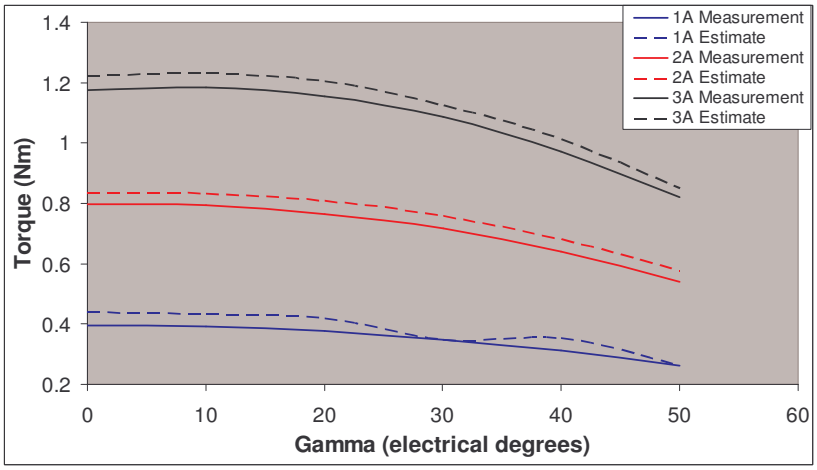

Figure 3-37: Torque Estimates versus Measurements under PI Control on SEM machine with respect to Gamma Advance at 1500rpm

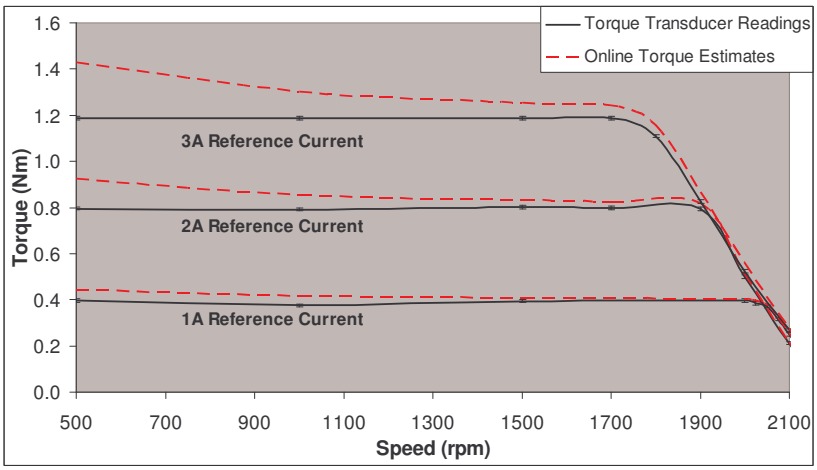

Figure 3-38: Torque estimates versus Torque measurements under SVPWM control on SEM machine – no field weakening.

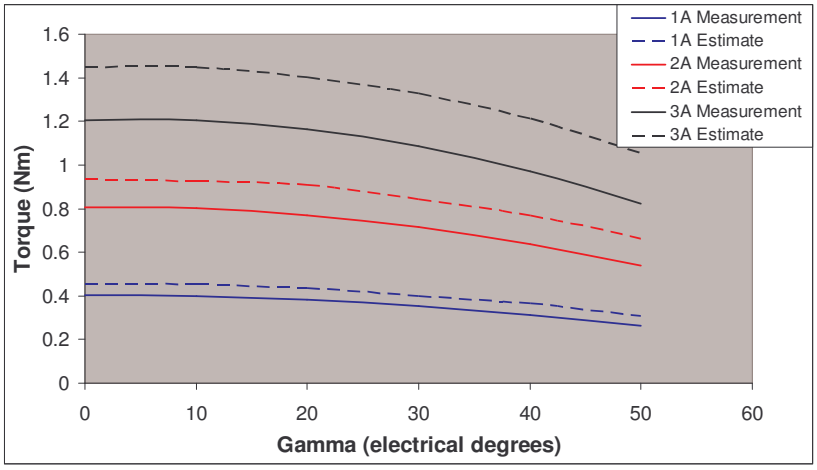

Figure 3-39: Torque Estimates versus Measurements under SVPWM Control on SEM machine with respect to Gamma Advance at 500rpm

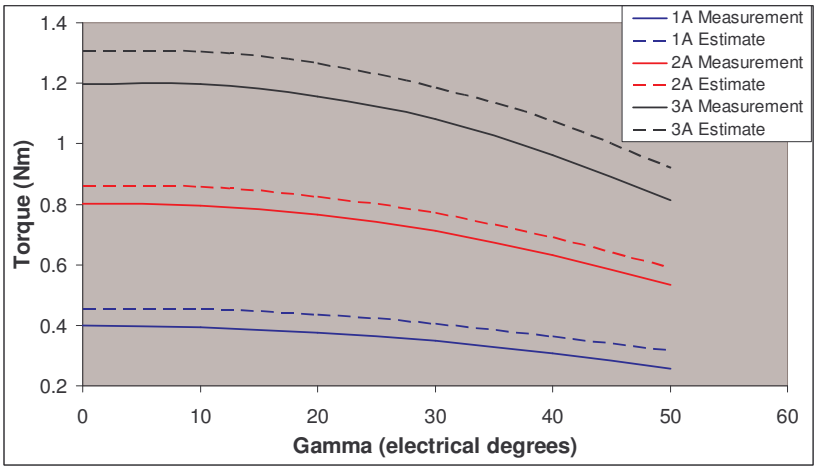

Figure 3-40: Torque Estimates versus Measurements under SVPWM Control on SEM machine with respect to Gamma Advance at 1000rpm

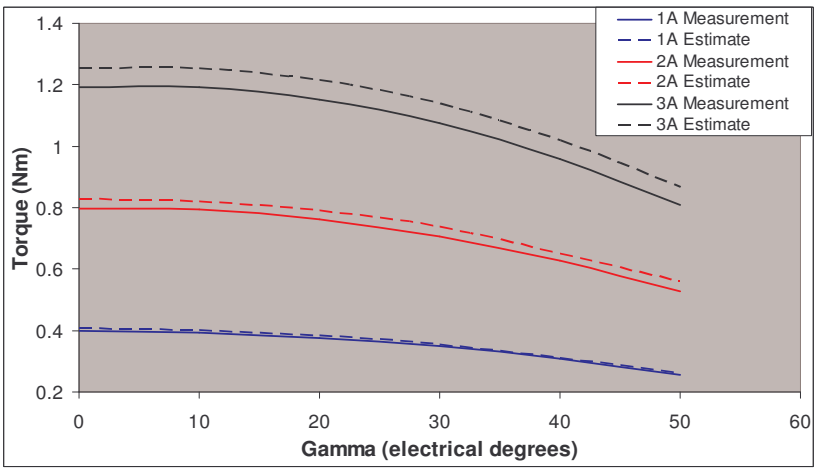

Figure 3-41: Torque Estimates versus Measurements under SVPWM Control on SEM machine with respect to Gamma Advance at 1500rpm

Figure 3-34 shows the comparisons obtained with the SEM machine under PI control with respect to the operating speed. In the low speed regions the estimated torque is higher in magnitude than the measured torque. This is an effect which worsens as the reference

current increases. At the 1A reference current the estimated torque is seen to accurately track the measured torque (albeit with an offset to the magnitude). Again at the higher speeds the estimates compare favourably with the measured torque results. At the lower speeds the indication is now that the voltage is being over estimated which leads to the higher torque estimates; whilst this was not the indication when considering the ψ-i loops. The torque considerations however carry greater weight in this respect given that the comparisons are based with measured results gathered under test and not based on FEA predictions. Figure 3-35 to Figure 3-37 shows the comparisons with respect to the gamma advance being applied. The estimates are seen to very accurately mimic the changes observed in the output torque across the gamma advance range. This validates the estimation technique with regards to predicting the torque output with respect to the applied gamma advance.

Figure 3-38 shows the comparisons obtained with the SEM machine under SVPWM with respect to the operating speed. The results obtained are very similar to those witnessed in the PI tests; at low speeds the torque is over estimated - an effect which worsens as the current increases. At higher speeds the torque estimates are largely accurate. Figure 3-39 - Figure 3-41 give the comparisons with respect to the gamma advance. As was previously the case, the estimates track the changes in torque with a high degree of accuracy. This is true at all speeds and all reference currents tested, thus providing strong validation of the technique outlined.

Considering all of the results displayed in Figure 3-34 to Figure 3-41 there are a number of similarities displayed. The estimates obtained under each of the control techniques show poorest accuracy at the lower speeds; this is an effect which worsens as the current is increased. The accuracy at higher speeds however is greatly improved and offers some encouragement in terms of validating the technique. Each of the techniques show good response to gamma advance tracking the changes in torque with a high degree of accuracy.

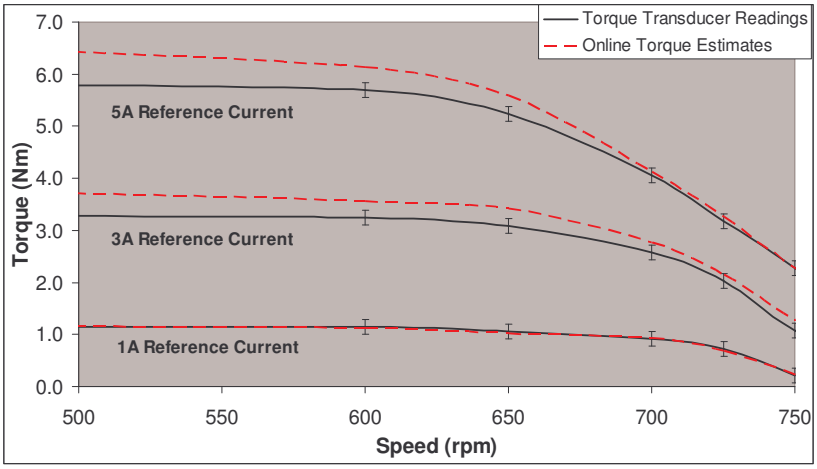

Figure 3-42: Torque estimates versus Torque measurements under PI control on Heidenhain machine – no field weakening.

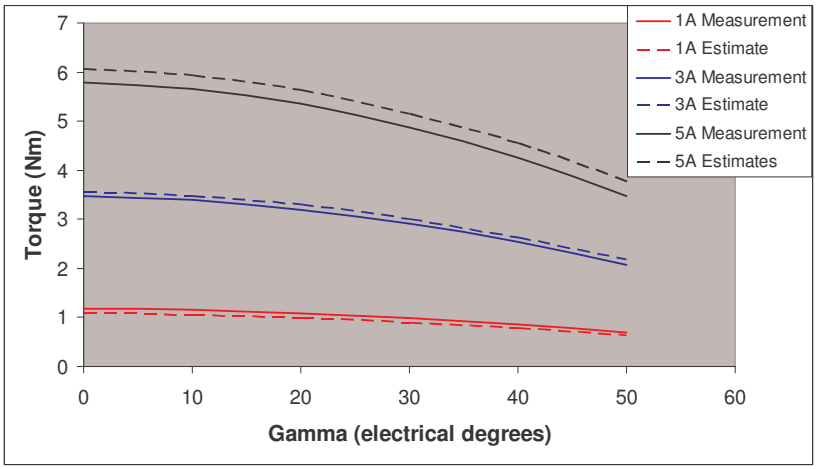

Figure 3-43: Torque Estimates versus Measurements under PI Control on Heidenhain machine with respect to Gamma Advance at 400rpm

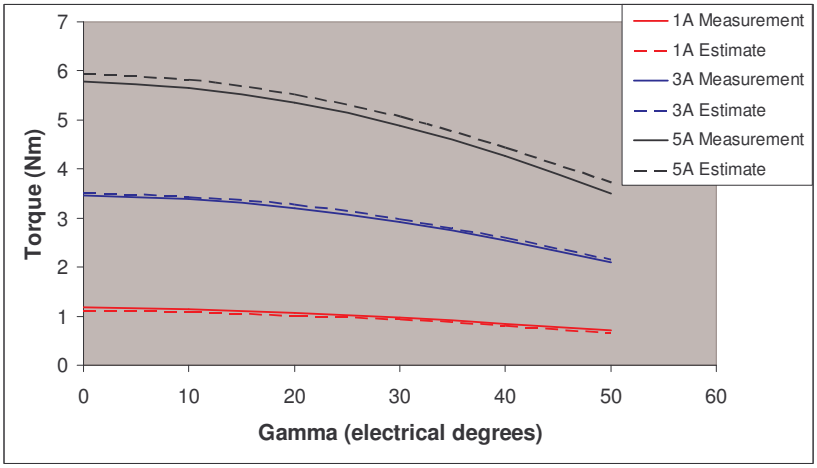

Figure 3-44: Torque Estimates versus Measurements under PI Control on Heidenhain machine with respect to Gamma Advance at 600rpm

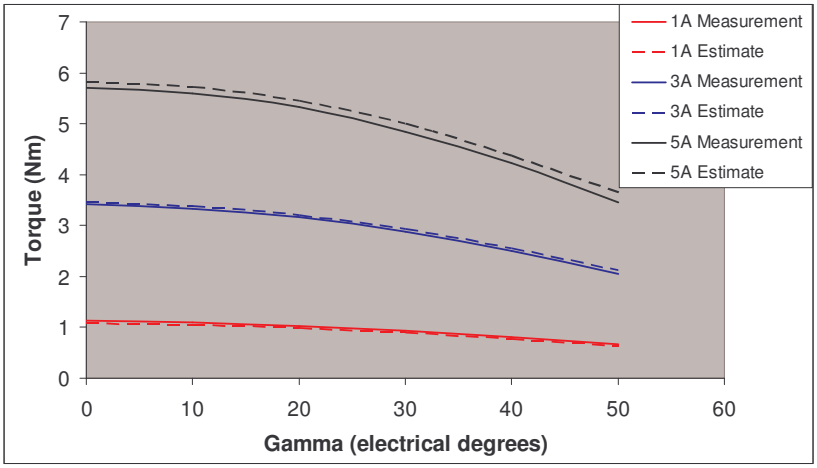

Figure 3-45: Torque Estimates versus Measurements under PI Control on Heidenhain machine with respect to Gamma Advance at 800rpm

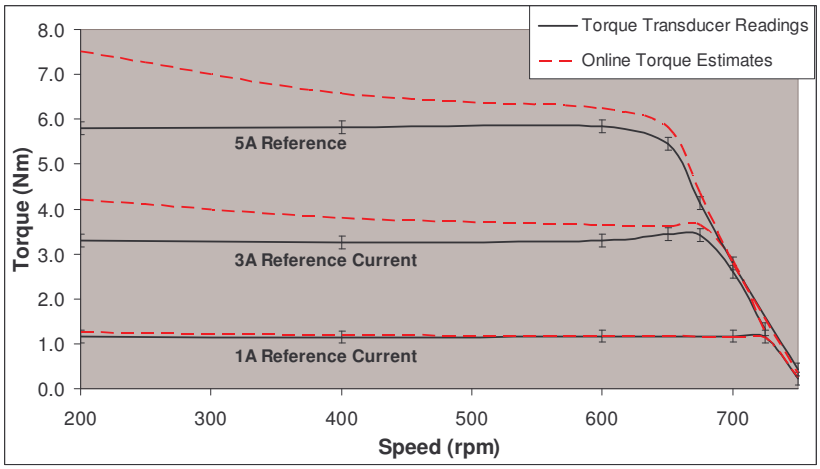

Figure 3-46: Torque estimates versus Torque measurements under SVPWM control on Heidenhain machine – no field weakening.

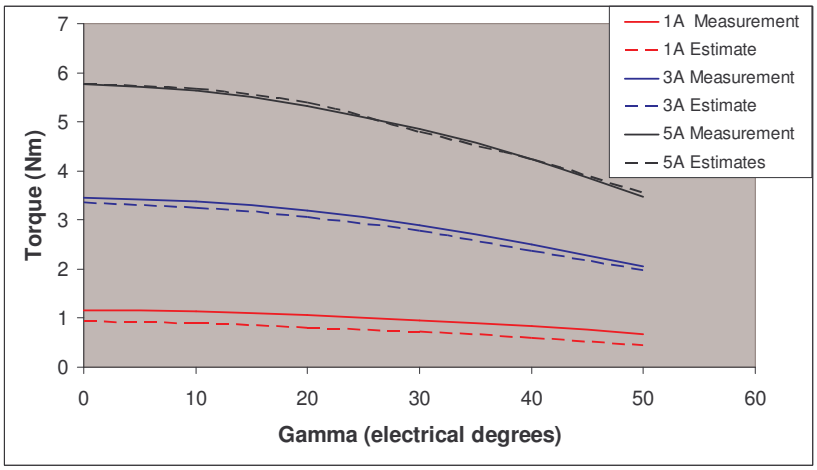

Figure 3-47: Torque Estimates versus Measurements under SVPWM Control on Heidenhain machine with respect to Gamma Advance at 400rpm

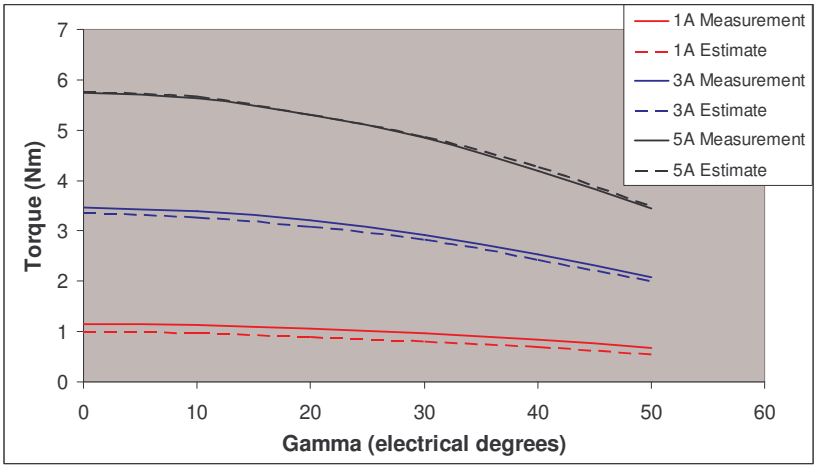

Figure 3-48: Torque Estimates versus Measurements under SVPWM Control on Heidenhain machine with respect to Gamma Advance at 600rpm

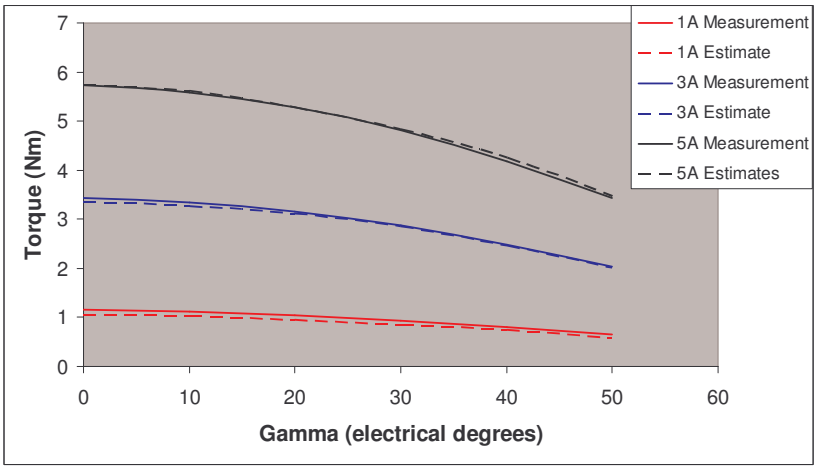

Figure 3-49: Torque Estimates versus Measurements under SVPWM Control on Heidenhain machine with respect to Gamma Advance at 800rpm

Figure 3-42 shows the comparison of the online torque estimates versus measured torque under PI control in response to the operating speed. As was expected the torque estimates show a higher level of accuracy across the speed range than was observed in the wye connected example. This is clearly demonstrated as the majority of the torque estimates reside within the error margins of the actual torque measurements. Figure 3-43 to Figure 3-45 show the comparisons with respect to the gamma advance under PI control. At the lower reference currents the estimates are slightly smaller than the measurements; however the estimates have been shown to be within the error range of the measurements. The estimate torque values track the changes in the measurements across the gamma range with a high level of accuracy.

Figure 3-46 shows the comparison of the online estimates and the measured torque under SVPWM control in response to the operating speed. The results on display are very similar to the PI results obtained. Once again the majority of torque estimates reside

within the error margins of the measured results. Figure 3-47 to Figure 3-49 show the comparisons with respect to the gamma advance under SVPWM control. In general the estimates are seen to track the measured torque results with good levels of accuracy, highly similar to the results obtained under the PI testing.

Considering Figure 3-42 to Figure 3-49 the delta connected estimators demonstrates a high level of accuracy when compared to the wye connected machine. In consideration of the estimators of both the wye and delta connected machines the results are mixed. The wye connected estimators are shown to improve in accuracy as the speed is increased however there is a serious loss in accuracy at reduced speeds. Considering the test range covered in this research there is no particular need to address the loss of accuracy in the low speed region of the delta estimators as the likelihood of operating at lower speeds is reduced for most applications. However in the case of the wye connected machines the estimators would certainly benefit from consideration of further losses that reside in the drive system. The gamma advance response in all cases is very consistent across the range of speeds and reference currents levels.

The consistency with which the PI and SVPWM estimators operate across both connection types indicates a high level of reliability in the respective voltage estimates; however there is clearly an inaccuracy in the wye connected estimator which must be addressed in order to claim validity of the voltage estimations. The low speed region for the wye connected estimator requires modification which affects a reduction in the resultant estimates. The considerations essentially need to affect an increasing reduction in the voltage estimate with respect to both decreasing speed and increasing reference current.

3.4. Consideration of Voltage Losses

Upon review of the estimations presented in section 3.3.2, a need to consider potential voltage losses in the system is required for the wye connected machine. It is shown in the torque estimator results that at lower operating speeds and higher reference currents that there is an over estimation of the average phase voltage which is producing an over estimation of the torque in this region. Thus considerations of voltage losses with respect to lower operating speed and higher reference current are required in the wye connected machine. The results presented for the delta connected machine show a far higher initial accuracy, however there is evidence in the trends of the estimation curves that loss

consideration may be required at lower speeds – however these speeds are rarely used in variable speed drives such as that outlined in this research. A probable explanation for the improved accuracy observed in the delta connected machine would be to consider that the full DC link potential is made available to the phase winding, not 1/3 or 2/3 as is the case in the wye connected machine. At this stage it may be beneficial to recall the operating DC link voltages for each of the machines under test which was presented in TABLE 2-1. Thus any potential losses contributed through the drive system – such as switch losses are a smaller fraction of the applied voltage during excitement. This explains the improved accuracy over the speed range for the delta connected estimator when compared to the wye connected case. There is therefore no need to pursue loss consideration in the delta connected estimator.

The technique as it has been described thus far has not given any consideration to the voltage losses associated with the use of IGBT based inverter technology. However given the need for consideration of voltage losses; the inverter is the most obvious system component to consider for voltage losses. There are 2 typical voltage losses which are immediately obvious when considering the voltage source inverter. These are freewheel diode voltage losses and losses associated with dead-band timings.

Considering first the dead-band losses, a dead-band time of 120ns is implemented in this system. This means that once a gate signal is made high, there is a 120ns delay before the DSP renders a high signal on the gate drive. This delay allows sufficient time for the complimentary gate to turn off ensuring that the two switches of the phase leg are not both active; preventing an instantaneous short circuit of the DC link. Consider the switch patterns indicated in Figure 3-8, it can be seen that in any switch cycle the number of transitions is 4. This means that at most 480ns of the 50µs switch period is lost to dead-band in any one phase. This means that dead-band time makes up a maximum of 0.96% of the switch period; this makes the impact of dead-time highly unlikely to impact significantly upon the voltage estimations.

3.4.1. Freewheel Diode Voltage Losses

Consider again the typical VSI schematic outlined in Figure 2-1. Clearly indicated are the freewheel diodes included which act to protect the IGBT switch devices which are commanded by the DSP controller. These diodes protect the switch devices from negative current flow which occurs as a result of the inductance of the windings in the

machine which is connected. Consider also the manner in which the voltage estimator presently operates; through consideration of the equivalent phase voltage during periods t_1 and t_2 (see Figure 3-4). The remainder of the switch period τ_{sw} is neglected as there is no apparent connection across the phase windings; given the need to consider losses in the wye connected machine perhaps the two diodes connected to each phase leg of the inverter should be considered during the remaining period. This is a consideration which is described in the authors work on the classical phasor diagram in which the voltage estimation technique is presented [106].

The voltage dropped across the freewheel diode fits the requirements (in terms of voltage losses) ideally given the results observed. The voltage drop across the diodes is proportional to current (this is subject to saturation). In addition to this it can be reasoned that at lower speeds the zero voltage vector period ($t_0 = \tau_{sw} - t_1 - t_2$) will be greater. This is based on the reasoning that at lower speeds the rate of change of the reference current is lower and thus the response of the controller is expected to be more reserved; this will affect a reduction in t_1 and t_2 and thus an increases t_0. The estimators can be modified such that the voltage estimations include a voltage loss representative of the diode voltage losses. Thus there is a direct consideration of the effects of both low operating speed and the effects of increased reference current.

A straightforward implementation of the diode voltage drop is to consider a linear estimation of the voltage dropped with respect to current and to then saturate this voltage at the value specified for the device being used. In the case of the VSI used throughout this research the IGBT module implemented is the Eupec BSM100GD120DLC half bridge module [118]. This device contains an integrated freewheel diode and this has a typical saturated forward voltage of 1.8V. This value is used to limit the voltage loss; the calculation of the loss in the non-saturated region is directly proportional to the measured phase current. The voltage loss is then saturated (where necessary) before being integrated into the existing voltage estimates. The voltage loss is applied in the opposite direction from the current flow calculated.

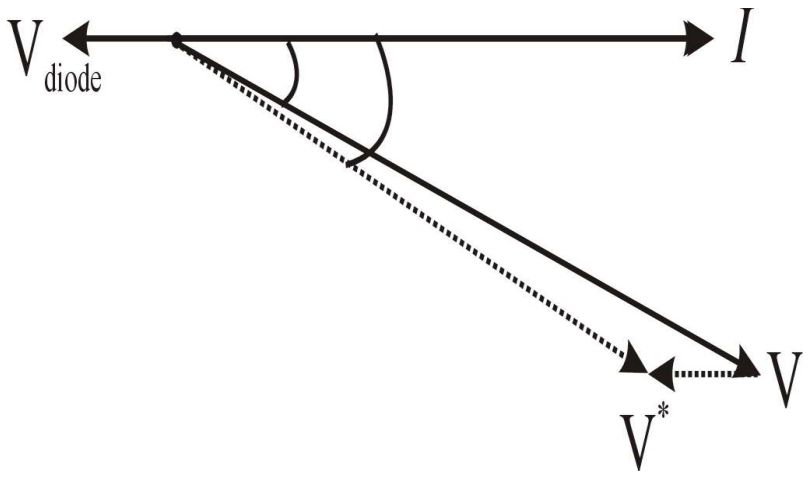

Figure 3-50: Correction of Average Phase Voltage due to Diode Forward Voltage losses

Figure 3-50 demonstrates the way in which the voltage dropped across the diode is applied to the existing phase voltage estimate. Owing to the application of V_{diode} in an opposite direction to the phase current - the power factor angle (which is typically less than 90° in all applications) is increased slightly which ensures the resultant phase voltage estimate V^* is smaller in magnitude than the initial estimate V.

Given that the torque estimates at higher speeds are generally regarded as satisfactory then it is clear that any loss consideration should not be noticeable in these regions, this is another aspect which makes the diode forward voltage losses the ideal solution. The voltage drop applied is in proportion to the zero voltage timing vector t_0. At higher speeds during which the rate of change of phase current is high, the controller typically requires a more substantial current response which is achieved through an increase of the timing vectors t_1 and t_2 which in turn results in a reduction in t_0.

Through consideration of the voltage lost across the freewheel diodes, Figure 3-34 to Figure 3-41 can be re-plotted indicating the impact that the diode voltage considerations have made to the estimated torque results.

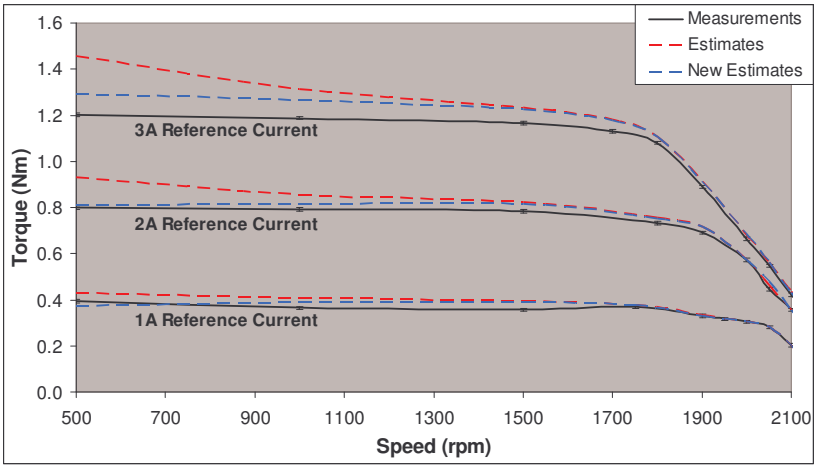

Figure 3-51: New and Original Torque estimates for SEM machine with respect to operating speed under PI control.

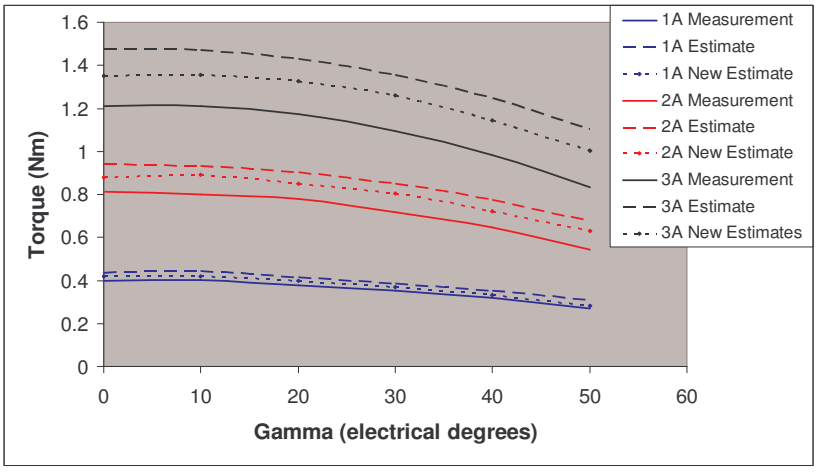

Figure 3-52: New and Original Torque estimates for SEM machine with respect to gamma under PI control at 500rpm operating speed.

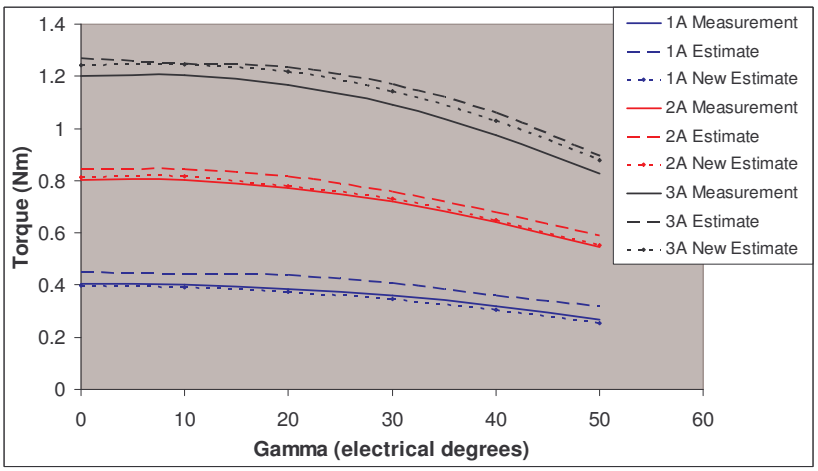

Figure 3-53: New and Original Torque estimates for SEM machine with respect to gamma under PI control at 1000rpm operating speed.

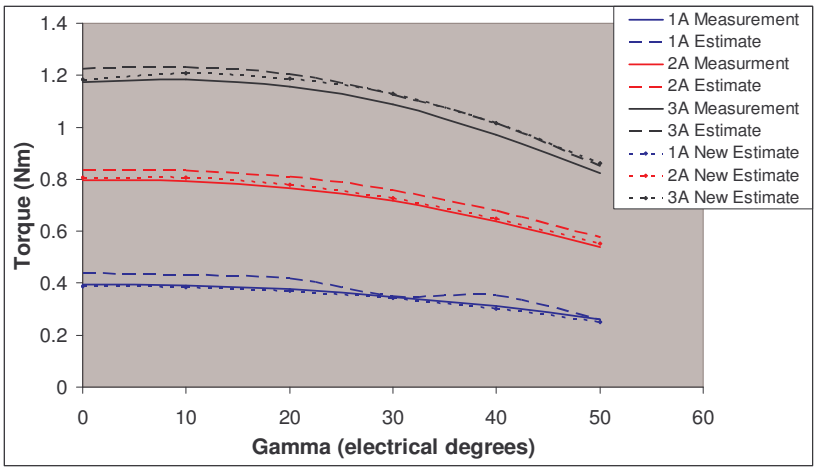

Figure 3-54: New and Original Torque estimates for SEM machine with respect to gamma under PI control at 1500rpm operating speed.

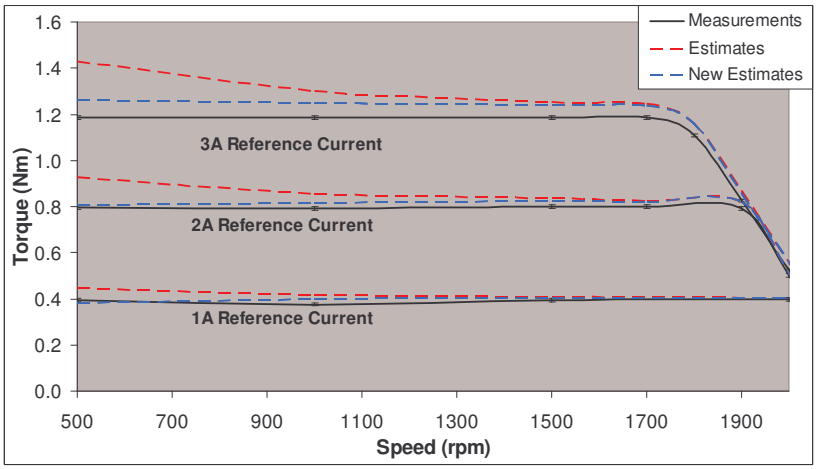

Figure 3-55: New and Original Torque estimates for SEM machine with respect to operating speed under SVPWM control.

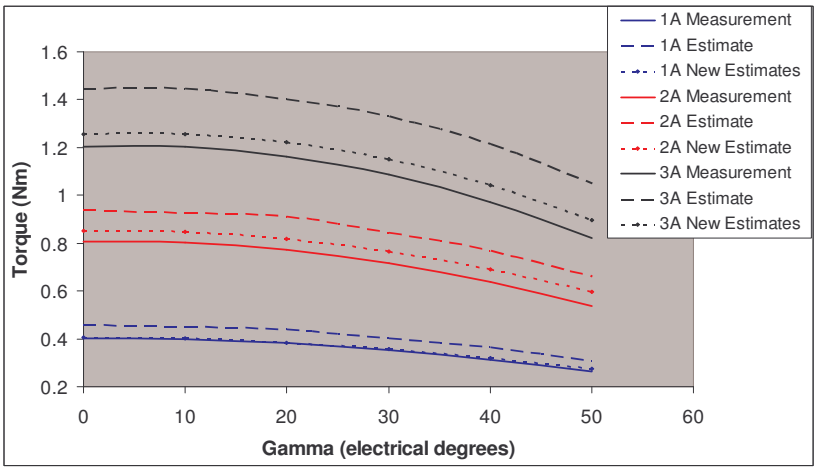

Figure 3-56: New and Original Torque estimates for SEM machine with respect to gamma under SVPWM control at 500rpm operating speed.

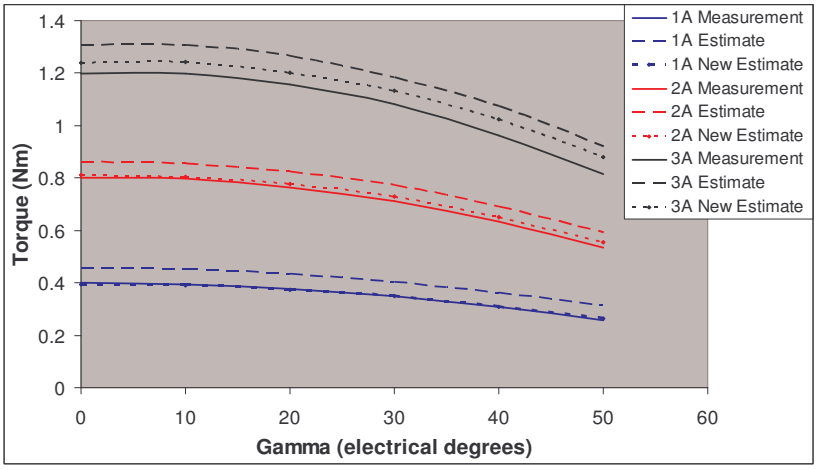

Figure 3-57: New and Original Torque estimates for SEM machine with respect to gamma under SVPWM control at 1000rpm operating speed.

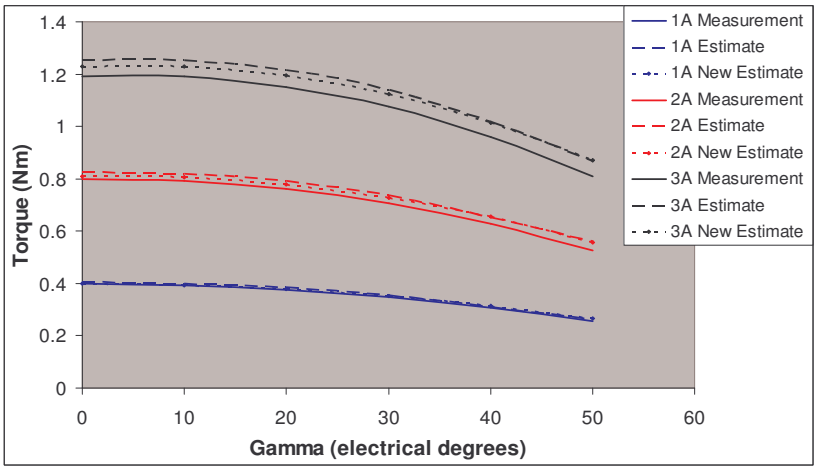

Figure 3-58: New and Original Torque estimates for SEM machine with respect to gamma under SVPWM control at 1500rpm operating speed.

Figure 3-51 to Figure 3-54 show Figure 3-34 to Figure 3-37 with additional curves representing the new online torque estimates. The results obtained using the PI controller are highly encouraging. The tests conducted with respect to speed (Figure 3-51) show that the diode voltage loss considerations effect a very significant improvement in the torque estimations in the low speed regions. Indeed a constant torque value is now predicted in the constant torque region, signalling a strong validity in the consideration of the diode voltage losses. In addition to this the results obtained with respect to the gamma advance applied highlight that the diode loss considerations act in order to reduce the difference between the measured results and the online estimates without affecting the general response to the gamma advances being applied.

Figure 3-55 to Figure 3-58 show Figure 3-38 to Figure 3-41 with additional curves representing the new online torque estimates under SVPWM control. The results obtained are nearly identical to those obtained under PI control. The constant torque

region now has constant torque predictions matching the measurements (in behaviour, not always magnitude) and the improvement in accuracy in the low speed regions is very obvious. The gamma advance tests also indicate a general reduction in the inaccuracy that the estimates previously had; the estimate response with respect to the gamma advance is not compromised by these changes. The consideration of switching losses has been validated through the improved accuracy of the torque estimates.

The motivation for making use of the online torque estimation techniques as a route for validating the average phase voltages estimators has been explained. Torque comparisons are the only method available for comparing estimate values with measurements taken from commercially available equipment. This allows for validation to be established not only in terms of estimation result patterns but also in terms of the accuracy of the estimated values.

The final results have indicated a number of consistent behaviours which go some way towards validating the voltage estimates. In virtually all examples the estimates obtained in the higher speed regions are highly accurate when compared to the measured values. This offers a reasonable level of validation of the voltage estimates; almost all behave as expected in the high speed region. In terms of response to changes in gamma advance all of the torque estimators are shown to respond very well to changes in the measured torque. The PI and SVPWM wye connected estimators show high levels of accuracy throughout the entire speed range (particularly when the diode losses are considered). This offers a strong validation of the voltage estimates. The delta connected versions offer the best accuracy across the entire speed and gamma test ranges – the estimates being sufficiently accurate that no additional loss consideration is required as is the case in the wye connected estimators. The results presented strongly validate the techniques outlined in this research.

3.5. Conclusions

This chapter has described techniques for the online estimation of average phase voltage, flux-linkage and average torque when implemented with the PI or SVPWM controllers in Chapter 2 and when using either a wye connected or delta connected machine. The voltage estimation is the fundamental technique described; flux-linkage and average torque estimates are essentially applications of the voltage estimations. The techniques presented were an expansion of those previously outlined which were implemented on a

wye connected machine using a stationary frame PI controller such as that outlined in chapter 2. The fundamental differences between the gate drive waveforms of the SVPWM controller and the PI controller were highlighted as were the difference in control timing variables that are available to the controller in each of the strategies. These differences give rise to the necessity for a dedicated average voltage estimator which should be used when operating a SVPWM control; this was described. Expanding the estimators further, the fundamental differences between the wye connected and delta connected machines were explained highlighting the necessity for modified techniques which make consideration of the phase connections. The delta based estimators were also described.

This chapter highlights the difficulty in validating the estimation techniques with direct measurements of the phase voltage; thus introducing the concept of validating the estimates through the application of them in the construction of flux-linkage (ψ) estimates. Based upon this principle the generation of ψ-i loops was described for each of the voltage estimators described. ψ-i loops were compared with predictions obtained from commercially available FEA software in an effort to validate the voltage estimations – however as this could only be done in the case of the wye connected machine, alternative avenues for validation were also explored. The average torque estimator was then introduced as a further application of the online voltage estimator which provided an ability to compare online estimates with measured results using commercial torque transducer equipment. It is through this avenue which the voltage estimators are validated in the chapter. The validation results themselves were strong. The PI and SVPWM wye connected estimators have been shown to be effectively validated since both the predicted ψ-i loops and measured torque results are accurately estimated. The delta connected methods have stronger claims to validity with respect to the torque estimates, the estimated results most closely matching the measurements.

The contributions of the study outlined in this chapter are numerous. After the introduction of the original PI based average phase voltage estimator, additional estimators based upon the SVPWM strategy and the delta connected machine were introduced. This represents a contribution of three unique phase voltage estimators. By application of the delta connected voltage estimators outlined, further original contributions have included delta connected ψ-i loop construction techniques and torque estimation techniques. These have been validated to the fullest extent possible;

inaccuracies in the estimations having been addressed through the consideration of losses in the drive system.

Chapter 4
Modelling the PMSM Test Bench

This chapter describes the development of a new simulation model for the PMSM test bench system described in Chapter 2. The particular novelty of this model lies in the ability to directly exchange software from the FCIV test platform to its equivalent component in the simulation model. The initial system is considered and the key components described in the context of their function within the system; this leads to a definition of the standalone components within the simulation model. The chapter continues with a description of how each of these components can be modelled in the simulation environment, focussing particularly on the architecture of the custom created FCIV C++ simulation model. There is also particular focus on how the modelling of the motor component and associated load component take into consideration both electrical and mechanical properties present in the system which allow these parts of the system to be modelled.

The chapter concludes with a partial validation of the FCIV C++ model; the validation focussing entirely upon the generation of the correct reference current signals and the subsequent regulation of motor phase currents. This serves to validate the FCIV C++ model and the role it plays in subsequent system simulations which will be presented in the next chapter.

4.1. Introduction

Engineers tasked with the design of electric motors or their associated applications benefit greatly from extensive machine simulation and modelling processes. In order to assess performance parameters such as those outlined in Chapter 2, simulation models of the machine, VSI and associated controller can be developed. The MATLAB/SIMULINK [119] simulation environment is often used to develop such models. Good examples of simulations using this environment are given in [120-123]; these examples focus

predominantly on the SVPWM control techniques outlined in Chapter 2. Whilst these studies go into great detail the methods for simulating the control techniques in question, the overall drive system considerations are generally under-described. Often these models are also based on many "ideal" considerations and fail to recognise common DSP associated failings; linearization and the size of DSP architecture are often overlooked in such simulations. Often the engineer will require simulation results for multiple machines and for varying control techniques (the motivations for this have been described in Chapter 2). Given these considerations there is a demand for a generalised simulation model which takes into consideration the system architecture as described in Figure 2-3.

The Adadpted Solutions/Portunus [124] simulation software environment offers an alternative option for the development of synchronous machine drive models. Portunus software is capable of simulating systems containing electrical, mechanical and magnetic components in a singular model; these capabilities are ideally suited for the modelling of the synchronous machine test system. Using this simulation tool a complex and in-depth simulation model of the generalised PMSM test bench (wye connection only) has been developed, addressing each of the key components of the system.

4.2. The PMSM test bench – Overall System Model.

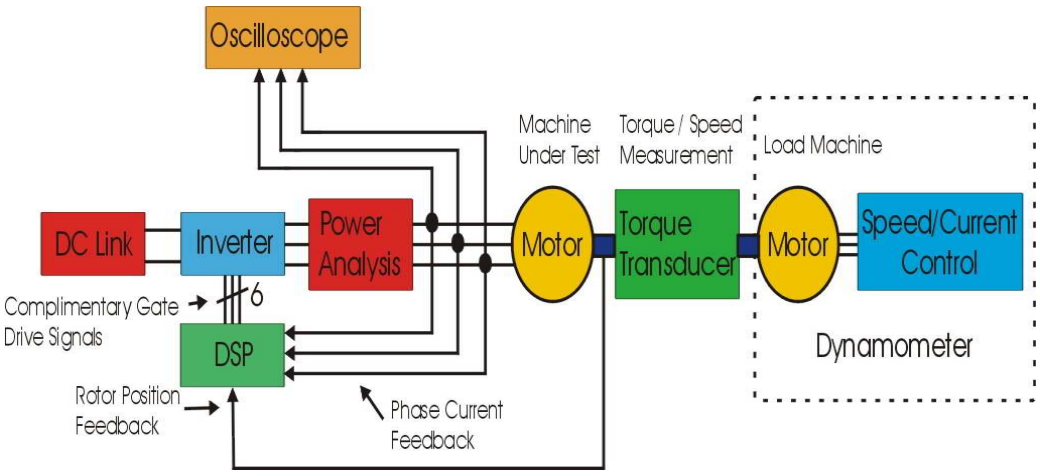

Figure 4-1: PMSM test bench diagram

Consider again the PMSM test bench diagram given in Figure 4-1 which highlights the key components of the test system which has been developed in this study. The components which are key to a thorough simulation model are:

- DC Link

- Inverter
- DSP Controller
- Motor
- Dynamometer

Considering the role of the DC link, this is not a difficult component to model given the minor role it plays in the system. In a simulation model it is simply included numerically as a constant. The inverter is a more complex component of the model and is dependant upon its semiconductor switch and diode component characteristics. The DSP controller is by far the most complex component of the simulation model. In this particular system the DSP component is based upon the SPEED laboratory FCIV controller. The control algorithms and online estimation techniques described in Chapter 2 and Chapter 3 are implemented on C coded software. Consideration of the effects of 32-bit fixed point architecture and the use of specific built-in motor control peripherals of the tms320 DSP technology of the FCIV must be taken into consideration in the model simulation. Indeed to be thorough the specific functions and processes of the software should be matched as closely as possible. The model of the motor is another complex model component which combines electrical, electromagnetic and rotational considerations. A number of considerations such as phase resistances, synchronous inductances, magnetic flux-linkage and pole number must be addressed in the motor component, as are output parameters such as rotor position and torque output. In a similar manner to the motor, the dynamometer model is also a complex component of the simulation model. The considerations of the motor type of the dynamometer are not of relevance in respect to its function within the system; to rotate the motor under test under constant speed or constant torque control.

Equipment such as power analysis, oscilloscope or the torque transducer are inherently provided within the simulation software's own analysis tools. Feedback signals such as the rotor position (obtained through the use of an encoder device) and phase currents (obtained through the use of hall-effect current sensors) do not require measurement components in simulations. These signals can simply be referenced thanks to the signal handling capabilities of the simulation software.

4.3. DC Link and Inverter Model components

In the Portunus simulation software, there is a number of pre-existing electrical components which can be placed upon the model design sheet. These can be used to implement both the DC link and VSI components of the system model thus simplifying the modelling process.

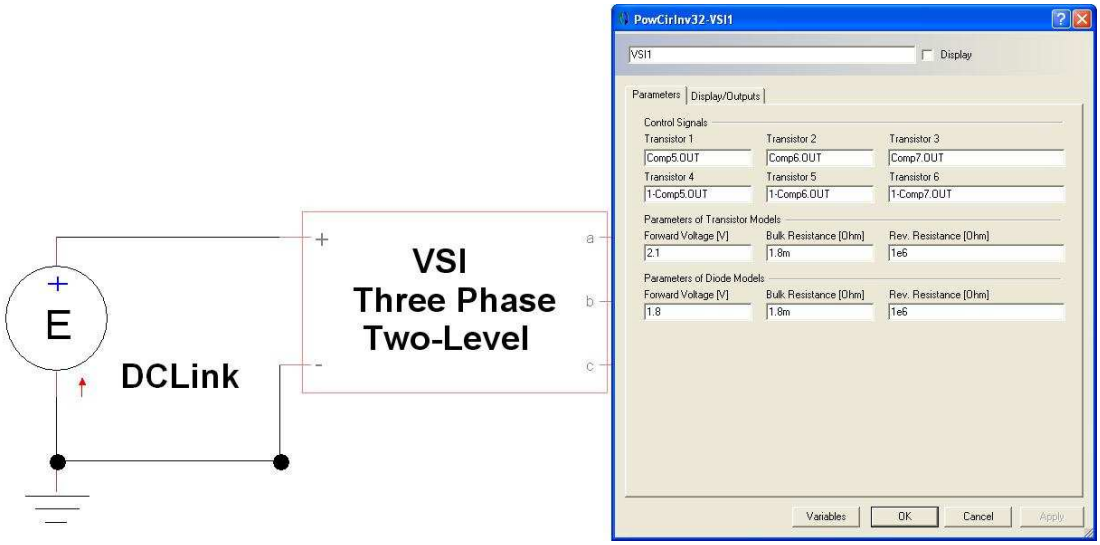

Figure 4-2: Portunus Model Design sheet highlighting DC link and VSI

Figure 4-2 is a screen capture of the Portunus model design sheet focussing on the DC link and Inverter modules used to simulate the equivalent components in the actual test system. The DC link component is a DC voltage source which has a magnitude set by a control variable. This simple implementation is a valid representation of the component which simply supplies a DC voltage supply to the VSI. The VSI model is implemented using the Portunus Inverter 3/2 circuit component. This component is a power electronics, AC/DC converter component which is available in the Portunus component library. Figure 4-2 highlights the parameter sheet for this module, allowing the user to specify the control signals (which come from other components of the design sheet) for each of the six transistors which form the inverter bridge circuit. In addition to this the transistor and diode characteristics can be input to reflect the IGBT devices which are used in the actual VSI. In the case of this study the VSI device implemented is constructed using EUPEC BSM100GD120DLC half bridge modules; the characteristics of which are inserted in the simulation component parameters.

Modelling the DC link and VSI in this manner adds a useful flexibility to the simulation model. Through use of a DC link control variable, any magnitude of flexible DC link voltage can be easily accommodated. Additionally the ability to specify the device

parameters of the VSI module allows the simulation model to be easily adapted to take into consideration alternative VSI switch devices.

4.4. DSP Controller – FCIV

As has been stated previously, the FCIV model is the most complex component of the test bench simulation model. Obviously the Portunus software is not distributed with an exiting FCIV model in place; a custom designed model is necessary to fulfil the role within the simulation model. The Portunus simulation software allows for custom C++ made models to be inserted into model design sheets and this is the method by which the FCIV can be included.

4.4.1. FCIV Inputs/Outputs

Perhaps the best place to begin in the description of this model is to consider the input variables and signals required by the FCIV. These can be split into two categories:

- Feedback Signals (phase currents and rotor position) – these are parameters required by the FCIV specifically for the current control process. They vary with respect to time.
- Operating Parameters (pole number, reference current etc) – these are parameters required by the FCIV potentially for use in the current control process but possibly only for online estimation techniques. They are typically constant with respect to time.

In the design of the FCIV these parameters must be included. The feedback signals and operating parameters can be input to the model in the same manner due to the architecture of the C++ model.

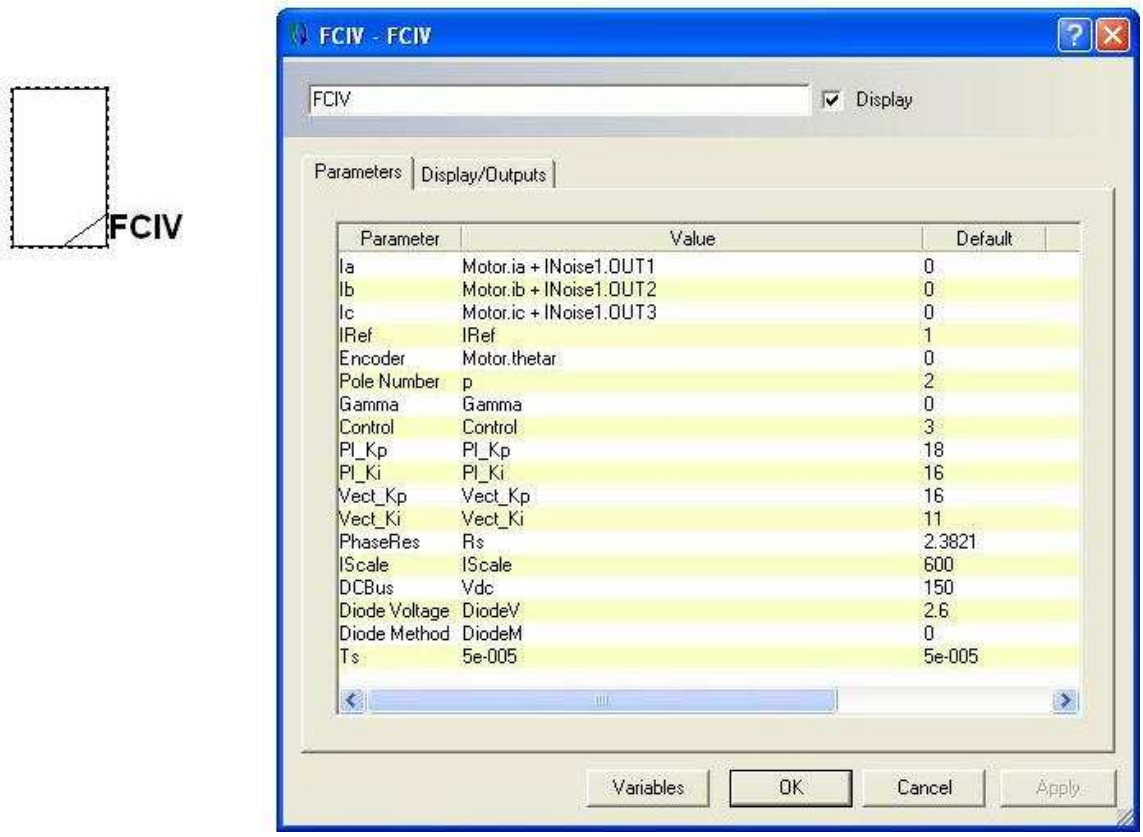

Figure 4-3: FCIV model component with input parameters

Figure 4-3 shows the input parameter sheet of the FCIV C++ component as is it accessed via the Portunus design sheet.

- **Feedback signals**
  - Ia, Ib and Ic are the input phase currents that would be measured via current sensors in the real drive system.
  - Encoder is the name of the signal which is used to input the rotor position of the motor under control.
- **Operating Parameters**
  - IRef is the reference current peak value
  - Pole number is the number of poles in the motor being controlled. The FCIV requires this information to correctly reconstruct the reference current wave upon which the regulators act.
  - Gamma is the Gamma advance angle used to simulate tests which apply field weakening.
  - PI_Kp, PI_Ki,Vect_Kp and Vect_Ki are the PI loop control gains for the stationary PI control technique and the SVPWM control technique respectively.

- PhaseRes is the resistance measured across a single phase of the motor being simulated. This is often supplied by the motor manufacturer; it is also very easily measured when this information is not provided.
- IScale refers to scale at which the Analogue-to-Digital converter (ADC) of the FCIV converts the current sensor feedback signals to a digital representation. In the case of the FCIV the ADC has 12-bits available for conversion giving a range of 0 – 4096 to represent the phase current. Given the AC nature of the current wave this range is set to return a count of 2048 at a 0A reading and thus $\pm I_{PK}$ must be represented in the range ±2048. Owing to the construction of the FCIV, it is possible for the user to calibrate a digital value per amp for use in current conversion; this is the variable IScale and accurate knowledge of it is required for accurate current control. Typical values are 300/A for the Heidenhain machine, 900/A for the interoll machine and 600/A for the SEM machine.
- DCBus is simply the value of the DC link voltage; it is not used in any of the control processes but is required in online voltage estimations.
- DiodeV and DiodeM refer to the magnitude of the diode voltage losses and the application of these losses respectively. This allows the FCIV simulation model to contrast the online estimations outlined in Chapter 3 with or without the voltage losses described therein. Being able to modify DiodeV means that integration of new IGBT technology in the actual VSI component can be mirrored in the simulation model.
- Ts is a timing parameter which determines the simulation model frequency. The FCIV operates on a 50µs interrupt which carries out its main loop (including control algorithms). The FCIV itself however operates on a much higher processor frequency, the setting of the period of the interrupt dictates the switching frequency the controller operates (e.g. 50µs = 20kHz). Ts is essentially the simulation equivalent of this switch period variable, it can be set to dictate any desired switching frequency.

Given this greater understanding of the input requirements of the FCIV, some consideration of the required outputs of the FCIV is also required. Upon review of Figure 4-3 it is clearly indicated that the primary control operation of the FCIV is to generate the gate drive signals required by the VSI for use by the inverter. These are three phase complimentary pair gate drive signals which each individually control one of the six switch

devices which make up the VSI. In addition to these outputs however, there are the estimated parameters outlined in Chapter 3. The benefit of simulating a drive system in this manner is the ability to observe the operations of each of the components of the overall system in great detail. With this in mind there are in fact a great number of outputs of the FCIV C++ model which are included in order to allow the user an opportunity to observe the different stages of the control and estimations processes. The details of these output parameters is best left for inclusion during the description of the model construction.

4.4.2. FCIV C++ Model Architecture

The architecture of the FCIV C++ model is very closely aligned with that of the software loop described in Chapter 2.

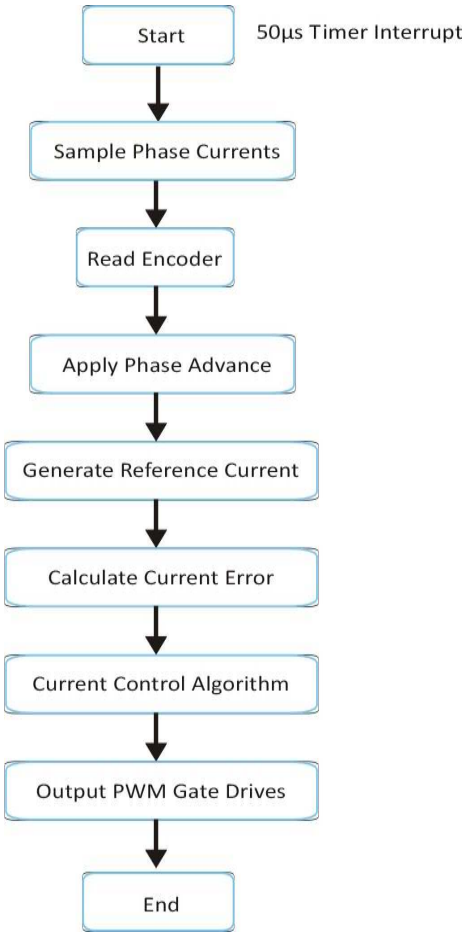

Figure 4-4: Block Diagram representing actual FCIV software architecture

Figure 4-4 shows a block diagram representation of the software architecture of the FCIV. In many respects the C++ model shares this architecture, there are however a number of differences to be discussed.

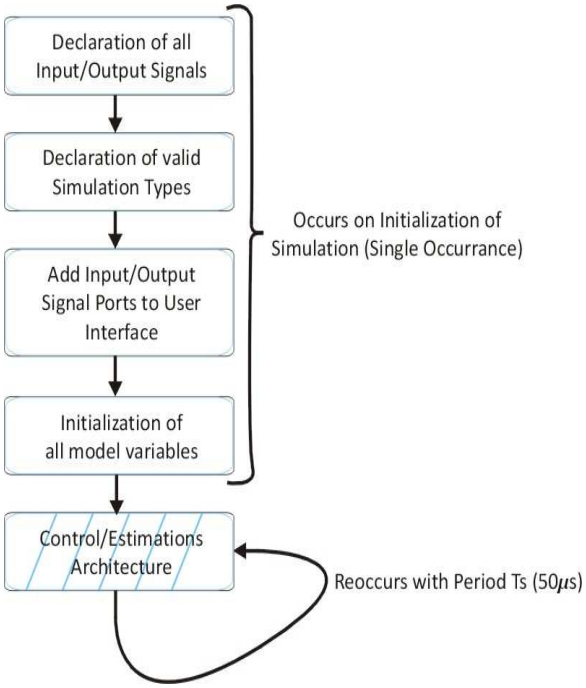

Figure 4-5: FCIV C++ Model Architecture

Figure 4-5 shows the overall C++ model architecture. The initialisation steps outlined are specific to the C++ model construction; these are responsible for the creation of the Portunus component interface and ensuring that the model is valid for the type of simulation being run. Portunus allows for four different simulation types; these are Steady State Analysis, Operating Point Analysis, Transient Analysis and Frequency Domain Analysis. The simulations developed in this study operate in Transient Analysis. The initialisation sequence also contains routines which initialise the model variables; this is similar to the initialisation process of the actual FCIV (not mentioned in Chapter 2). The control and estimation routines repeat every 50μs (Ts) and require a separate flow diagram to describe their architecture.

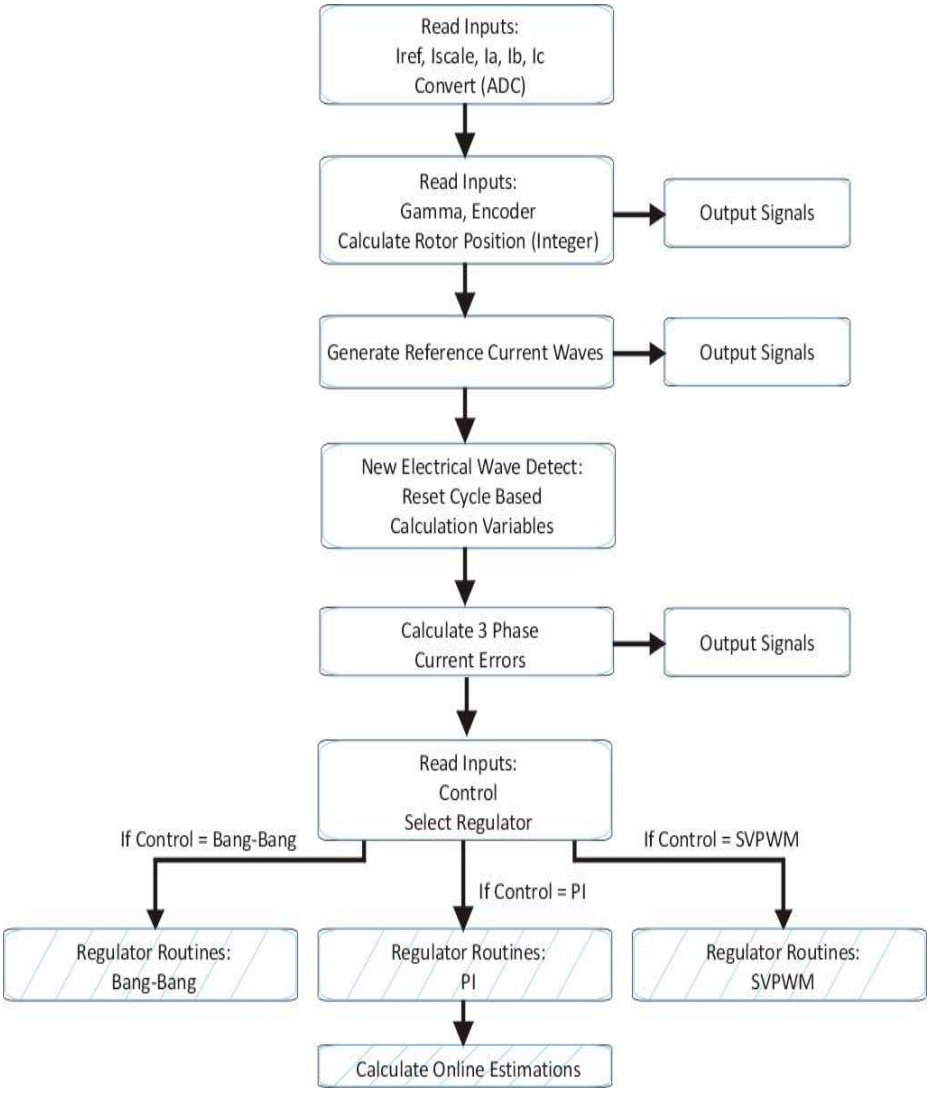

Figure 4-6: Architecture of Control/Estimations Block of FCIV C++ Model

Figure 4-6 shows a more detailed view of the Control/Estimations block described in Figure 4-6. The process begins with the FCIV reading the state of the Iref, Iscale and 3 phase current input (Ia, Ib and Ic) signals. The Iref signal, Ia, Ib and Ic signals are all input as decimal values; IScale is input as an integer. The model must then manipulate these inputs in order to represent the three phase currents in the manner outlined in section 4.4.1 which replicates the fixed point integer operation of the FCIV.

Following this the Gamma and Encoder input signals are read. The Gamma signal is input in degrees as an integer number; the Encoder signal is input in radians as a decimal value. The encoder value is first converted to a 0 – 4096 integer value representative of the rotor position counter within the DSP which is clocked by the 1024 line incremental encoder; the gamma advance is also converted in this manner. The combination of the rotor position and the gamma give the electrical angle at which the phase A reference

current waves should reside (120° spatial separation is present in the three phases). This integer value is then made available as an output in order for it to be verifiable during simulation of the system; it is a value of interest since the generation of the reference current waves is based upon it.

The next step in the process is to make use of the rotor position (plus gamma) angle in order to generate the reference current value. This angle (having been manipulated to be represented in integer range 0 – 2047) is used to access a wave lookup table of length 2048 which contains values representative of a single sinusoidal wave. The magnitude of the lookup table wave value is then scaled such that it has a magnitude equal to its equivalent value in a wave of magnitude Iref. The three phase reference currents are then output for access during simulation so that they may be verified, they also (naturally) are used as a reference signal against which the regulated currents can be verified during simulation.

Following this step a routine which is used to detect a new electrical cycle is carried out. The vast majority of cycles see this routine doing nothing, however when it detects a new cycle it is responsible for resetting the variables used in the calculation of cycle based estimations such as the flux or torque values.

The next stage of the process is to calculate the three phase current errors which may be used by either the Bang-Bang or PI controllers; these errors are output to allow them to be validated but to also then allow for validation of controller response. The next stage of the process is to read the control input signal; its result determines which of the control algorithms are then active.

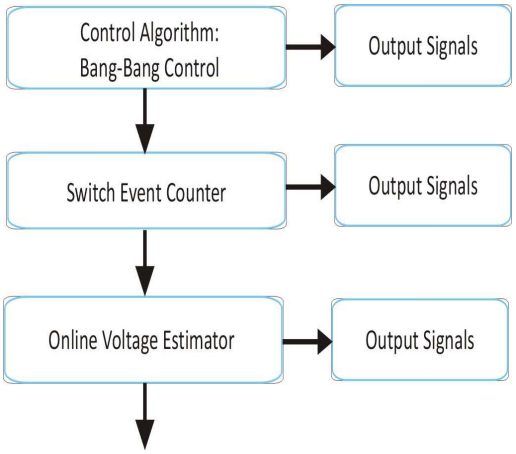

Figure 4-7: Architecture of Bang-Bang Block of FCIV C++ Model

Figure 4-7 shows the block representation of the Bang-Bang control path of the FCIV C++ model. The first step is to calculate the Bang-Bang regulator response with respect to the phase current errors calculated (see Figure 4-6). The control algorithm is outlined in greater detail in Chapter 2. The control algorithm outputs the three phase duty cycle values (0% or 100%); these are in integer format and lie in the same integer range that the actual FCIV uses. These are output not only for validation of the regulator but also for use in the generation of the inverter drive signals; this process will be described in greater detail. Following the Bang-Bang control algorithms and outputs a routine which detects a switch in output state per phase is carried out. This routine is responsible for the calculation of the average number of switch events per electrical cycle; in the Bang-Bang controller this is used to provide a measure of the average switch frequency since this is not fixed. The results of this process are output for capture that they may be compared to the real life measurements presented in Chapter 2.

The final part of the Bang-Bang control algorithm is the online voltage estimator; the estimation process is outlined in greater detail in Chapter 3 but never for the Bang-Bang control strategy. However with the availablility of this new simulation model, techniques have been tentatively explored for estimating the average phase voltage when running the Bang-Bang controller – the results of these are presented in Chapter 5. In the previously referenced publication by Cossar [1], the average voltage estimator is said to be valid for any PWM regulation technique. In consideration of the Bang-Bang controller described in this study, this is shown be true. The Bang-Bang controller described in Chapter 2 is an example of an independent phase controller also. However, it is described as non linear due to the nature of the commanded duty cycles outputted by the Bang-Bang control algorithm. The output duty cycles have only two states – 100% (fully on) or 0% (fully off). The Bang-Bang controller implemented in this study makes use of the same triangle comparison PWM generation technique which is demonstrated in Figure 3-2 and described in detail in section 3.2.1. Thus for a 0% duty cycle the T_{DUTY} value will simply be equal to T_{PWM} and for 100% it will be equal to 0. Consider the case when phase A = 100%, phase B = 0% and phase C = 100% (T_{DUTYA} = 0; T_{DUTYB} = T_{PWM}; T_{DUTYC} = 0). Using the methods outlined in TABLE 3-3 suggests that both configuration 3 and 4 will be applicable in this case. Selecting configuration 3 results in t_1 = 0 and t_2 = T_{PWM}. This results in a resultant phase voltage given as:

$$V_{ph} = \frac{V_{DC}}{3\tau_{sw}}(T_{PWM}) \tag{1}$$

Equation (1) can be simplified; as explained previously $T_{PWM} = \tau_{sw}$, thus the average phase voltage for this scenario is given as:

$$V_{ph} = \frac{1}{3} V_{DC} \tag{2}$$

Equation (2) gives the resultant phase voltage estimate for the scenario described. If we consider phase A = 100%, phase B = 0% and phase C = 100% can be expressed as 101 or V_5 then upon consultation with TABLE 3-2 it can be seen that this estimate is accurate. Equation (2) would also have been reached had configuration 4 been applied to this consideration and in fact given that the Bang-Bang controller will only ever command V_0 – V_7 in any given control cycle a new table equating the potential outputs to the configurations in TABLE 3-3 can be constructed.

TABLE 4-1: Average Phase Voltage during control cycle under Bang-Bang control

Phase A	Phase B	Phase C	Voltage Vector	Valid Configurations	Resultant Phase Voltage
0	0	0	V_0	1 – 6	$V_{ph} = 0$
0	0	1	V_1	1 + 3	$V_{ph} = -\frac{1}{3} V_{DC}$
0	1	0	V_2	2 + 5	$V_{ph} = -\frac{1}{3} V_{DC}$
0	1	1	V_3	1 + 2	$V_{ph} = -\frac{2}{3} V_{DC}$
1	0	0	V_4	4 + 6	$V_{ph} = \frac{2}{3} V_{DC}$
1	0	1	V_5	3 + 4	$V_{ph} = \frac{1}{3} V_{DC}$
1	1	0	V_6	5 + 6	$V_{ph} = \frac{1}{3} V_{DC}$
1	1	1	V_7	1 - 6	$V_{ph} = 0$

TABLE 4-1 contains the resultant phase voltages under Bang-Bang control when each potential Bang-Bang output configuration is calculated using TABLE 3-3. It should be worth noting that while TABLE 4-1 describes the estimations under Bang-Bang control, TABLE 3-3 is the method implemented in the online estimator.

This technique has not been trialled in the actual test equipment which features in Chapter 3. The simulation allows for a trial of the technique for the Bang-Bang strategy that has been unavailable with the actual test equipment

Looking back to Figure 4-7 the online voltage estimator is the final stage of the Bang-Bang architecture, however at this stage the estimate is not output, there are steps taken at later stages of the model architecture which handle this.

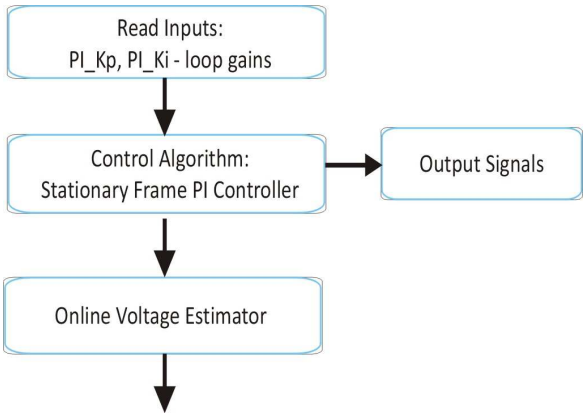

Figure 4-8: Architecture of PI Block of FCIV C++ Model

Figure 4-8 shows the block representation of the PI control path of the FCIV C++ model. The first stage of its process is to read the PI control loop gains which are input in integer format meaning that no conversion in number format is required. The next step in the process is the control algorithm (this is described in greater detail in Chapter 2). The outputs of this process are numerous; the duty cycle signals (0% - 100%) are output for both validation and gate drive signal generation. Again the duty cycle outputs are in the same integer format that the FCIV utilizes. This is an important feature as the effects of fixed point integer operation and quantisation effects due to bit-length of the DSP are taken into consideration in the simulations. Also the critical algorithm parameters such as previous cycle current errors and duty cycles are output for use in validating the regulator. The PI controller architecture also ends with the online voltage estimator outlined in Chapter 3. Once again the resultant phase voltage estimate is not made available as an output at this stage.

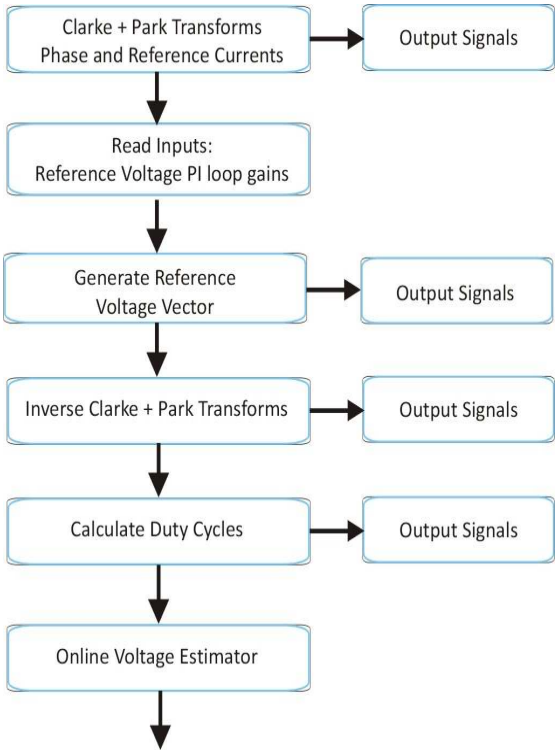

Figure 4-9: Architecture of SVPWM Block of FCIV C++ Model

Figure 4-9 shows the block representation of the SVPWM component architecture. Given the more complex nature of the SVPWM control process, it is worth developing the blocks in a little more detail than in the previous two examples. A detailed description of the SVPWM control algorithm is provided in Chapter 2. The process begins with the Clarke and Park transforms which act upon the previously measured phase currents and predetermined reference currents. This process then makes the resultant (2-axis, rotating frame) and intermediate (2-axis, stationary frame) currents and reference currents available as outputs for validation. This is followed by the reading of the control loop gains Vect_Kp and Vect_Ki which are used in regulation of both reference voltage vector components (V_q & V_d). The regulation routines for both synchronous voltage components are then carried out and this process makes a wealth of information available for output. In addition to the Vq and Vd components, the previous cycles synchronous current errors and output voltage components are made available. Outputting all of this information allows the regulators to be validated and as always the process also allows for investigation of the effects of quantisation experienced in the DSP. Following this the Inverse Clarke and Park transforms occur making the reference voltage vector available in the stationary frame in both the 2-axis representation and the three phase representation. The process for calculating the duty cycle commands is then carried out; this also makes a number of parameters available as outputs. The timing

vectors and the two adjacent voltage vectors which are usually used to generate the gate drive signals (see Chapter 2) are made available as is the present hexagon sector; these allow for validation of the control process. In addition to these parameters, the three phase duty cycles derived using the process outlined in Chapter 3 are also output; these are made available for use in the generation of the gate drive signals and for further validation. Following this the online voltage estimator outlined in Chapter 3 is carried out; once again the resultant estimation is not made available for output at this stage.

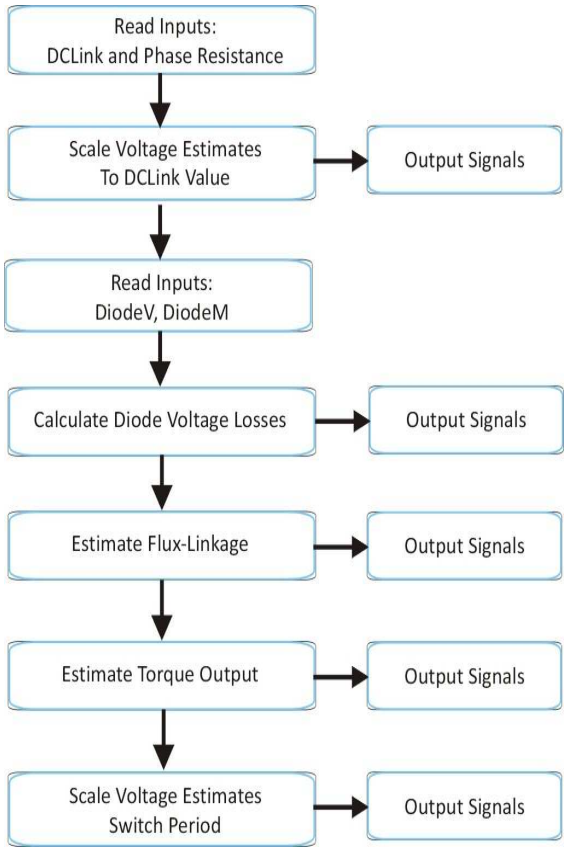

Figure 4-10: Architecture of Estimations Block of FCIV C++ Model

The final stage of the FCIV Control/Estimations architecture is the estimations process which is outlined in Figure 4-10. It begins by first reading the phase resistance input and converting it to the integer format that the DSP architecture operates with. The DC Link voltage is input as an integer value and requires no reformatting. Following this the estimated average phase voltage (which was calculated during which ever control process has been followed) is scaled with respect to the applied DC Link voltage and wiring configuration (simulations are developed for the wye connected scenario only). The voltage estimates are output prior to this scaling and also following; this allows for validation of the estimates and the scaling process. Following this stage the diode voltage magnitude and the control signal for its application (DiodeV and DiodeM respectively) are

read. This allows for the estimation of the voltage losses as a result of the freewheel diodes; it is important that the value DiodeV matches the value inserted in the panel give in Figure 4-2. This would represent an accurate consideration of the diode voltage losses contributed to the simulation results from the inverter module of the model. Upon completion of the diode related loss calculations, the model then outputs the time interval for which the losses are applied, the magnitude of diode losses applied and the adjusted voltage estimates (previous estimates minus the losses calculated). These outputs are for validation purposes, they are not compared against measured results. Following this process the voltage estimates are used in the calculation of the flux-linkage which is then made available as an output which can be used for both validation but also for comparison with measured results. The torque output estimates are then carried out; the intermediate calculations involved in these estimations are made available as outputs alongside the final output torque estimation. This allows for the various parameters of the final calculation to be validated in addition to the final estimation being compared to measurements from the actual FCIV. A more detailed description of the online estimation techniques is available in Chapter 3.

4.5. Symmetrical PWM Gate Drive Generation

The FCIV makes use of symmetrical PWM gate drive signals (complimentary pairs) in order drive the VSI switch devices thus regulating the current in the inverter (this process is described in greater detail for the PI and SVPWM techniques in Chapter 3). The FCIV generates these PWM waves using a hardware peripheral which carries out the wave generation during the 50µs period between control cycles; acting upon the duty cycle values calculated during the previous control cycle. Therefore in order to simulate this process accurately the gate drive generation must be conducted using design sheet components which are external to the FCIV C++ module and that operate at the time step of the overall simulation itself instead of the 50µs FCIV cycle period. This process is easily achieved using standard Portunus modelling components.

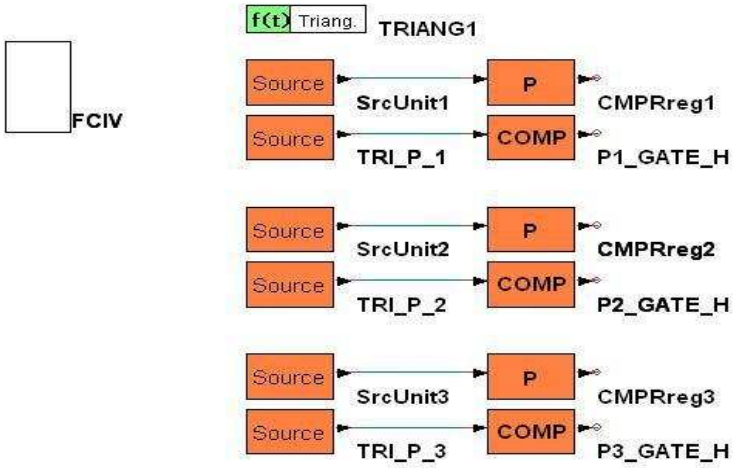

Figure 4-11: PWM Peripheral Model Components

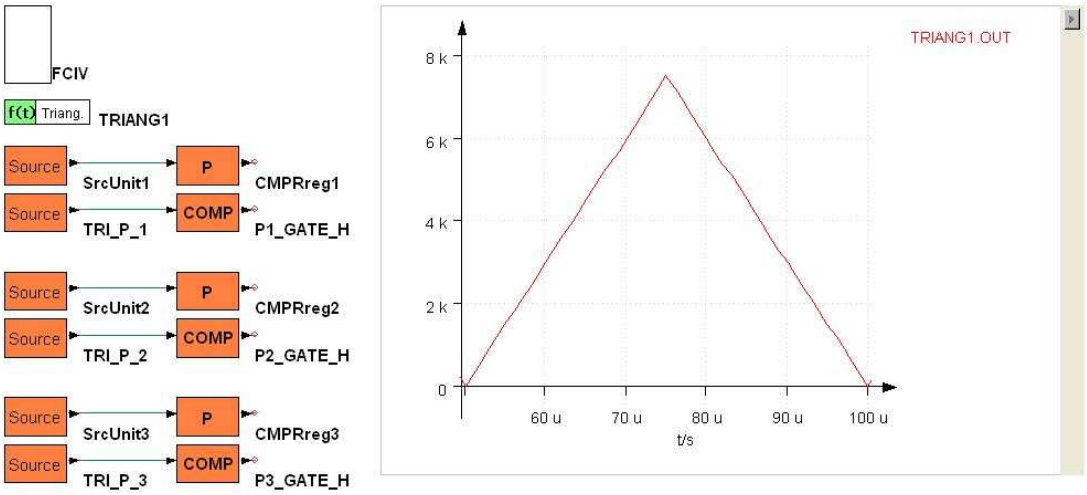

Figure 4-12: Triangular Reference Waveform used in PWM Peripheral

Figure 4-11 shows the components used to model the FCIV PWM hardware peripheral. The FCIV component is shown as it supplies the duty cycle commands which are used to generate the gate drive signals. The first part of the model to consider is the triangular wave source (labelled as TRIANG1).

Figure 4-12 shows the triangular waveform used as the reference wave against which the duty cycle outputs of the FCIV C++ model are compared in order to generate the gate drive waveforms. The wave is clearly seen to have a period of 50µs and its magnitude is equal to 7500 (which is the integer magnitude of the PWM compare register in the FCIV when the switch period is set to 50µs). To illustrate the characteristic of the reference wave, a duty cycle output from the FCIV of 3750 would result in a 50% gate drive waveform.

The process for the generation of the gate drive waveform then relies upon the network of source, gain and comparison blocks shown in Figure 4-12. In the case of phase A, SrcUnit1 feeds a unit input to the gain block CMPRreg1 which amplifies its input signal by the phase A duty cycle output of the FCIV module. Source TRI_P_1 then feeds the TRIANG1 waveform into the comparison block P1_GATE_H which compares the output of CMPRreg1 with the TRIANG1 waveform (essentially comparing the duty cycle against the reference triangle waveform); this is repeated across the three phases.

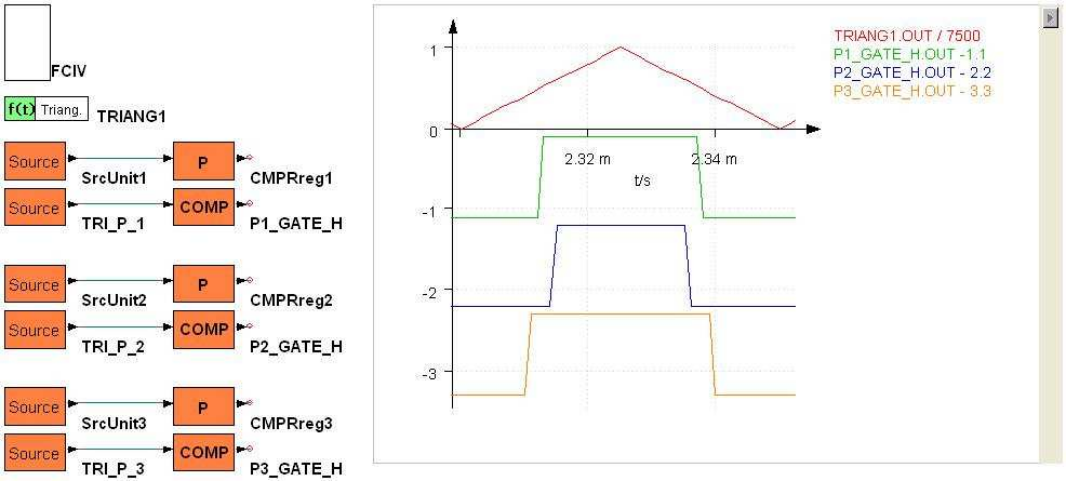

Figure 4-13: Triangular Reference Waveform and subsequent three phase drive signals under SVPWM regulation

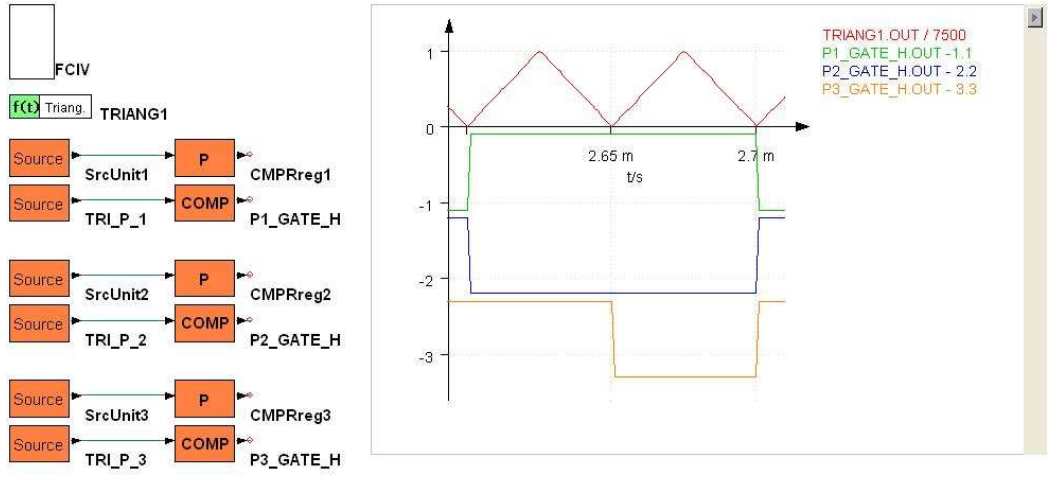

Figure 4-14: Triangular Reference Waveform and subsequent three phase drive signals under Bang-Bang regulation

Figure 4-13 shows the triangle reference waveform against the symmetrical PWM waveforms it produces (This particular example was gathered using the SVPWM controller but are representative of the waveforms which would be produced under PI control also; the SVPWM waveforms are generated using the method outlined in section 3.2.1).

Figure 4-14 is similar to Figure 4-13 however the waveforms are captured under Bang-Bang control. What is clearly demonstrated is that the output state during each cycle is continuously held at either high (100%) or low (0%). In this particular case it is shown that in phase A and B there is no requirement for the gate drive signal to switch, however this is required in phase C. This is a perfect example of the unpredictable nature of the Bang-Bang control.

4.6. The Motor model

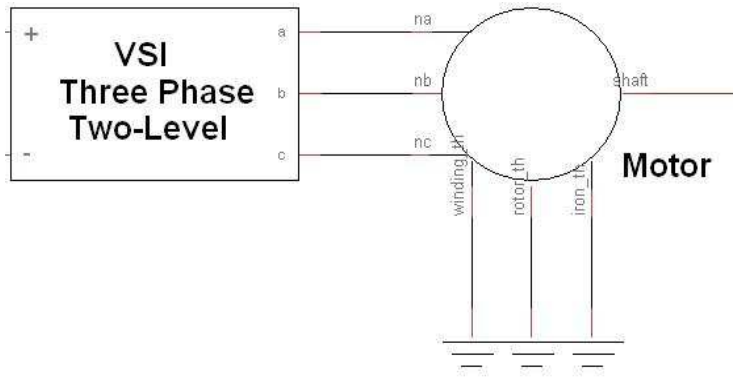

Figure 4-15: VHDL-AMS Motor Model used in Portunus Models

The simulation model being presented here makes use of a machine model supplied by Dr Mircea Popescu of Motor Design Ltd [2]. The model has been developed in VHDL-AMS which is another model development tool which Portunus makes available. This capability of Portunus allows for a complex mixed signal model representing a wye connected synchronous machine to be developed. There are many input parameters required by this motor model as its uses are not restricted to the electrical/mechanical performance of the machine; it is also implemented in simulations which simulate the thermal properties of such a system. In the context of the study being presented, the following input parameters are of interest:

- Phase Resistance – this parameter is required by the model for use in its synchronous voltages and loss calculations. This value is often available via the faceplate fitted to the motor and is easily measured when not provided.
- d-q axis reactances [ohms] – these parameters are required by the model as they are used to recreate equivalent circuits upon which the performance of the machine is based. These values can typically be obtained through the use of FEA software such as PC-BDC; measurement techniques such as those described in the author's publication [106] can also be used.

- Flux-Linkage due to permanent magnets – this parameter is used in the calculation of the torque output, specifically the magnet related torque contribution. It can be obtained via software such as PC-BDC and also through integration of the open circuit back EMF waveform of the machine (this was described in Chapter 3).
- Pole Number – this parameter is required in various different calculations carried out within the motor model. These calculations include the electromagnetic, permanent magnet and reluctance torque calculations. The Pole Number is an essential machine parameter and usually available via a faceplate or manufacturers documentation. It is easily determined if necessary through observation of the open circuit back-EMF.
- Rotor Inertia – this parameter is also used in the final torque calculations made by the model. It is obtained through the use of FEA software such as PC-BDC using models of the machine.

There are three output parameters of the machine model which are of interest to the study presented in this research; these are as follows:

- Speed – the speed is not controlled by the motor model itself and is in fact determined by the machine model based on its input parameters and phase current inputs. It is required by the load machine module (this will be described in greater detail at a later stage) for speed control of the motor under the current control of the FCIV.
- Rotor position – this is output by the motor model in radians. It is the simulation equivalent of the encoder feedback that is used in the actual drive system. This parameter is fed directly to the FCIV C++ module encoder input (a description of how the FCIV handles this input is given in section 4.4.2)
- Torque – this is the parameter of the motor model which is used in the validation of the overall system simulation model. The output values recorded under simulation will be compared to those measured and presented in Chapter 2 for comparison and ultimately for validation of the model. This parameter is not output in a simple integer or electrical form. The mixed signal modelling capabilities of VHDL-AMS support in Portunus allows the output torque of the machine to be transferred to a rotational torque output via a rotor shaft; this rotor shaft is crucial to the modelling of the system as it provides the means to apply a load to the motor model.

4.7. Load Module and Load Controller (Dynamometer Model)

The dynamometer component of the motor test system being described is every bit as complex as the drive system with which it is coupled. It in essence is another machine being driven by similar inverter technology which itself will be controlled using algorithms similar to those described thus far. However its application in this research determines the method with which it is modelled. The load controller is used with a speed controller in the tests that have been described in this research; this essentially means that the dynamometer adjusts the torque output on its rotor shaft (which is coupled to the rotor shaft of the motor under test) in order to maintain the reference speed value input by the user. This is the role required by the load module of the simulation; a module which adjusts the torque on the rotor shaft (which is common between the load module and motor module) in order to maintain the speed being commanded (which is input by the user).

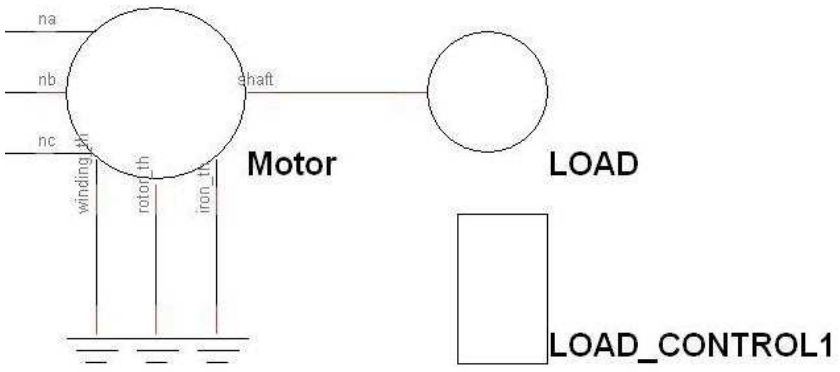

Figure 4-16: VHDL-AMS Load module with C++ Load Control Module and Motor Module Connections

The load module shown in Figure 4-16 is achieved through a combination of a custom constructed VHDL-AMS module and a separate custom constructed C++ controller module; both of these models have very small architectures in comparison to the other modules presented, this is a reflection of the simplified approach adopted in considering only the function they perform in the system. The C++ load controller module accepts 4 input parameters of importance in addition to its time period input Ts (this will not be described as it has been described in greater detail in section 4.4.2); these inputs are as follows:

- Reference Speed – this is input to the model by the user. It is read so that a speed error variable can be created within the module as part of the control process.

- Actual Speed – this parameter is taken directly from the motor itself which measures it from the rotor shaft. This variable is also required in developing the speed error upon which the load controller operated.
- PI loop gains – there are two PI gain values used by the module to regulate the speed.

The speed control loop operated is an identical PI loop to that described in Chapter 2. The output parameter is torque which is adjusted in response to changes in the speed error.

The VHDL-AMS module is very simplistic in its architecture as it fulfils a simple role. The module accepts only one input – a decimal number representing the torque in Nm. There is only one routine in its architecture which reads the torque input value (updated from the C++ load controller module) and transfers this torque to the output rotor shaft. The combination of the VHDL-AMS Load module and the C++ Load Controller module ensure the role carried out by the dynamometer system is effectively modelled. This is allows for a comparison of simulated torque output against actual torque measurements.

4.8. Validation of the FCIV C++ simulation module

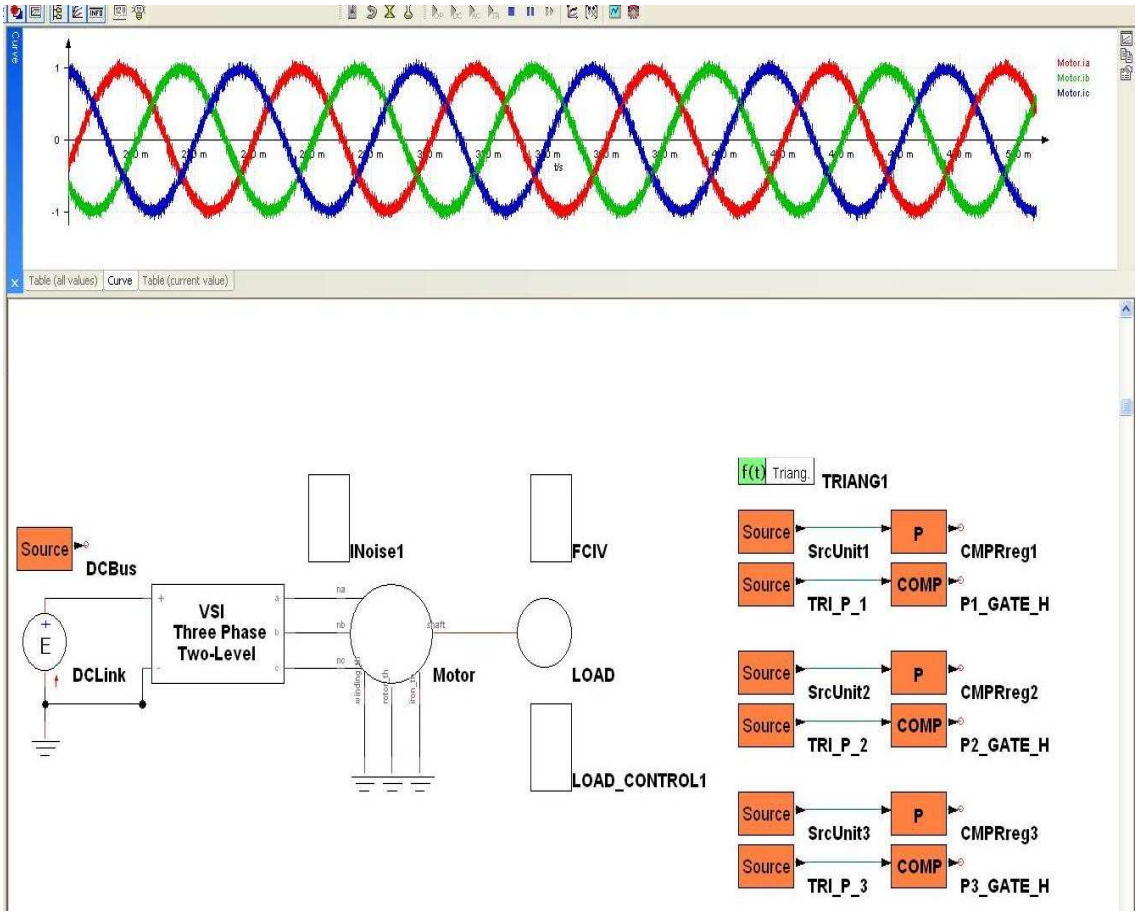

Figure 4-17: Full Portunus Simulation Model

Figure 4-17 shows a screenshot of the full motor test simulation model in the Portunus simulation environment. Before simulation predictions can be compared versus measured results, a validation of the FCIV simulation module is required. There is an extensive set of output parameters available which can be observed in order to validate correct operation.

If the control architecture outlined in Figure 4-6 is considered again, the first few stages of the process are clearly validated upon the generation of three phase reference current signals which match the magnitude of the reference current magnitude and the count per amp ratio of the variable IScale.

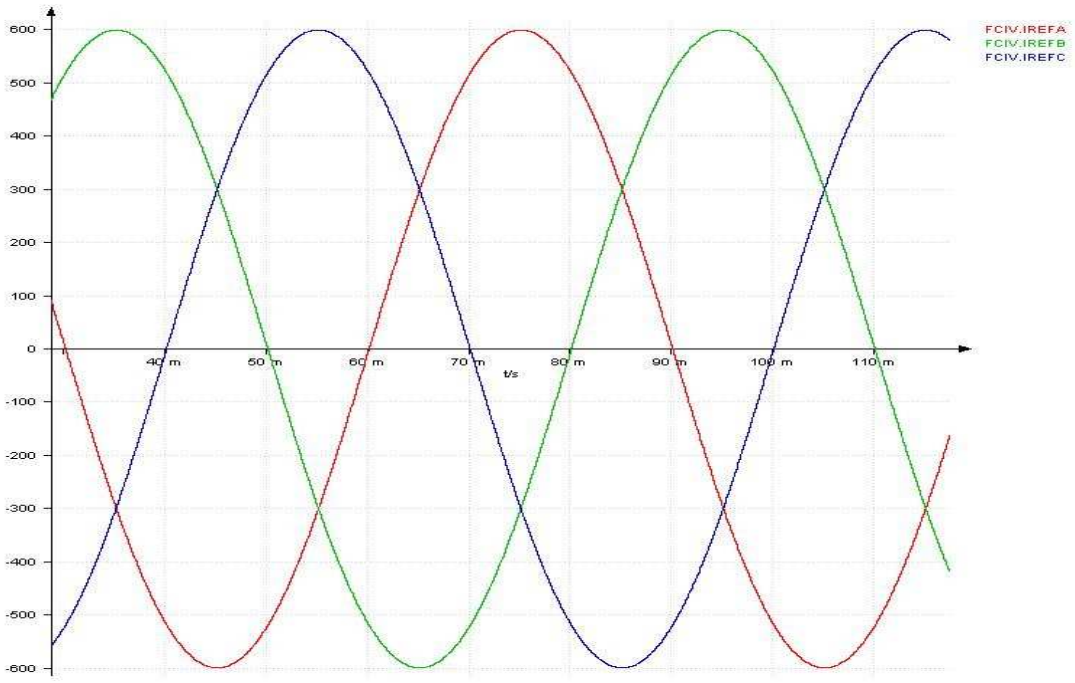

Figure 4-18: Reference Current Waves produced by FCIV C++ Simulation Model

Figure 4-18 shows the three phase reference current waves. These waves were captured under simulation of a motor which is characterised as having 4 poles, at a speed of 500rpm, a reference current of 1A and an Iscale value of 600. As a result the waveforms shown in Figure 4-18 are in the form required by the control algorithms; they have the expected magnitude (IScale * reference current), the expected 120° spatial separation and with a period of 60ms are at the frequency required by a 4 pole machine operating at 500rpm. It can also be noted that the fixed frequency of the waveforms shown indicates that the load controller and load modules are also validated as they are clearly regulating the reference speed input by the user. These waveforms validate the FCIV model up to the point of generating reference currents, but do not validate any further stage of the C++ module.

Following from the validation of the reference current waveforms, the simplest method of validating the FCIV processes is through the successful current regulation of the three phase currents in the motor module (the quality of this regulation shall be investigated in greater detail at a later stage).

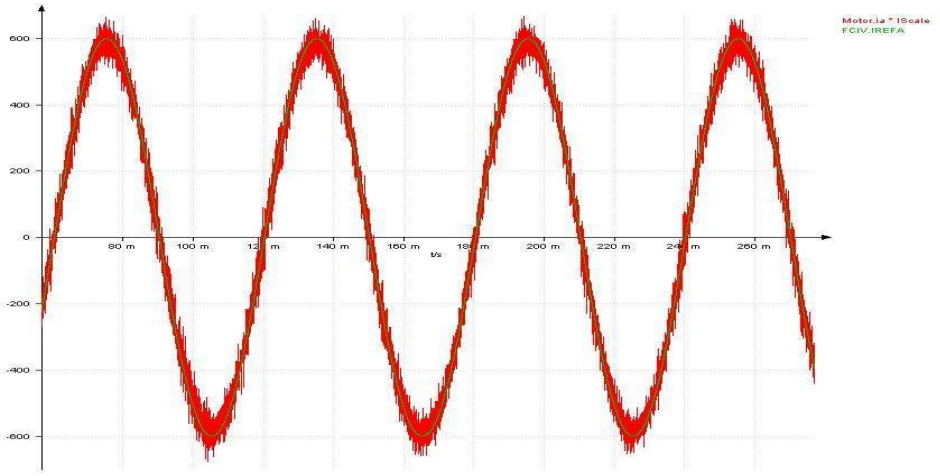

Figure 4-19: Validation of Bang-Bang control simulation

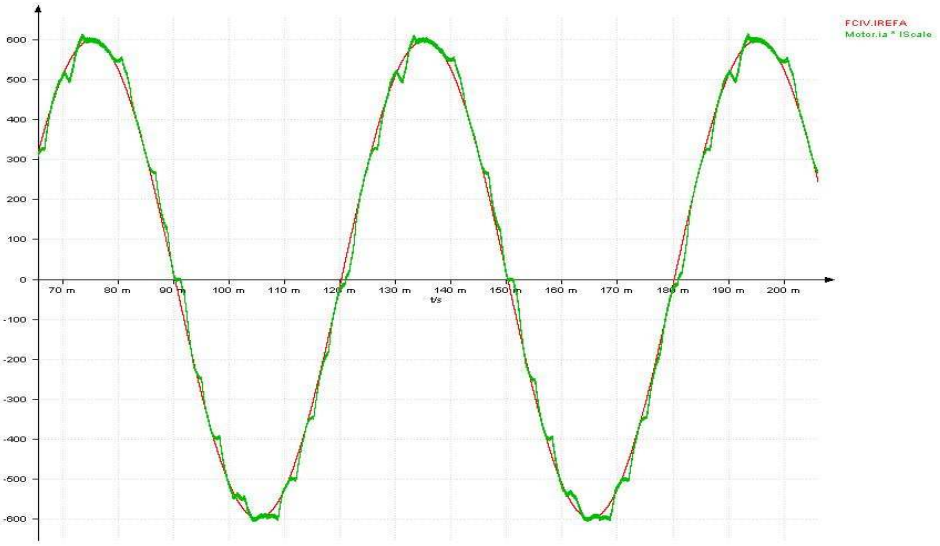

Figure 4-20: Validation of PI control simulation

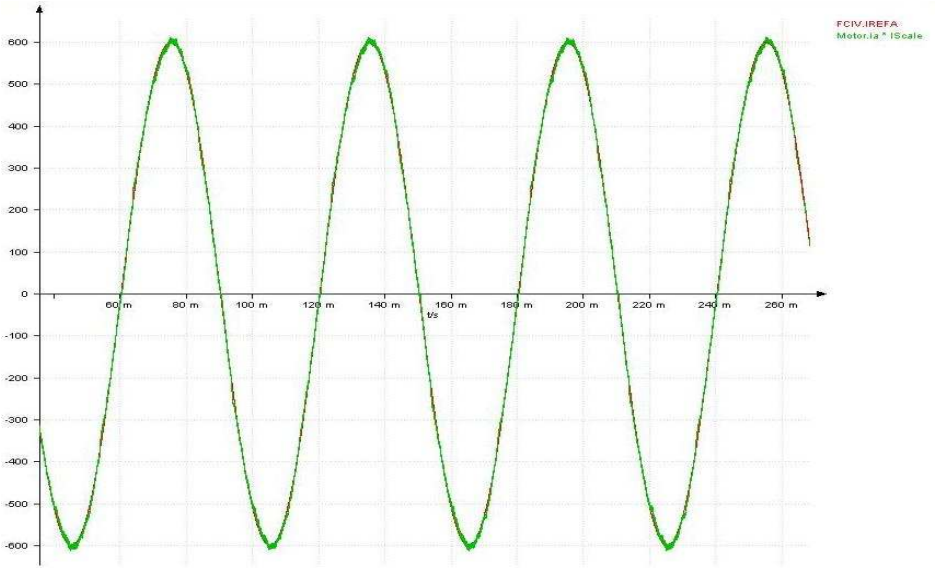

Figure 4-21: Validation of SVPWM control simulation

Consider the case when a 1A reference current is required to be regulated in the phases of the motor under test at a steady state speed of 500rpm. The FCIV C++ module is required to first generate the reference current waveforms (this has been verified). Following this the control techniques are required to respond to the measured phase current feedback in order to regulate this current to the reference value. Thus the validation of the techniques and there associated routines (and any intermediate output parameters that have been described) can be achieved through observing the current waveforms. The waveform given in Figure 4-19 clearly validates the Bang-Bang current controller, the waveform in Figure 4-20 clearly validates the PI controller and similarly Figure 4-21 validates the SVPWM controller. Each of these controllers has been validated over a range of reference current values, reference speeds and IScale factors – matching the ranges experimented with using the actual FCIV. Successful current regulation essentially validates each of the intermediate parameters that have been described as being output during the regulations processes (SVPWM has the largest number of these). Whilst they are not presented in this study; they are worth mentioning due to their highly useful presence particularly when debugging faults.

Beyond the control processes of the FCIV C++ module reside the online estimation techniques which have been described in full detail in Chapter 3. The process of validating these simulated online estimates is to make the same type of comparisons as were made when validating the actual FCIV's estimations. This is a largely results based validation and will be presented at a later stage.

4.9. Conclusions

This chapter has described the construction of a new motor test-bench simulation model. The model has been constructed using the Portunus simulation environment due to the ease with which mixed signal models can be developed, a feature which is essential in simulating the electric motor. Each component of the PMSM test bench that was outlined in Chapter 2 has been modelled in the new simulation model. The less complex components such as the DC Link and VSI have been implemented using stock model components available with Portunus; this is a reflection of the simple role which these components fulfil in the actual drive system. As is the case in the actual system, the DSP stage (the FCIV), is the most critical and complex component in the simulated system. The architecture of the custom constructed C++ FCIV model is described and

demonstrated graphically in the form of flow diagrams and the subsequent operations of each stage have been described (or referred to in the case of the control and estimation techniques). A prime focus of the model has been to ensure that the architecture of the FCIV C++ model operates with the same 32-bit fixed point arithmetic architecture in order to fully simulate the quantisation effects and resolution limitations that the actual FCIV experiences. In addition to the description of the FCIV C++ model architecture, there was also a description of how the standard simulation blocks of the Portunus package can be used to reconstruct and simulate the PWM gate drive signal generating peripheral of the DSP device. This study has not been involved in the development of the motor component used in this model; this was kindly provided for integration into this model by its original developers. A description of how this model operates has been provided and also a description of its integration into the system model; particular emphasis has to be placed upon the ability of the model to transfer a rotational torque output onto its output rotor shaft – a rotating mechanical signal which can then be acted upon by the dynamometer component. The dynamometer model component is somewhat understated in relation to the complexity of its actual system equivalent; the reasoning for this (focussing upon the role it carries out) and the resultant modelling approach taken have been described. This has allowed for a comprehensive description of the new PMSM test bench simulation model.

This chapter has addressed the validity of the custom created FCIV C++ model component up to the point of (but not including) the online estimation techniques. The approach to this validation was presented in several stages. The initialisation routines and subsequent reading of rotor position feedback, current scaling and referencing inputs is validated through successful construction of reference current waveforms. Following this the validation of each of the control techniques previously outlined is achieved by observing the resultant phase current waveforms of the motor component being regulated to match the reference current waveforms.

The original contribution of this study which has been described in this chapter is the new simulation model of the drive system upon which this research is based. The description and subsequent development of the FCIV C++ module is the most valued contribution made in this study. This component models entirely the capabilities of the FCIV motor controller technology; the main advantages of which are the flexible control options available and ease with which the user has in adapting it for use with different

configurations of PMSM. These are qualities which are also present in the equivalent model. The FCIV component is validated up to the point of its current regulation options by observing the successful regulation of the reference currents which it is also responsible for constructing. This is the method used for validating newly developed control techniques and routines with the actual FCIV and thus the validation of the equivalent model is identical.

Chapter 5
Validating the PMSM Test Bench Simulation Model

This chapter presents the validation of the simulation model outlined in Chapter 4. First an aesthetical analysis of the predicted phase currents under each of the stated control strategies is presented – the appearance of these waves and the successful regulation of the commanded currents is contrasted against measured waveforms which were presented in Chapter 2. This is followed by frequency domain analysis of these phase currents. Again this is compared to the observations made in the measured results which were previously presented. This analysis is completed with a comparison of the predicted average switching frequency of the Bang-Bang controller against the measurements previously made.

The chapter then goes on to compare the simulation model predicted torque versus speed profiles of the Interroll and SEM models with the measured results which were presented in Chapter 2. This is supplemented by considering the torque profile under field weakening and comparing the predictions against the measurements which were presented in Chapter 3. These considerations are further expanded by comparing the overall drive system input and output powers and efficiencies against the measured results presented in Chapter 2.

The chapter concludes by exploring the simulation of the online estimation techniques presented in Chapter 3. Using the SEM system model the average phase voltage estimator is simulated in the FCIV model component and the results obtained under each control strategy are compared to the values obtained from the real system which were presented in Chapter 3. This is followed by comparison of the online torque estimator and includes the modifications to the technique which implement inverter based losses in order to correct over prediction in the low speed regions.

5.1. Introduction

Chapter 4 outlined the development of the PMSM test bench simulation model in the Portunus simulation environment. There are a number of motivations for the development of such a model. Considering the motor component which is available in the simulation; during the motor design and analysis processes the key parameters of the motor (which are required by the model component) are either known as a result of the design process or can be estimated using FEA tools such as PC-BDC. This allows for simulations of the machines performance to be carried out in advance of the tests which were described in Chapter 2. Indeed many of the tests described previously can be simulated in advance of the actual tests (examples of this include sourcing torque transducer equipment which can provide the greatest resolution in the range of likely torque output). In addition to this, an initial validation of motor designs can also be explored in such a simulation model, allowing for an understanding of the expected performance characteristics. This is invaluable to the motor designer in that it can help to validate performance in which ever parameters are being targeted with any particular design. Indeed the added flexibility of the FCIV in trialling performance parameters with respect to the control strategy is also made available in the simulation thanks to the inclusion of the equivalent C++ component.

A further advantage to the use of accurate simulation models is the safe trialling of control loop gain variables. As has previously been stated, often the control loop gains of a PI control loop (in either stationary frame or as part of a synchronous variable control) are obtained through trial and error. This can, given high levels of due care and attention, be conducted with minimal risk of system damage or indeed risk to the safety of users. However this practise is far from ideal and often an engineer will be tasked with the complex duty of deriving suitable loop gains (which in truth still require trialling at some stage). The existence of an accurate system model minimises the risk to the equipment or the user as it allows for repeated trial tests in an environment which bears no consequence for error. In keeping with the notion of trialling the design of system functions or features; the ability to modify the source code of the FCIV C++ model allow for the testing of the online parameter estimation techniques described in Chapter 3. The simulation model allows the user a platform upon which to experiment with the capabilities and desirable features of the PMSM test bench.

5.2. Aesthetical (time and frequency domain) Analysis

Chapter 2 included in its performance comparisons some consideration of the aesthetical appearance of each control strategies respective current waveforms, determining from these the extent of current ripple that is present in each. The simulation has been configured to represent both the Interroll and SEM machines described previously. The results obtained from the simulation trials have been compared against the results obtained and presented in Chapter 2.

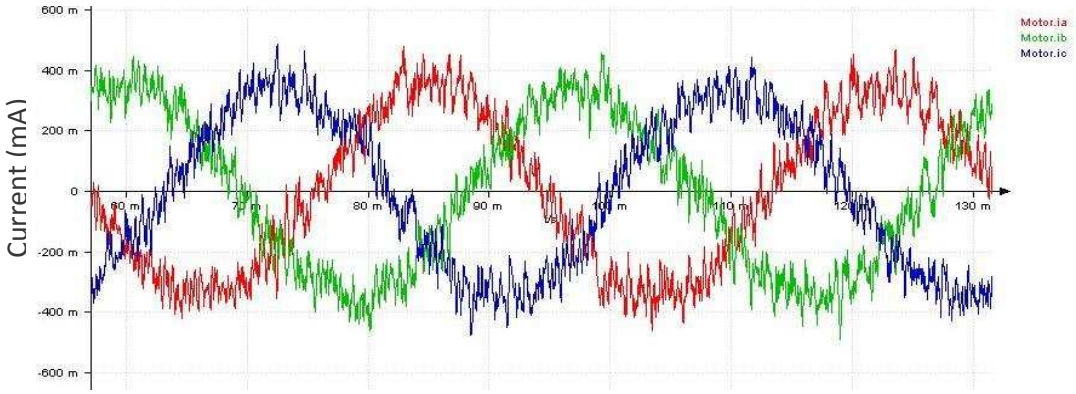

Figure 5-1: Simulated 3 phase current waveform of Interroll machine using Bang-Bang regulation operating at 400rpm, 0.4A reference current operating point.

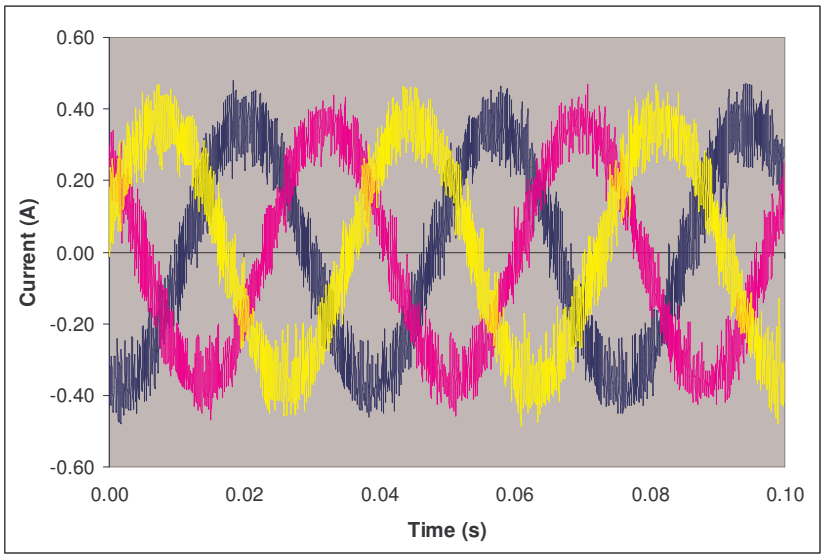

Figure 2-21: Measured 3 phase current waveform of Interroll machine using Bang-Bang regulation operating at 400rpm, 0.4A reference current. This is reproduced here to allow for easier comparison.

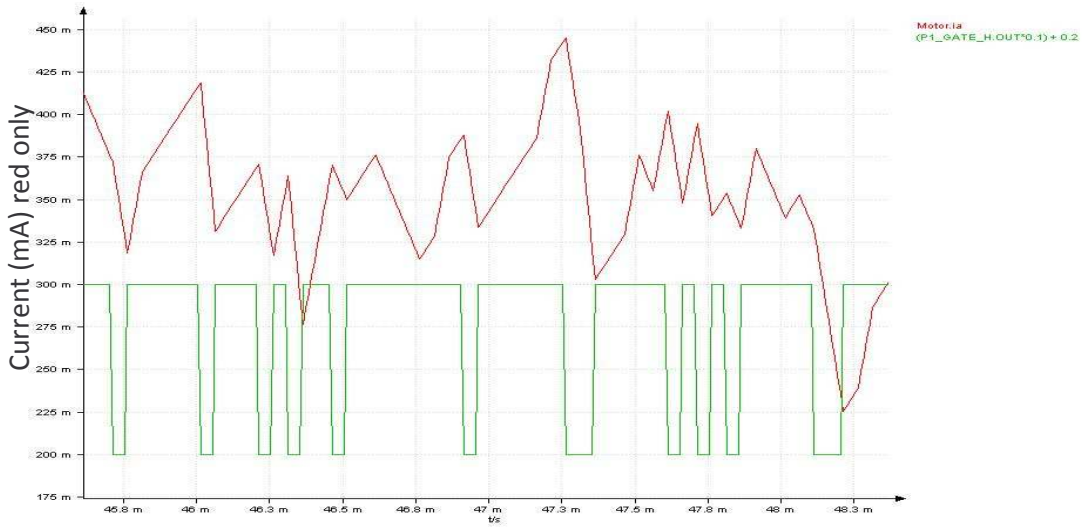

Figure 5-2: Simulated Phase A Current wave and Gate Drive Signal of Interroll machine using Bang-Bang regulation at 400rpm, 0.4A reference current

Figure 5-1 shows the resultant current signals measured on the motor component's 3 phase connections under Bang-Bang control; this is the simulated equivalent of Figure 2-21. The simulation also shows phase current signals which significantly oscillate around the reference current signal, this is typical of a Bang-Bang controlled phase current wave. The ripple observed in the simulations appears to be around 0.1A worst case whereas the measurements presented in section 2.8 indicate a ripple magnitude of more than 0.2A. Given the simulations make very little consideration of noise that may be present throughout the system, this difference is not so unreasonable; this could however have a significant bearing on other results obtained. Figure 5-2 shows a higher resolution image of the phase A current given in Figure 5-1 in addition to the phase A gate drive signal. This figure should demonstrate clearly the relationship between the switch pattern and resultant current waveform – however there are clear cases where the expected behaviour due to the gate drive signal is not apparent. In these instances (for example a negative change in current during a high gate signal) the phase interactions could be responsible for the direction of the current waveform. It also demonstrates clearly the unpredictable nature of the Bang-Bang control technique. The appearance of these figures further validates the simulation of the FCIV C++ model operating a Bang-Bang control as it conforms to the common characteristics of the strategy.

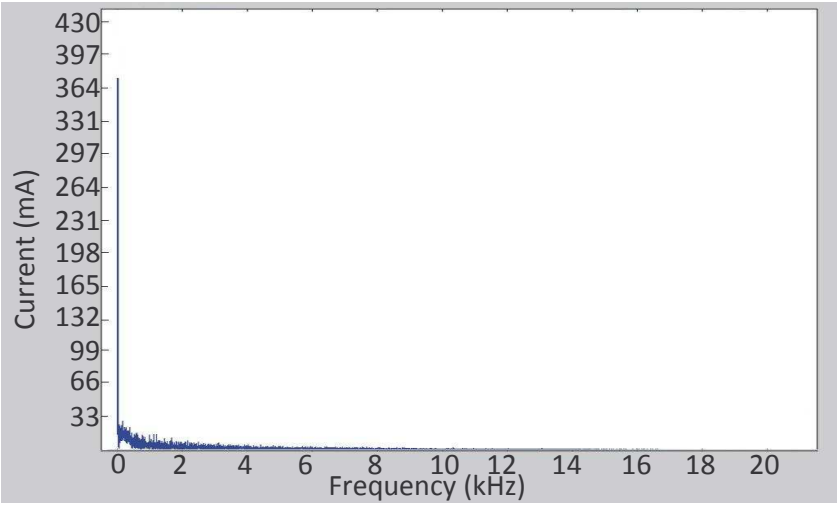

Figure 5-3: Harmonic Spectra of Simulated Interroll Machine Phase Current under Bang-Bang Control at 400rpm 0.4A Reference Current

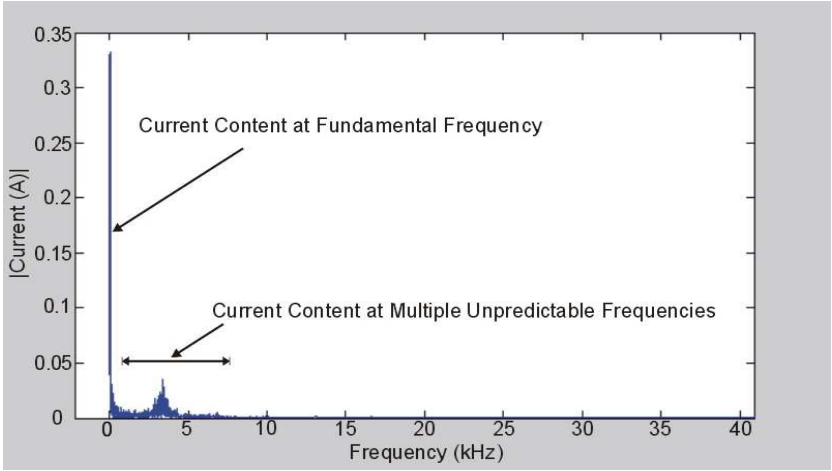

Figure 2-27: Harmonic Spectra of Interroll Machine Phase Current under Bang-Bang Control at 400rpm 0.4A Reference Current

Figure 5-3 shows the frequency domain analysis of the simulated phase current observed in the motor component. This graph is representative of the expectations of Bang-Bang control in as much as there is a relatively high magnitude of current content at a relatively random number of frequencies other than the fundamental frequency of the system (26.667Hz in this case). This is clearly associated with the unregulated current error margins and the non-fixed switching frequency of the controller. Figure 5-3 shows a general decrease in the current magnitude as the frequency increases; this is at odds with the analysis given in the equivalent presented in Figure 2-27. The actual test results indicate that there is a grouping of switch events around the 4kHz frequency. This difference doesn't allow for a further degree of validation on the simulation model, nor does it invalidate the model. It has been commented previously that the frequency analysis of the Bang-Bang controller is difficult owing to the nature of the technique; these results appear to reinforce that notion.

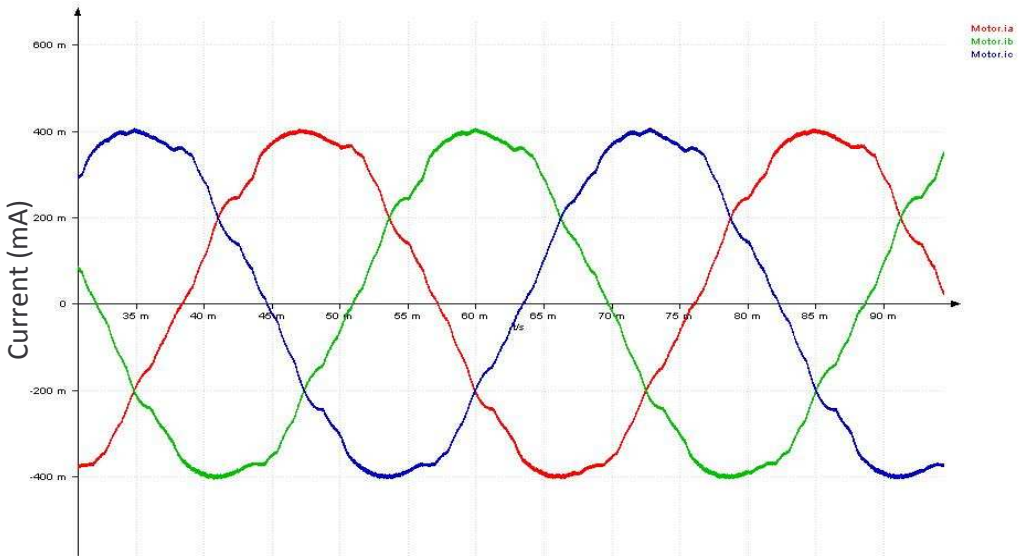

Figure 5-4: Simulated 3 phase current waveform of Interroll machine PI regulation operating at 400rpm, 0.4A reference current operating point.

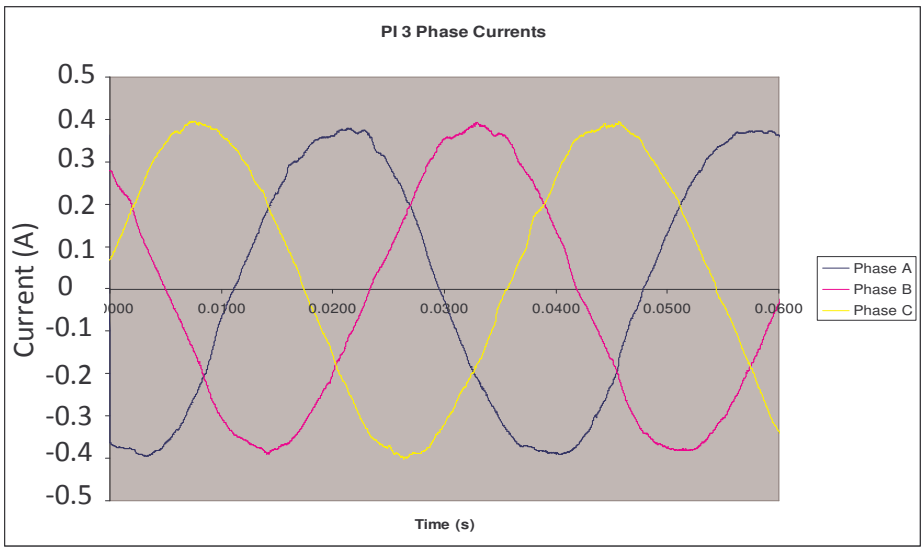

Figure 5-5:Measured 3 phase current waveform of Interroll machine PI regulation operating at 400rpm, 0.4 reference current.

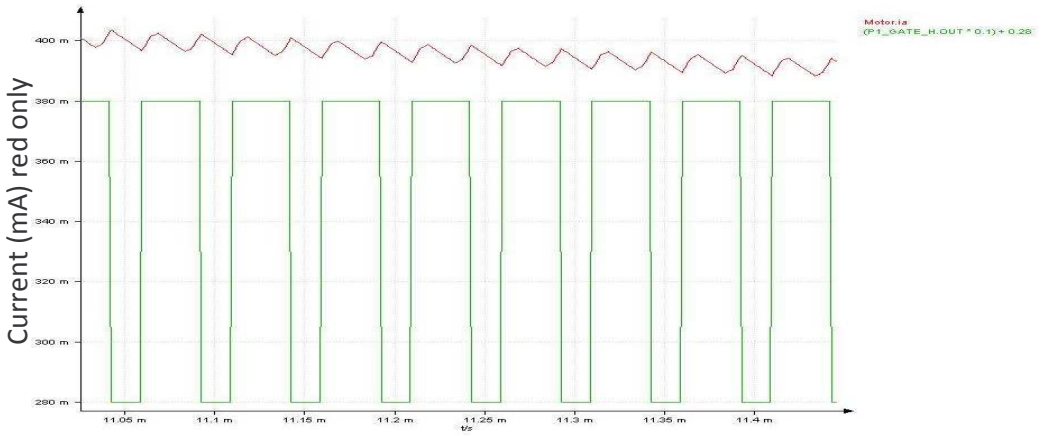

Figure 5-6: Simulated Phase A Current wave and Gate Drive Signal of Interroll machine using PI regulation at 400rpm, 0.4A reference current

Figure 5-4 shows the current waveforms observed in the motor component's 3 phase windings under PI control. The simulation demonstrates the significantly reduced current ripple that has consistently been observed when operating the PI controller (when compared to Bang-Bang regulation). The ripple observed in the simulations appears to be very similar to results captured and demonstrated in Figure 5-5. This does offer a further validation of the FCIV C++ component in the simulation up to the point of the PI based current regulator. Figure 5-6 shows a higher resolution image of the phase A current given in Figure 5-4 in addition to the phase A gate drive signal, the figure is typical of what is expected in the regulted current and corresponding gate drive signals. The strong similarities between the sets of results appear to validate the overall simulation whilst operating a PI regulator.

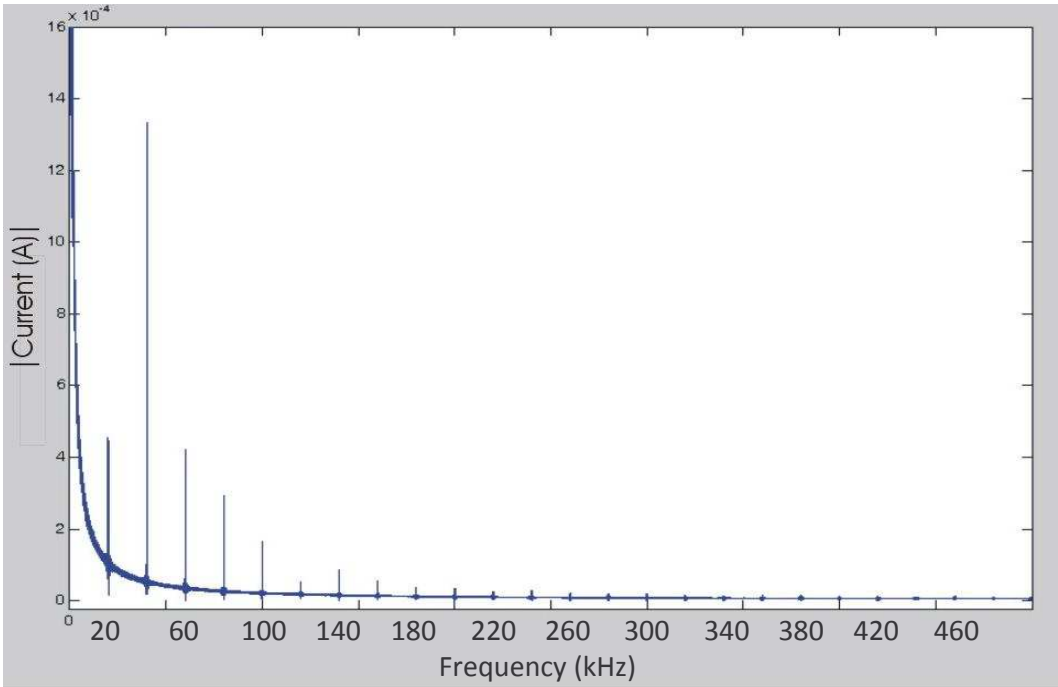

Figure 5-7: Harmonic Spectra of Simulated Interroll Machine Phase Current under PI Control at 400rpm 0.4A Reference Current

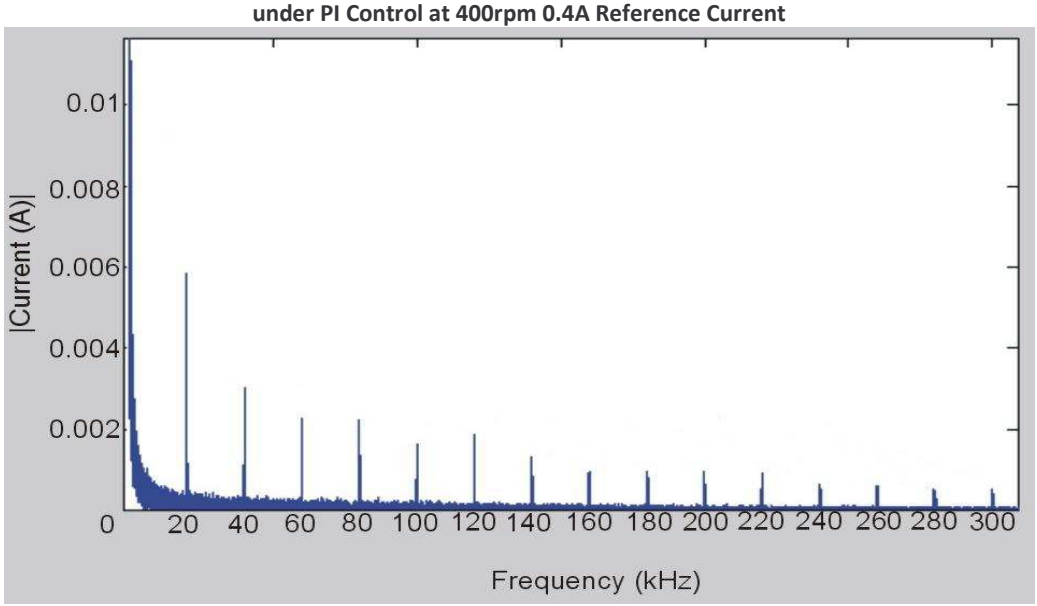

Figure 5-8: Harmonic Spectra of Interroll Machine Phase Current under PI Control at 400rpm 0.4A Reference Current

Figure 5-7 shows the frequency domain analysis of the simulated phase current observed in the motor component. The results clearly demonstrate there a very small magnitude of current content which exists at multiples of the switching frequency – clearly defined harmonic content. This is typical of any control strategy which implements a fixed switching frequency. Owing to the nature of the simulation environment the presence of current content at multiples of the switch frequency beyond 500kHz can not be verified. The general appearance of Figure 5-7 is very similar to the FFT results presented in Figure 5-8 which capture the performance measured with the actual FCIV. The similarities

between the simulations and the measured results presented validate the simulation model to an even greater extent when operating in a PI control strategy.

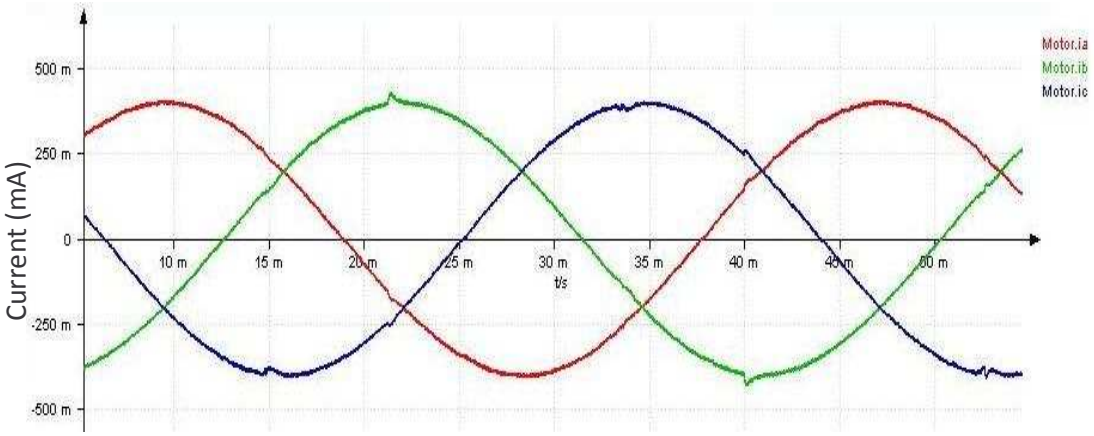

Figure 5-9: Simulated 3 phase current waveform of Interroll machine under SVPWM regulation operating at 400rpm, 0.4A reference current operating point.

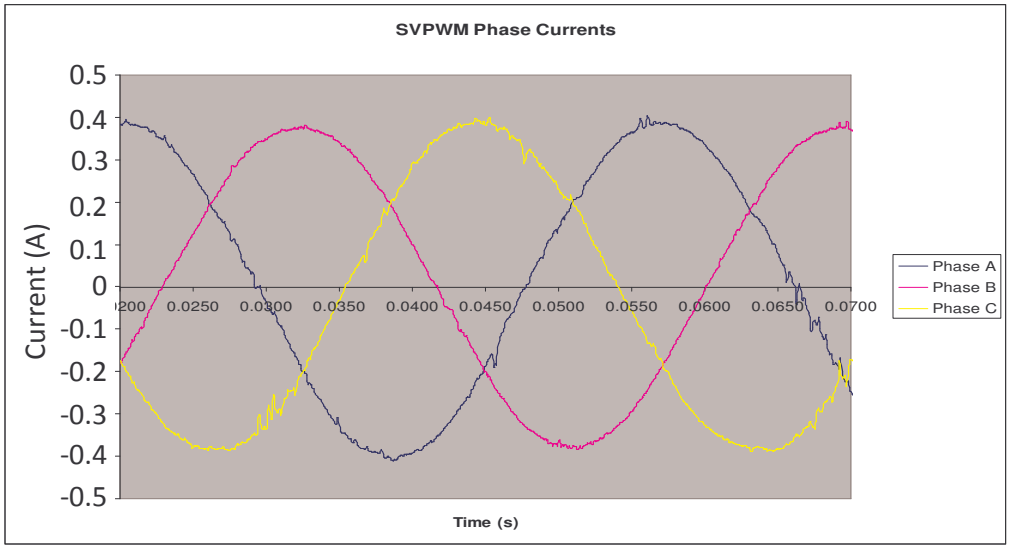

Figure 5-10: 3 phase current waveform of Interroll machine under SVPWM regulation operating at 400rpm, 0.4A reference current operating point.

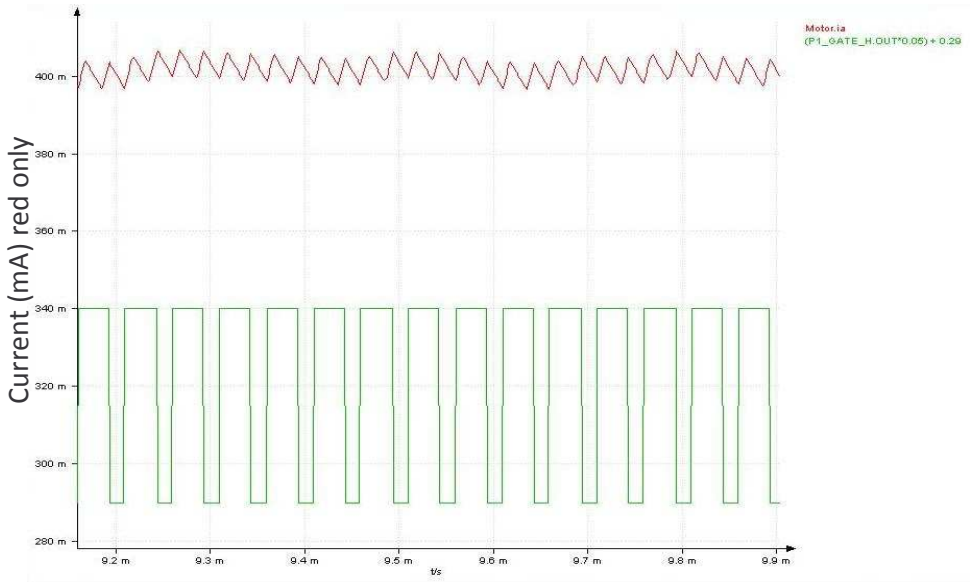

Figure 5-11: Simulated Phase A Current wave and Gate Drive Signal of Interroll machine using SVPWM regulation at 400rpm, 0.4A reference current

Figure 5-9 shows the current waveforms observed in the motor component's 3 phase connections under SVPWM control, it is the simulated equivalent to the results presented in Figure 5-10. Clearly shown again is the significantly reduced current ripple when compared against the Bang-Bang controller. This is a ripple once again in the region of 0.05A which is similar to the ripple observed in the measurements made in Figure 5-10. This further validates the simulation model. Figure 5-11 shows a higher resolution image of the phase A current given in Figure 5-9 in addition to the phase A gate drive signal.

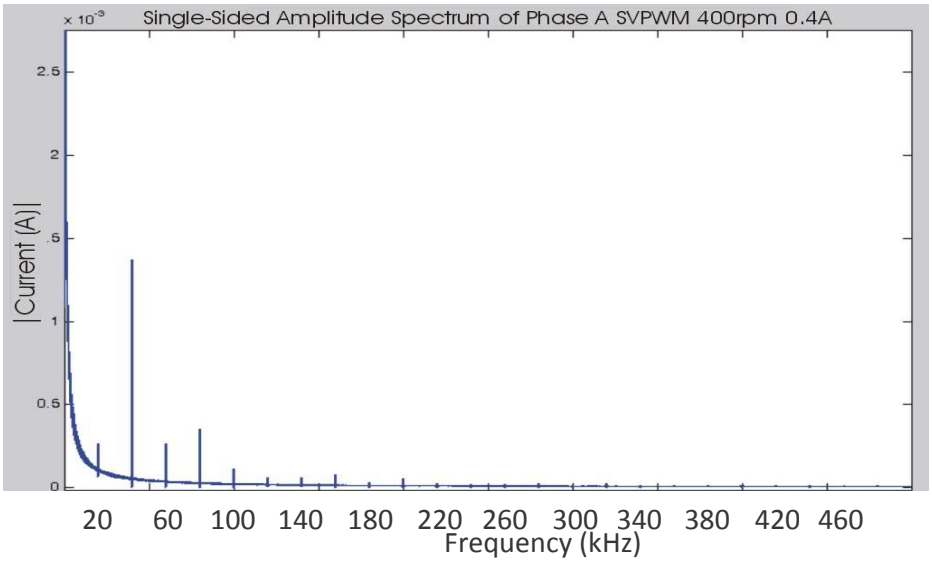

Figure 5-12: Harmonic Spectra of Simulated Interroll Machine Phase Current under SVPWM Control at 400rpm 0.4A Reference Current

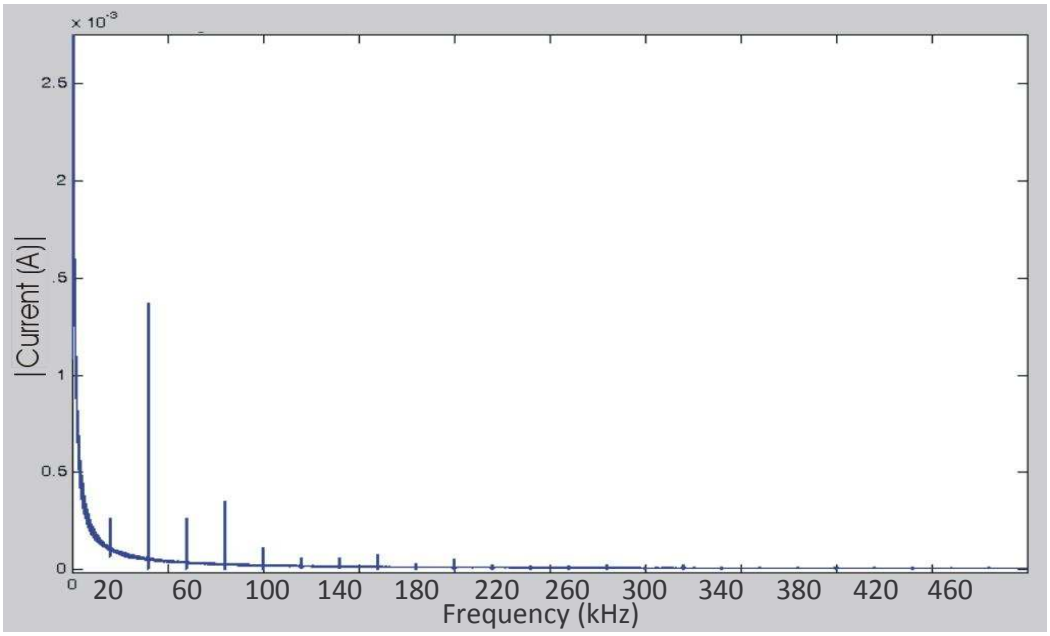

Figure 5-13: Harmonic Spectra of Interroll Machine Phase Current under SVPWM Control at 400rpm 0.4A Reference Current

The tests were also repeated for a simulation profile which matches the SEM machine which has been tested (due to the limitations of the motor model component only the wye connected machines can be simulated).

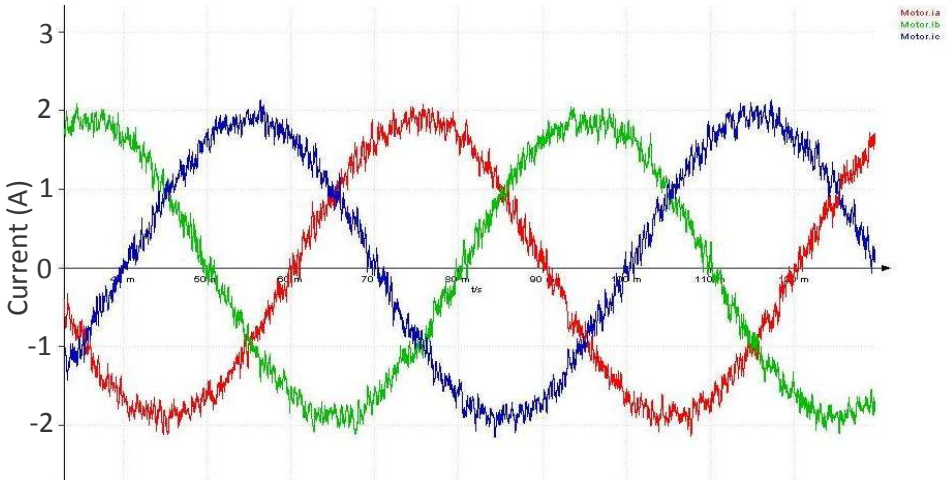

Figure 5-14: Simulated 3 phase current waveform capture of SEM machine using Bang-Bang regulation operating at 500rpm, 2A reference current operating point.

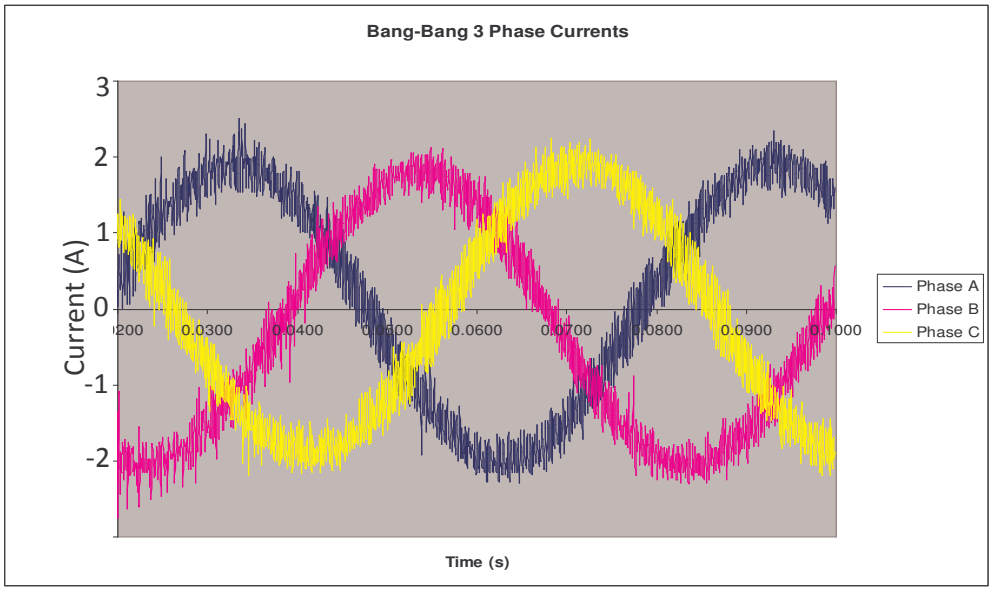

Figure 5-15: 3 phase current waveform capture of SEM machine using Bang-Bang regulation operating at 500rpm, 2A reference current operating point.

Figure 5-14 shows the resultant 3 phase current signals observed in the motor component phase connections under Bang-Bang control. Again the simulation shows that the Bang-Bang regulator results in phase current signals which oscillate heavily around the reference current values. The ripple observed in this simulation appears to have a magnitude around 0.2A, similar to the results exhibited in Figure 5-15. In comparison to measured results which appeard to be closer to 0.6A. This difference in current ripple was observed in the Interroll motor simulation which suggests that the simulation model is not taking into consideration the noise that may be present in the actual test system.

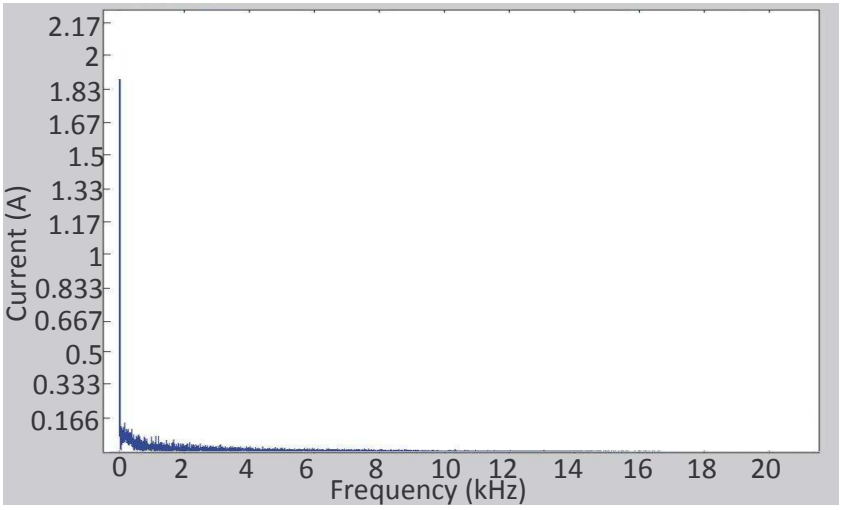

Figure 5-16: Harmonic Spectra of Simulated SEM Machine Phase Current under Bang-Bang Control at 500rpm 2A Reference Current

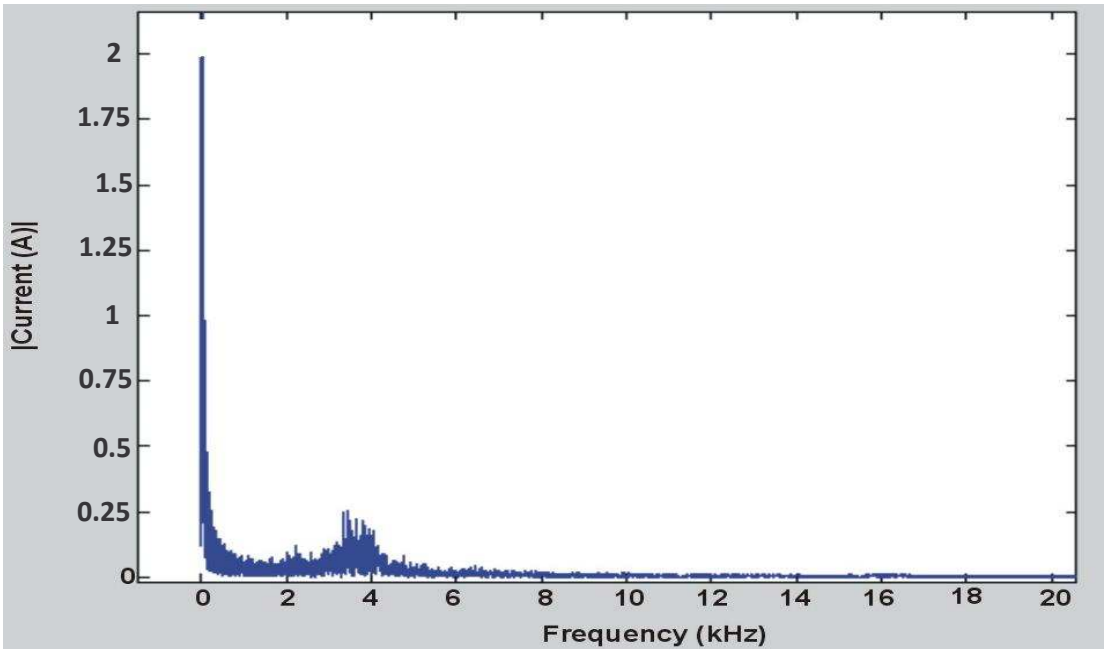

Figure 2-27: Harmonic Spectra of SEM Machine Phase Current under Bang-Bang Control at 500rpm 2A Reference Current

Figure 5-16 shows the frequency domain analysis of the simulated phase current observed when running the SEM simulation model; Once again the unpredictable spread of current content at a wide range of frequencies is observed, this has been strongly established as typical Bang-Bang control behaviour. However in the comparison of the two frequency domain analysis it is yet again observed that the two representations are somewhat different. Figure 2-27 clearly indicates groupings of greater current magnitude around a frequency of 4kHz (this is repeated across the majority of the Bang-Bang test range); this is less emphatically indicated in the simulation results, the spread of current content being far more even across the frequency range. This again highlights the difficulty in predicting the behaviour of a Bang-Bang controller.

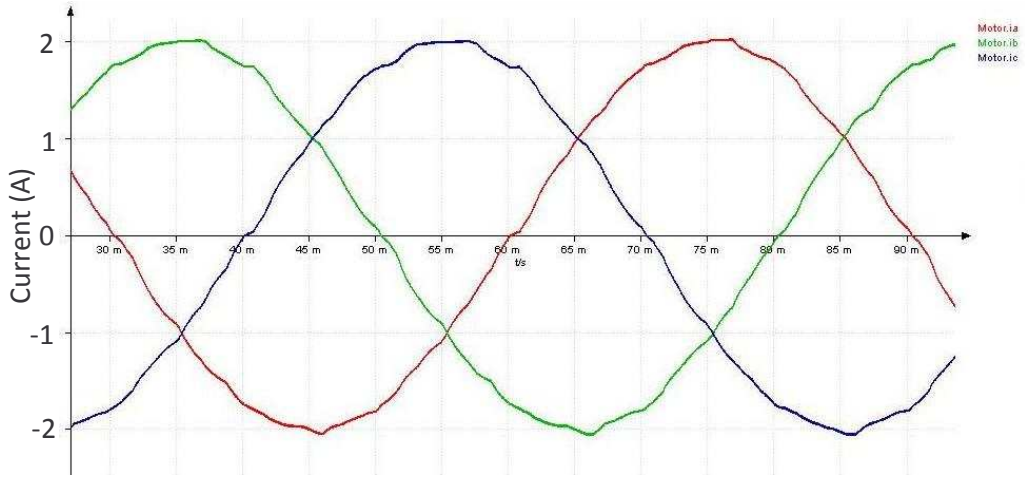

Figure 5-17: Simulated 3 phase current waveform capture of SEM machine using PI regulation operating at 500rpm, 2A reference current operating point.

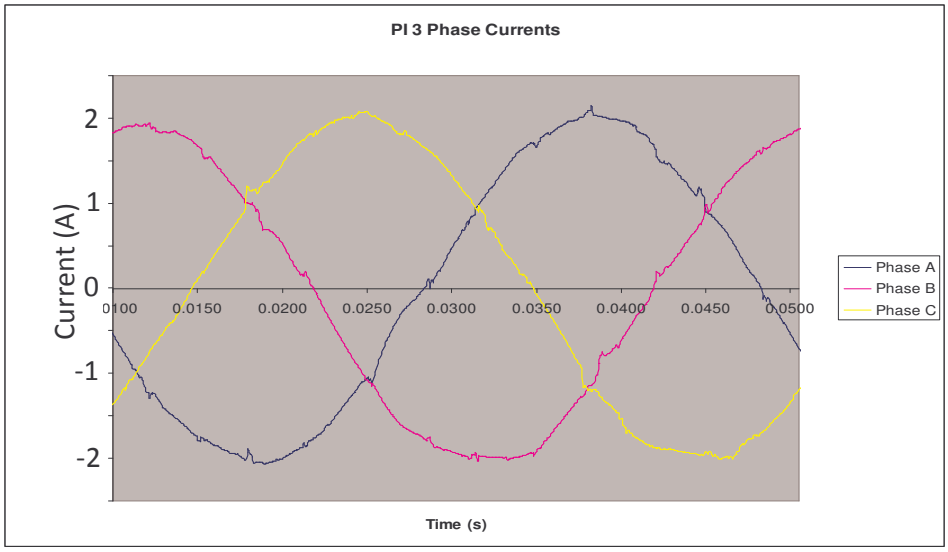

Figure 2-23: 3 phase current waveform capture of SEM machine using PI regulation operating at 500rpm, 2A reference current operating point.

Figure 5-17 shows the resultant 3 phase current signals observed in the SEM simulation model under PI control, the simulation equivalent of Figure 2-23. Again a massively reduced current ripple is apparent when compared to the Bang-Bang controller, indeed judging based solely upon Figure 5-17 the current ripple can be said to be negligible. Figure 2-23 does demonstrate a few occurrences of current ripple, but in general the simulation results are strongly similar to the actual results.

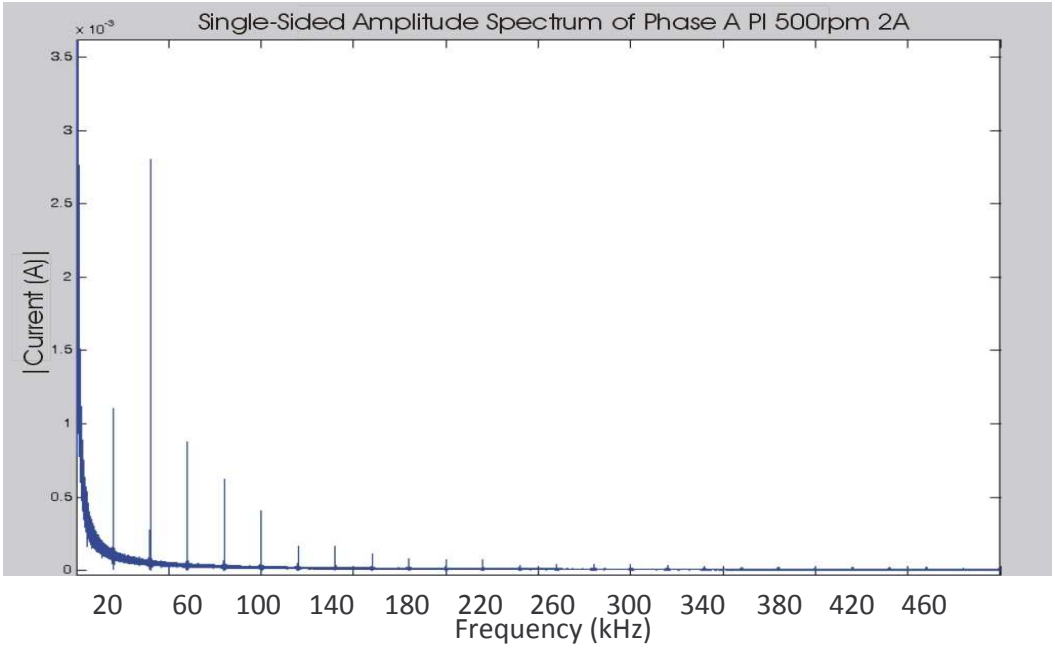

Figure 5-18: Harmonic Spectra of Simulated SEM Machine Phase Current under PI Control at 500rpm 2A Reference Current

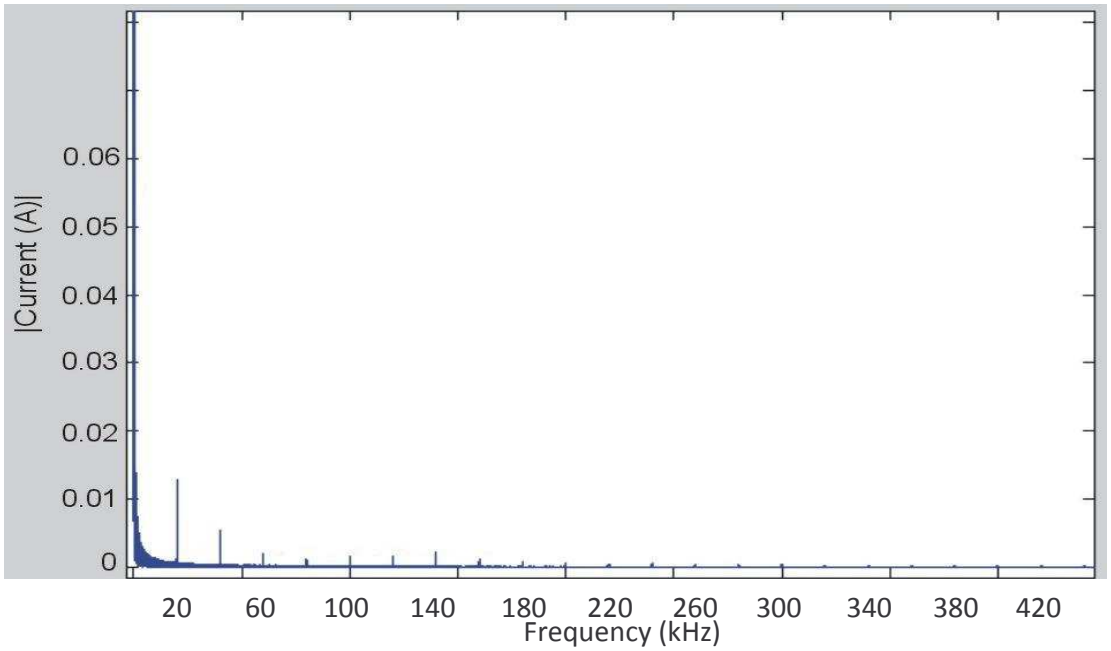

Figure 2-24: Harmonic Spectra of SEM Machine Phase Current under PI Control at 500rpm 2A Reference Current

Figure 5-18 shows the frequency domain analysis of the simulated current observed in the SEM simulation model. Yet again the clearly defined harmonics of the switching frequency can clearly be seen. This is very similar to the analysis which was presented in the equivalent results of Figure 2-24. The similarity in these results validates the SEM model when operating the PI control strategy.

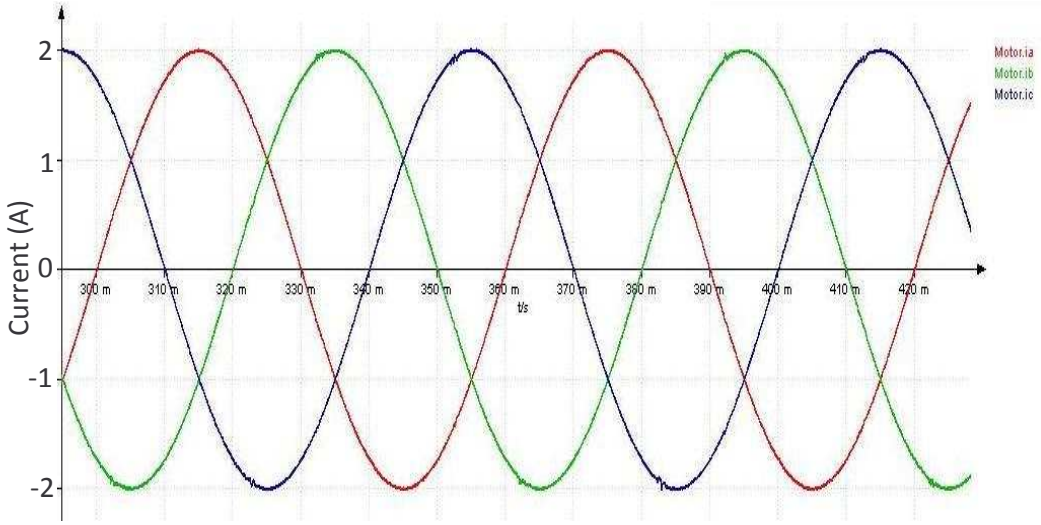

Figure 5-19: Simulated 3 phase current waveform capture of SEM machine using SVPWM regulation operating at 500rpm, 2A reference current operating point.

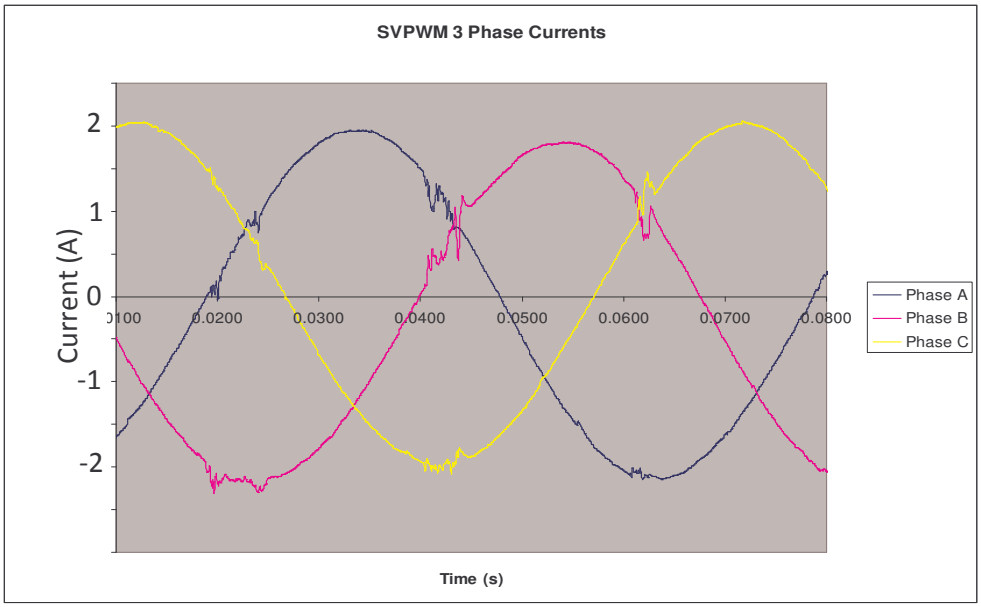

Figure 5-20: 3 phase current waveform capture of SEM machine using SVPWM regulation operating at 500rpm, 2A reference current operating point.

Figure 5-19 shows the current waveforms observed in the motor connections when the SEM simulation model is tested. As is now expected the current ripple present is essentially negligible as a result of operating the SVPWM regulator; this is largely the case in the results presented in Figure 5-20. These results supplement further the notion that the simulation model is fully validated when considering the SVPWM control strategy.

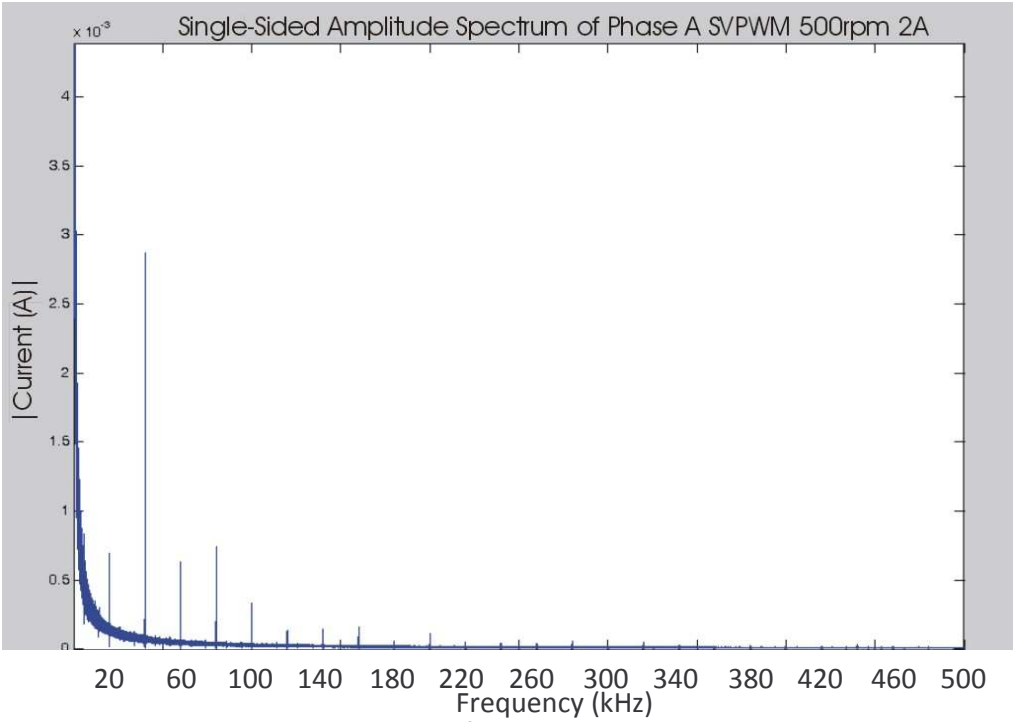

Figure 5-21: Harmonic Spectra of Simulated SEM Machine Phase Current under SVPWM Control at 500rpm 2A Reference Current

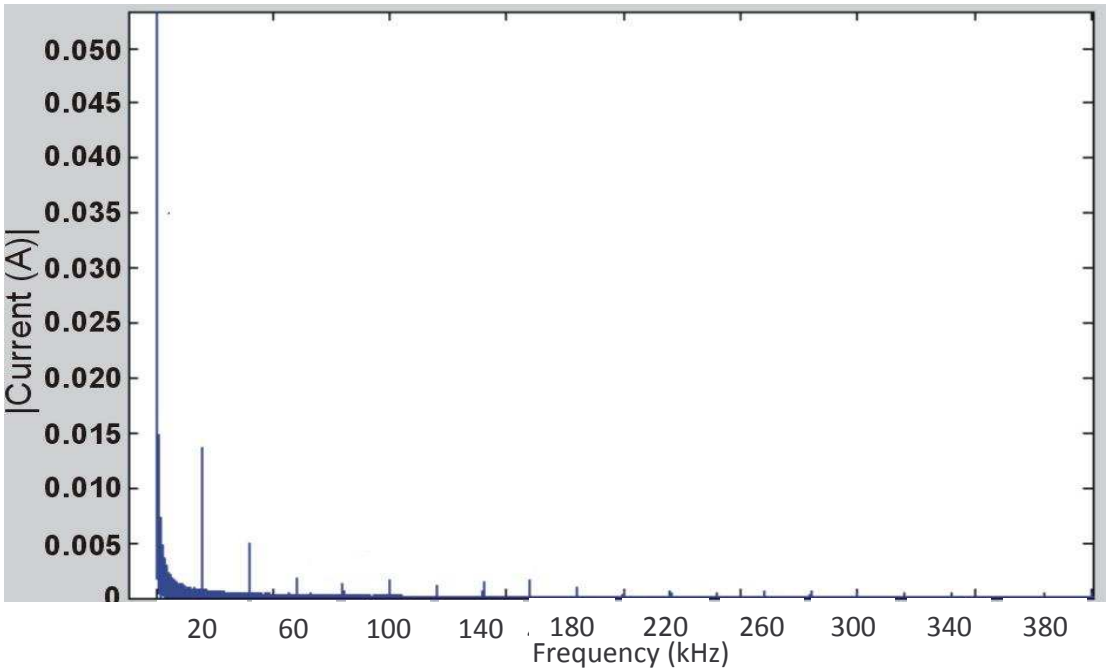

Figure 5-22: Harmonic Spectra of SEM Machine Phase Current under SVPWM Control at 500rpm 2A Reference Current

Figure 5-21 shows the frequency domain analysis of the simulated current observed when operating the SVPWM control technique. As is to be expected, the current content is very clearly defined at multiples of the switch frequency. This is consistent in both the simulation and actual results (Figure 5-22) and offers further validation of the model with respect to the SVPWM controller.

In addition to being concerned with the aesthetics and frequency components of the waveform, there also exists the opportunity to further explore the average switch frequency adopted under Bang-Bang control in the two respective simulation models (SEM and Interroll). In fact the results obtained and presented in Chapter 2 in this respect were obtained using routines for the switch counting method which were initially developed and trialled in the Portunus simulation environment before being implemented in the actual FCIV. Whilst the routines were validated in terms of correct operation, the following analysis is the first to compare the machine specific simulation model results with those obtained in the actual test system.

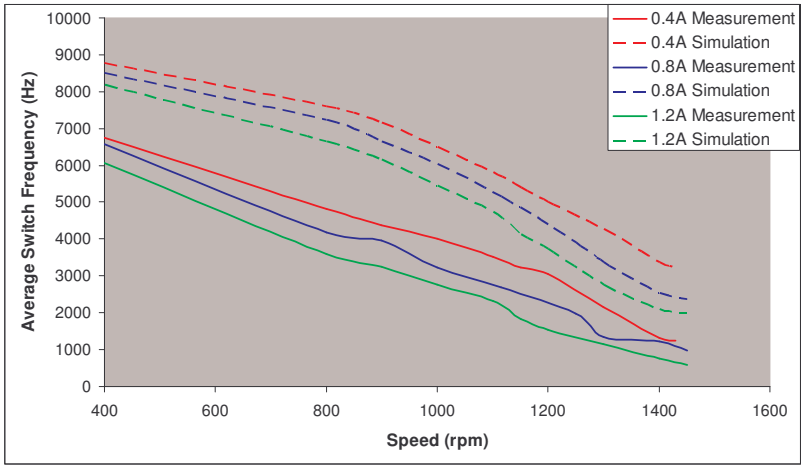

Figure 5-23: Average Switch Frequencies of Bang-Bang controller of Interroll machine, actual results versus simulated results.

Figure 5-23 shows a comparison of the average switch frequencies of the Bang-Bang controller in both the actual and simulated system tests on the Interroll machine; this is essentially Figure 2-48 updated to include the results gathered via the simulation model. Reviewing this comparison it is clear that there is significant difference between the actual measured averages and the predicted simulation averages. The simulations over predict the expected switch frequency on a consistent basis for each of the reference current values; this indicates that there is a consistent flaw in the simulation model. If we consider that too many switch events are being predicted in the simulation results then it can be deduced that the current requires switching more frequently in the model because the rate of change of current (di/dt) is too great. This is not a parameter the user has control over in any aspect of the simulation model, nor is the individual phase winding inductances which will have a direct impact upon the di/dt parameter. The user is however capable of influencing the synchronous inductance values (via control of the synchronous reactance parameters). This may be where the source of the discrepancy lies, the synchronous inductance values used in the model which generated the results presented in Figure 5-23 are either inaccurate to a degree or the manner in which the di/dt parameter is derived from them is inaccurate.

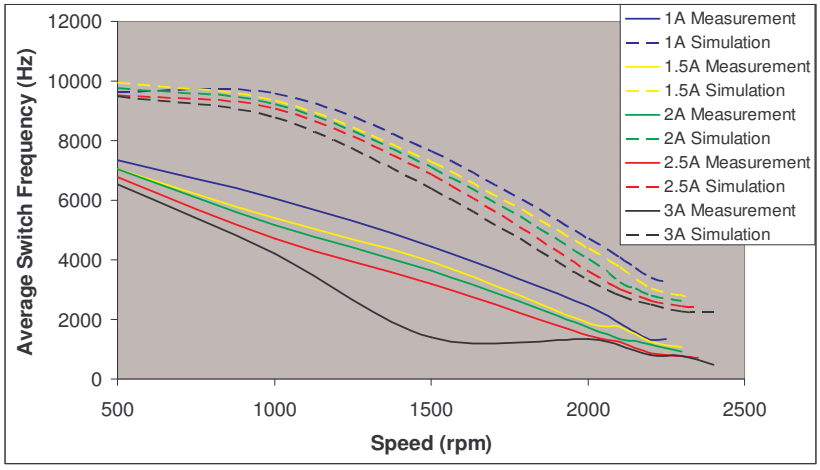

Figure 5-24: Average Switch Frequencies of Bang-Bang controller of SEM machine, actual results versus simulated results.

Figure 5-24 shows a comparison of the average switch frequencies of the Bang-Bang controller in both the actual and simulated system tests on the SEM machine; this is essentially Figure 2-49 updated to include the results gathered via the simulation model. As is clearly evident the pattern of over predicting the average switch frequency at each reference current is repeated. Given that the results of Figure 5-23 and Figure 5-24 are obtained from two separately calibrated simulation models, the idea that the user inputs for synchronous reactances being inaccurate seems the less plausible explanation; it seems more likely that the motor model has an inaccuracy in its description which leads to higher rates of change in current than are observed in the actual system.

In summary, when considering the aesthetics and the frequency analysis of the simulations against the actual measurements, there are a number of comparisons between the different sets of results which further validate the model. This validation comes in the form of not only successful current regulation (in the case of all three techniques) but also from convincing frequency domain analysis in the case of the PI and SVPWM regulators. In addition to this validation however, are a number of discrete differences in the results which could be interpreted as inaccuracies of the model. These include different orders of current ripple, unconvincing frequency domain analysis (in the case of the Bang-Bang regulator) and most convincingly through the difference in measured and predicted average switch frequencies of the Bang-Bang regulator.

5.3. Torque Profile Validation

Torque profiles for each machine under the different control strategies were presented in Chapter 2. Torque profiles are usually referred to when considering the operational

characteristics of a machine with regards to its intended application. This being the case it is certainly advantageous that the simulation model can make accurate predictions of the expected torque versus speed profile for the machines under consideration. Using the models of both the interroll and SEM machines, comparisons can be made between the simulated torque outputs and the measured results which were presented in Chapter 2.

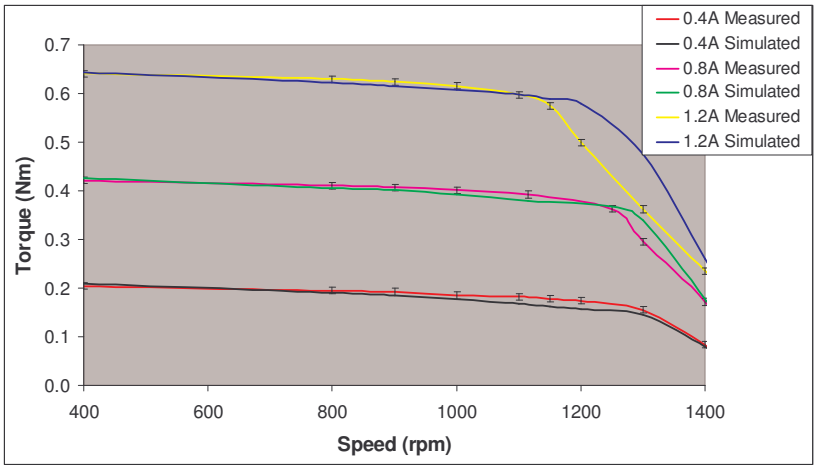

Figure 5-25: Torque/Speed profile comparisons of 8 pole Interroll motor running under Bang-Bang control

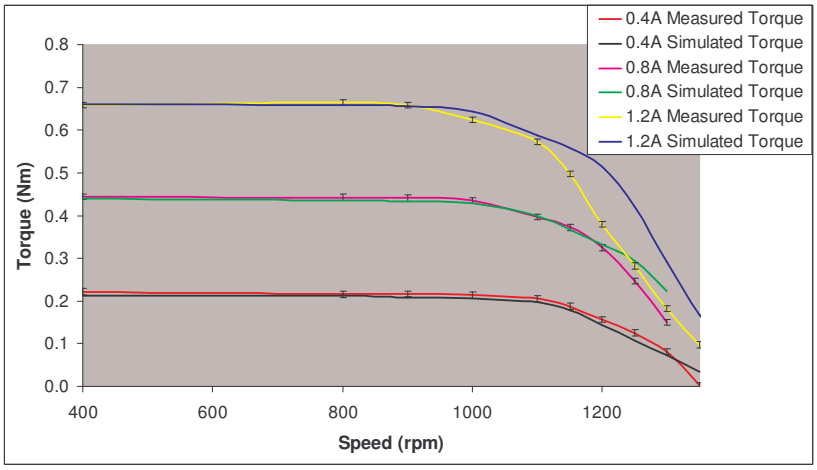

Figure 5-26: Torque/Speed profile comparisons of 8 pole Interroll motor running under PI control

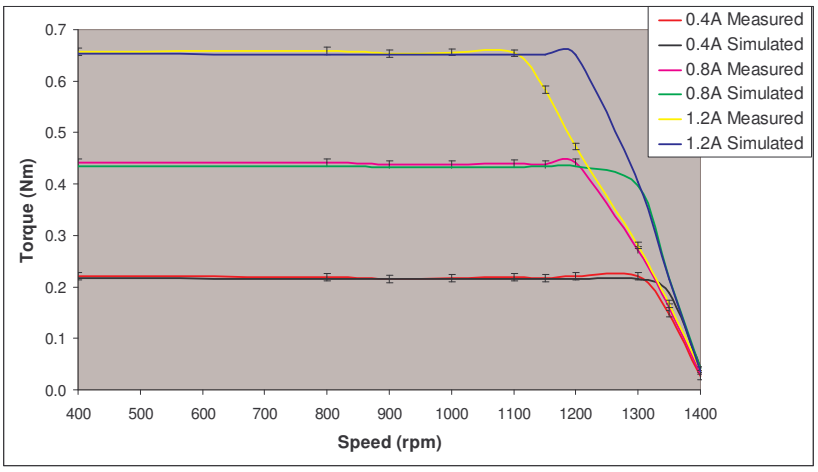

Figure 5-27: Torque/Speed profile comparisons of 8 pole Interroll motor running under SVPWM control

Figure 5-25, Figure 5-26 and Figure 5-27 give comparisons of the measured torque profiles against the simulated torque profiles. These tests are based upon the Interroll motor running under the respective control strategies. Upon review of the figures, the results seem to largely validate the simulation model with respect to prediction accuracy. Certainly in each case the low reference current profile comparisons show that the simulation results reside within the error bounds of the measured results for the entire speed range. At higher reference currents the predicted torque is still observed largely residing within the measured values error markers but this is only maintained until the high speed sections of the profile at which this level of accuracy is lost. This observation is true for the results obtained in each of the control strategies. These results validate the model in the low speed or constant torque regions but perhaps also indicate that in the high speed regions the model needs to make greater consideration of losses which are present in the actual test system; this is indicated by an over estimation of the torque output in the high speed region.

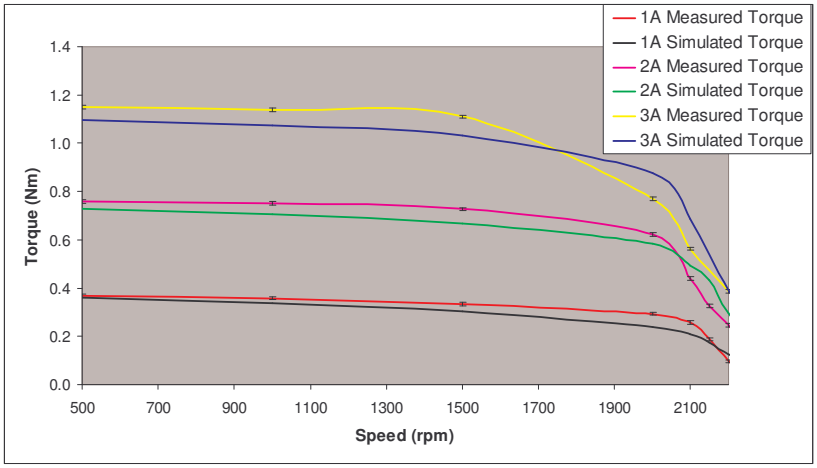

Figure 5-28: Torque/Speed profile comparisons of 4 pole SEM motor running under Bang-Bang control

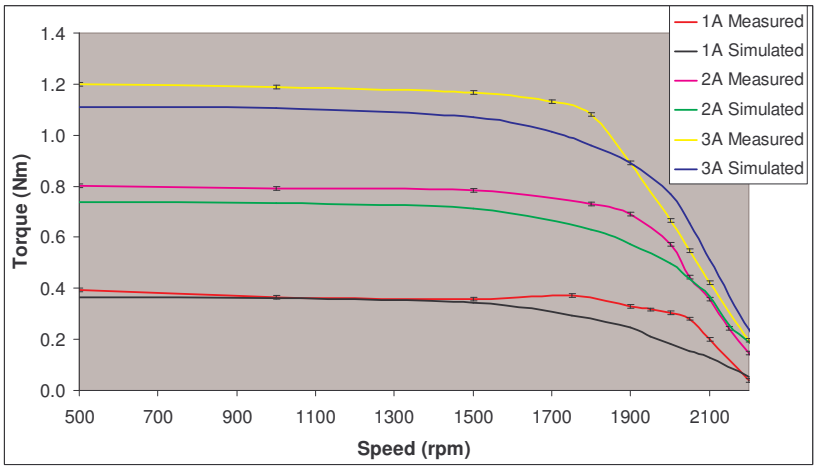

Figure 5-29: Torque/Speed profile comparisons of 4 pole SEM motor running under PI control

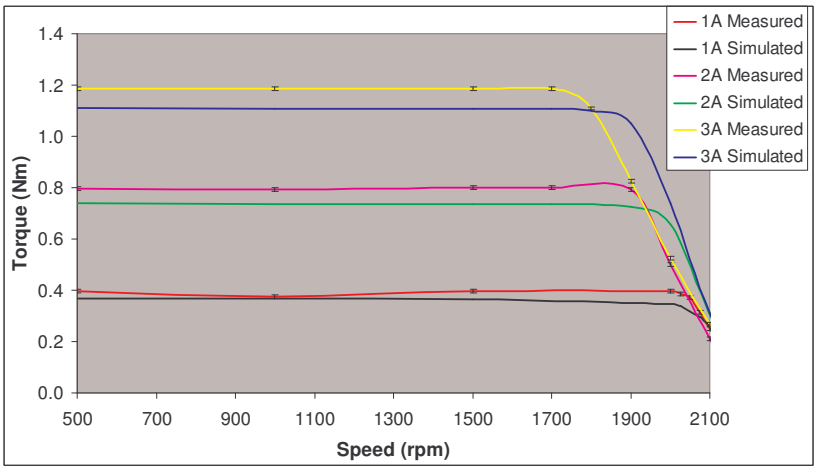

Figure 5-30: Torque/Speed profile comparisons of 4 pole SEM motor running under SVPWM control

Figure 5-28, Figure 5-29 and Figure 5-30 give the equivalent comparisons on the model developed for the SEM machine. The results presented offer somewhat poorer results by comparison with the Interroll model. The highest levels of prediction accuracy are again

observed in the lowest reference current testing, however the predictions do not maintain results within the error markers of the measured results with the same regularity as occurs in the interroll results. Indeed, upon review of the figures it can be seen that in general the predicted torque is under estimated when compared to the measured results; however in the high speed regions there is again an over prediction observed. These results do not allow for a strong validation of the SEM simulation model. Comparisons of the two models however does suggest that the overall system modelling is largely satisfactory and perhaps only the modelling of the specific motor is where the vulnerability of the system model resides. This is based on the fact that the motor component parameters and associated operating parameters is the only difference between the two simulation models.

5.4. Field Weakening Response

Field Weakening was described in Chapter 1 and it was used in the validation of online torque estimation techniques in Chapter 3. Given its prevalence in a wide variety of PMSM applications, the appropriate response to an applied gamma advance is another aspect of the simulation models which ideally would reflect the behaviour of the actual test system. Using the SEM model only, the torque response to field weakening can be simulated and compared with the measured results which were presented in Chapter 3.

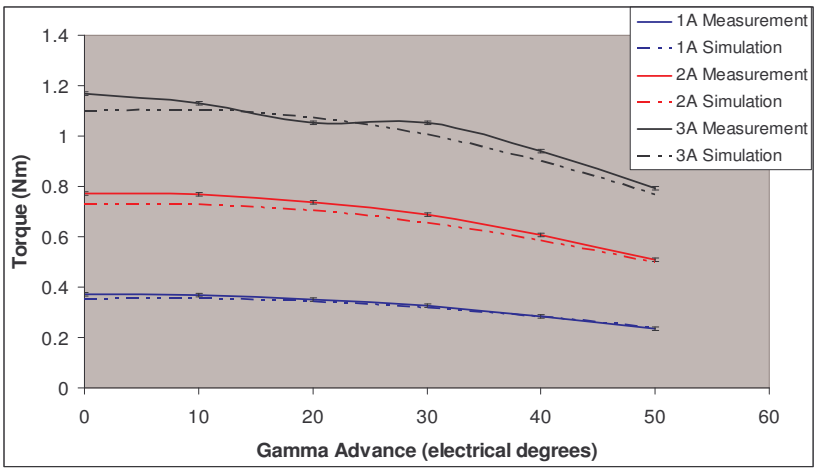

Figure 5-31: Torque Response to Field Weakening under Bang-Bang Control on SEM machine at 500rpm, Comparison of simulations with measurements

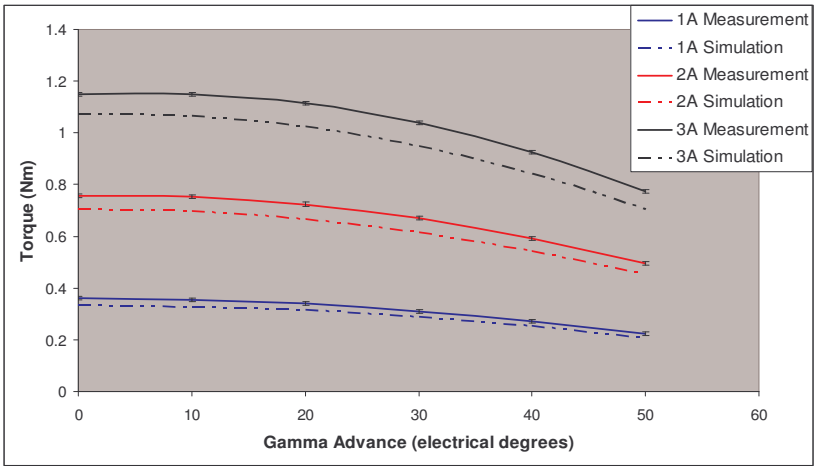

Figure 5-32: Torque Response to Field Weakening under Bang-Bang Control on SEM machine at 1000rpm, Comparison of simulations with measurements

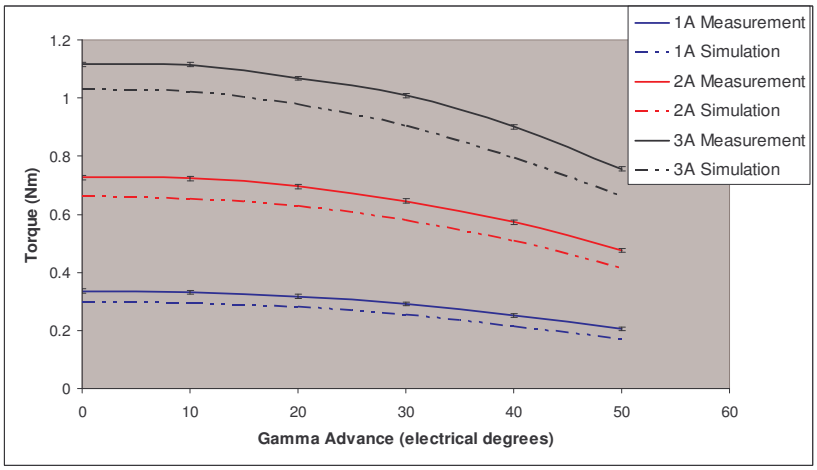

Figure 5-33: Torque Response to Field Weakening under Bang-Bang Control on SEM machine at 1500rpm, Comparison of simulations with measurements

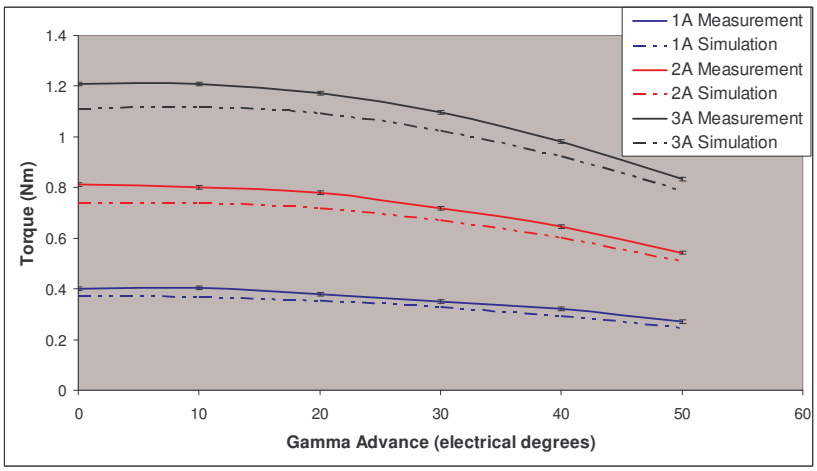

Figure 5-34: Torque Response to Field Weakening under PI Control on SEM machine at 500rpm, Comparison of simulations with measurements

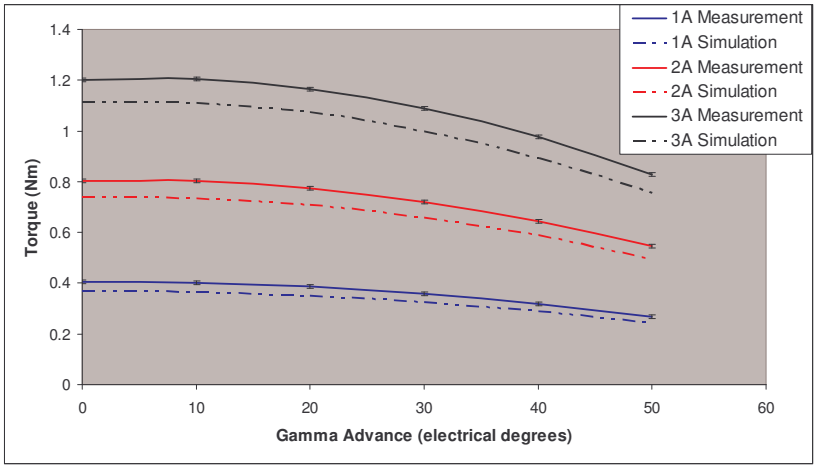

Figure 5-35: Torque Response to Field Weakening under PI Control on SEM machine at 1000rpm, Comparison of simulations with measurements

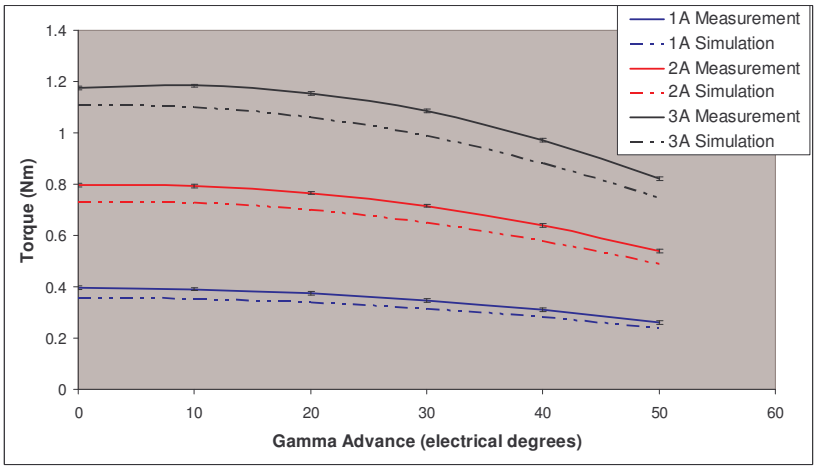

Figure 5-36: Torque Response to Field Weakening under PI Control on SEM machine at 1500rpm, Comparison of simulations with measurements

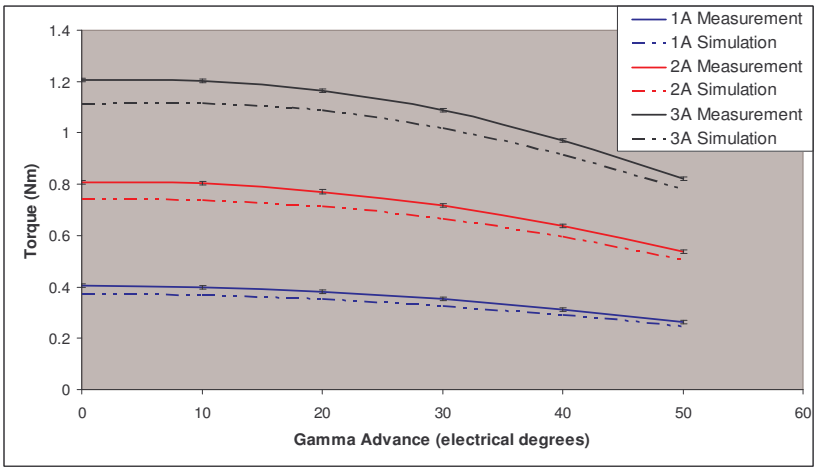

Figure 5-37: Torque Response to Field Weakening under SVPWM Control on SEM machine at 500rpm, Comparison of simulations with measurements

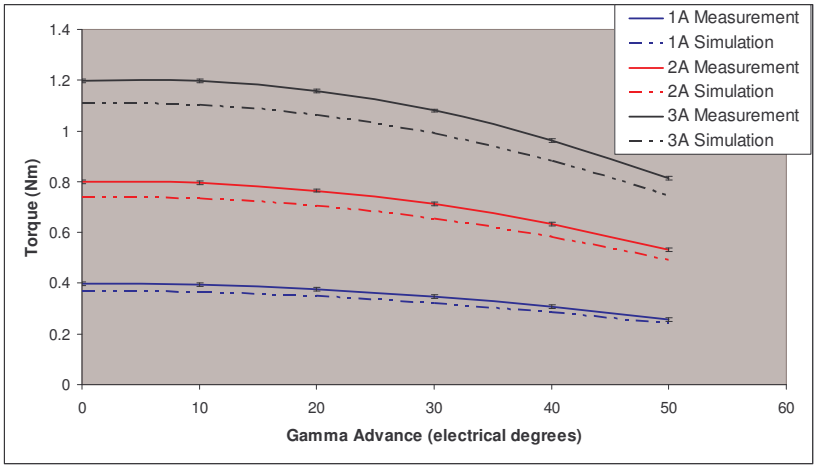

Figure 5-38: Torque Response to Field Weakening under SVPWM Control on SEM machine at 1000rpm, Comparison of simulations with measurements

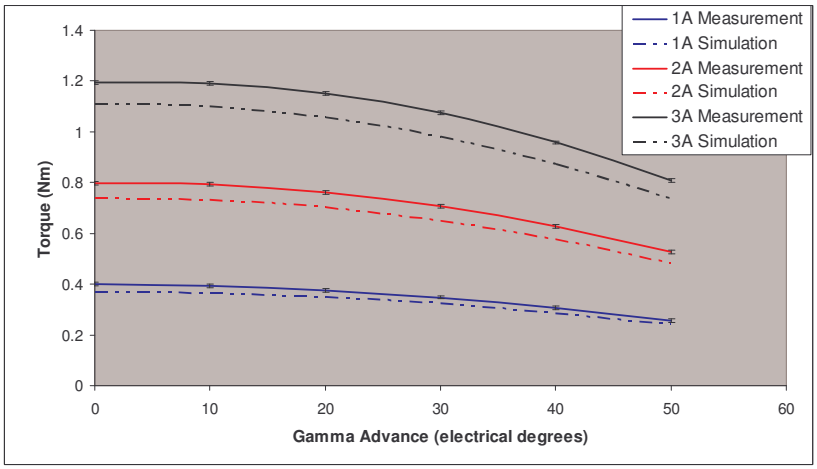

Figure 5-39: Torque Response to Field Weakening under SVPWM Control on SEM machine at 1500rpm, Comparison of simulations with measurements

Figure 5-31, Figure 5-32 and Figure 5-33 show the simulated torque response with respect to applied field weakening in both the simulation models and the actual measured results. These tests were carried out using the Bang-Bang control. The results offer a great deal of encouragement in terms of validating the correct response from the simulation model. As is the case in each of the test sequences presented, the simulated torque output matches the trend of the measured torque output in response to the gamma advance range. The offset in each of the simulation results appears to be consistent with the offsets observed for each of the reference current tests at their respective speed intervals; this is clearly demonstrated in the figures presented in section 5.3. This suggests that the torque response to field weakening is, in effect, ideally matched with the actual system.

Figure 5-34, Figure 5-35 and Figure 5-36 show the field weakening response of the model when operating the PI controller. The results are very similar to those observed in the Bang-Bang controlled tests which reinforce the validity of the model.

Figure 5-37, Figure 5-38 and Figure 5-39 are the results of the SVPWM controlled tests. Once again the torque response of the simulation model is shown to be favourably comparable to the measurements.

Reflecting upon the torque response of the simulation model when tested under the various conditions given it seems only fair to conclude that the simulation model matches the expected response that was measured in the actual system. This allows for strong validation of the simulation model in this respect, further to this the results indicate that no modifications are required in relation to the response of the model to changes in the gamma advance as the offsets observed in the results have been established as being present irrespective of field weakening.

5.5. Drive System Powers and Efficiencies Validation

In Chapter 2 the input and output power considerations of the overall drive system were presented for each of the control strategies; these also included estimates of the drive efficiency. These considerations are also important in the consideration of PMSM based applications, not least due to the modern systems engineer having to consider efficiency with greater emphasis. Using the simulation models, it is again possible to make comparisons of the simulations predictions against the measurements presented in Chapter 2.

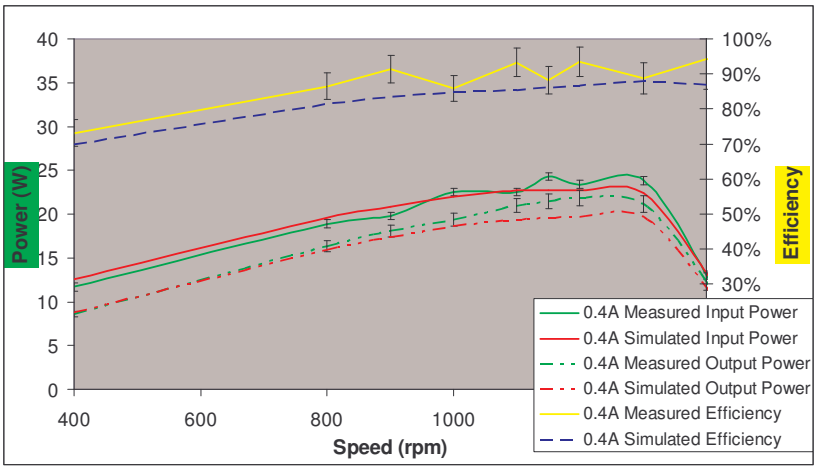

Figure 5-40: Bang-Bang Drive Efficiency and Power Calculations (Simulations and Measurements) for 0.4A Reference Current on Interroll Machine

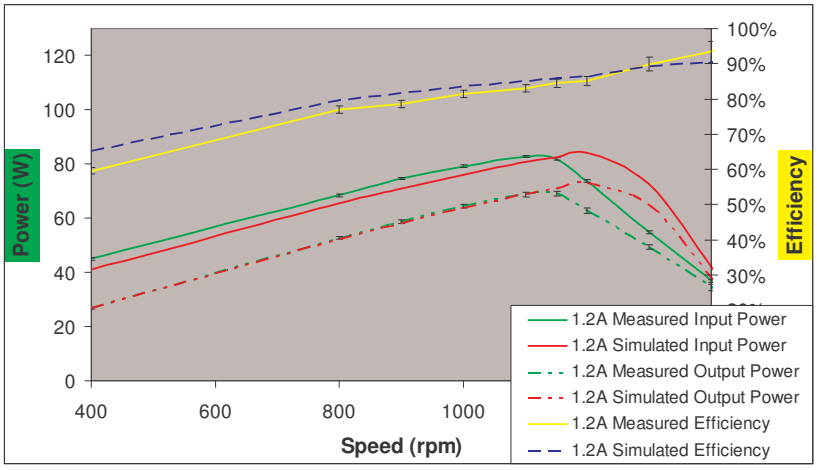

Figure 5-41: Bang-Bang Drive Efficiency and Power Calculations (Simulations and Measurements) for 1.2A Reference Current on Interroll Machine

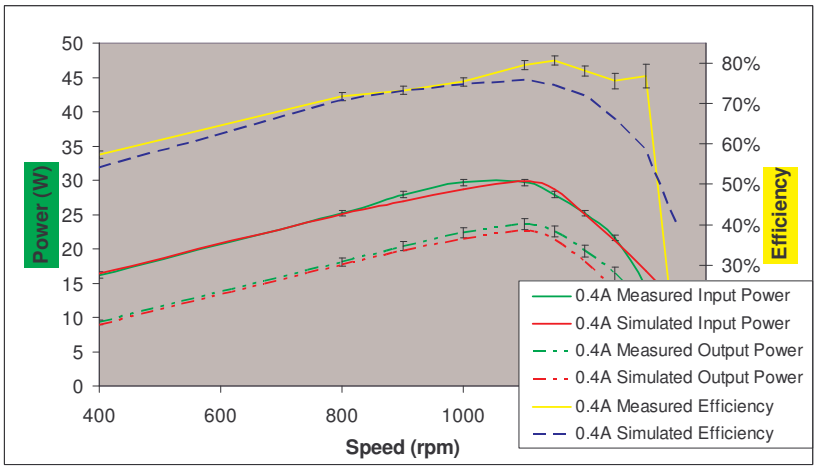

Figure 5-42: PI Drive Efficiency and Power Calculations (Simulations and Measurements) for 0.4A Reference Current on Interroll Machine

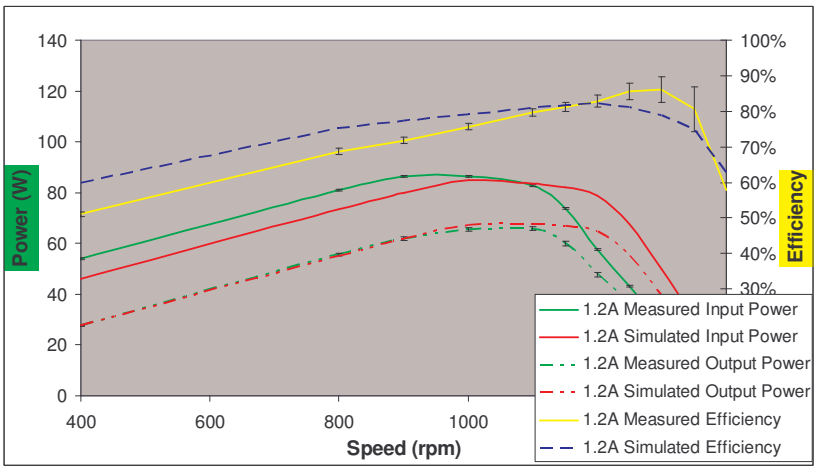

Figure 5-43: PI Drive Efficiency and Power Calculations (Simulations and Measurements) for 1.2A Reference Current on Interroll Machine

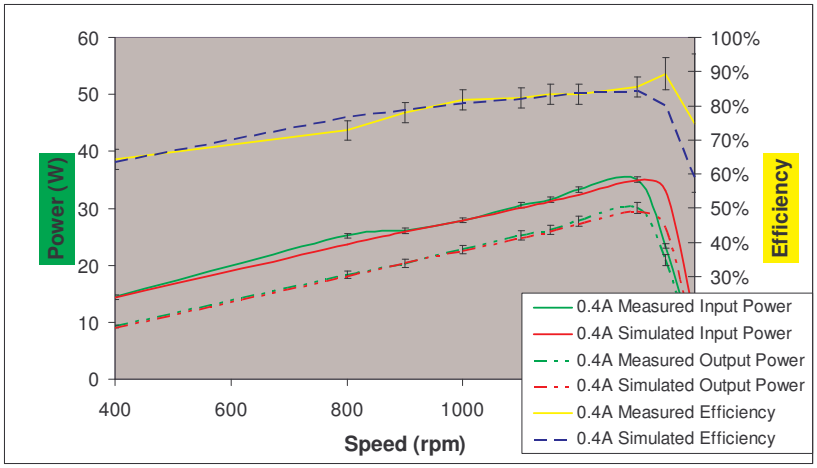

Figure 5-44: SVPWM Drive Efficiency and Power Calculations (Simulations and Measurements) for 0.4A Reference Current on Interroll Machine

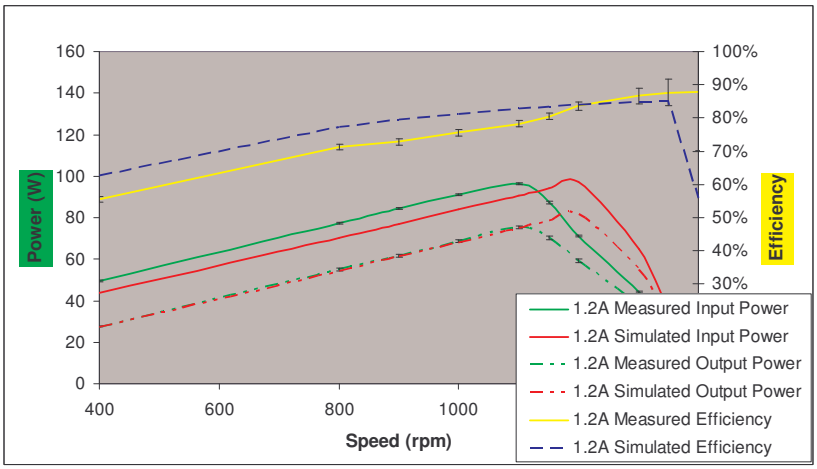

Figure 5-45: SVPWM Drive Efficiency and Power Calculations (Simulations and Measurements) for 1.2A Reference Current on Interroll Machine

Figure 5-40 and Figure 5-41 shows the simulations versus measurements results when considering the drive power and efficiency under Bang-Bang regulation for the Interroll motor. These two figures represent the measurements at each end of the tested reference current range. Looking initially at the 0.4A reference current results (Figure 5-40), it can be seen that at both power measurements, the simulations track the speed response observed in the measurements with a large degree of accuracy – staying within or very near to the error markers of both measurements. This is also observed in the simulated drive efficiency which also resides in a number of the measurement error markers. However when considering the 1.2A reference current tests (Figure 5-41), there is clearly inaccuracy in the simulations in the high speed regions for both power measurements. The simulations over estimate both the power input by the DC link and then output by the motor. This overestimation appears in equal measure however which results in the overall efficiency simulations to closely match the measurements (although

the simulations do not reside within the error markers as frequently as they did at the lower reference current).

Figure 5-42 and Figure 5-43 show the simulations under PI control. Again looking at the lower reference current, the power simulations match very closely with the measured results. The efficiency simulation however does not have the same accuracy as was observed in the Bang-Bang case, it appears to roll off sharper than was observed in the measurements and generally under predicts the measured efficiency. Looking at the higher reference current again it is observed that in the high speed region the simulations over predict the power measurements. However in addition to this, in the low speed region the input power is significantly under predicted and this leads to a largely inaccurate simulation of the overall drive efficiency.

Figure 5-44 and Figure 5-45 shows the simulations under SVPWM control. A similar pattern is observed with the SVPWM results as was observed with the PI results. The lower reference current shows particularly good accuracy between the power measurements and simulations and this is reflected in good accuracy for the efficiency predictions. However at the higher reference current the input power is significantly under predicted when compared to measurements and then in the high speed region both power measurements are seen to be over predicted. This again results in a significantly inaccurate overall efficiency prediction from the simulation model.

In review of the Interroll simulation model, the results offer reasonable levels of validation. At the lower reference currents the predictions are largely accurate when compared to the measured results however there are noticeable inaccuracies introduced when the higher reference currents are simulated; despite this the trends in the measurements are very similarly reflected in the simulations. This allow for a minor validation of the simulation model in that it models behaviour very well but does not have a strong numerical accuracy. The results however do make a suggestion that the simulation models are not making sufficient consideration of losses throughout the system. Under prediction of the input power provided by the DC link suggests that the VSI component perhaps does not include any sufficient loss consideration and the over estimated power outputs in the high speed regions also indicate that the motor component also fails to make due consideration to power losses in this region. These tests and comparisons must be repeated for the simulation model of the SEM motor before such conclusions can be given serious consideration.

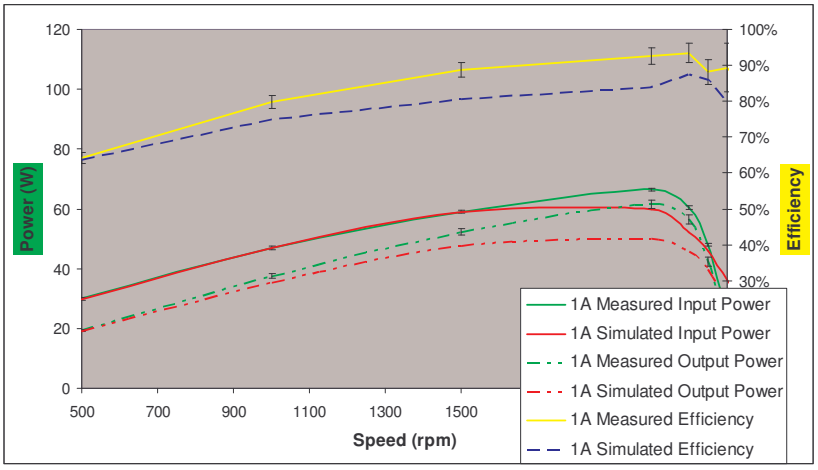

Figure 5-46: Bang-Bang Drive Efficiency and Power Calculations (Simulations and Measurements) for 1A Reference Current on SEM Machine

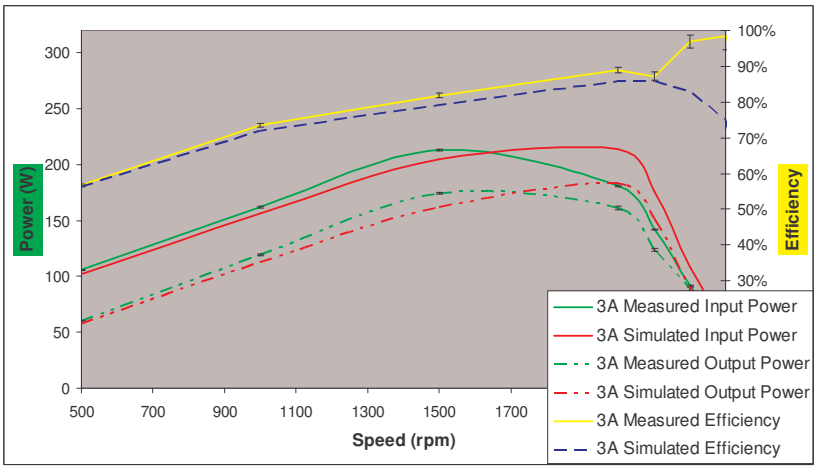

Figure 5-47: Bang-Bang Drive Efficiency and Power Calculations (Simulations and Measurements) for 3A Reference Current on SEM Machine

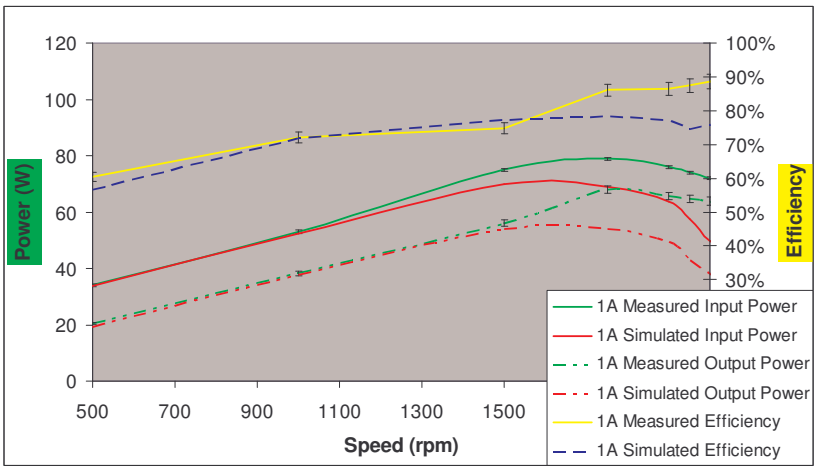

Figure 5-48: PI Drive Efficiency and Power Calculations (Simulations and Measurements) for 1A Reference Current on SEM Machine

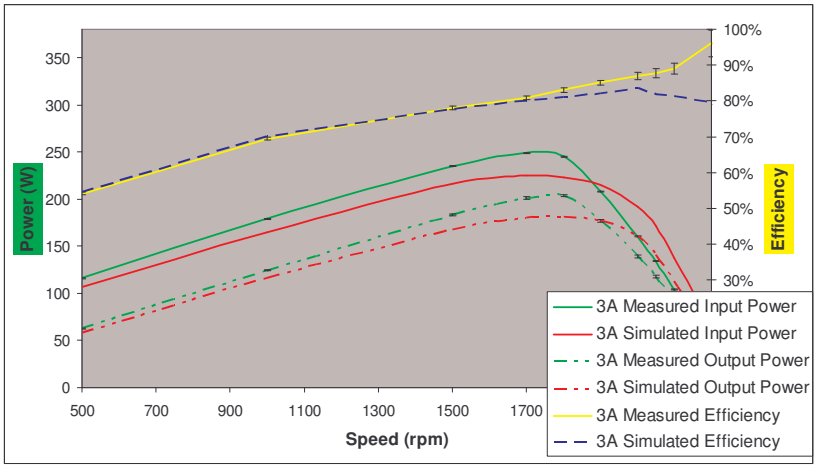

Figure 5-49: PI Drive Efficiency and Power Calculations (Simulations and Measurements) for 3A Reference Current on SEM Machine

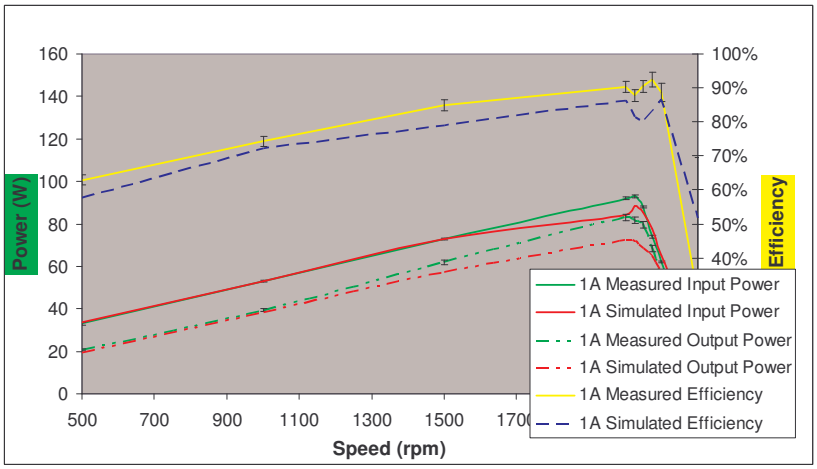

Figure 5-50: SVPWM Drive Efficiency and Power Calculations (Simulations and Measurements) for 1A Reference Current on SEM Machine

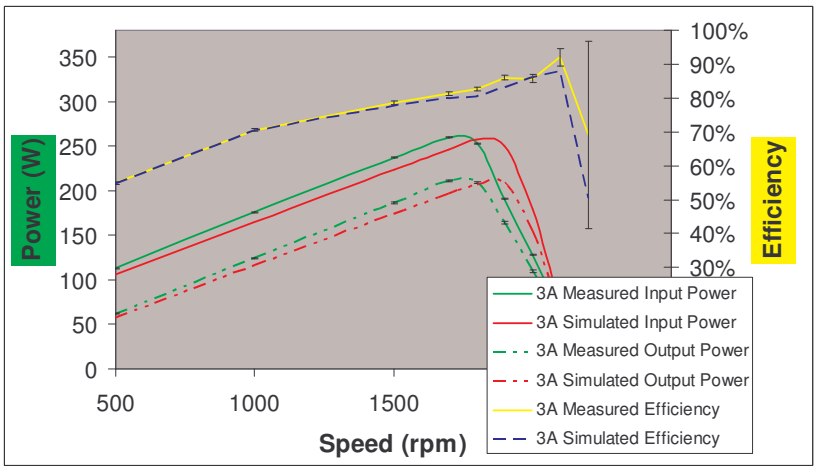

Figure 5-51: SVPWM Drive Efficiency and Power Calculations (Simulations and Measurements) for 3A Reference Current on SEM Machine

Figure 5-46 and Figure 5-47 both show the results obtained on the SEM motor model under Bang-Bang control. Again the results presented are obtained at both ends of the reference current range that was tested. In the case of the 1A reference current range

the output power seems to be significantly under estimated when compared to the measurements, although the input power is also observed under predicting at higher speeds. This inaccuracy is also reflected in the efficiency predictions which are noticeably lower than the measurements; however the general efficiency trend is at least predicted with good accuracy. When considering the 3A reference current results the trends observed in the Interroll results are still slightly evident. There is a noticeable increase in the under prediction of the input and output powers, however at the higher speed regions the simulations significantly over predict these. Despite this the efficiency predictions follow a reasonably similar trend as the measurements albeit not with a strong degree of accuracy.

Figure 5-48 and Figure 5-49 show the results for the SEM motor running under PI control. The 1A reference current results show that the power predictions are highly accurate when compared to the measurements in the lower speed regions but eventually become significantly lower than the measurements as the speed increases. This pattern is repeated in the efficiency calculations which until reaching higher speeds are quite accurate before again becoming significantly lower than the efficiency based upon measurements. At the 3A reference current, the under prediction of the two power measurements is again present before a slight over prediction at the highest speed regions. Despite this general inaccuracy in power measurements, the efficiency calculation is largely accurate until the high speed region at which point the predictions are significantly lower then the measurements.

Figure 5-50 and Figure 5-51 show the results obtained when operating the SVPWM control. Looking initially at the 1A reference current results we see that the simulations follow the trends shown in the measurements for both of the power measurements and the efficiency calculations. There is however a clearly noticeable under prediction of the input power beyond a certain speed and this effect is also observed in the output power predictions. This results in the efficiency estimations maintaining a consistent level of under prediction when compared to the measurements. Looking at the 3A reference current, the results are now typical for those observed at the highest reference current. The power predictions are significantly lower than the measurements until the high speed region at which stage they over predict. This however does not appear to have an impact upon the efficiency which shows a high degree of accuracy when compared to the measurements up until the very end of the speed range.

In review of the SEM simulation model, the results are slightly less encouraging with regards to validating the simulation models than the Interroll results. In the case of the low reference current results there are again noticeable degrees of inaccuracy throughout each of the control techniques at the higher speed regions of each test. This has the effect of inaccurately predicting the overall efficiency of the drive system. The power predictions are seen to become even less accurate in the high reference current tests, however this does not seem to impact upon the efficiency predictions which have relatively good accuracy when compared to the measurements. Some element of validation is achieved through the predictions generally following the trends of the measured parameters across the speed range in each of the tests given. Looking again at potential causes for the inaccuracies observed, attention to losses in the VSI component seems to be required in order to address the simulation under estimating the power consumption of the drive system from the DC link. Similarly the motor model appears to require some adjustment in order to both increase the power output but in turn make more consideration of the losses at the higher speed regions.

5.6. Online Parameter Estimations – Voltage Estimation Techniques

The online estimation of phase voltage was introduced in Chapter 3 and the techniques adopted were also described. Chapter 4 described how these techniques are also included in the Portunus simulation model of the FCIV DSP component. This allows for the techniques to be rapidly trialled and adjusted in a simulation environment before being tested in the actual system.

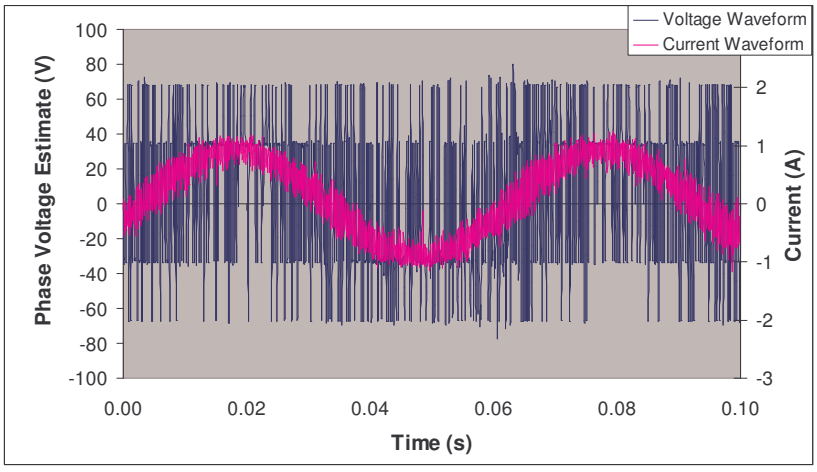

Figure 5-52: Phase A Current and Voltage Estimate of SEM simulation operating under Bang-Bang control

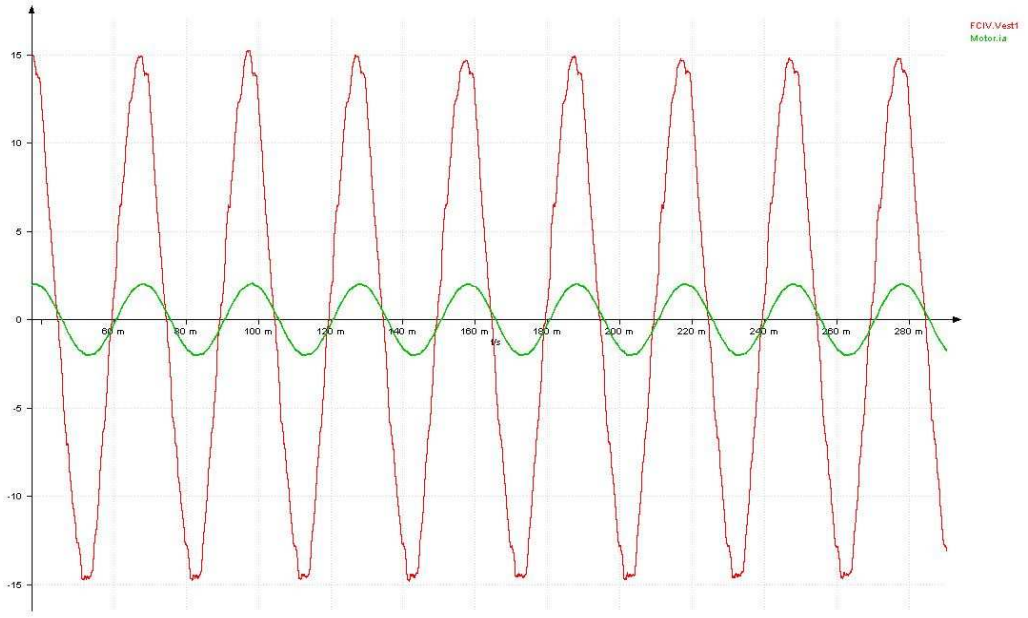

Figure 5-53: Phase A Current and Voltage Estimate of SEM simulation operating under PI control

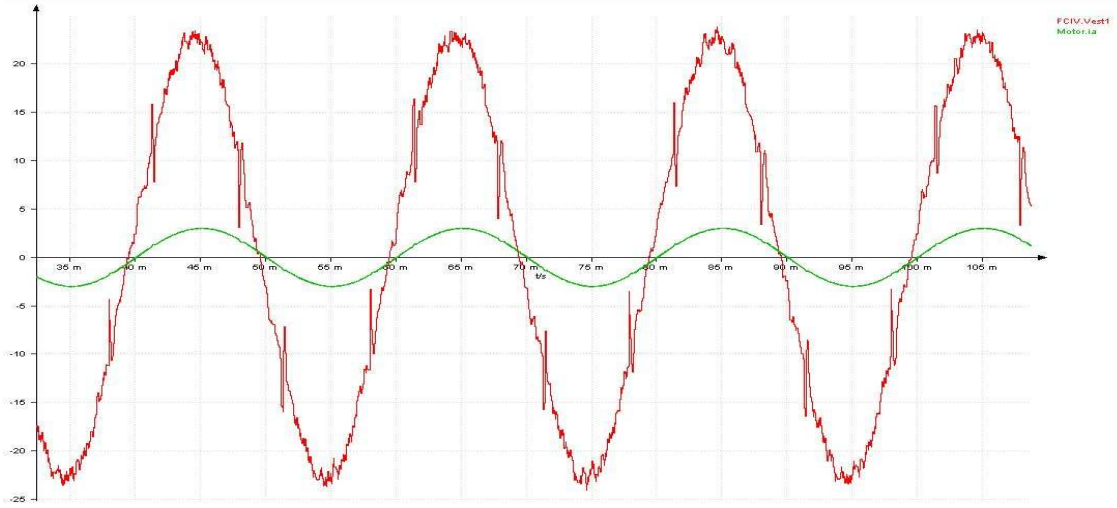

Figure 5-54: Phase A Current and Voltage Estimate of SEM simulation operating under SVPWM control

Figure 5-52 shows the online voltage estimation that the FCIV model component generates when operating the SEM machine under Bang-Bang control; an estimation that has not been presented before this stage in the research and that has been developed in this simulation model. The results are noteably different from the estimated waveforms given in Chapter 3 when operating the PI or SVPWM strategies, in that the voltage waveform does not take a sinusoidal form but rather a step like response between the two extremes of ± (2/3)V_{DC}. However, this may be accurate when the technique is considered as it does operate on a basis of stepping between these extreme values when required as limited by the switch period. Stronger validation of this technique will be

offered in terms of torque estimation – which was the case in the estimations presented in Chapter 3.

Figure 5-53 shows the simulated voltage estimation of the PI controller running at 2A reference current and 1000rpm (the green waveform is the phase A current waveform and the reconstructed voltage waveform is red); it can be compared with the actual results presented in Figure 3-11. The comparison immediately highlights the similarity between the results and the simulations. The voltage waveforms generally correctly align with their respective current waveforms since there is no field weakening being applied there is expected to be very little phase difference between the waveforms.

Figure 5-54 shows the simulated voltage estimation of the SVPWM controller running at 3A reference current and 1500rpm (the green waveform is the phase A current waveform and the reconstructed voltage waveform is red); it can be compared with the results presented in Figure 3-12. There must however be consideration of the fact that despite the SVPWM voltage estimator outlined in Chapter 3 being used in this reconstruction, the actual SVPWM technique outlined in Chapter 2 has not been implemented in the simulation model, instead the technique has been adapted as was described in section 3.2.2 in order to allow for appropriate gate drive signal generation. As only the estimation technique is of interest in this analysis, this adaptation is not of significance. The comparison highlights identical behaviour to the results identified in the PI operated example. The predicted phase voltage estimate magnitude is not significantly different from the measured value obtained in Chapter 3 and the phase alignment and sinusoidal nature of the waveform indicates that the estimator is operating correctly.

If the results of the three techniques are considered, a summary of the simulation results can be provided. Firstly considering the Bang-Bang operated phase voltage measurements and simulations, there is reasonably cause to be satisfied with the results. This is explained by the rigid nature of the control technique which allows only a finite range of voltage levels to be observed on phase A, this means that the FCIV simulation component is essentially forced to use strongly similar control signals to those which are used in the actual test equipment. The explanation for the voltage estimates of the PI and SVPWM being strongly matched in magnitude to their measurements can also be explained in this manner. These two techniques operate a far more flexible approach to determining the inverter control pulses through alternating the duty cycle ranges through a linear 0% to 100% range. The voltage estimation results indicate that the simulation

model is progressing through a similar set of gate drive commands as is used in the actual test system; this notionally validates the model however true validation is very difficult without being capable of comparing the simulated results or actual system estimations with results measured using commercially available equipment. This validation issue can only be solved by integration of the voltage waveform into the online torque estimator.

5.7. Online Parameter Estimations – Torque Estimations

The difficulty in validating the online voltage estimation technique was outlined in Chapter 3. Indeed the lack of a measured phase voltage waveform obtained on commercially available analysis equipment against which to compare the estimations obtained on both the real FCIV and its simulated equivalent gives rise to the ambiguity in the results described in section 5.6. With this being the case then there is an argument for attempting to follow the same validation path in order to verify whether or not the simulation techniques are performing adequately; this gives rise to investigation of the online torque estimations.

Reviewing the torque predictions that were presented in section 5.3, it was shown that for the majority of the speed range the Interroll model predictions were highly accurate particularly at lower reference current levels. The SEM model did not make such accurate predictions but did still manage to predict torque/speed profiles which matched the trends of the measured results. This allows the FCIV simulation model to then attempt to reconstruct the average torque output as was described in Chapter 4. This process can also be compared with the measured results presented in order to validate the technique in simulation.

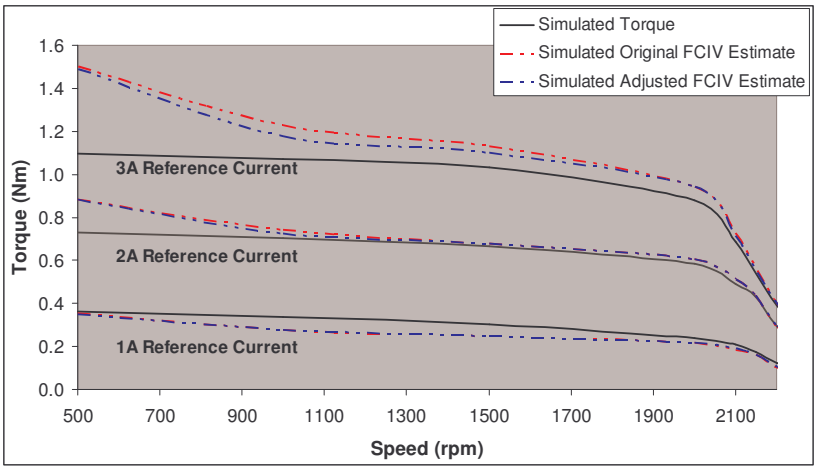

Figure 5-55: Simulation of motor torque versus FCIV torque estimations for SEM machine under Bang-Bang control.

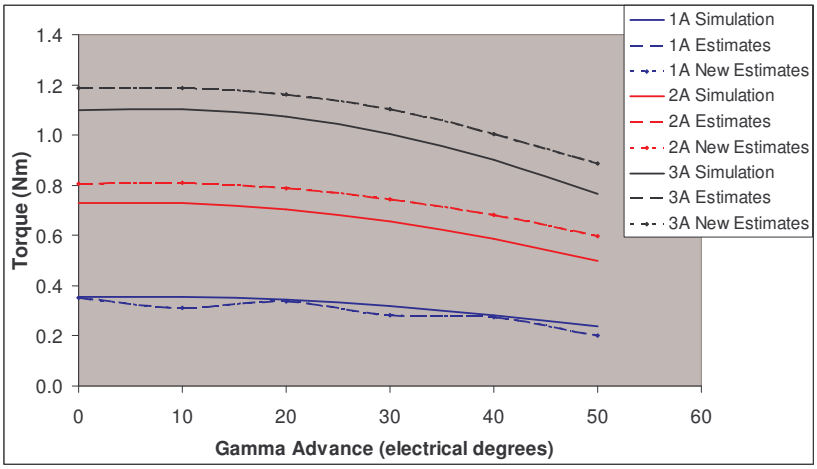

Figure 5-56: Simulation of FCIV Torque estimates response to field weakening for SEM machine under Bang-Bang control at 500rpm operating speed.

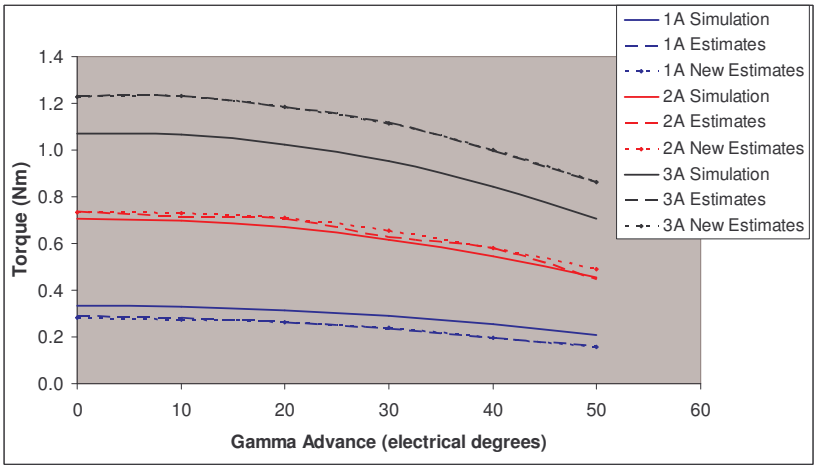

Figure 5-57: Simulation of FCIV Torque estimates response to field weakening for SEM machine under Bang-Bang control at 1000rpm operating speed.

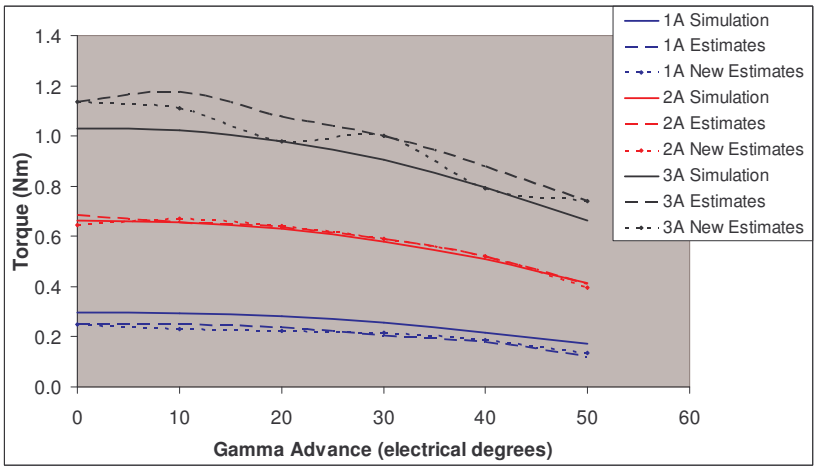

Figure 5-58: Simulation of FCIV Torque estimates response to field weakening for SEM machine under Bang-Bang control at 1500rpm operating speed.

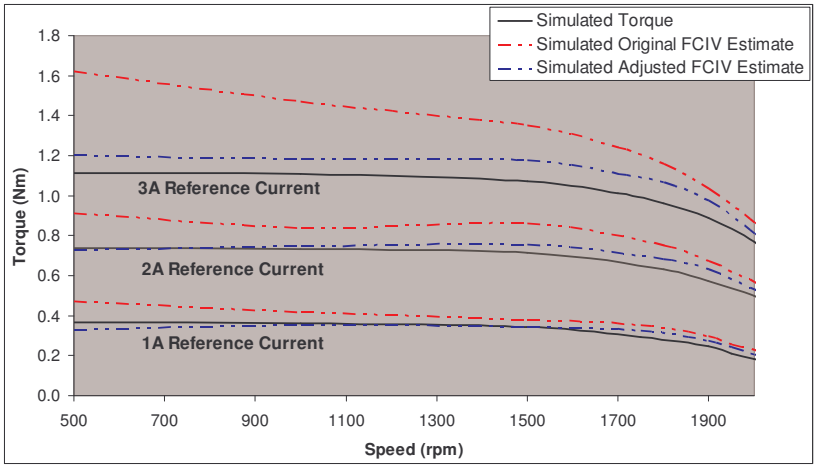

Figure 5-59: Simulation of motor torque versus FCIV torque estimations for SEM machine under PI control.

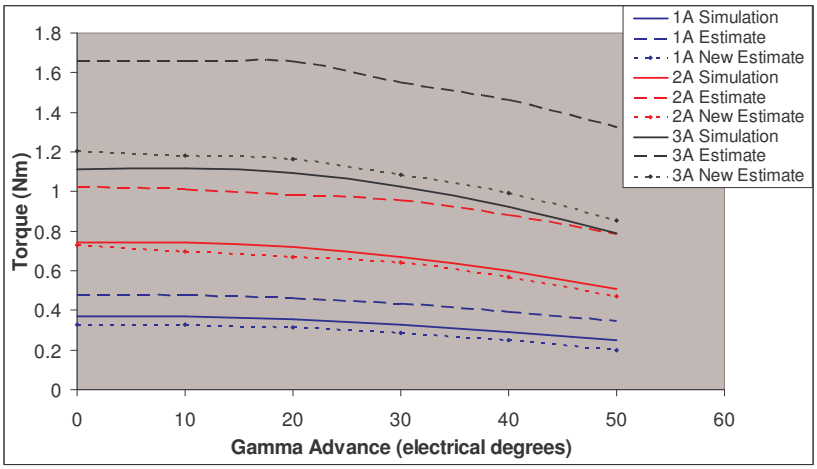

Figure 5-60: Simulation of FCIV Torque estimates response to field weakening for SEM machine under PI control at 500rpm operating speed.

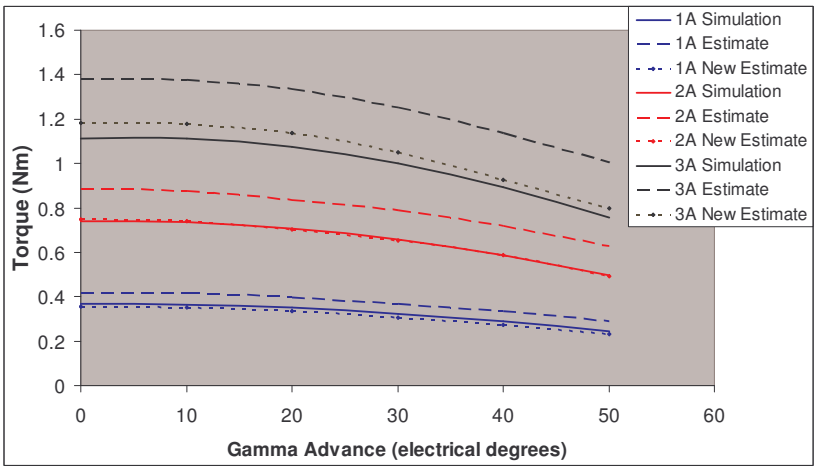

Figure 5-61: Simulation of FCIV Torque estimates response to field weakening for SEM machine under PI control at 1000rpm operating speed.

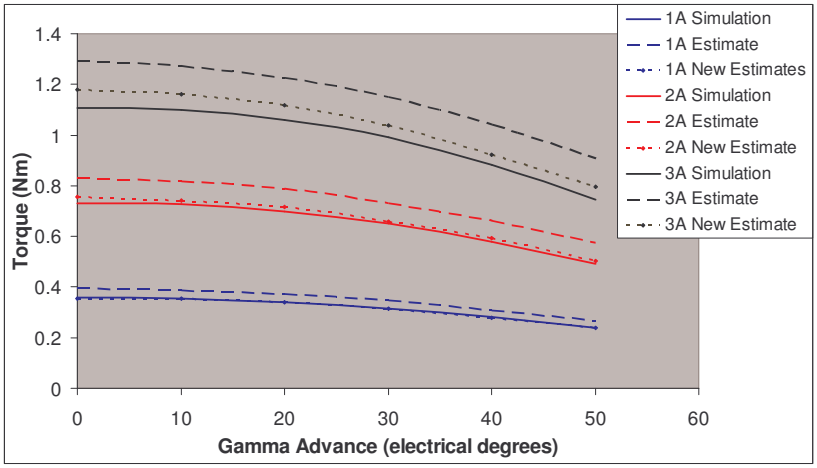

Figure 5-62: Simulation of FCIV Torque estimates response to field weakening for SEM machine under PI control at 1500rpm operating speed.

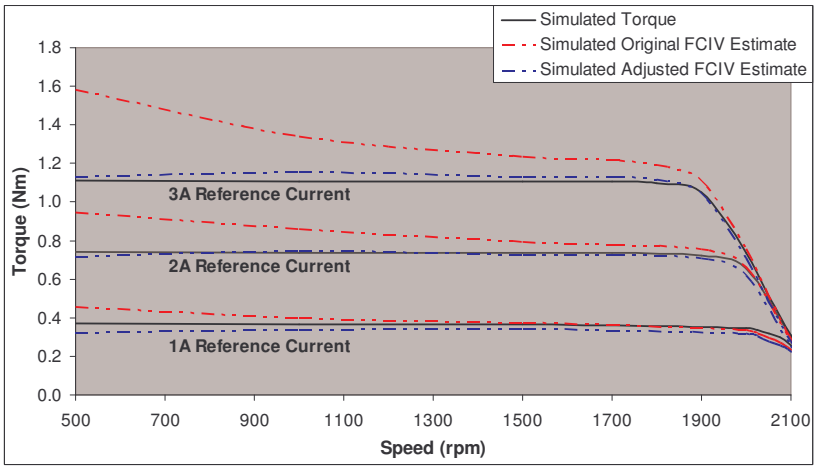

Figure 5-63: Simulation of motor torque versus FCIV torque estimations for SEM machine under SVPWM control.

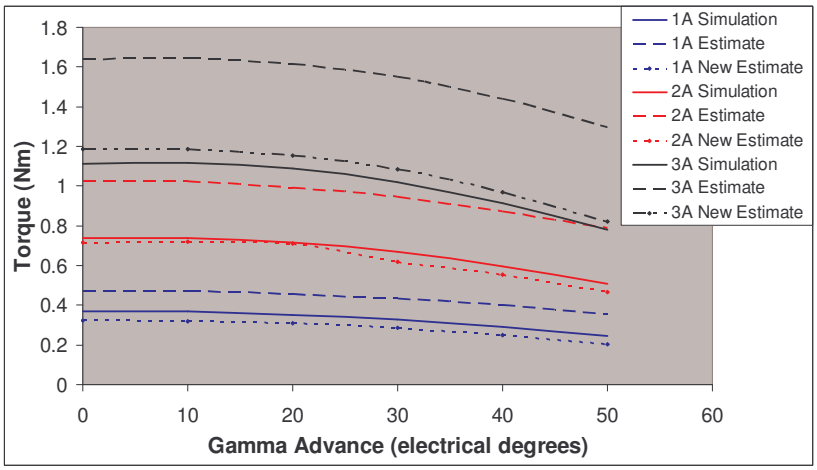

Figure 5-64: Simulation of FCIV Torque estimates response to field weakening for SEM machine under SVPWM control at 500rpm operating speed.

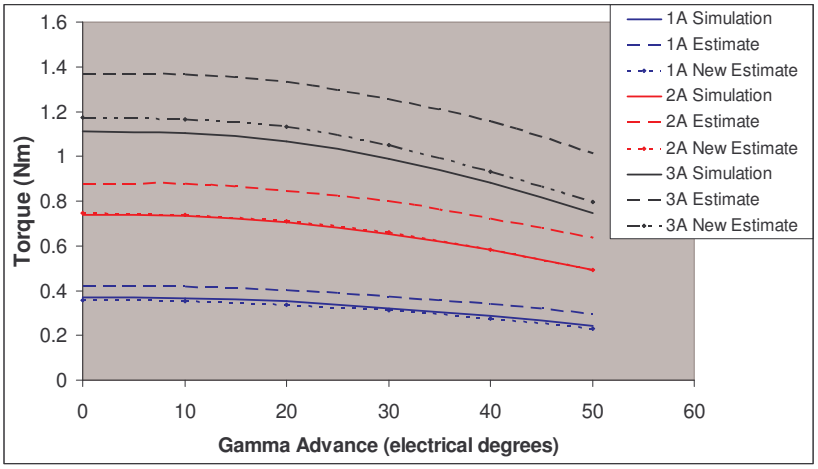

Figure 5-65: Simulation of FCIV Torque estimates response to field weakening for SEM machine under SVPWM control at 1000rpm operating speed.

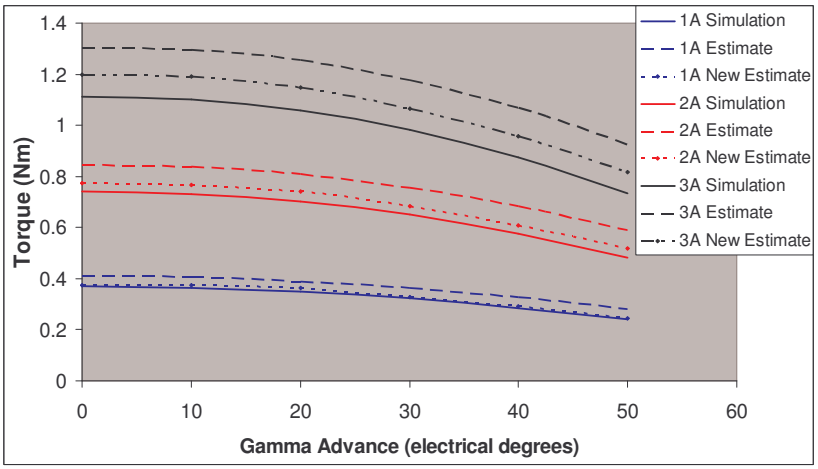

Figure 5-66: Simulation of FCIV Torque estimates response to field weakening for SEM machine under SVPWM control at 1500rpm operating speed.

Figure 5-55 to Figure 5-66 show the predicted performance of the FCIV online torque estimators against the simulated torque outputs. All the results presented in these figures are obtained via the Portunus simulation model of the SEM machine. The simulated torque signals are taken from a signal probe on the output of the motor component. The FCIV estimates are taken from signal probes on the modelled FCIV component. Figure 5-55 shows the torque predictions using the online estimation technique (based on the principles outlined in section 3.2.1). In the initial estimations the poor low speed estimation accuracy is once again observed to be present in the predictions. Further consideration of voltage losses such as those outlined in section 3.4 does not result in the improved accuracy of estimation as has been observed when utilising the PI or SVPWM techniques. This is an indication that further work is required to the Bang-Bang based technique in order to improve this accuracy.

Figure 5-56, Figure 5-57 and Figure 5-58 show the FCIV torque estimations in response to field weakening. The changes in torque output are generally very accurately tracked by the torque estimator across the gamma range, albeit with an offset difference between the torque and its estimated equivalent. The change between the two estimation techniques (with and without considering voltage losses) is also shown to have very little impact upon this offset in all cases. This gives the model some validity however some work is still required before the technique can be trialled on the actual test equipment.

Figure 5-59 shows the predicted performance of the FCIV online torque estimators when operating under PI control; this is the simulated equivalent of Figure 3-51. Comparison of the two figures offers encouraging similarity in performance of the torque estimator in both the actual FCIV and its simulated equivalent. Ignoring the difference in torque magnitudes between the simulation and actual measurements (this has already been highlighted and an explanation has been offered) the trend of over prediction in the low speed region is clearly demonstrated in the original torque estimation technique in both the actual test system and its simulation equivalent. Figure 5-59 clearly shows that this issue is successfully addressed when voltage losses in the VSI stage are considered and this is also the case in the measurements presented in Figure 3-51. The near precise reproduction of the measured results in the simulations makes the model highly suitable for use in the development of modifications and improvements to the technique which could be developed in order to address the constant offset observed in the predictions at the higher reference current levels.

Figure 5-60, Figure 5-61 and Figure 5-62 show the FCIV torque estimations in response to field weakening when operating under PI control; these are the simulated equivalents of Figure 3-52, Figure 3-53 and Figure 3-54 respectively. The results between the simulations and the actual system measurements are again very similar, as was seen to be the case in the Bang-Bang control. Both estimation techniques track the changes in torque output in response to applied gamma advance, however the improved estimation which considers the VSI losses is seen to dramatically improve accuracy of the actual torque estimate in comparison to its value given by the motor component of the model. This is a reflection of the actual results which show that the loss considerations result in the estimations being far closer in value to the measured torque than was originally the case.

Figure 5-63 shows the predicted performance of the online torque estimators when operating under SVPWM control; this is the simulated equivalent of Figure 3-55. In a similar manner as to that observed in the PI case, the comparison of the two figures demonstrates that the simulation is performing very similarly to the actual test system. There is once again some difference in values but the respective trends of the simulation torque and measured torque are identical and the corresponding torque estimator's performance is also near identical between the measurements and the simulations. The introduction of the VSI based losses clearly has a positive impact upon the accuracy of the online torque estimations and this is again demonstrated in Figure 5-63 as it was in Figure 3-55. This adds further use to this simulation model as there are still reference current related loss considerations which would benefit the technique. Such adaptations could be trialled in the simulation model.

Figure 5-64, Figure 5-65 and Figure 5-66 show the FCIV torque estimations in response to field weakening when operating under SVPWM control; these are the simulated equivalents of Figure 3-56, Figure 3-57 and Figure 3-58 respectively. The results of the simulations are again shown to very effectively replicate the results obtained in the actual test measurement. Both estimation techniques track the changes in torque with respect to the gamma advance and the estimate value is far closer to the torque output when the VSI losses are considered.

Reviewing the results presented in this section, the simulation model has shown itself to be of value in the development and validation of the online estimation techniques which have been described in this research. The results have in most cases mirrored the results which were obtained using the online estimation techniques in the actual test system. Intriguingly the simulation of the Bang-Bang estimation technique shows voltage estimation waveforms which, whilst not matching the typical average voltage waveforms observed, do have some credibitly in theoretical analysis. The torque estimates however indicate that the technique requires further development. In the case of the PI and SVPWM controlled versions of the online torque estimators, the performance of simulation is essentially identical to that observed in the actual system measurements. There is a basic offset in torque predictions when compared to the measured values but this has been explained previously as being an issue related to the modelling of the system and is not an effect of the estimation techniques themselves. The similarity of the results obtained also validate the control operation of these two regulators in the FCIV

model component; this is due to the voltage estimation techniques being related to the duty cycle commands generated in the control algorithms. The resultant similarity in simulation and actual measurements indicates that there is strong similarity between the commands being produced in the test system and in the simulations; thus making the simulation model an effective tool in the development of new techniques for the test drive system.

5.8. Conclusions

This chapter has presented the results of tests aimed towards validating the simulation model of the PMSM test system, used throughout this research, which was described in detail in Chapter 4. This validation proceeded through an initial aesthetical analysis of the key characteristics of the two systems (real and simulated), namely the nature of the phase current signals produced under each of the different control strategies which have featured throughout this research. This initial analysis offers strong validation of the system model through consideration of the phase current waveform and how it is directly related to the associated gate drive signals produced by the controller; this validation was supplemented further by consideration of the harmonic analysis of the phase current waveforms. This approach highlighted a strong series of similarities between the measured results and their simulated equivalents; the only exception being in the case of the frequency domain analysis of phase current waveforms obtained under Bang-Bang control. Indeed through further exploration of the frequency behaviour of the Bang-Bang regulator, the simulation model provided a platform upon which algorithms measuring the average switching frequency were developed. This not only allowed for successful verification of such techniques before implementation in the real system but the results obtained from such measurements highlighted that there is significant difference between the average switching frequencies of the actual implementation and its simulated equivalent. This provides suitable motivation for future work to be carried out on modifying the simulation model in order to address this fundamental difference in operation.

This chapter also sought to validate the system model via the production of torque vesus speed profiles which closely resemble that of the measured results presented in Chapter 2. This was carried out on simulations models of both the Interroll machine and the SEM machine. The Interroll simulation model in nearly all tests produced torque values which

were within the error margins of the measured torque taken from tests which were presented in Chapter 2. The only real inaccuracies in the torque profile comparisons were apparent in the high speed regions where there was a noticeable over estimation of the output torque which was proportional to the reference current. These results indicate that the model component was validated to a large extent however the overall simulation model (possibly including the motor component) would have benefitted from consideration of losses that occur in the constant power region. The results from the SEM model however contrasted with this to a significant degree. The same over estimation in the constant power region was noticeable, reinforcing the notion that losses specific to this region of operation are required in the system model. However, during the constant torque region of testing the simulation model was shown to consistently under estimate the output torque of the machine and this was also proportional to the reference current. These results indicate that the SEM motor was not so effectively modelled in the overall simulation model.

In addition to the speed versus torque profiles, the torque profile with respect to field weakening was also addressed in an effort to validate the system model. Field weakening tests were presented in Chapter 3 and have only been made available for the SEM simulation model. Despite this simulation model having inaccuracies in the torque predictions the results have shown that with respect to field weakening the model has an appropriate torque response. In all of the tests results provided the simulation model is shown to track the change in torque output that was observed in measurements taken on the actual system; this is the case regardless of the operating parameters or control strategy being implemented. Thus it can be said that testing with regards to field weakening with the simulation model is very reliable, further validating it for use in PMSM test systems.

The final component of the simulation model's validation is a comparison of the predicted system input and output powers and resultant efficiencies. This involved comparing simulated equivalents of the power and efficiency results presented in Chapter 2. When considering the Interroll model the predictions were closely matched to the measured results, similar in nature to the comparisons of the torque predictions and measurements. At low reference current the comparisons were most similarly matched, the higher reference currents appeared to suffer once again from over prediction in the constant power region. In contrast with these observations, the same comparisons with

the SEM model (which has been shown to be poorer) are less closely matched. The comparisons show that at the lower reference currents the power predictions are generally lower than the measurements particularly in the constant power region, but then at the higher reference current the predictions once again are larger than the measurements in this region. These results indicate that the model is capable of accurately tracking the trends in powers and efficiencies that are observed in the actual test system but that the model would benefit from further work in order to improve accuracy of the predictions.

In addition to contributing a comprehensive validation of the system model, this chapter also sought to further validate the online estimation techniques that were presented in Chapter 3. These tests were conducted specifically on the SEM model as the actual measurements were available for this motor. Considering initially the online voltage estimation technique, the PI and SVPWM voltage waveforms were shown to very closely predict the estimated phase voltage magnitude when compared to the measured results, highlighting the match in operating conditions between the simulation model and the system. In addition to this a technique for making estimations under Bang-Bang control is also explored and the results appear reasonable when reviewed against the criteria which dictate the Bang-Bang technique. In addition to the average phase voltage reconstructions, the online torque estimators were also trialled. The results presented in the case of the Bang-Bang control technique demonstrate that there are further loss considerations which must be made in order to address the poor accuracy of the estimation technique at low speed – the freewheel diode considerations alone do not have a sufficient impact upon the inaccuracy at low speeds. The PI and SVPWM predictors largely replicate the results which were measured with the actual test equipment and were presented in Chapter 3. This contributes evidence supporting the need for future work on the implementation of the Bang-Bang voltage estimation technique as it is clearly demonstrated as having the potential for more accurate prediction. Modification to the voltage estimators which consider inverter related voltage losses were also shown in the simulation model results to be valid, improving the low speed torque estimations in a manner very similar to that which was demonstrated in Chapter 3. This further validates the system simulation model and also the torque estimation techniques that have been presented.

Chapter 6
Conclusions

This thesis has investigated common switching strategies implemented in modern DSP controlled 3 phase permanent magnet synchronous machine drives. This investigation was based upon comparisons of extensive sets of performance criteria obtained on a range of machines under these control strategies. In addition to this the development of online parameter estimation techniques which can be implemented into such a PMSM drive system were developed and validated. Finally this research has also described and sought to validate as extensively as possible a new PMSM test bench simulation model using the simulation development tool Portunus. In this chapter a summary of the key outcomes of each chapter will be summarised and the original contributions of the research will be highlighted. In addition to this any notes on potential future development of the research will also be made where possible.

6.1. Comparing Common PMSM Switching Strategies

Chapter 2 describes in detail the characteristics of the PMSM test bench system that was implemented throughout this research and provides an in depth analysis of the DSP specific implementation of each of the control strategies outlined commenting upon the computational and commercial cost of each approach. This contributes a detailed understanding of the implications that each step of the different controller algorithms has upon the quality of phase current regulation. This analysis also provides greater insight into the proliferation of the PI control technique in industrial PMSM applications.

The analysis of each of the controllers based upon certain performance criteria led to several interesting observations. The major contribution of this analysis is the “on-the-fly” nature of switching the control algorithms such as to minimise the experimental variables being changed between each data acquisition process. The analysis shows that in pursuit of an optimal torque profile the SVPWM controller outperforms the alternatives; however when targeting the largest possible speed range then the Bang-Bang controller would be the more ideal selection. When considering only power losses

and efficiency of the system then all aspects of the analysis highlight the Bang-Bang controller as valid a selection as the other controllers; however this observation must be qualified with the suggestion that the inverter switch device selection has prompted such favourable power loss data.

6.2. Online Parameter Estimation

In Chapter 3 a series of online parameter estimation techniques were presented along with a series of tests designed to validate the techniques outlined. The research describes in greater detail the application of previously developed average phase voltages estimation techniques which were applicable originally to the PI control strategy upon a wye connected machine. This research has expanded upon these strategies contributing a technique for the average phase voltage estimation when operating either a PI or SVPWM controller on either a wye or delta connected machine. Of particular interest in this contribution is the development of the techniques which are implemented whilst operating the specific SVPWM gate drive peripheral of the TMS320 series DSP controller which utilises a minimised switch event strategy in the production of its gate drive signals.

The chapter progresses through efforts to validate the voltage estimation techniques previously outlined. This is done through the development of flux-linkage (ψ) waveforms which have been developed using the average phase voltage estimates. The chapter therefore contributes techniques for generating the flux-linkage waveforms when operating the SVPWM controller and when controlling a delta connected machine. Validation for these techniques is sought through comparison of the ψ-i loops generated in testing with loops generated through the use of the FEA tool PC-BDC. This largely validated the performance of the PI and SVPWM estimation techniques. This however was only possible in the case of the wye connected machine as a delta connected model was unavailable.

In order to validate the techniques developed in the delta connected case, average torque estimators were developed for each of the strategies upon both machine connections. Yet again the chapter contributes an expansion of the existing technique which applied originally only to the wye connected machine. The torque estimator allowed for comparison of estimations with measured results. These results indicate that the PI and SVPWM based techniques are shown to have a high level of accuracy and

reliability (once appropriate loss considerations are taken in the wye connected machine) and thus these techniques are strongly validated.

6.3. Modelling the PMSM Test Bench

In Chapter 4 the development of a new simulation model which describes the PMSM test bench that has been used throughout the research presented in Chapter 2 and Chapter 3. The development of this model focused particularly upon the development of the FCIV DSP controller component and on the inclusion of the motor component which had been developed elsewhere. The main contributions of this chapter include a detailed consideration of the DSP architecture in order to ensure effects such as quantisation and limited resolution – issues the actual test system has to handle. In addition to this the inclusion of the mixed signal motor component allows for detailed analysis of both the electrical input characteristics and the mechanical output properties; parameters which can be directly compared to the actual test equivalents. The chapter validates the model as much as possible in ensuring the theoretically correct operation of each of the current controllers available to the FCIV. The successful regulation of the reference currents validates the model in this capacity.

6.4. Validating the PMSM Test Bench Simulation Model

In Chapter 5 an extensive validation of the simulation model was presented. Initially this was approached via an aesthetical comparison of the phase current waveforms produced under test with those produced in the simulation model. In the time domain the simulations were shown to produce phase current waveforms under each control strategy similar to those which were presented in Chapter 2. This was supplemented in the case of the PI and SVPWM controllers through analysis of the predicted performance in the frequency domain. However investigation in to the frequency domain performance of the Bang-Bang controller was less conclusive and the further investigation into the average switching frequency of this technique showed that the simulated predictions were significantly greater than in the measured case.

The validation of the simulation models then looked into a comparison of the predicted torque profiles versus speed and under field weakening conditions. The results in this analysis varied between the two separate motor models. In the interroll case the simulation model was shown to accurately predict the torque performance under each

control strategy in all tests, the only areas of poor accuracy were in the constant power regions at the higher reference currents. In the case of the SEM model the results were less convincing due to a consistent under prediction of the estimated torque except in the constant power regions where again torque would be over predicted. This leads to a validation of the simulation models but highlights the level of detail which is required in the accurate modelling of the motor component. All simulation tests under field weakening indicate a valid prediction performance when compared to the measured results obtained in Chapter 3.

This chapter continued its validation of the simulation model through comparisons of the drive power and efficiency calculations; taking into consideration the input electrical power to the drive system and the output rotational power, calculating the efficiency based on this power conversion and then comparing these predictions to the measured results presented in Chapter 2. The results of this comparison are similar in general to the results of the torque profile comparisons. The Interroll model predicts performance which is most closely matched to its measured performance however there are inaccuracies introduced in the constant power regions which are proportional to the reference current. The SEM model continues to under predict the power measurements except in the constant power regions where over prediction is prominent once again.

The chapter concludes with further validating the online estimation techniques which were outlined in Chapter 3. The average phase voltage estimator was tested in the FCIV component of the simulation model. The results obtained show that the voltage estimates predicted in the simulation model closely match those which are presented in Chapter 3. This leads to the implementation of the online torque estimators which have varying results. A version of the Bang-Bang torque estimator is predicted to operate in the same manner as has been observed for the PI and SVPWM controllers – however is not shown to respond to voltage drop considerations in as positive manner as is the case in the PI and SVPWM techniques. This indicates a potential for the development of a successful online torque estimator under Bang-Bang control conditions; however additional considerations need to be made in order to address the over estimation at lower speeds. In the case of the PI and SVPWM control based estimators, these are shown to behave in a very similar manner to that which was observed in Chapter 3. Further to this the modification to each technique which considers voltage losses in the inverter stage is shown through simulation to have the same effect it has in practise (as

was shown in Chapter 3). This outcome validates not only the renewed torque estimation techniques but also the simulation model in general.

6.5. Future Work

Throughout this research and the subsequent compilation of this thesis, a number of issues have arisen which would be suitable for further exploration in order to supplement this research. These are as follows:

- In the work on comparing current control strategies, further testing could be conducted on the same set of motors using alternative VSI devices. This would allow for evaluation of the impact that switch device selection has on the calculated power losses and efficiency measured throughout the drive system.
- In the work regarding online estimation there is clearly an opportunity to develop the Bang-Bang dedicated average phase voltage estimator and its subsequent flux-linkage and torque estimators. The results obtained from the new simulation model described in Chapter 5 highlight the potential for the methods described to reliably predict the output torque of the motor – albeit some additional work is clearly required to achieve this. In respect to the comparison of measured and predicted i-ψ loops, a suitable delta connected model could also be acquired in order to generate FEA based data which can be compared to measured results.
- The new simulation model described in Chapter 4 could still benefit from a great deal of further development. In general a motor component which could be applied to the delta connected machine would allow for a greater volume of comparison with measured results. In addition to this there are greater loss considerations which could be investigated in order to address the over prediction of torque in the constant power regions of the torque profile which was observed in most test results. In addition to this an additional development of the model could include the development of the SVPWM gate drive generation system used by the tms320 DSP controller of the FCIV which is described in Chapter 3. This could replace the version used in the existing FCIV simulation model.

References

[1] C. Cossar, T. J. E. Miller, M. Popescu, M. McGilp, and M. Olaru, "A New On-Line Torque Estimator for Brushless Permanent Magnet Motor Drives: Validation through the i-psi Diagram," Conference Record of the 2006 IEEE 41st IAS Annual Meeting in Industry Applications Conference, 2006 pp. 1657-1662.

[2] D. Staton, M. Popescu, T. Barucki, "Brushless Permanent Magnet Motor Modelling in Portunus: Inputs of Stator and Rotor Temperature and Outputs of Losses and link to Reduced Node Thermal Model Imported from Motor-CAD," 2010.

[3] K. J. Binns, "Permanent magnet synchronous motors," IEE Colloquium in Permanent Magnet Machines, 1988, pp. 3/1-3/3.

[4] J R Hendershot and T.J.E. Miller, Design of Brushless Permanent-Magnet Machines. 102 Triano Circle, Venice, Florida, 34292, USA: Motor Design Books LLC, 2010. pp. 3, 375.

[5] T. M. Jahns and W. L. Soong, "Pulsating torque minimization techniques for permanent magnet AC motor drives - A review," IEEE Transactions on Industrial Electronics, vol. 43, pp. 321-330, Apr 1996.

[6] B. Grcar, P. Cafuta, G. Stumberger, and A. M. Stankovic, "Control-based reduction of pulsating torque for PMAC machines," IEEE Transactions on Energy Conversion, vol. 17, pp. 169-175, 2002.

[7] D. M. Ionel, M. Popescu, M. I. McGilp, T. J. E. Miller, and S. J. Dellinger, "Assessment of torque components in brushless permanent-magnet machines through numerical analysis of the electromagnetic field," IEEE Transactions on Industry Applications, vol. 41, pp. 1149-1158, 2005.

[8] T. Nakai and H. Fujimoto, "Harmonic current suppression method of PMSM based on repetitive perfect tracking control," Iecon 2007: 33rd Annual Conference of the IEEE Industrial Electronics Society, Vols 1-3, Conference Proceedings, pp. 1049- 1054, 2007.

[9] S. Lerdudomsak, S. Doki, and S. Okuma, "A novel current control system for PMSM considering effects from inverter in overmodulation range," 2007 International Conference on Power Electronics and Drive Systems, Vols 1-4, pp. 999-1005 1897, 2007.

[10] Jacek F. Gieras and Mitchell Wing, “Permanent Magnet Motor Technology: Design and Applications”, Second Edition, Revised and Expanded, 2nd ed. Basel: Marcel Dekker, Inc, 2002, pp 16-28

[11] Lee Suk-Hee, Lee Geun-Ho, Kim Sung-Il, and Hong Jung-Pyo, "A novel control method for reducing torque ripple in PMSM applied for Electric Power Steering," International Conference in Electrical Machines and Systems, ICEMS 2008, pp. 3142-3145.

[12] Chen Hui, Jin Canlong, Jiang Ping, Gong Xiaoping, and Feng Xiangzhi, "PMSM Servo Drive System for Electric Power Steering Based on Two-Degree-of-Freedom Torque Control," IEEE International Conference in Industrial Technology, ICIT 2006, pp. 2901-2906.

[13] F. Fukudome, "Technical Trend of Electric Components for Electrical Power Steering Systems," KOYO Engineering Journal, vol. No. 163, pp. 31-35, 2003.

[14] R. G. Shriwastava and M. B. Diagavane, "Electric power steering with Permanent magnet synchronous motor drive used in automotive application," 2011 1st International Conference in Electrical Energy Systems (ICEES), pp. 145-148.

[15] I. Edward, S. Wahsh, and M. a Badr, "Analysis of PMSM drives for electric vehicles," in SICE '98. Proceedings of the 37th SICE Annual Conference, International Session Papers, 1998, pp. 979-984.

[16] Chung Myung-Jin and Chun Jang-Sung, "Development of driving motor system for small electric vehicle," International Conference in Control, Automation and Systems, ICCAS 2008, pp. 1429-1432.

[17] J. O. Estima and A. J. M. Cardoso, "Performance analysis of a PMSM drive for hybrid electric vehicles," International Conference in Electrical Machines (ICEM 2010 XIX), pp. 1-6.

[18] A. M. Bazzi and P. T. Krein, "Comparative evaluation of machines for electric and hybrid vehicles based on dynamic operation and loss minimization," Energy Conversion Congress and Exposition (ECCE), 2010, pp. 3345-3351.

[19] Jiaqun Xu, Yanliang Xu, and Renyuan Tang, "Development of full digital control system for permanent magnet synchronous motor used in electric vehicle", Proceedings of the Fifth International Conference in Electrical Machines and Systems, ICEMS 2001, pp. 554-556 vol.1

[20] U.S.A Toyota Motor Sales. "Toyota Prius - 2011 Performance & Specifications." Internet: http://www.toyota.com/prius-hybrid/specs.html, 2011 [Accessed: 18/04/2011] – A copy of this webpage has been taken and can be accessed in the DVD appendix.

[21] D. G. Dorrell, M. Popescu, L. Evans, D. A. Staton, and A. M. Knight, "Comparison of permanent magnet drive motor with a cage induction motor design for a hybrid electric vehicle," Power Electronics Conference (IPEC) 2010, pp. 1807-1813.

[22] J. R. Hendershot and T. J. E. Miller, Design of Brushless Permanent Magnet Motors: Magna Physics Publishing Oxford Clarendon Press, 1994. pp 2-1 to 2-49.

[23] N. Matsui and H. Ohashi, "DSP-based adaptive control of a brushless motor," Conference Record of the 1988 IEEE Industry Applications Society Annual Meeting, 1988, pp. 375-380 vol.1.

[24] P. Pillay, C. R. Allen, and R. Budhabhathi, "DSP-based vector and current controllers for a permanent magnet synchronous motor drive", Conference Record of the IEEE Industry Applications Society Annual Meeting, 1990, pp. 539-544 vol.1.

[25] D. W. Novotny and T. A. Lipo, Vector Control and Dynamics of AC Drives. New York: Oxford University Press Inc., 1996. pp 10

[26] F. Blaabjerg, U. Jaeger, and S. Munk-Nielsen, "Power losses in PWM-VSI inverter using NPT or PT IGBT devices," IEEE Transactions on Power Electronics, 1995, Vol. 10, pp. 358-367.

[27] B. P. Muni, A. V. Gokuli, and S. N. Saxena, "Gating and protection of IGBT in an inverter", Proceedings from the International Conference in Industrial Electronics, Control and Instrumentation, IECON '91, vol. 1, pp 662-667.

[28] Tatsuo Morita, Satoshi Tamura, Yoshiharu Anda, Masahiro Ishida, Yasuhiro Uemoto, Tetsuzo Ueda, Tsuyoshi Tanaka, and Daisuke Ueda, "99.3% Efficiency of three-phase inverter for motor drive using GaN-based Gate Injection Transistors," Twenty-Sixth Annual IEEE Applied Power Electronics Conference and Exposition (APEC), 2011, pp. 481-484.

[29] S. Tamura, Y. Anda, M. Ishida, Y. Uemoto, T. Ueda, T. Tanaka, and D. Ueda, "Recent Advances in GaN Power Switching Devices," Compound Semiconductor Integrated Circuit Symposium (CSICS), 2010, pp. 1-4.

[30] Randall D. Adams and Robert S. Fox, "Several Modulation Techniques for a Pulsewidth Modulated Inverter", IEEE Transactions on Industry Applications, 1972, vol. IA-8, pp. 636-643.

[31] Trevor L. Grant and Thomas H. Barton, "Control Strategies for PWM Drives", IEEE Transactions on Industry Applications, 1980, vol. IA-16, pp. 211-216.

[32] M. P. Kazmierkowski and L. Malesani, "Current control techniques for three-phase voltage-source PWM converters: a survey", IEEE Transactions on Industrial Electronics, 1998, vol. 45, pp. 691-703.

[33] David M. Brod and Donald W. Novotny, "Current Control of VSI-PWM Inverters", IEEE Transactions on Industry Applications, 1985, vol. IA-21, pp. 562-570.

[34] William McMurray, "Modulation of the Chopping Frequency in DC Choppers and PWM Inverters Having Current-Hysteresis Controllers", IEEE Transaxtion on Industry Applications, 1984, vol. IA-20, pp. 763-768.

[35] P. Freere and P. Pillay, "Design and Evaluation of Current Controllers for PMSM Drives," IECON 90, Vols 1 and 2, pp 1193-1198, 1343.

[36] B. K. Bose, "An adaptive hysteresis-band current control technique of a voltage fed PWM inverter for machine drive system", IEEE Transactions on Industrial Electronics, 1990, vol. 37, pp 402-408.

[37] L. Malesani, P. Tenti, E. Gaio, and R. Piovan, "Improved current control technique for VSI PWM inverters with constant modulation frequency and extended voltage range", Conference Record of the 1988 IEEE Industry Applications Society Annual Meeting, pp 722-727.

[38] A. Kovari, "Hybrid Current Control Algorithm for Voltage Source Inverters", First IEEE Eastern European Conference on the Engineering of Computer Based Systems ECBS-EERC '09, pp 65-70.

[39] A. N. Tiwari, P. Agarwal, and S. P. Srivastava, "Performance investigation of modified hysteresis current controller with the permanent magnet synchronous motor drive", IET Electric Power Applications, vol. 4, pp 101-108.

[40] S. Bolognani and M. Zigliotto, "Full-digital predictive hysteresis current control for switching losses minimisation in PMSM drives," International Conference on in Power Electronics, Machines and Drives, 2002, pp 61-67.

[41] Guoqiang Chen and Jianli Kang, "Simulation and Analysis of Hysteresis Current Controller in Motor Control", International Conference in Electrical and Control Engineering (ICECE), 2010, pp 4196-4199.

[42] Z. Yu, A. Mohammed, and I. Panahi, "A review of three PWM techniques", Proceedings of the 1997 American Control Conference, vol. 1, pp 257-261.

[43] A. I. Maswood, "A PWM voltage source inverter with PI controller for instantaneous motor current control", Proceedings of 1995 International Conference in Power Electronics and Drive Systems, vol.2, pp 834-837.

[44] A. Suyitno, J. Fujikawa, H. Kobayashi, and Y. Dote, "Variable-structured robust PI controller by fuzzy logic for servomotor", Conference Proceedings of the IEEE International Symposium on Industrial Electronics, ISIE'93 - Budapest, pp 734-739.

[45] I. Miki, T. Kumano, S. Takahashi, and T. Yamada, "Fuzzy PI auto-tuning system for vector-controlled induction motor drives," Conference Record of the Power Conversion Conference, Yokohama, 1993, pp 678-682.

[46] Siong Tan Chee, B. Ismail, M. F. Mohammed, M. F. N. Tajuddin, S. Rafidah, A. Rahim, and Z. M. Isa, "Study of Fuzzy and PI controller for Permanent-Magnet Brushless DC motor drive", 4th International Power Engineering and Optimization Conference (PEOCO), 2010, pp 517-521.

[47] Rupprecht Gabriel, Werner Leonhard, and Craig J. Nordby, "Field-Oriented Control of a Standard AC Motor Using Microprocessors", IEEE Transactions on Industry Applications, 1980, vol. IA-16, pp 186-192.

[48] Edith Clarke, "Problems Solved by Modified Symmetrical Components," Ibid, Nov. 1938 vol. 41, pp. 488-94.

[49] R. H. Park, "Two-reaction theory of synchronous machines generalized method of analysis-part I,", Transactions of the American Institute of Electrical Engineers, 1929, vol. 48, pp 716-727.

[50] R. H. Park, "Two-reaction theory of synchronous machines-II," Transaction of the American Institute of Electrical Engineers, 1933, vol. 52, pp 352-354.

[51] Edward W. Kimbark, "Two-Phase Co-ordinates of a Three-Phase Circuit", Transactions of the American Institute of Electrical Engineers, 1939, vol. 58, pp 894-910.

[52] Mo-Shing Chen and W. C. Duesterhoeft, "Transients in Synchronous Machines with Balanced Capacitive Loads", IEEE Transactions on Power Apparatus and Systems, 1964, vol. 83, pp 1242-1245.

[53] R. E. Vowels, "Transient analysis of synchronous machines," Proceedings of the IEE Institution Monographs, 1952, vol. 99, pp 204-216.

[54] M. Stulrajter, V. Hrabovcova, and M. Franko, "Permanent magnets synchronous motor control theory," Journal of Electrical Engineering-Elektrotechnicky Casopis, 2007, vol. 58, pp 79-84.

[55] Peter Vas, Vector control of AC machines. Oxford [England]: Oxford University Press, 1990.

[56] Gerhard Pfaff, Alois Weschta, and Albert F. Wick, "Design and Experimental Results of a Brushless AC Servo Drive", IEEE Transactions on Industry Applications, 1984, vol. IA-20, pp 814-821.

[57] Karoly Pal Kovacs and Istvan Racz, “Transiente Vorgänge in Wechselstrommaschinen”, Budapest, Verlag der Ungarischen Akademie der Wissenschaften, 1959.

[58] Alberto J. Pollmann, "Software Pulsewidth Modulation for Control of AC Drives," IEEE Transactions on Industry Applications, 1986, vol. IA-22, pp 691-696.

[59] J. Holtz and E. Bube, "Field-oriented asynchronous pulsewidth modulation for high performance AC machine drives operating at low switching frequency", Conference Record of the 1988 IEEE Industry Applications Society Annual Meeting, pp 412-417.

[60] J. Holtz and U. Boelkens, "Direct frequency convertor with sinusoidal line currents for speed-variable AC motors," IEEE Transactions on Industrial Electronics, 1989, vol. 36, pp 475-479.

[61] J. Holtz and E. Bube, "Field-oriented asynchronous pulse-width modulation for high-performance AC machine drives operating at low switching frequency," IEEE Transactions on Industry Applications, 1991, vol. 27, pp 574-581.

[62] J. Holtz, W. Lotzkat, and A. M. Khambadkone, "On continuous control of PWM inverters in the overmodulation range including the six-step mode," IEEE Transaction on Power Electronics, 1993, vol. 8, pp 546-553.

[63] J. Rodriguez, E. Wiechmann, J. Holtz, A. Suarez, and M. Sepulveda, "IGBT inverter with vector modulation," IEEE International Symposium on Industrial Electronics, 1994, Symposium Proceedings, pp 131-136.

[64] L. Springob and J. Holtz, "High-bandwidth current control for torque-ripple compensation in PM synchronous machines," IEEE Transactions on Industrial Electronics, 1998, vol. 45, pp. 713-721.

[65] C. Bader and W. Stephan, "Comparison of electrical drives for road vehicles," IEEE Transactions on Vehicular Technology, 1977, vol. 26, pp. 123-128.

[66] Akira Nabae, Kenichi Otsuka, Hiroshi Uchino, and Ryoichi Kurosawa, "An Approach to Flux Control of Induction Motors Operated with Variable-Frequency Power Supply", IEEE Transactions on Industry Applications, 1980, vol. IA-16, pp 342-350.

[67] W. L. Soong and T. J. E. Miller, "Field-weakening performance of brushless synchronous AC motor drives," Electric Power Applications - IEE Proceedings, 1994, vol. 141, pp 331-340.

[68] S. Chaithongsuk, B. Nahid-Mobarakeh, J. Caron, N. Takorabet, and F. Meibody- Tabar, “Optimal Design of Permanent Magnet Motors to Improve Field Weakening Performances in Variable Speed Drives," IEEE Transactions on Industrial Electronics, pp. 1-1.

[69] M. F. Rahman, L. Zhong, and Lim Khiang Wee, "A direct torque-controlled interior permanent magnet synchronous motor drive incorporating field weakening," IEEE Transactions on Industry Applications, 1998, vol. 34, pp. 1246-1253.

[70] Tang Lixin, Zhong Limin, M. F. Rahman, and Y. Hu, "A novel direct torque controlled interior permanent magnet synchronous machine drive with low ripple in flux and torque and fixed switching frequency," IEEE Transactions on Power Electronics, 2004, vol. 19, pp 346-354.

[71] G. W. Penney, "Short-Circuit Torque in Synchronous Machines without Damper Windings," Transactions of the American Institute of Electrical Engineers, 1929, vol. 48, pp 1230-1240.

[72] D. Howe and W. Low, "Design and dynamic calculations for miniature permanent magnet stepper motors," IEEE Transactions on Magnetics, 1984, vol. 20, pp 1768-1770.

[73] S. Clenet, S. Astier, J. Cros, Y. Lefevre, and M. Lajoie-Mazenc, "An efficient torque speed characteristic calculation method for brushless CAD using optimization techniques," Fifth European Conference in Power Electronics and Applications, 1993, pp 474-479.

[74] T. J. E. Miller, "Optimal design of switched reluctance motors," IEEE Transactions on Industrial Electronics, 2002, vol. 49, pp 15-27.

[75] Huang Surong, M. Aydin, and T. A. Lipo, "Torque quality assessment and sizing optimization for surface mounted permanent magnet machines," Conference Record of the 2001 IEEE Thirty-Sixth IAS Annual Meeting in Industry Applications Conference, pp 1603-1610.

[76] A. P. Wu and P. L. Chapman, "Cancellation of torque ripple due to nonidealities of permanent magnet synchronous machine drives," IEEE 34th Annual Specialist Conference in Power Electronics, PESC '03, pp 256-261.

[77] T. J. E. Miller, M. Popescu, C. Cossar, and M. McGilp, "Performance estimation of interior permanent-magnet brushless motors using the voltage-driven flux-MMF diagram," IEEE Transactions on Magnetics, 2006, vol. 42, pp 1867-1872.

[78] T. J. E. Miller, M. Popescu, C. Cossar, M. McGilp, and J. A. Walker, "Calculating the interior permanent-magnet motor," IEEE International Conference on Electric Machines and Drives, IEMDC'03, pp 1181-1187.

[79] T. J. E. Miller, M. Popescu, C. Cossar, M. I. McGilp, M. Olaru, A. Davies, J. Sturgess, and A. Sitzia, "Embedded Finite-Element Solver for Computation of Brushless Permanent-Magnet Motors," IEEE Transactions on Industry Applications, 2008, vol. 44, pp. 1124-1133.

[80] G. Morton and C. Cossar, "A performance comparison of three common PWM switching current control strategies," IECON 2010 - 36th IEEE Annual Conference on Industrial Electronics, pp 754-759.

[81] B. K. Bose, "Adjustable speed AC drives: A technology status review," Proceedings of the IEEE, vol. 70, pp. 116-135, 1982.

[82] B. K. Bose, "Power Electronics - an Emerging Technology," Industrial Electronics Society IECON '88 Proceedings, pp. 501-508.

[83] B. K. Bose, "Technology trends in microcomputer control of electrical machines," IEEE Transactions on Industrial Electronics, 1988, vol. 35, pp. 160-177.

[84] SPEED Laboratory. "SPEED Flexible Controllers." Internet: http://www.speedlab.co.uk/hardware.pdf, [Accessed: 30-03-2012]. This webpage can no longer be accessed and no copies have been taken for inclusion on the DVD appendix.

[85] Texas Instruments. "TMS320F2812 eZdsp Start Kit (DSK)." Internet: http://www.ti.com/tool/TMDSEZD2812, [Accessed: 30-03-2012]. A copy of this webpage is stored on the DVD appendix.

[86] Texas Instruments, "TMS320F2810, TMS320F2811, TMS320F2812, TMS320C2810, TMS320C2811, TMS320C2812 Digital Signal Processors Literature Number: SPRS174O," 2007.

[87] P. Pillay and R. Krishnan, "Modelling, simulation, and analysis of permanentmagnet motor drives. II. The brushless DC motor drive," IEEE Transactions on Industry Applications, 1989, vol. 25, pp 274-279.

[88] M. A. Rahman, T. S. Radwan, A. M. Osheiba, and A. E. Lashine, "Analysis of current controllers for voltage-source inverter," IEEE Transactions on Industrial Electronics, 1997, vol. 44, pp 477-485.

[89] B. K. Bose, "An Adaptive Hysteresis-Band Current Control Technique of a Voltage- Fed Pwm Inverter for Machine Drive System," Annual Conference of Industrial Electronics Society, IECON '88, pp 684-690.

[90] M. S. Dawande and G. K. Dubey, "Bang bang current control with predecided switching frequency for switch mode rectifiers," Proceedings of 1995 International Conference on Power Electronics and Drive Systems, pp. 538-542.

[91] P. C. Kjaer, C. Cossar, and T. J. E. Miller, "Very high bandwidth digital current controller for high-performance motor drives," Sixth International Conference on Power Electronics and Variable Speed Drives, 1996, pp 185-190.

[92] S. Bennett, “A History of Control Engineering,” 1930-1955: IEE Control Engineering Series.

[93] J G Ziegler and N B Nichols, "Optimum settungs for automatic controllers," Trans. ASME, vol. 64, pp. 759-768.

[94] Song Wang, Shuang-shuang Shi, and Chao Chen, "Simulation of PMSM vector control system based on non-linear PID and its easy DSP realization," Control and Decision Conference, CCDC '09, p 949-953.

[95] P. Kazmierkowski and M. A. Dzieniakowski, "Review of current regulation techniques for three-phase PWM inverters," 20th International Conference on Industrial Electronics, Control and Instrumentation, IECON '94, pp.567-575.

[96] Hwang Seon-Hwan and Kim Jang-Mok, "Dead Time Compensation Method for Voltage-Fed PWM Inverter," IEEE Transactions on Energy Conversion, vol. 25, pp. 1-10.

[97] C. Grolling, W. Schumacher, and B. Amlang, "Modelling of quantization effects in current control for a synchronous servo drive," European Conference on Power Electronics and Applications, 2007, pp. 1-11.

[98] D. N. Zmood and D. G. Holmes, "Stationary frame current regulation of PWM inverters with zero steady-state error," IEEE Transactions on Power Electronics, 2003, vol. 18, pp. 814-822.

[99] Ang Kiam Heong, G. Chong, and Li Yun, "PID control system analysis, design, and technology," IEEE Transactions on Control Systems Technology, 2005, vol. 13, pp. 559-576.

[100] R. Souad and H. Zeroug, "Comparison between direct torque control and vector control of a permanent magnet synchronous motor drive," Power Electronics and Motion Control Conference, EPE-PEMC 2008, pp. 1209-1214.

[101] Yu Shuanghe, Yang Zhenqiang, Liu Shuang, and Zheng Kai, "Analysis and implementation of digitalized vector control for PMSM with switching control”, 3rd International Symposium on Systems and Control in Aeronautics and Astronautics (ISSCAA), 2010, pp. 912-917.

[102] R. K. Sharma, V. Sanadhya, L. Behera, and S. Bhattacharya, "Vector Control Of A Permanent Magnet Synchronous Motor," Proceedings of the INDICON 2008 IEEE Conference & Exhibition on Control, Communications and Automation, Vol I, pp. 81-86.

[103] H. W. van der Broeck, H. C. Skudelny, and G. V. Stanke, "Analysis and realization of a pulsewidth modulator based on voltage space vectors," IEEE Transactions on Industry Applications, 1988, vol. 24, pp. 142-150.

[104] V. Blasko, "A hybrid PWM strategy combining modified space vector and triangle comparison methods," 27th Annual IEEE Conference in Power Electronics Specialists PESC '96, pp. 1872-1878.

[105] Juming Song, Ming Zhou, and Yanmin Su, "Study of optimal efficient control of permanent magnet synchronous motor," Sixth International Conference on Electrical Machines and Systems ICEMS 2003, pp. 41-44.

[106] G. H. Morton and C. Cossar, "The accuracy of the classical machine phasor diagram and on-line measurements for permanent magnet machines," Proceedings of the 2011-14th European Conference on Power Electronics and Applications (EPE 2011), pp. 1-9.

[107] "Recommended Phasor Diagram for Synchronous Machines," IEEE Transactions on Power Apparatus and Systems, 1969, pp. 1593-1610.

[108] L. Petkovska and G. Cvetkovski, "FEM Based Simulation of a Permanent Magnet Synchronous Motor Performance Characteristics," IEEE 5th International Conference in Power Electronics and Motion Control, IPEMC 2006, pp. 1-5.

[109] A. Gebregergis, M. Islam, T. Sebastian, and R. Ramakrishnan, "Evaluation of inductance in a permanent magnet synchronous motor," 2011 IEEE International Conference on Electric Machines & Drives (IEMDC), pp. 1171-1176.

[110] Zhai Li and Li Hefei, "Modeling and simulating of SVPWM control system of induction motor in electric vehicle," IEEE International Conference on in Automation and Logistics, ICAL 2008, pp. 2026-2030.

[111] YingYing Jia, XuDong Wang, LiangLiang Mao, ShuCai Yang, and HaiXing Zhang, "Application and Simulation of SVPWM in three phase inverter," 6th International Forum on in Strategic Technology (IFOST 2011), pp. 541-544.

[112] Xuelei Song, Xuhui Wen, Xinhua Guo, and Feng Zhao, "Dead-time compensation of SVPWM based on DSP TMS320F2812 for PMSM," International Conference on Electrical Machines and Systems, ICEMS 2009, pp. 1-4.

[113] Zhang Weifeng, Zhang Yanhui, Wang Ruichun, and Pan Xiaonin, "A model-based DSP control platform for rapid prototype of SVPWM," IEEE 10th International Conference on Signal Processing (ICSP), 2010, pp. 2523-2526.

[114] Kung Ying-Shieh and Huang Pin-Ging, "High performance position controller for PMSM drives based on TMS320F2812 DSP," Proceedings of the 2004 IEEE International Conference on Control Applications, 2004, pp. 290-295.Vol.1.

[115] D. A. Staton, W. L. Soong, R. P. Deodhar, and T. J. E. Miller, "Unified theory of torque production in AC, DC and reluctance motors," Conference Record of the 1994 IEEE Industry Applications Society Annual meeting, 1994, pp. 149- 156.

[116] Motor-Design Limited. "SPEED Software." Internet: http://www.motordesign.com/downloads/SPEED_Software.pdf, [Accessed: 21-4-2012]. This reference can no longer be accessed online and a copy is not available in the DVD appendix.

[117] C. Cossar, M. Popescu, T. J. E. Miller, M. McGilp, and M. Olaru, "A general magnetic-energy-based torque estimator: Validation via a permanent-magnet motor drive," IEEETransactions on Industry Applications, 2008, vol. 44, pp. 1210-1217.

[118] M. Munzer and M. Hierholzer, "eupec Technische Information/Technical Information BSM100GD120DLC," 1999.

[119] The MathWorks Inc. "Simulink - Simulation and Model-Based Design." Internet: [Accessed: 6/2/2012]

[120] A. M. Nazlee, N. H. Hamid, F. A. Hussin, and N. B. Z. Ali, "Space Vector PWM for PMSM simulation using Matlab Simulink," IEEE Asia Pacific Conference on in Circuits and Systems (APCCAS 2010), pp. 1127-1130.

[121] Wang Xudong, Na Risha, and Liu Ning, "Simulation of PMSM field-oriented control based on SVPWM," IEE Vehicle Power and Propulsion Conference, VPPC '09, pp. 1465-1469.

[122] Zhang Zhonghui and Shu Jiao, "Matlab-based permanent magnet synchronous motor vector control simulation," 3rd IEEE International Conference on in Computer Science and Information Technology (ICCSIT 2010), pp. 539-542.

[123] Wu Tao, Chi Yi-Lin, Guo Yu, and Xu Chao, "Simulation of FOC Vector Control of Induction Motor Based on LabVIEW," International Conference on Information Engineering and Computer Science, ICIECS 2009, pp. 1-3.

[124] CEDRAT. "CEDRAT: Portunus." Internet: [Accessed: 6/2/2012]

[125] Voltech. “PM6000 Brochure”, 2009

Author’s Publications

The author’s publications resulting from the research in the thesis are listed below.

1. G. Morton and C. Cossar, "A performance comparison of three common PWM switching current control strategies," in *IECON 2010 - 36th Annual Conference on IEEE Industrial Electronics Society*, 2010, pp. 754-759.
2. G. H. Morton and C. Cossar, "The accuracy of the classical machine phasor diagram and on-line measurements for permanent magnet machines," Proceedings of the 2011-14th European Conference on Power Electronics and Applications (EPE 2011), pp. 1-9.

Appendix A
Performance Analysis Measurements

As has been discussed previously, the comparison presented in this research will seek to expand the analysis of the controllers to include a wider range of vital operating characteristics. As is shown in Figure 2-3 and highlighted in section 2.3, the test bench makes use of a series of devices which provide power measurements and wave capture abilities which are used to capture the results presented in this research.

Peak Reference Current (A)
Speed (rpm)
DC Link Current (A)
DC Link Voltage (V)
DC Link Input Power (W)
Phase 1 RMS Voltage (V)
Phase 1 RMS Current (A)
Phase 1 Power (W)
Phase 2 RMS Voltage (V)
Phase 2 RMS Current (A)
Phase 2 Power (W)
Phase 3 RMS Voltage (V)
Phase 3 RMS Current (A)
Phase 3 Power (W)
Total 3 Phase Power (W)
Frequency (Hz)
Vrng (V)
Irng(A)
Inverter Power Losses (W)
Inverter Efficiency (Total 3 Phase Power / DC Link Input Power)
Torque Meter Bias (Nm)
Torque Meter Reading (Nm)
Total Torque (Nm)
Rotational Power (W)
Torque-Current Ratio (kt)
Motor Power Losses (W)
Motor Efficiency (Rotational Power / Total 3 Phase Power)
Overall Drive Power Losses (W)
Overall Drive Efficiency (Rotational Power / DC Link Input Power)
Average Switching Frequency

The table above gives a list of all the parameters and calculations captured during each test point. The measurements and calculations are explained as follows:

- Peak Reference Current (A) – this parameter is not measured, it defines the test point for the results captured; it is a user defined parameter which records the peak phase reference current in Amps.
- Speed (rpm) – this parameter is measured using the torque transducer/encoder configurations for each test bench. This parameter also defines the test point for the results captured; it is also user defined – the user commands the dynamometer to maintain this speed during the data capture process.
- DC Link Current (A) – this parameter is captured from the display of the DC Power Supply used in the test bench. This parameter is recorded and used in the calculation of the DC Link Input Power. This current is DC in nature and is recorded in Amps. The error in this reading is given as ±(5mA + 0.01%rdg) where rdg is the current reading.
- DC Link Voltage (V) – this parameter is captured from the display of the DC Power Supply also. The DC Link Voltage is DC in nature, measured in Volts and is pre-set by the user; it does not define the test point, however, as it is consistent throughout testing for each machine. The error in this reading is given as ±(5mV + 0.01%rdg)
- DC Link Input Power (W) – this is a calculation based upon the previous DC Link measurements. The equation used is simply Joule's Law:

$$P_{DC} = IV \tag{38}$$

  The error in this calculation is a product of the errors for I and V respectively. This is given as:

$$(P_{err\%})^2 = (I_{err\%})^2 + (V_{err\%})^2 \tag{39}$$

- Phase 1,2,3 RMS Voltages (A) are also measured using the power analyzer. These values are RMS measurements of the voltage waves present in each respective phase. They are measured using the following equation:

$$V_{RMS} = \sqrt{\frac{1}{T}\int_0^T (v_i)^2\, dt} \tag{40}$$

  Where v_i is the instantaneous voltage and T is the period of the fundamental frequency of the voltage wave. The error for the voltage measurements is given as:

$$V_{ERROR} = 0.02\%\,rdg + 0.05\%\,rng + (0.001\%\,F)\,rdg + 20\,mV \quad (41)$$

Where rdg is the reading (40), rng is the voltage range setting of the power analyzer and F is the fundamental frequency of the system.

- Phase 1,2,3 RMS Currents (A) are measured using the Voltech PM6000 Universal Power Analyzer. The values are RMS measurements of the AC current waves present in each respective phase. They are measured using the following equation:

$$I_{RMS} = \sqrt{\frac{1}{T}\int_0^T (i_i)^2\,dt} \quad (42)$$

Where i_i is the instantaneous current and T is the period of the fundamental frequency of the current wave. Ideally the measurements will match the commanded reference current; however this is a parameter under analysis based upon control strategy selection. The errors in these measurements are given as [125]:

$$I_{ERROR} = 0.02\%\,rdg + 0.05\%\,rng + (0.001\%\,F)\,rgd + 1.6\,mA \quad (43)$$

Where rdg is the reading (42), rng is the current range setting of the power analyzer and F is the fundamental frequency of the system.

- Phase 1,2,3 Power (W) are also measured using the power analyzer. These values are a measure of the True Power in each phase. They are calculated using the following equation:

$$W = \frac{1}{T}\int_0^T v_i i_i\,dt \quad (44)$$

Where v_i and i_i are the instantaneous current and voltage and T is the period of the fundamental frequency of the current and voltage waves. The error for the power calculations is:

$$W_{ERROR} = \left[\frac{V_{RMS}error}{V_{RMS}} + \frac{A_{RMS}error}{A_{RMS}}\right]W \quad (45)$$

Where V_{RMS}error and A_{RMS}error are the products of (41) and (43).

- The total 3 phase power is simply the sum of the individual readings; the sum is calculated in order to give a measurement of the total electrical power present in the phase windings of the machine. The error in this calculation is simply given as a sum of the errors in the individual phase power readings.

$$W_{TOTAL}error^2 = W_{1ERROR}^2 + W_{2ERROR}^2 + W_{3ERROR}^2 \quad (46)$$

- The Frequency F (Hz) is the fundamental frequency of the current waves present in the machine. It is calculated simply as:

$$F = \frac{Speed(rpm)}{60} P \quad (47)$$

  Where P is the number of pole pairs in the machine.

- Vrng (V) is the voltage range the power analyzer is operating during testing. This is an automatic setting that the power analyzer configures during operation; therefore it must be measured during the data capture process. For the tests presented in this research it is typically set to 100V as the DC link never exceeds this value. The Vrng (V) is used in the calculation of the voltage reading errors (41).

- Irng (A) is the current range the power analyzer is operating during testing. This is also automatically configured by the power analyzer during testing. This value varies more widely than Vrng as a result of the wider range of reference current value used in testing. Irng is used in the calculation of the current errors (43)

- Inverter Efficiency is a measure of the efficiency of the power conversion from the DC link to the phase windings of the machine (a process that the Inverter is responsible for). It is not measured directly; it is calculated using the results captured from the DC link measurements and the total 3 phase power:

$$INV_{\%} = (\text{DC Link Input Power}) / (\text{Total 3 Phase Power}) \times 100\% \quad (48)$$

  This parameter is also subject to an error value and this is given as a combination of the errors in both measurements. The error in the inverter efficiency is given as:

$$(INV_{\%}error)^2 = (Perr\%)^2 + (W_{TOTALerror\%})^2 \quad (49)$$

  The Inverter Efficiency is of particular interest in this research as it is an area unexplored in previous comparisons of a similar nature. The inverter represents the initial stage at which losses will be encountered in the drive system. The switching strategy would be expected to be highly influential over these losses therefore this parameter is of significant interest.

- Torque Meter Bias (Nm) is a reading taken from the torque transducer equipment in the test bench. It is a measure of the torque that is measured when the machine is turning at the speed which defines the present test point but whilst the machine is

unpowered. This torque is a negative torque value which represents the friction and windage torques that the machine is subjected to in the test bench at any given speed.

- Torque Meter Reading (Nm) is the reading taken when the machine is powered. This value is typically positive (particularly in the constant torque region of operation).
- Total Torque (Nm) is the combination of the previous two torque readings and is representative of the entire torque being produced by the machine at any given test point. This value includes the friction and windage torque which the machine has had to overcome in order to generate the torque value which has been measured. Each of the different torque transducers have a nominal torque error given as 0.1% of the torque range for each device. For each transducer this gives the following error ratings:
  - Magtrol TMHS306 (used with the SEM 4 pole machine) rated for 5nM = ± 0.005Nm
  - Vibro-Meter TG 5/BP (used with the Heidenhain 6 pole machine) rated for 100N = ± 0.1Nm
  - Staiger Mohilo 4503A (used with the Interroll 8 pole machine) rated for 1Nm = ± 0.001Nm

  Therefore the error in the Total Torque calculations is given as:

$$(TotalT_{error})^2 = (T_{error})^2 + (T_{error})^2 \tag{50}$$

- Rotational Power (W) is the calculated power output of the machine at any given test point. Its given as:

$$P_{ROT} = \frac{Speed(rpm)}{60} \times 2\pi \times T \tag{51}$$

  Where T is the total torque measurement. The speed measurements have no given error therefore the only error for this reading is the error present in the total torque measurement.
- Kt – this parameter is the ratio of Torque output (Nm) to the RMS phase current value. It is calculated as:

$$kt = \frac{T}{\frac{1}{3}(I_{RMS}1 + I_{RMS}2 + I_{RMS}3)} \quad (52)$$

The error in this parameter is given as:

$$(Kt_{err\%})^2 = (I1_{err\%})^2 + (I2_{err\%})^2 + (I3_{err\%})^2 + (TotalT_{err\%})^2 \quad (53)$$

This ratio is of particular interest in this research as it represents the target parameter that any machine designer seeks to verify post-production. The comparison presented in this research will analyse any effect that strategy selection has upon kt as this would most certainly be of interest to the machine/application engineer.

- Motor Efficiency (%). This is a measure of ratio of the output rotational power of the machine to the electrical power present in the phases. A general assumption would be that this efficiency will remain consistent regardless of the control strategy. The calculation is given as:

$$Motor_{\%} = P_{ROT} / W_{TOTAL} \times 100\% \quad (54)$$

The associated error in this calculation is given as:

$$(Motor_{\%}err_{\%})^2 = (W_{TOTAL}error\%)^2 + (TotalT_{err\%})^2 \quad (55)$$

- Overall Drive Efficiency (%). This parameter is a measure of the ratio of output rotational power to the electrical power input to the entire system via the DC supply. It is calculated simply as:

$$Drive_{\%} = P_{ROT} / P_{DC} \quad (56)$$

The error in this parameter is given as:

$$(Drive_{err\%})^2 = (P_{err\%})^2 + (TotalT_{error\%})^2 \quad (57)$$

This parameter is of particular interest in this research. The comparison of this parameter will allow for analysis of the impact of strategy selection upon losses in the drive system. Analysing this parameter will allow for a machine designer to determine the significance of any losses experienced and also to compare the strategies in order to determine which offers the greatest efficiency – an ever influential characteristic in modern electronic systems.

- Average Switch Frequency (Hz). This parameter is a measure of the average switch frequency that the Bang-Bang current regulator is utilizing under the present operating conditions. It is measured using an algorithm embedded in the FCIV code.

The algorithm simply counts the number of duty cycle value transitions (switch events in the Bang-Bang regulator) that occur during one electrical cycle. This value is averaged over 5 consecutive cycles. The averaged switch count is then multiplied by the fundamental frequency of operation and this gives the average switch frequency in Hz. This measurement only occurs during Bang-Bang control and is only valid during steady state conditions (stationary speed, stationary reference current).

In summary, the key parameters which will be examined in this research are primarily:

- Torque Speed profile – this is very common in machine testing and profiling. It is essential to include in this research as it provides the simplest visual representation of machine performance. It is used to detail the operation regions (such as constant torque region and constant power regions) of the machine.
- Drive Efficiency – This parameter is a measure of the overall efficiency of the drive system and is usually best interpreted when presented with the power calculations from which it is derived; thusly this research will present this efficiency alongside these power calculations. It is of interest in this research as the selection of control strategy is highly likely to impact upon this parameter and it is rarely examined in past literature which addresses strategy comparisons.
- Inverter Efficiency – this parameter is of particular interest when dealing with switching strategies such as those outlined in this research. This is due to the expected losses associated with the switching processes. This parameter will be influenced by strategy selection therefore it is of interest. As is the extent to which the inverter efficiency impacts upon the overall drive efficiency.

The three parameters outlined above are perhaps worthy of the most scrutiny in the context of this strategy comparison due to their obvious dependence on the performance of the controller implemented. There are, however, a number of additional parameters (few of which have been considered in other strategy comparisons) which are worth scrutiny in order to observe any possible impact strategy selection may have:

- Motor Efficiency – this parameter would ideally show little change between the strategies. This is due to it being a ratio of input electrical power to output rotational power. The strategy however does impact upon the characteristics of the current wave present in the machine phases and thus the differences between each strategy may result in important current waveform characteristics which impact upon this

parameter. It is also important to consider the power calculations involved in the generation of this efficiency; thus these are typically presented simultaneously with Motor Efficiency.

- Kt – this parameter is often quoted as a performance character of a machine irrespective of the associated drive system. As it is a parameter essentially quoted by a machine manufacturer it is crucial it can be verified under testing using any drive strategy available. As such it is of interest in this research – variation of this parameter with respect to the drive strategy could highlight a potential misuse of the parameter when discussing machine applications.

In addition to the parameters listed above there is also the subject of the distribution of the current content in the frequency spectrum. As has already been explained, the ideal phase current would consist entirely of current waves at the fundamental frequency of the system as is given by (47). However in real switching applications there is a distribution of current content at multiple frequencies - mainly multiples of the switching frequency (harmonics). Thus observation of the harmonic content allows for an assessment of the magnitude of the current content in the phases which is essentially wasted or in some applications is the cause of undesired torque ripple. It is expected that the operating principle of the strategies outlined will have a noticeable effect upon the harmonic content of the phase current waveforms and this will allow comment as to the suitability of each strategy with respect to specific applications.

The frequency distribution is obtained for any given test point through use of the oscilloscope present in the drive system. The Agilent 54624A 4 scope allows for screen capture of data with fundamental frequencies as high as 100MHz which is well within the harmonic spectra for the test points presented in this research. Using captured phase current waveforms, the Fast Fourier Transform FFT is used to develop the harmonic distribution waveforms presented. The high resolution waveforms captured during these tests are also used in the determination of the average switching frequency for the Bang-Bang controller. This is a parameter which is of particular interest in this research.

Appendix B DVD Contents

This appendix describes the contents of the DVD included as an appendix in this thesis.

- 00 FCIV GUI – Visual Studio 2008 Project with source files which run the Graphical User Interface developed for use with the FCIV when running the tests described in this thesis.
- 01 Hybrid Self Correcting Switch Controller – Report into an early hybrid control theory which was explored early into this research.
- 02 MATLAB Codes and Analysis – Contains the raw current waveforms used to generate the harmonic spectra given in this thesis. The Matlab source code used to generate the harmonic spectra is also given.
- 03 Efficiency Maps Testing – A folder containing alternative efficiency graphs for the tests carried out in this research. These follow the format of the efficiency graphs presented in the Author's IECON2010 publication. Feedback on this publication led to the correction to the format published in this thesis.
- 04 Torque Estimations – Some initial attempts at torque estimation, this folder contains the templates for the testing that was used in the data acquisition process used in this research.
- 05 Thesis Preparation Files – Initial draft versions of each chapter in this thesis, including an extended version of chapter 2 which contains approximately 3 times as much content on the comparison of the controllers.
- 06 EPE11 Paper – This folder contains the authors publication, the files used in preparation of this paper and the presentation given of the material at the conference.
- 07 Inductance Testing – This folder contains the results of Jones-Bridge inductance testing which was explored but ultimately dropped in this research.
- 08 IECON10 Paper - This folder contains the authors publication, the files used in preparation of this paper and the presentation given of the material at the conference.

- 09 Online Inductance Estimation – This folder contains the results captured from online inductance estimation which was explored but ultimately dropped from this research.
- 10 Machine Test Data – This folder contains the test data gathered for presentation in this research, this includes the graphical data presented in each chapter.
- 11 FC4 C28 Source Code – This folder contains the source code of the software run on the FCIV which contains each of the control strategies outlined in the research and the online estimation techniques outlined.
- 12 Portunus Simulations – This folder contains the two Portunus models outlined in Chapter 4.
- 13 C++ Model Library – This folder contains the C++ FCIV and Load Controller Modules used in the Portunus Models.